To the Graduate Council:

I am submitting herewith a dissertation written by Philip James Maziasz entitled "Effects of Helium Content on Microstructural Development in Type 316 Stainless Steel under Neutron Irradiation." I have examined the final copy of this dissertation for form and content and recommend that it be accepted in partial fulfillment of the requirements for the degree of Doctor of Philosophy, with a major in Metallurgical Engineering.

Carl J. McHargue

Carl J. McHargue, Major Professor

We have read this dissertation
and recommend its acceptance:

Paul H. Stelson

J. E. Spruiell

C. R. Brooks

E. E. Stansbury

Ben T. Cleveland

Accepted for the Council:

Lew Minkel

The Graduate School

EFFECTS OF HELIUM CONTENT ON MICROSTRUCTURAL DEVELOPMENT IN TYPE 316 STAINLESS STEEL UNDER NEUTRON IRRADIATION

A Dissertation

Presented for the

Doctor of Philosophy

Degree

The University of Tennessee, Knoxville

Philip James Maziasz

December 1984

ACKNOWLEDGMENTS

The author would like to express thanks to his major professor, Dr. C. J. McHargue, for direction, patience and encouragement, together with the Metallurgical Engineering Department at the University of Tennessee, Knoxville, during these ten years of instruction and research. Particular thanks go to the members on this doctoral committee: Profs. J. E. Spruiell, B. F. Oliver, C. R. Brooks, E. E. Stansbury, all from the Metallurgy Department, and P. H. Stelson from the Physics Department.

This research was carried out in the Radiation Effects and Microstructural Analysis Group (REMAG) of the Metals and Ceramics Division at the Oak Ridge National Laboratory under contracts with Union Carbide Corporation and, more recently, Martin Marietta Energy Systems, Inc. The work was funded by the Office of Fusion Energy in its various forms under first the U.S. Atomic Energy Commission, then the Energy Research and Development Administration, and at present by the U.S. Department of Energy. Sincere thanks go to Dr. T. C. Reuther, who has administered the funding as well as supported and encouraged the work of this author. The group leaders of REMAG have been particularly instrumental in encouraging this thesis. This author is grateful to Dr. J. O. Stiegler for guidance into the Ph.D. program and moral support thereafter, to Dr. E. E. Bloom for many of the samples irradiated earlier in the Experimental Breeder Reactor-II (EBR-II) and the High Flux Isotope

Reactor (HFIR) and then direct guidance of this author's own experiments, and finally to Dr. A. F. Rowcliffe for the inducements to write. Experimental help is acknowledged to J. Woods for assembling HFIR and EBR-II experiments, Dr. J. A. Horak and B. L. Cox for having helium preinjected in some of the specimens at the Oak Ridge Isochronous Cyclotron (ORIC), and the workers at the hot cells, H. Blevins, E. Gilbert, and W. Henry, led by A. A. Walls for experimental disassembly (together with Dr. M. L. Grossbeck in some cases). This author thanks Drs. F. W. Wiffen, M. L. Grossbeck, W. A. Coghlan (now at Arizona State), P. S. Sklad, E. A. Kenik, E. H. Lee, L. K. Mansur, N. H. Packan, and K. Farrell in REMAG for helpful discussions on many aspects of radiation damage related to the work. Discussions and encouragement from Dr. N. M. Ghoniem at the University of California, Los Angeles (UCLA), and especially Dr. G. R. Odette at the University of California, Santa Barbara (UCSB), with regard to this thesis and particularly the effects of helium, are gratefully acknowledged.

Special mention and thanks must go to those involved with introducing this author to the fields of radiation damage and TEM (and AEM). This author owes thanks to Drs. D. Vincent and J. King at the University of Michigan, Ann Arbor, for an introduction to general radiation damage, and to Drs. H. Wiedersich and P. R. Okamoto at the Argonne National Laboratory (ANL) for an introduction to Radiation Induced Solute Segregation and Phase Stability studies at the Summer Materials Science Institute attended in 1974 in pursuit of a Master's degree. This author is appreciative of the introduction to TEM by Dr. W. Bigelow at U.M. and Dr. P. R. Okamoto at ANL, and especially the intense personal training

received under Dr. R. W. Carpenter at ORNL and UT (now at Arizona State). This author is indebted to Dr. N. J. Zaluzec (now at ANL) for invaluable instruction at ORNL in both the methods and theory of AEM (together with Dr. J. Bentley) and for the computer software so necessary for data reduction. This author thanks B. L. Cox and more recently N. Rouse for thinning and handling of many radioactive as well as unirradiated TEM disks so necessary to this work. Also special thanks to Frances Scarboro for patient and extremely proficient typing (and editing) of this manuscript.

Personal appreciation goes to this author's family, especially my wife Veronica, and my sons Andrew (for nearly seven years) and Matthew (several weeks) for supporting him through this arduous time (approximately ten years) with love and encouragement that make it all worthwhile, together with encouragement from my father and mother, Chester and Frances Maziasz, brother Bob and in-laws (Edmund, Joan, Steve, and Jeffery Sadowski). Finally, I humbly thank God, who enables me through Jesus Christ in all I do.

ABSTRACT

This work investigated the sensitivity of microstructural evolution, particularly precipitate development, to increased helium content during thermal aging and during neutron irradiation. Helium (110 at. ppm) was cold preinjected into solution annealed (SA) DO-heat type 316 stainless steel (316) via cyclotron irradiation. These specimens were then exposed side by side with uninjected samples. Continuous helium generation was increased considerably relative to EBR-II irradiation by irradiation in HFIR. Data were obtained from quantitative analytical electron microscopy (AEM) in thin foils and on extraction replicas.

Normal aging produced small amounts of $M_{23}C_6$ (τ) precipitation at 560 to 600°C, and τ plus large amounts of Laves phase at 650 to 700°C. Preinjected helium eliminated τ and replaced it with Laves at 600 and 700°C. Interstitial "black-dot" Frank loops were introduced via preinjection. These grew and coarsened upon long-term aging at 400 to 600°C, and then unfaulted at 700°C, apparently to provide vacancies for growing helium-vacancy clusters and bubbles.

Normal EBR-II irradiation produced dislocation loops and network, precipitate-associated and matrix voids, and precipitation of mainly M_6C (η) plus a minor assortment of irradiation-produced phases [G, γ' (Ni_3Si) plus A and B phosphides] at 500 to 630°C and 8.4 to 36 dpa (except at 630°C and 36 dpa, where Laves plus η formed). Helium preinjection eliminated void formation and eliminated RIS-induced or -modified precipitation at 500 to 625°C and 8.4 dpa. Early fine bubble

nucleation apparently caused an overwhelmingly bubble-dominated sink structure that also diluted RIS to eliminate precipitation at 500°C and yet allow enhanced thermal precipitation at 625°C.

The results of HFIR irradiation at 500 to 650°C were intermediate to those described above due to intermediate levels of bubble nucleation and evolution. Void formation was initially suppressed but then, at higher fluences, enhanced; maximum RIS was observed at 425 to 450°C, but RIS intensity was reduced at 515 to 555°C and virtually eliminated at higher temperature. Enhanced thermal precipitation dominated above 550°C, and void swelling appeared cut off above 650°C.

This thesis includes an extensive literature survey of data on SA 316 and of relevant theoretical work which provides the perspective necessary to discuss and understand the data.

PREFACE

The field of Radiation Damage or Effects was born from the predictions of Dr. Eugene P. Wigner that materials intensely irradiated in nuclear reactors would undergo physical properties degradation. As the nuclear age developed, many researchers studied radiation damage of crystalline materials and their subsequent effects on properties changes in materials under irradiation. These studies provided a foundation for the development of commercial nuclear power and also contributed much to our knowledge of the physics of the solid state. The field of transmission electron microscopy (TEM) was ideally suited to the study of minute microstructural effects of irradiation. Many TEM analysis techniques have developed in parallel with specific problems posed by irradiation damage. Studies of irradiation effects have progressed from moderator graphite for early atomic piles to uranium (metal and oxide) fuels and their claddings for both thermal and fast (breeder) fission reactor systems. Currently, the fusion reactor environment is a growing area of challenge for irradiation effects studies. Though earlier studies had for years concentrated on the development of cavities and dislocations, one of the most exciting areas opened up by recent advances in analytical electron microscopy is the study of precipitation and microcompositional changes. This new information should hopefully advance the understanding of chemical reactions in the solid state.

TABLE OF CONTENTS

CHAPTER		PAGE
I.	INTRODUCTION	1
II.	LITERATURE SURVEY AND SUMMARY	7
	Primary Damage	7
	Vacancies and Interstitials	7
	Gaseous Transmutants: Helium and Hydrogen	14
	Solid Transmutants: Manganese and Vanadium	20
	Secondary Damage	23
	Dislocation Microstructure	24
	Cavity Microstructure	36
	A. Bubbles	36
	B. Voids	46
	Precipitation and Microcompositional Development	75
	A. Radiation-Enhanced Diffusion and Induced Solute Segregation	76
	B. Thermal Precipitation	83
	C. Precipitation Under Irradiation	102
	Summary of Literature Survey	121
	Primary Damage	121
	Secondary Damage	122
III.	EXPERIMENTAL	126
	Specimen Preparation	126
	Exposure Environments	127
	Helium Preinjection	127

CHAPTER PAGE

III. (Continued)

Thermal Aging 128

EBR-II Irradiations 129

HFIR Irradiation 130

Specimen Examination 132

Immersion Density 132

Conventional Transmission Electron Microscopy (CTEM) 133

Analytical Electron Microscopy (AEM) 137

IV. RESULTS 142

Thermally Aged SA 316 142

Dislocation Evolution 142

Precipitation 143

A. Microstructural Data 143

B. Microcompositional Data 150

Helium Preinjected and Thermally Aged SA 316 155

Dislocation Evolution 155

Cavity Evolution 161

Precipitation 163

EBR-II Irradiated SA 316 Data 165

Dislocation Evolution 165

Cavity Evolution 168

Precipitation 170

A. Microstructural Data 170

CHAPTER PAGE

IV. (Continued)

B. Microcompositional Data 177

Helium Preinjected and EBR-II Irradiated SA 316 185

Dislocation Evolution 185

Cavity Evolution 187

Precipitation 188

A. Microstructural Data 188

B. Microcompositional Data 190

HFIR Irradiated SA 316 190

Dislocation Evolution 191

Cavity Evolution 198

Precipitation 207

A. Microstructural Data 207

B. Microcompositional Data 214

V. DISCUSSION 221

Microstructural Couplings and Mechanisms Suggested from the Data 221

Dislocation Evolution 222

Cavity Evolution 226

Precipitate Evolution 230

Comparison of Microstructural Couplings and Mechanisms with Theory/Modeling Work of Others 239

Dislocation Evolution 239

Cavity Evolution 240

CHAPTER PAGE

V. (Continued)

Precipitate Evolution 245

Suggested Future Experimental Work and Implications for Fusion Application 249

VI. CONCLUSIONS 251

Conclusions and Summary of Results 251

Thermally Aged SA 316 251

Helium Preinjected and Aged SA 316 251

EBR-II Irradiated SA 316 252

Helium-Preinjected and EBR-II Irradiated SA 316 . . 253

HFIR Irradiated SA 316 253

Comparison with Previous Data 254

Conclusions and Summary of Discussion 255

Suggested Couplings and Mechanisms from Results . . . 255

Comparison of Results with Theory and Modeling Effects 256

Suggested Future Experimental Work and Implications for Fusion Application 258

REFERENCES 259

APPENDIXES 293

Appendix A 294

Appendix B 299

VITA 302

LIST OF TABLES

TABLE		PAGE
1.	Dpa, Gaseous, and Solid Transmutant Production per Year for Type 316 Stainless Steel Irradiated in Various Reactors	16
2.	Compositions of Type 316 Stainless Steel Investigated in Other Work	27
3.	Fluence Exponents of Void Growth for Limiting Cases and Different Mechanisms of Point Defect Absorption at Void	64
4.	A Summary of Solute Information Relevant to Radiation-Induced Solute Segregation and Austenite Stability in Type 316 Stainless Steel	81
5.	General Crystallographic and Compositional Information on Phases Found in Type 316 Stainless Steel or Related Alloys During Aging or Neutron Irradiation	88
6.	Composition of DO-Heat Type 316 Stainless Steel	126
7.	Exposure Parameters for SA 316 (DO-Heat) Specimens Irradiated in HFIR	131
8.	Dislocation and Precipitate Microstructural Data on Thermally Aged SA 316	144
9.	XEDS Compositional Information for Matrix and Precipitate Phases in Thermally Aged SA 316	151
10.	Dislocation and Cavity Microstructural Data for Helium Preinjected (110 at. ppm) and Thermally Aged SA 316	156
11.	Dislocation and Cavity Microstructural Data for SA 316 Irradiated in EBR-II	166
12.	Precipitate Microstructural Data for SA 316 Irradiated in EBR-II	171
13.	XEDS Compositional Information for Matrix and Precipitate Phases in SA 316 Irradiated in EBR-II	178
14.	Dislocation and Cavity Microstructural Data for SA 316 Irradiated in HFIR	195

TABLE PAGE

15. Precipitate Microstructural Data on SA 316 Irradiated in HFIR 208

16. XEDS Compositional Data for Precipitate Phases in SA 316 Irradiated in HFIR 216

17. A Summary Correlation of Data Trends and Couplings, Suggested Mechanisms, and Their Comparison with Theory/ Modeling Work for Dislocation Evolution in SA 316 223

18. A Summary Correlation of Data Trends and Couplings, Suggested Mechanisms, and Their Comparison with Theory/ Modeling Work for Cavity Evolution 227

19. A Summary Correlation of Data Trends and Couplings, Suggested Mechanisms, and Their Comparison with Theory/ Modeling Work for Precipitate Evolution in SA 316 232

LIST OF FIGURES

FIGURE		PAGE
1.	A schematic representation of a displacement cascade produced by a neutron collision with the lattice	9
2.	A plot of differential neutron flux as a function of neutron energy for HFIR, ORR, EBR-II, and a fusion spectrum (at 3 MW/m^2 wall loading)	13
3.	A plot of helium generation as a function of displacement damage level for type 316 stainless steel irradiated in HFIR, EBR-II, or a Magnetic Fusion Reactor (MFR)	17
4.	Transmutation-induced compositional changes calculated for type 316 as a function of fluence for (a) vanadium and (b) manganese for several irradiation environments . .	22
5.	A plot of dislocation structure character as functions of temperature and fluence for FBR-irradiated SA 316	26
6.	Frank loop size, loop concentration and total dislocation density are plotted as functions of temperature (a,c,e, respectively) and fluence (b,d,f, respectively) for FBR-irradiated SA 316 from various investigators	30
7.	A plot of qualitative observations of loop and bubble growth as functions of time and temperature for the data of Mazey and Francis on SA 316 aged with 100 at. ppm preinjected helium	39
8.	Plots of bubble size and concentration for aged SA 316 containing 100 at. ppm preinjected helium	39
9.	A plot of cavity character as functions of temperature and fluence for FBR-irradiated SA 316	50
10.	Void size, void concentration, and total swelling are plotted as functions of temperature (a, c, e, respectively) and fluence (b, d, f, respectively) for FBR-irradiated SA 316 from various investigators	51
11.	A schematic representation of the swelling-fluence relationships possible as the balance between total dislocation and cavity sink strength changes	65

FIGURE PAGE

12. A schematic of the correlated relationship between microchemical evolution and macroscopic swelling behavior, as envisioned by Garner (reference found in text) 74

13. Correlation of matrix nickel content and the presence or absence of voids in type 316 stainless steel, after EBR-II irradiation to the conditions indicated, from the data of Brager and Garner (data reference found in text) . . . 74

14. Auger electron spectroscopy (AES) compositional profiles of ion-bombarded surfaces as functions of sputtering depths for the irradiation conditions and alloys indicated . . . 80

15. An Fe-Cr-Ni-X quaternary phase diagram calculated for type 316 stainless steel for aging at 650°C by Shoa and Macklin [Met. Trans. 10A (1979) 585–590)] 84

16. A plot of precipitate phase formation as functions of time and temperature for precipitation in aged SA 316 94

17. A schematic of solute depletion (a) and enrichment (b) in precipitate phase particles during thermal aging and the associated concentration profiles (dc/dx) and solute flow directions ($j\mu_i$) needed to accomplish this during particle growth 101

18. A plot of various precipitation phenomena as functions of temperature and fluence for FBR-irradiated SA 316 108

19. Schematic conceptual representation of how the mechanisms of (a) cascade recoil dissolution and (b) formation of microcompositional regions due to RIS affect phase stability under irradiation 115

20. A schematic of (a) solute depletion and (b) solute enrichment induced in precipitate particles by RIS during irradiation 117

21. Drawings and dimensions of tensile specimens which were irradiated and then sectioned to obtain TEM specimens . . 127

22. Specimens and target assembly used for helium preinjection in ORIC 128

23. A schematic drawing of a specimen holder and buttonhead tensile specimens used in EBR-II X-100 materials irradiation experiment 130

FIGURE PAGE

24. Calculated axial temperature distribution for (a) specimens irradiated in earlier HFIR experiments (SS-2 through -8) and (b) specimens irradiated in later HFIR experiments (CTR-9 through -13) 133

25. A comparison of (a) replica film and (b) thin foil in-hole background XEDS spectra for these specimens prepared from SA 316 stainless steel irradiated in EBR-II at 630°C to 36 dpa 138

26. A schematical representation of the extraction replica process illustrating (a) surface cleaning via electropolishing, (b) surface relief attained via light electroetching, (c) carbon film deposition, and (d) replica removal via further electroetching 139

27. Comparative TEM of (a) an extraction replica and (b) a thin foil produced from SA 316 irradiated in EBR-II at 630°C to 36 dpa 140

28. A low magnification TEM photomicrograph of a replica produced from SA 316 irradiated in EBR-II at 500°C to 31 dpa to illustrate the preservation of grain boundary imprints and precipitate association 141

29. Total dislocation network concentration (Λ) plotted as a function of aging temperature for SA (DO-heat) 316 . . . 143

30. Micrographs showing the dislocation contents and configurations in SA (DO-heat) 316 aged at (a) 470°C for 4400 h (no precipitation) and (b) 650°C for 10,000 h ($M_{23}C_6$, M_6C, and Laves precipitation) at lower magnification and at (c) 600°C for 10,000 h ($M_{23}C_6$ precipitation) at higher magnification 145

31. A plot of precipitate phase formation (grain boundary phases included) as functions of aging time and temperature for SA (DO-heat) 316 146

32. A plot of relative and total phase volume fractions for matrix precipitation as functions of aging temperature and time for SA (DO-heat) 316 147

33. Microstructures illustrating intragranular precipitate coarsening with increasing temperature for SA (DO-heat) 316 aged for 4400 h 148

FIGURE PAGE

34. (a) Phase particle size (d_p), represented by the maximum linear dimension, for various morphological variants, and (b) total precipitate concentrations (N_p) are plotted as functions of aging temperature for several different aging times 149

35. Progressive nucleation of $M_{23}C_6$ (τ) as time increased for SA (DO-heat) 316 aged at 560°C for (a) 2770 h and (b) 4400 h 149

36. SA (DO-heat) 316 aged for 10,000 h at 650°C to illustrate clustered nucleation of particles about common centers 150

37. Histograms of compositional distributions of metallic elements in the various phases found in thermally aged SA (DO-heat) 316: (a) $M_{23}C_6$ (τ), (b) M_6C (η), (c) Laves, (d) χ, and (e) σ, with aging temperatures indicated . . 153

38. Broad beam averaged compositions of the total precipitate for chromium, molybdenum, iron, and nickel plotted as functions of temperature for aging times of 2770 and 10,000 h 154

39. Loop, bubble, and precipitate microstructural observations are plotted as functions of aging temperature and time for SA (DO-heat) 316 cold preinjected with 110 at. ppm He 157

40. Comparison of loop structures of helium preinjected (110 at. ppm) SA (DO-heat) 316 158

41. (a) Frank loop concentration (N_ℓ), (b) Frank loop diameter (d_ℓ) and total dislocation concentration (Λ) plotted as functions of aging temperature after 1000 and 10,000 h for helium preinjected SA (DO-heat) 316 (110 at. ppm) 159

42. Microscopy which identifies Frank interstitial loops found in helium preinjected SA (DO-heat) 316 aged at 400°C for 1000 h [(a), (b),(d), and (e)], at 500°C for 10,000 h (c), and at 600°C for 1000 h [(f),(g), and (h)] 160

43. Bubble evolution in helium preinjected SA (DO-heat) 316, aged for 10,000 h at (a) 500°C, (b) 600°C, and (c) 700°C 162

FIGURE PAGE

44. A comparison of grain boundary in (a) uninjected and (b) helium preinjected SA (DO-heat) 316 aged for 10,000 h at 700°C to illustrate bubble formation at the boundaries and at the interfaces of σ phase particles in (b) 162

45. A comparison of precipitation in SA (DO-heat) 316 aged for 10,000 h at 600°C without (a)—(c) and with (b)—(d) preinjected helium; (a) and (b) show grain boundaries and matrix at lower magnification and (c) and (d) show TiN inclusions in the matrix at higher magnification 164

46. Dislocation evolution as functions of fluence in SA (DO-heat) 316 irradiated in EBR-II at 500 to 525°C and 625 to 630°C 167

47. Void evolution in SA (DO-heat) 316, irradiated in EBR-II at (a) 500°C and (b) 625°C to 8.4 dpa, (c) 525°C to 31 dpa, and (d) 630°C to 36 dpa 168

48. Cavity microstructural evolution in EBR-II-irradiated SA (DO-heat) 316 at 500 to 630°C, showing (a) bubbles, matrix voids, and precipitate-associated void concentrations as functions of fluence, and (b,c) size distributions of bubbles and voids at 500 to 525°C and 625 to 630°C, respectively 169

49. Fine matrix bubbles observed in SA (DO-heat) 316 irradiated in EBR-II at 525°C to 31 dpa 170

50. Bubble development in SA (DO-heat) 316 irradiated at 625 to 630°C in EBR-II to (a) 8.4 dpa and (b) 36 dpa . . . 172

51. A plot of relative and total phase volume fraction for matrix precipitation as functions of temperature and fluence for EBR-II-irradiated SA (DO-heat) 316 173

52. (a) Particle size (d_p) (maximum linear dimension) for various morphological variants and (b) particle concentrations plotted as functions of temperature and fluence, respectively, for various phases formed in EBR-II-irradiated SA (DO-heat) 316 175

53. Sympathetic nucleation and/or coupled growth of (a) M_6C (η) phase particles around voids, and (b) phosphide B needles clustered about TiN particles in SA 316 irradiated in EBR-II at 625°C to 8.4 dpa 176

FIGURE PAGE

54. Histographs of metallic element composition for the various radiation-induced or -modified phases formed in neutron-irradiated SA (DO-heat) 316 180

55. Correlation between morphology and characteristic XEDS spectra that helped distinguish between phosphides A and B in SA (DO-heat) 316 irradiated in EBR-II at 500°C to 8.4 dpa 181

56. Characteristic XEDS spectra of (a) $M_{23}C_6$ (τ) and (b) M_6C (η) particles found at grain boundaries on a replica produced from SA (DO-heat) 316 irradiated in EBR-II to 31 dpa at 525°C 182

57. Individual phase (a) and broad-beam whole precipitate (b–d) compositional analyses from XEDS performed on extraction replicas for molybdenum and nickel contents as functions of temperature (a,b) and manganese (c) and phosphorus (d) contents as functions of fluence 183

58. The effects of 110 at. ppm preinjected helium on dislocation evolution in SA (DO-heat) 316 irradiated side by side in EBR-II to 8.4 dpa at 500°C (a,c) and at 625°C (b,d) 186

59. The effect of preinjected helium on void formation and precipitation in SA (DO-heat) 316 irradiated side by side in EBR-II at 625°C to 8.4 dpa 187

60. The effect of irradiation temperature on bubble formation in helium preinjected SA (DO-heat) 316, irradiated in EBR-II to 8.4 dpa at (a) 500°C and (b) 625°C 188

61. Dislocation development with increased temperature for SA (DO-heat) 316 irradiated in HFIR to 5.3 to 12 dpa at (a) 325 to 350°C, (b) 425 to 450°C, (c) 515 to 540°C, and (d) 615 to 640°C 192

62. Dislocation evolution in SA (DO-heat) 316 irradiated in HFIR with (a) loop diameter (d_ℓ), (b) loop concentration (N_ℓ), (c) total dislocation concentration (Λ) plotted as functions of temperature, and (d) Λ plotted as a function of fluence 193

63. Mixed Frank interstitial and "black-dot" loop damage in SA (DO-heat) 316 irradiated at 55°C to 7.8 dpa in HFIR . . 197

FIGURE PAGE

64. Cavity character plotted as functions of temperature and fluence for HFIR irradiated SA (DO-heat) 316 199

65. Evolution of cavity sizes (d_b and d_v) and distributions with fluence increased for SA (DO-heat) 316 irradiated in HFIR at (a) 425 to 450°C, (b) 515 to 555°C, (c) 600 to 640°C, and (d) 730 to 755°C 200

66. Swelling plotted as functions of (a) temperature and (b) fluence for SA (DO-heat) 316 irradiated in HFIR . . . 201

67. Plots of concentrations of the various cavity components found in HFIR irradiated SA (DO-heat) 316 as functions of (a) irradiation temperature and (b) fluence 202

68. Cavity evolution in SA (DO-heat) 316 irradiated in HFIR at 515 to 555°C (a,c,e) and 600 to 640°C (b,d,f) as functions of fluence; (a) 12 dpa, (b) 10 dpa, (c) 17.8 dpa, (d) 16.6 dpa, and (e),(f) 47 dpa 203

69. The transition from voids (especially precipitate-associated voids) to coarse, high-temperature bubbles for SA (DO-heat) 316 irradiated in HFIR at (a) 580 to 605°C and (b) 730 to 755°C to 64 to 68.5 dpa and 4000 to 4140 at. ppm He 204

70. Evolution of grain boundary bubbles with increased helium generation at 600 to 630°C, comparing SA 316 irradiated in (a) EBR-II to 36 dpa and 22 at. ppm He and (b) HFIR to 47 dpa and 3000 at. ppm He, and with increased temperature for the high helium generation in HFIR, comparing (b) with (c) HFIR irradiated at 730 to 755°C to 53 dpa and 3300 at. ppm He 205

71. Strange appearance of many fine bubbles among voids; these were not visible among coarser bubbles at lower fluence, comparing SA (DO-heat) 316 irradiated in HFIR at 515 to 555°C to (a) 12 dpa and (b) 47 dpa 206

72. A plot of precipitate phase formation (grain boundary phases included) as functions of temperature and fluence for SA (DO-heat) 316 irradiated in HFIR 207

73. A plot of relative and total phase volume fractions for matrix precipitation as functions of temperature and fluence for HFIR irradiated SA (DO-heat) 316 209

FIGURE PAGE

74. Phase particle sizes (d_p), represented by the maximum linear dimension, for various morphological variants as function of temperature and (b) total precipitate concentrations (N_p) as functions of fluence for SA (DO-heat) 316 irradiated in HFIR at various conditions 210

75. Microstructural evolution of (a) and (b) M_6C phase, using bright-field imaging, and (c) and (d) γ' (Ni_3Si) phase, using dark-field imaging, for SA (DO-heat) 316 irradiated in HFIR at 425 to 450°C to 9.2 dpa (a),(c) and 14.3 dpa (b),(d) 211

76. Precipitate development in SA (DO-heat) 316 irradiated at 515 to 555°C (a),(c),(e) and 615 to 640°C (b),(d),(f) for fluences ranging from 10 to 47 dpa 212

77. Sigma phase formation in SA (DO-heat) 316 irradiated in HFIR to (a) 17 dpa at 615 to 640°C and (b) 48 dpa at 730 to 755°C 213

78. (a) Individual phase and (b) broad beam whole precipitate compositional analyses from XEDS performed on extraction replicas for molybdenum and nickel concentrations as functions of temperature at several fluences for SA (DO-heat) 316 irradiated in HFIR 217

79. Silicon and vanadium concentrations as functions of fluence for whole precipitate broad beam XEDS analyses performed on extraction replicas obtained from SA (DO-heat) 316 irradiated in HFIR at 515 to 555°C at 12 and 47 dpa 219

80. A spectrum of correlated phase formation, compositional enrichments, and RIS effects for neutron irradiated type 316 stainless steel 236

CHAPTER I

INTRODUCTION

The purpose of this study was to observe the sensitivity of microstructural evolution to varying irradiation parameters like temperature, fluence, and especially helium generation or content, for solution-annealed type 316 stainless steel (SA 316) under neutron irradiation. This study is of interest because it contributes understanding to a major class of alloys being developed for irradiation resistance by the Magnetic Fusion Energy (MFE) materials effort.[1,2] The irradiation resistance of SA 316 is not of direct interest, but it was chosen for this study because microstructural development is simpler, more straightforward, and easier to observe via TEM than complex, heavily cold-worked steels which are more irradiation resistant.[2-5]

Austenitic stainless steel application in various fission energy systems forms an experience base for their consideration in designs of fusion energy systems. Type 316 in particular offers excellent corrosion/oxidation resistance (especially in aqueous environments) and good creep resistance at elevated temperatures.[6,7] These alloys are steels because they contain dissolved carbon (less than 1.4 wt % C in Fe), and are stainless because they contain more than 12 wt % Cr. The addition of molybdenum (2—3 wt % Mo) enhances their corrosion and elevated-temperature strength relative to type 304 stainless steel (304). These steels are austenitic because they contain

sufficient nickel (at least 12% Ni) to suppress the austenite [face-centered cubic (fcc) phase] to martensite [body-centered tetragonal (bct) phase] transformation upon cooling or a transformation of the austenite to ferrite [body-centered cubic (bcc) phase] upon aging. Manganese (2 wt % Mn) further stabilizes the austenite in types 304 and 316 SS. The austenitic structure furthers the corrosion resistance, allows greater latitude and ease during fabrication, and makes these steels much easier to weld than transformable or heat-treatable steels.[6,7] Furthermore, the austenitic steels do not suffer a ductile-to-brittle transition with decreasing temperature, as do most tempered martensitic steels, thus permitting use to temperatures as low as —196°C. Commercial type 316 steels will have impurities of silicon (up to 1 wt % Si) and traces of phosphorus, sulfur, oxygen, or aluminum (less than 0.05 wt %) from the starting ores, the particular refining process, or from intentional addition as de-oxidizing agents.[8] Although the temperatures in some applications approach 800°C, some types of 316 SS will suffer properties degradation due to precipitation reactions that occur upon long-term aging above ~650°C.[7,9-11]

Due to the properties mentioned above, types 304 and 316 stainless steels find wide application as structural components in light-water reactor (LWR) systems.[12,13] These systems depend upon water to moderate or slow down the high (1—3 MeV) energy neutrons borne from fission events in order to induce continued fission via the low energy or thermal neutrons. Example systems are boiling or pressurized water

reactors (BWR and PWR, respectively). The higher temperature systems (like PWRs) sometimes necessitate use of these steels as fuel cladding as well. Stress corrosion cracking is a problem, but it is not unique to the irradiation environment. Embrittlement, however, is an effect of the serious degradation of properties due to the effects of irradiation on the microstructure.[14-16] Generally the embrittlement occurs from hardening due to defect clusters at lower temperatures and collection of helium at grain boundaries at higher temperatures.

Austenitic stainless steels also have wide application and a long history in experimental and developmental liquid metal fast breeder reactor (LMFBR) fission systems as fuel cladding and structural materials.[17-19] The Experimental Breeder Reactor (EBR-I) used type 347 SS in 1951, the Dounreay Fast Reactor (DFR) type 316 SS in 1959, EBR-II type 304 SS in 1963, the Prototype Fast Reactor (PFR) type M316 in 1974, and the Fast Flux Test Facility (FFTF) currently uses 316 SS. The core design, coolant, and materials are selected to cause the fast fission neutrons minimal energy loss through down-scattering. These neutrons then induce fission in the highly enriched fuel through the high energy fission cross section and diffuse to the blanket to breed new fuel. The core has a minimum volume configuration to enhance breeding and operates at a temperature range (~350–650°C) set by the coolant inlet and outlet temperatures. Additional properties of austenitic stainless steels that make these attractive are their compatibilities both with the mixed oxide fuel and the liquid metal coolant (usually sodium). The major engineering concerns for failure

under irradiation were creep and embrittlement until 1966–67, when Cawthorne and Fulton discovered swelling due to voids in SA 316 SS clad irradiated in DFR.[20,21] Swelling could expand and distort the core, causing coolant blockage or stresses if the components are constrained, or decreased breeding if more space is allowed for them to swell.[22] Void swelling then became the major topic of fundamental and applied studies of the effects of fast breeder irradiation.[23,24]

Fusion presents a new set of nuclear physics and materials engineering problems, but is generally linked to previous technologies by the consideration of the effects of radiation on materials. Deuterium and tritium fuse in the plasma according to the reaction

$$D_1^2 + T_1^3 = He_2^4 + n + 17.6 \text{ MeV} \quad , \qquad (1)$$

where the 17.6 MeV reaction energy is distributed between the neutron (~10–14.1 MeV) and the helium ion. The neutrons breed tritium and heat a coolant in the blanket, but also cause damage in the first wall and structural components. A leak or rupture in the first wall will quench the plasma and force repair of the MFE device, whereas fission reactors can often operate with a few failed fuel clads. Probably the most difficult problem is that no fusion reactors exist today to serve as a test bed or to give experience with an actual fusion environment. Conceptual designs have existed only since 1973 (ref. 25), and design variations make material requirements general rather than specific.[26,27] Further, engineering relevant levels of radiation damage must be simulated. The factors that favor austenitic stainless steels in design

are its existing technological base and previously mentioned properties.[27] The radiation effects that generally limit temperature or lifetime of the first wall are swelling and embrittlement.[28] The energy of damaging neutrons will be higher and the accompanying helium and hydrogen generation will also be higher than in LMFBR irradiation environments,[29,30] making the exact character and nature of the properties effects unknown. Both theory and experiment indicate strong effects of helium on increased embrittlement for fusion irradiation, but suggest several possible helium effects on swelling.[28,31-33] Experimental evidence is not strong for hydrogen effects.[34] With increased helium, swelling could be considerably less[31] or considerably greater,[33,35] depending intimately on the nature of the microstructural development as well as its sensitivity to increased helium generation. Controversy, however, further complicates consideration of any effects of helium on either microstructural evolution or swelling.[36,37] This sets the stage for the current study.

Development of the total microstructure of a single heat of SA 316 SS was observed via TEM and compared after exposure in several different environments over a range of temperatures. The emphasis was on the effects of helium on the overall microstructural evolution with particular emphasis on precipitate component of the microstructure. Previous studies have examined the thermal aging[9] and fast reactor irradiation[38-40] responses of SA 316 SS prior to the application of AEM. Hence, these earlier studies lacked some of the phase identification and compositional study only possible through this technique.[41] Irradiations in EBR-II at 500 to 630°C at fluences up to

36 dpa formed the base-line for evaluating the effects of displacement damage at very low helium generation rates. Samples were aged at 280 to 900°C for times of 2770 to 10,000 h to provide an unirradiated base-line for comparison of thermal to irradiation effects, unlike previous studies.[38,39] Additional samples were pre-injected with helium and aged for up to 10,000 h from 400 to 700°C or irradiated in EBR-II at 500 to 625°C to 8.4 dpa as additional measures of helium perturbations of microstructural development. Both represent new work.[42-46] Irradiation of austenitic stainless in the water-moderated High Flux Isotope Reactor (HFIR) is particularly important to fusion studies because experimental positions near the fuel have large populations of both fast and thermal neutrons.[47] Thermal neutrons produce helium via a two-step transmutation reaction with nickel,[48] thus allowing continuous co-generation of helium and displacement damage of the fast neutrons.[1,28-31] Although the helium generation rate in HFIR for 316 SS is higher and nonlinear with time compared with fusion, it does provide another measure of the microstructural development sensitivity to that parameter when compared with EBR-II irradiation of the same material.[33,36,37,48] The irradiation temperatures in HFIR ranged from 55 to ~750°C at fluences from ~7 to ~69 dpa, including some data from previous comparisons.[49,50] This is among the broadest temperature ranges covered for fast neutron-irradiated materials. Among the new information to emerge for SA 316 SS are: (a) the effects of helium on void formation under neutron irradiation, (b) the nature of precipitation development under irradiation compared to aging, and (c) the sensitivity of precipitation to helium under irradiation as well as during aging.

CHAPTER II

LITERATURE SURVEY AND SUMMARY

The literature on radiation damage as well as on the effects of irradiation on stainless steel is immense. This chapter is divided into two major sections, one dealing with primary damage in a general way and the other in more detail on secondary damage, focusing on austenitic stainless steel. The primary damage section further deals separately with the generation of vacancy and interstitial point defects as well as gaseous and solid transmutation products. The secondary damage section treats the microstructure visible through TEM and is subdivided into portions on dislocation, cavity, and precipitate phase components of the total microstructure. Both sections deal primarily with neutron data and focus toward fusion application. The secondary damage section reviews both experimental data and related theoretical work. No apology is made for the length of this section, because seldom has the total microstructural evolution been treated in its entirety. A very condensed summary of this survey is included at the end for those not wishing to read this entire section.

Primary Damage

Vacancies and Interstitials

Vacancies and their corresponding interstitials (Frenkel pairs) are produced by collisions of energetic irradiating particles with atoms in the crystal lattice. Displacements can occur for a variety of incident

particles (electrons, light and heavy ions, neutrons), but this work emphasizes the effects of neutrons. A large body of excellent reviews and summary articles provide the background and contain the detailed physics for this section.[16,50-56] Seitz[57] initially introduced the idea that an atom is displaced by receiving a kinetic energy above a threshold value, E_d, from the bombarding particle. Lattice atoms displaced directly by the incident neutrons (or any bombarding particles) are termed primary-knock-on (PKA) atoms. Kinchin and Pease[58] have presented the simplest and best known model for the interaction of the PKA with the lattice. In their model, the PKA moves through the lattice if it receives kinetic energy greater than E_d, but must have energy greater than 2 E_d to displace other lattice atoms. The PKA dissipates its energy elastically and comes to rest as an interstitial defect. The general region of collisional energy loss by the PKA is called a displacement cascade. A simple schematic of a cascade is shown in Fig. 1. Of central interest are the number of defects produced, their spatial arrangement, and the defect survival and migration within the cascade region.

One measure of irradiation damage is the total number of displaced atoms (ν) produced by the PKA; another is that fraction of the initial PKA energy that produces displacements, termed the damage energy ($\hat{E}$). A simple relationship between these is given by Robinson[52,59] as

$$\nu = \kappa \hat{E}/2\,E_d \;, \quad E > 2\,\hat{E}_d/\kappa \;, \tag{2}$$

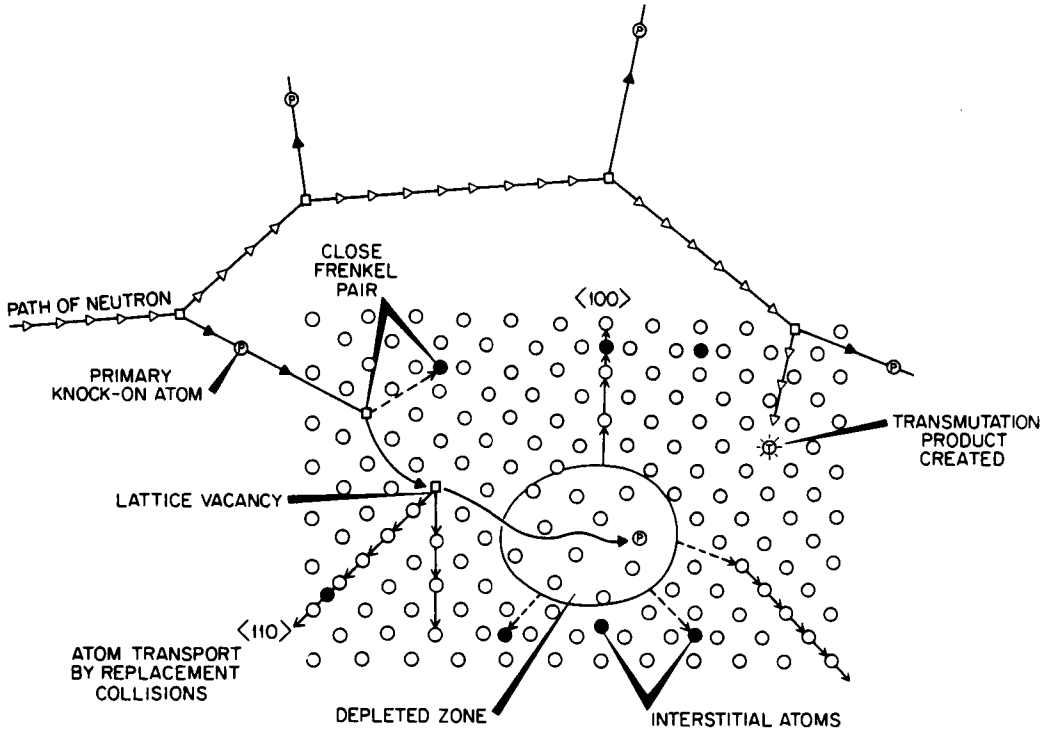

Fig. 1. A schematic representation of a displacement cascade produced by a neutron collision with the lattice. Related processes are identified.

where κ is the so-called cascade efficiency. Values for E_d range from 25 to 60 eV, with E_d = 40 eV, typically used for 316 stainless steel.[30] Clearly the number of defects increases as the PKA energy increases. PKA energies can range up to hundreds of kiloelectron volts, but generally only elastic collisions result in displacement of atoms in metals. Above about 60—100 keV, PKA collisions will result in energy loss by excitation of the electrons of lattice atoms rather than atomic displacement. Kinchen and Pease treated this situation very simply with a cutoff energy (E_c) for the PKA, above which only electron excitation occurred and below which only elastic collisions occurred. Lindhard et al.[60,61] offered a more sophisticated treatment of the PKA collision

processes using interatomic potentials and a continuous partitioning of energy between nuclear stopping processes which result in displacements, and electron stopping processes which result in electron excitation. Often referred to as LSS theory, this formalism is the basis of the procedure recommended by the International Atomic Energy Agency (IAEA) for damage calculations.[30,52,62] The simple analytic treatment of defect production in the cascade regions must be corrected for PKA energy lost into events that produce no displacements in the cascade, such as focusing, channeling, and replacement sequences (dynamic crowdion[16]). These effects necessitate consideration of crystal structure[63] and cause ν to be reduced for a given $\hat{E}$ of the PKA [Eq. (2)]. Several of these processes are also pictured in Fig. 1.

It is important to know the spatial extent and configuration of point defects in the cascade region. Brinkman[64] first addressed this analytically and envisioned the cascade spike as a hollow core of vacancies surrounded by a shell of interstitials. Seeger[65] modified this idea by allowing for focusing and other crystal effects that spread the PKA energy transfer to a larger volume; he imagined a depleted zone that is vacancy rich but not completely hollow, as shown in Fig. 1. Modern computer technology has allowed simulation of the collision cascade to produce a quantitative picture that generally confirms Seeger's picture.[66-71] Early computer simulations of the cascades were often done at very low temperatures (~0 K) and allowed no thermal migration of the point defects. Such restrictions define the nascent damage state.[52] Computer simulations also allow vacancies and interstitials

within a given capture radius (r_v) to recombine spontaneously. This effect reduces stable defect concentration (ν) by 15 to 50% compared to the simple analytical model,[58] depending on PKA energy. In general, these calculations show the cascade volume (and ν) increases with increasing PKA and that it elongates along the initial PKA direction. At PKA energies of about 20 to 50 keV, distinct lobes or subcascade regions form; these lobes then increase in separation as the PKA energy increases.[71] Heinisch[72] more recently has included lattice vibrations to simulate higher temperature irradiations (300 K); he finds that the frequency of subcascade formation increases, but that both size and separation of subcascades decrease, with increased lattice temperature.

Computer simulations also allow short-term annealing of the nascent cascade, at various temperatures, to determine the surviving defect concentrations which then migrate to produce the secondary damage structure.[73,74] The nascent cascade occurs in $\sim 10^{-13}$ to 10^{-12} s and then becomes somewhat stable after about 10^{-7} to 10^{-6} s. Annihilation of defects now occurs by clustering or mutual recombination and reduces the nascent defect content by ~80% (ref. 73). Interstitials are able to migrate at nearly all temperatures, but vacancies are immobile until about 0.2 to 0.3 of the melting temperature (T_m). In general, annihilation increases with increasing temperature. However, for a given annealing condition, the residual point defect fraction (defects after annealing/defects initially produced) is independent of PKA energy from ~10 to 500 keV (refs. 72,74). This result is critical to the validity of fission reactor simulation of fusion irradiations.

Finally, the agreement between theory and experiment is important and both must be considered for damage correlations between fission and fusion irradiations. Fission reactor neutrons produce PKAs via isotropic, elastic collisions during irradiation, for neutron energies from 200 eV to 1 to 2 MeV (refs. 16,56). The PKA energy increases proportionally to the neutron energy below 1 to 2 MeV, but at higher neutron energies inelastic and anisotropic scattering events degrade the transfer of kinetic energy to PKAs. In general, however, the PKAs will also have a spectrum of energies related to the neutron energy spectrum. Several reactor neutron energy spectra are shown in Fig. 2 for comparison. Experimental verification comes from field-emission microscopy (FIM) studies[53] or TEM observations.[54,75,76] The TEM techniques of either observing "black dots" due to cascade collapse to form vacancy loops or imaging "disordered zones" in ordered Cu_3Au are quite useful for studying higher energy cascades. The latter technique, in particular, correlates well with calculated number and sizes for cascades produced by heavy ion or various neutron irradiations. It also confirms the formation of distinct subcascades at higher PKA energies. Coupled annealing and resistivity studies are consistent with the computer-simulated cascade annealing studies as well.[55,74]

Initial concerns about strange features of the primary damage unique to the high energy neutrons (~14 MeV) borne in fusion plasmas have been laid to rest by both earlier[77,78] and more recent[72,75] experimental and theoretical work. Wiffen and Stiegler[77] concluded in 1976 that no new effects of 14 MeV neutrons were observed experimentally and

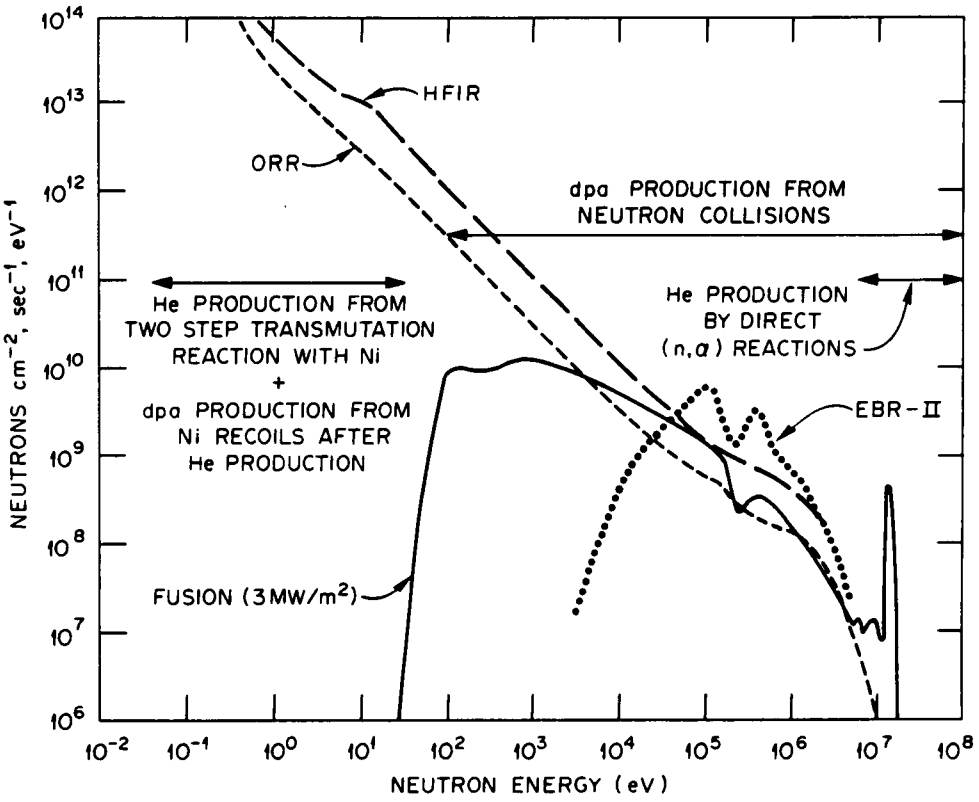

Fig. 2. A plot of differential neutron flux as a function of neutron energy for HFIR, ORR, EBR-II, and a fusion spectrum (at 3 MW/m^2 wall loading).

that generally the physics of damage production was adequate to scale increased defect production with increased PKA energy. Odette and Doran[78] were less certain and called for better dosimetry and computer simulation of higher energy cascades. However, these latter authors point out that the 14 MeV neutrons make up only a small portion of the overall fusion neutron energy spectrum (see Fig. 2) and that the overall PKA and cascade spectra are of greater concern. There is considerable overlap between fission and fusion PKA spectra. Heinisch[71,72] through computer simulation studies found that high energy cascades split into

lobes and formed widely separated subcascades which in turn are similar to 25 to 35 keV cascades. Jenkins and English[75] confirmed this directly by TEM studies of 14 to 15 MeV neutron damage in Cu_3Au. The majority of fission damage is produced by cascades in the 10–100 keV range[79] and it appears that the 25 to 35 keV cascades are the basic unit for relating fission to fusion primary damage. However, at elevated temperatures (above 300–400°C for type 316), primary damage will not survive directly and the defects generated are important mainly for their influence on the development of the secondary damage structure.

Gaseous Transmutants: Helium and Hydrogen

Transmutation gases like helium and hydrogen are produced by (n,α) or (n,p) reactions, respectively, with various non-fissile elements; these are another form of neutron radiation damage introduced into the lattice. At thermal neutron energies, it has long been known that helium is produced in austenitic stainless steels primarily from direct (n,α) reaction with boron as well as nitrogen. More recently,[80,81] however, helium production has been found to arise from a two-step reaction with natural nickel, $^{58}Ni(n,\gamma)^{59}Ni$ followed by $^{59}Ni(n,\alpha)^{56}Fe$. At higher neutron energies typical of LMFBRs, direct (n,α) and (n,p) reactions occur with iron, chromium, and nickel as well as with boron and nitrogen.[82,83] At still higher neutron energies, above the 4 to 6 MeV typical of fusion, the cross sections for direct (n,α) and (n,p) reactions become much greater for nearly all elements.[29,30,83] Regions of gas production as a function of neutron energy are indicated in Fig. 2, and

typical annual productions of helium, hydrogen, and displacement damage are given in Table 1 for various reactors.

It has been traditional to dismiss hydrogen production in small quantities as being unimportant due to its solubility and high diffusivity.[16,77,82,84] Some concern has been expressed about it altering stacking fault energy, forming insoluble CH_4 molecules[77,78] and aiding cavity formation. However, triple-beam ion irradiations (helium, deuterium, and nickel ions) by Packan and Farrell[34] have found no significant effect on cavity formation and swelling in high-purity austenitic stainless steel. Further, the hydrogen generation rate is similar in EBR-II and HFIR, so that it is not a variable parameter in their comparison. Therefore, we will consider it no further.

Helium generation varies considerably from reactor to reactor, both in actual rate and in ratio to the dpa rate (He/dpa). Helium generation as a function of dpa generation is plotted in Fig. 3 for type 316 stainless steel in several reactor environments. The ratio is about 0.5 at. ppm He/dpa in the core of EBR-II, 12 to 15 at. ppm He/dpa in the first wall of a fusion reactor, and ranges from 10 to 70 at. ppm He/dpa in the peripheral target positions (PTPs) of the flux trap in HFIR. The He/dpa ratio is a linear function of time for both EBR-II and a fusion first wall, but is nonlinear and increases with time in HFIR. The helium generation in HFIR is proportional to the flux raised to the 1.6 power.[85] The He/dpa ratio in mixed spectrum fission reactors like ORR can better match fusion through spectral tailoring.[1] Comparison of EBR-II and HFIR irradiations allows assessment of the effect of a large change in helium

Table 1. Dpa, Gaseous, and Solid Transmutant Production per Year for Type 316 Stainless Steel Irradiated in Various Reactors

Reactor Environment	Displacement[a] Damage (dpa)	Gas Content (at. ppm)		Transmutation-Induced Compositional Change (at. %)[c]	
		Helium[a]	Hydrogen[b]	Manganese	Vanadium
MFR[d] (first wall)	32.1	465	1490	+0.19	+0.05
ORR (C-3)[e]	7.5[f]	76.9[g]	90	n.c.	n.c.
HFIR (PTP)[e]	36[f]	2187[g]	390	−0.76	+0.4
EBR-II	39.2	15.1	320	~0	0

[a]Numbers obtained from T. A. Gabriel, B. L. Bishop, and F. W. Wiffen, "Calculated Irradiation Response of Materials Using Fission Reactors (HFIR, ORR, and EBR-II Neutron Spectra,)" Oak Ridge National Laboratory Report ORNL-TM-6361 (August 1979).

[b]Numbers obtained from J. L. Scott, M. L. Grossbeck, and P. J. Maziasz, J. Vac. Sci. Technol. 20 (1982) 1297–1303.

[c]Normal type 316 composition for that element multiplied by relative changes obtained from J. F. Bates, F. A. Garner, and F. M. Mann, J. Nucl. Mater. 103&104 (1981) 999–1004. These are not linear with time in HFIR.

[d]Calculated for neutronic wall loading of 3 MW/m^2.

[e]Maximum flux position.

[f]dpa values include contribution from recoils resulting from helium produced nickel transmutation, as calculated by L. R. Greenwood, "Neutron Source Characterization for Materials Experiments," pp. 66–86 in ADIP Semiann. Prog. Rept. Mar. 31, 1982, DOE/ER-0045/8.

[g]Not linear with time, but proportional to about $(\phi t)^{1.6}$.

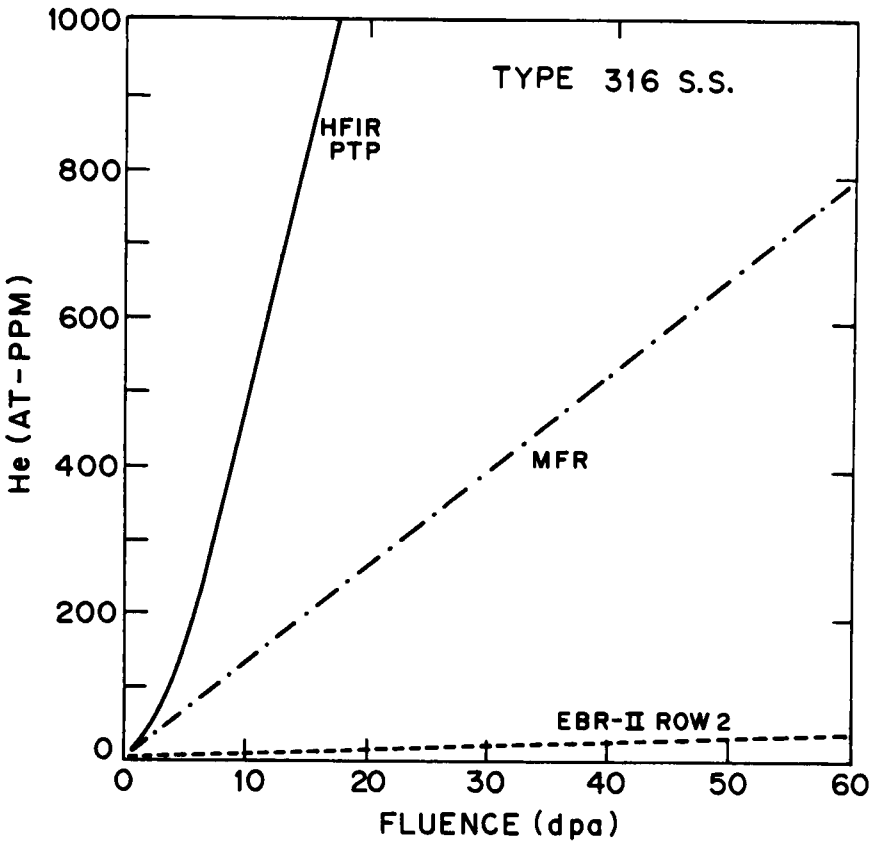

Fig. 3. A plot of helium generation as a function of displacement damage level for type 316 stainless steel irradiated in HFIR, EBR-II, or a Magnetic Fusion Reactor (MFR). Irradiation positions are indicated for EBR-II and HFIR, and the MFR case is for the first wall of the blanket. All are maximum flux positions.

generation rate on the property of interest (swelling and secondary damage microstructure in this case). Important to data interpretation and extrapolation to fusion conditions is an understanding of the interaction of radiation-induced helium atoms with vacancies and interstitials in the primary damage state.

Studies of the defect nature of helium stem primarily from theoretical atomistic calculations and from interpretation of helium diffusion and release measurements.[86,87] Apparently, studies of helium

permeation through metals began shortly after helium was isolated as an element, in about 1897 (ref. 86). It was puzzling that inert gas atoms like helium, which should be insoluble, would be retained in metals. Researchers first postulated compound formation between the metal and the inert gas and later suspected some sort of trapping in the metal lattice, if the helium was introducted by irradiation. Cottrell and Rimmer[88] presented a classic study in 1957 about the defect configurations between various inert gas atoms and vacancies and interstitials that revealed strong trapping of inert atoms such as helium in vacancies. In a macroscopic sense the helium appeared soluble because once introduced it was generally not released until near the melting temperature of the metal.[87] However, on an atomic scale, the helium atom strongly retains its electrons rather than contributing them to the electronic cohesive structure of the lattice, as metal atoms do with their valence electrons. Thus, even though the helium atoms occupy a substitutional lattice site when trapped in vacancies, they do not lose their identity to the lattice and the positions remain vacant of metal atoms.[88] Thus, they are considered insoluble and are a permanent feature of damage. The basis, then, for interaction between helium atoms and point defects is elastic strain energy.

Transmutation-produced or energetic ion-injected helium atoms initially possess enough energy to displace other lattice atoms, but eventually they come to rest in interstitial positions. Interstitial helium has about the same low migration energy as self-interstitials or small interstitial impurity atoms (like carbon), and is therefore able

to migrate freely even at very low temperatures. Experimental evidence indicates some low temperature release after low-temperature helium implantation.[89-92] Calculations show the helium is strongly bound to vacancies in fcc metals (e.g., nickel and copper), with a binding energy of about 2 eV (refs. 88,90,92). Rimmer and Cottrell found that helium would remain in interstitial positions until vacancies became available either by irradiation or increased temperature; this is in contrast to the behavior of larger rare gas atoms that were able to create and occupy vacancies due to their large interstitial strains. Helium therefore has several migration modes, depending upon its defect character. Helium atoms under irradiation can migrate rapidly until they find and become trapped in one or more vacancies. Both experiments and calculations indicate preferred stable clustering of about one helium atom for every vacancy.[43,87,93-96] The migration of a single vacancy is reduced by a helium atom, but a di-vacancy with a helium atom is stabilized against dissociation and can migrate easily. The dominant mode of helium migration in the presence of vacancies, however, appears to be the helium atom popping out of the vacancy and then migrating interstitially until it is trapped by another vacancy.[89,90,96] The detrapping can occur thermally at higher temperatures and is confirmed by helium release and diffusion measurements.[89,90,92,97] At lower temperatures under irradiation, helium can be dislodged from its vacancy by spontaneous self-interstitial recombination, by the disruption caused by a displacement cascade, or by a direct neutron collision.[88,98] Higher order clusters would be destroyed only by the latter two events.

Clusters with more helium atoms than vacancies may be stable against recombination with self-interstitials.

From this discussion we conclude that the strong interaction between helium and vacancies will result in some clustering in the primary damage state, and possibly coupled diffusion as the primary damage products migrate to form the secondary damage structure at higher temperatures. There is reason to suspect a dependence of the primary damage state upon helium concentration that reflects the fraction of free vacancies as compared to those trapped by helium atoms (and any subsequent effect of this on spontaneous recombination). This makes a strong case for considering He/dpa ratio as an important variable parameter in relating fission reactor to fusion irradiation results.

Solid Transmutants: Manganese and Vanadium

Transmutation of the metal lattice atoms can introduce new chemical species as well as burn out existing isotopes through a variety of neutron absorption reactions, thereby changing the composition with increasing fluence. This represents a permanent form of "chemical" damage that is probably more important to development of the secondary damage structure than to the nascent primary damage state, especially in an already complex and concentrated solid solution such as type 316 stainless steel. The reactions are specific to particular isotopes and sensitive to neutron energy.

Kulcinski[99] initially noted that transmutation calculations indicated significant quantities of manganese and vanadium generation for irradiation of type 316 in a fusion first wall, with trace amounts of

titanium produced as well. This work and both reviews of damage correlation for fusion in 1976 (refs. 77,78) indicated no obvious effect of these transmutation-induced compositional changes particularly on the primary damage state, because they were all well within the solubility limits of these elements in stainless steel. This can be contrasted to the clustering and precipitation of insoluble silicon produced via transmutation in aluminum.[99,100] More recent calculational work confirms and better quantifies the results on vanadium and manganese, indicates negligible effects of titanium,[101,102] and includes vanadium burnout as well as production.[103] Results from this work, adapted to the DO heat of type 316, are given for one year of exposure in Table 1 (p. 16) and as functions of fluence in Fig. 4.

Compositional changes for vanadium and manganese are negligible in an LMFBR environment (i.e., EBR-II). Vanadium is produced in the high energy fusion neutron spectrum via the reaction $^{52}Cr(n,2n)^{51}Cr \rightarrow {}^{51}V$. In HFIR, a different reaction with lower energy thermal neutrons produces vanadium from chromium via $^{50}Cr(n,\gamma)^{51}Cr \rightarrow {}^{51}V$ and then transmutes the vanadium back to chromium via $^{51}V(n,\gamma)^{52}V \rightarrow {}^{52}Cr$. Thus, in Fig. 4 the production of vanadium is linear in a fusion device and nonlinear in HFIR due to burnout time being much longer than the buildup time.[102] Somewhat similar to the case of He/dpa ratio, vanadium production for fusion falls between the EBR-II and HFIR results with HFIR production being much greater than fusion and EBR-II production being nil. The difference in HFIR is a transient and the burnout eventually approaches the fusion results at higher fluence.

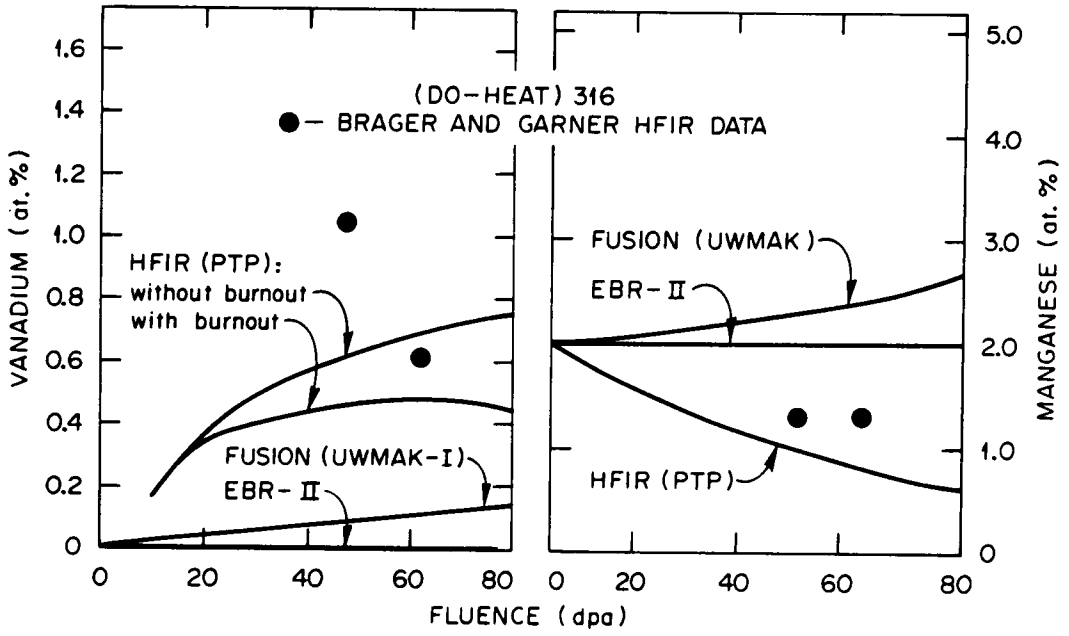

Fig. 4. Transmutation-induced compositional changes calculated for type 316 as a function of fluence for (a) vanadium and (b) manganese for several irradiation environments. Actual HFIR data after H. R. Brager and F. A. Garner, J. Nucl. Mater. 108&109 (1982) 347–358.

Manganese compositional changes are opposite for HFIR and for fusion. For high energy neutrons, manganese production is dominated by the reaction $^{54}Fe(n,p)^{54}Mn \rightarrow {}^{54}Fe$ with contribution from $^{56}Fe(n,p)^{56}Mn \rightarrow {}^{56}Fe$. For thermal neutron irradiation, manganese burns out according to the reaction $^{55}Mn(n,\gamma)^{56}Mn \rightarrow {}^{56}Fe$. Thus it is seen in Fig. 4 that manganese is produced in small quantity for fusion and undergoes significant burnout for HFIR irradiation.

Uncertainty in spectral dosimetry and reaction cross-section measurements makes agreement between experimental measurements and calculations an important consideration. Brager and Garner[37] have reported measurements on vanadium and manganese changes occurring in the DO heat

of type 316 stainless steel after HFIR irradiation, and the results are included in Fig. 4. The manganese measurements show little scatter and confirm burnout; however, they show less burnout and a trend toward saturation considerably earlier than the calculations. The vanadium measurements confirm production, but the results do not follow the calculated trend curves. The difference in vanadium content for the two samples is much greater than can be explained on the basis of small flux differences in HFIR, as Brager and Garner[37] have done, especially given the flux (position) sensitivity of the calculations.[101-103] If the difference represents measurement scatter, then in general, the vanadium production is greater than calculated. If the difference represents a true fluence dependence, then both the production and burnout are considerably greater than calculated. In any case, there is certainly room for better data on both manganese and vanadium changes, and room for scrutiny of the accuracy of the calculations for anything more than trends. Moreover, the impact of the transmutation-induced compositional changes will come from the data on the secondary damage structure reflecting sensitivity to these changes. There is little data indicating such sensitivity, and acquiring such data is beyond the scope of this thesis.

Secondary Damage

The secondary damage structure results from migration and agglomeration of the primary damage products, and therefore generally exhibits nucleation and growth characteristics that often depend on temperature and fluence/time (and damage rate). The secondary damage structure may

also depend upon helium content or generation rate. This section will concentrate mainly on literature data for neutron irradiations of unstressed specimens of SA 316, as well as appropriate aging data. Electron and ion irradiation data will be generally considered to complement the neutron data. Theoretical treatments of microstructural evolution will also be considered.

Dislocation Microstructure

Dislocations are extended line defects that are large in extent compared to point defects and result in mismatch of atomic planes in the crystal. A Burgers vector, $\bar{b}$, defines the sense of planar displacement around the line defect and if $\bar{b}$ is parallel to the line tangent, the dislocation is screw in nature, and if perpendicular, then edge in nature. Dislocations in unirradiated fcc metals (i.e., type 316 stainless steel) are generally $\bar{b} = a_0 \langle 110 \rangle$ type (a_0 = lattice parameter, $\langle\ \rangle$ denotes general crystallographic directions) that slip or glide on $\{111\}$ type planes. Irradiated fcc metals contain dislocation loops which result from collections of vacancies or interstitials to form planar disks that correspond to missing (intrinsic) or extra (extrinsic) atomic planes in the perfect crystal. These generally form on $\{111\}$ type close-packed planes and are prismatic (perfect) loops if $\bar{b} = a_0/2\langle 110 \rangle$ or Frank (faulted) loops if $b = a_0/3\langle 111 \rangle$. The prismatic loops are glissile and can glide in response to stress, but the Frank loops are sessile and unable to glide; Frank loops can climb, however, by absorbing or emitting point defects and can unfault to become prismatic loops. TEM characterization should include care to identify the type

(loop, line), $\bar{b}$, and nature (extrinsic, extrinsic) of the components. However, this can be very difficult for very small loops.[104]

Well-annealed material will generally contain a very low concentration of $b = a_0/2\langle 110\rangle$ type dislocation network, usually 10^{12} m/m^3 or less. At low fluences and low temperatures [~0.2 to 0.3 T_m, T_m = melting temperature (K)] tiny vacancy and interstitial loops will be produced by displacive irradiation.[105,106] Tiny vacancy clusters can result from cascade collapse,[54] and hence stem directly from the primary damage state. The larger interstitial loops, however, are generally considered secondary damage because interstitials must migrate and coalesce to form them. Tiny loops or "black-spot" damage generally require higher threshold fluences to form in complex alloys, such as types 304 or 316 stainless steel, relative to pure materials. For example, in neutron-irradiated SA 304 at 40 to 90°C "black-spot" loop damage was not observed at a fluence of 1×10^{23} n/m^2 ($E > 1$ MeV, <0.05 dpa) (ref. 107) but was found at higher fluences of 1×10^{24} n/m^2 ($E > 1$ MeV, <0.5 dpa) (refs. 108, 109). At fluences of 1 to 7.3 dpa, Maziasz[110] observed many larger (20—30 nm diam) Frank loops together with "black-spot" damage (2—3 nm diam) in SA 347 and SA 316 irradiated at 55°C in HFIR. The SA 304 data of Bloom et al.[109] from ORR and the SA 316 (DO heat) data of Maziasz are included in a temperature-fluence-phenomena map in Fig. 5. This diagram helps illustrate the dislocation microstructure which evolves with increasing fluence and how phenomena change with increasing irradiation temperature. Larger Frank loops appear to be interstitial in nature, consistent with the high mobility of interstitials and low mobility of vacancies at these temperatures.

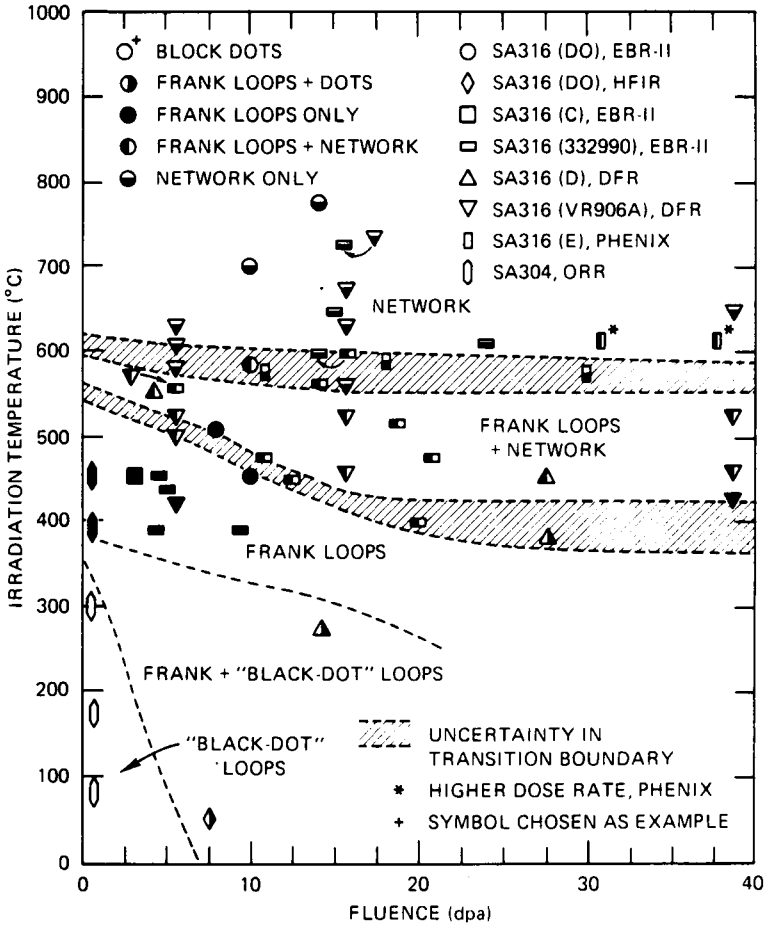

Fig. 5. A plot of dislocation structure character as functions of temperature and fluence for FBR-irradiated SA 316. Phenomena regions are identified to illustrate the transitions from "black-spot" loops to Frank loops to network as temperature and fluence increase. Data references are found in Table 2 and in text.

Cawthorne and Fulton[20] first observed irradiation-induced dislocation structures at elevated temperatures (~300°C and above) in SA 316. Their observations are included in Fig. 5 and the composition of their steel given in Table 2. At temperatures of 450°C and above, they observed a microstructure of a loose dislocation network and large faulted loops but no "black-spots." Bloom et al.[109] observed "black-spots" at 90 to 300°C for SA 304 in ORR, but found larger Frank loops at ~400°C and above.

Table 2. Compositions[a] of Type 316 Stainless Steel Investigated in Other Work

Alloy Designation	Element, wt %											Investigators/Environment
	Cr	Ni	Mo	Mn	Si	C	Ti	P	S	N	B	
316 (A)[b]	17.3	13.3	2.33	1.72	0.4	0.06	0.003	0.012	0.007	--	--	J. E. Spruiell and co-workers/ thermal aging
316 (B)	17.4	12.3	2.05	1.57	0.21	0.066	--	--	--	--	--	B. Weiss and R. Stickler/thermal aging
316 (DO-heat)	18.0	13.0	2.58	1.90	0.80	0.05	0.05	0.013	0.016	0.05	>0.0005	E. E. Bloom and J. O. Stiegler; P. J. Maziasz/EBR-II
316 (heat 332990)	17.8	13.55	2.33	1.78	0.38	0.05	--	0.012	0.02	0.04	>0.0005	H. R. Brager and J. L. Straalsund/ EBR-II
316 (heat 65808)	17.3	13.3	2.33	1.72	0.4	0.06	--	0.012	0.007	0.05	~0.0005	H. R. Brager and co-workers/ EBR-II
316 (C)	16.5	13.7	2.41	1.64	0.46	0.056	--	0.013	0.006	0.006	0.0008	H. R. Brager and J. L. Straalsund/ EBR-II
316 (M2783)	16.4	13.3	2.51	1.77	0.51	0.06	--	0.022	0.015	0.026	0.0002	T. A. Kenfield and co-workers; E. H. Lee and co-workers/EBR-II
316 (VR906A)	17.3	11.4	2.5	1.54	0.32	0.039	--	0.011	0.003	0.023	0.0018	P. J. Barton and co-workers; J. I. Bramman and co-workers; Williams/DFR
												D. J. Mazey and S. Francis; D. J. Mazey and R. S. Nelson/ Helium-preinjected and thermal aging
316 (D)	16.7	13.06	2.43	1.56	0.57	0.02	--	0.017	0.015	0.02	0.0004	C. Cawthorne and E. J. Fulton/ DFR
316 (E)	16.6	13.9	2.1	1.6	0.4	0.034	--	0.027	0.005	0.018		L. LeNaour and co-workers/ Phenix

[a]Balance iron.

[b,c]indicate arbitrary alphabetical designation to distinguish heats.

At temperatures of about 350 to 375°C in FBRs, the first visible damage is "black-dots" followed by Frank loops as fluence increases.[111] At very low fluence, "black-spot" damage disappears with increased irradiation temperature (~495—525°C) or gives way to Frank loops plus dislocation network with increasing fluence.[111] The "black-spot" damage observations by Cawthorne and Fulton[20] (Fig. 5) are difficult to interpret, given their micrographs. Thomas and Beeston[112] recently found larger (20—30 nm diam) Frank loops without "black-spot" loops after irradiation of SA type 348 stainless steel at 300 to 350°C to 33 to 44 dpa in the Experimental Test Reactor and Advanced Test Reactor (ETR and ATR, respectively; irradiations similar to ORR and HFIR), consistent with the scheme of Fig. 5.

Results on FBR-irradiated SA 316 at ~380°C and above indicate progressive development of solely Frank loops into structures of loops plus dislocation network to solely network as irradiation temperatures increase (Fig. 5). Data most relevant to this work come from Bloom and Stiegler[40] and Brager and Straalsund[38] from EBR-II and Barton et al.[39] from DFR. Qualitative observations are included in Fig. 5 and steel compositions given in Table 2. Work from Bramman et al.,[113] Brager et al.,[114] Brager and Straalsund[115] and LeNaour et al.[116] are also included, but treated in less detail. Below about 10 dpa, Frank loops are observed below about 500°C, but they appear together with dislocation network at 500 to 600°C and are completely replaced by dislocation networks at higher temperatures (Fig. 5). As fluence increases at any temperature, many of the Frank loops tend to unfault and form a dislocation network. However, nucleation and growth continue even to 30 to

40 dpa at ~550°C and below. Thus the region of Frank loops without a dislocation network moves to lower temperature as fluence increases. This sequence of events is confirmed directly by in situ TEM observations during electron irradiation.[23] Mazey[117] proved that large Frank loops in C^{+2} ion-irradiated SA 316 are indeed interstitial loops. The overall dislocation evolution therefore reflects the accommodation of excess interstitial atoms.[23,35,118]

Only a few researchers obtained quantitative data on dislocation evolution during FBR irradiation, as most put their emphasis on void formation data. Figure 6(a–c) are, respectively, plots of Frank loop size and concentration and the total dislocation concentration (loops plus network) as functions of temperature from the data of Bloom and Stiegler, Brager and Straalsund, and Barton et al. Figure 6(d–f) are the same parameters as functions of fluence for the data of the latter two groups of authors, and Fig. 6(e) also includes the data of LeNaour et al.[116]

Scatter among data sets probably reflects heat-to-heat differences in composition on loop behavior, but certain trends are clear with each set. Figure 6(a) shows that at any fluence, Frank loops grow larger as temperature increases. Figure 6(d) shows that loop growth tends toward saturation with fluence below about 500 to 550°C, but that growth at higher temperatures peaks before decreasing with increased fluence. Loop concentrations decrease very strongly with increasing temperature [from Fig. 6(b)], particularly above ~500 to 550°C. Brager's and Straalsund's loop concentrations increase and then tend to saturate with

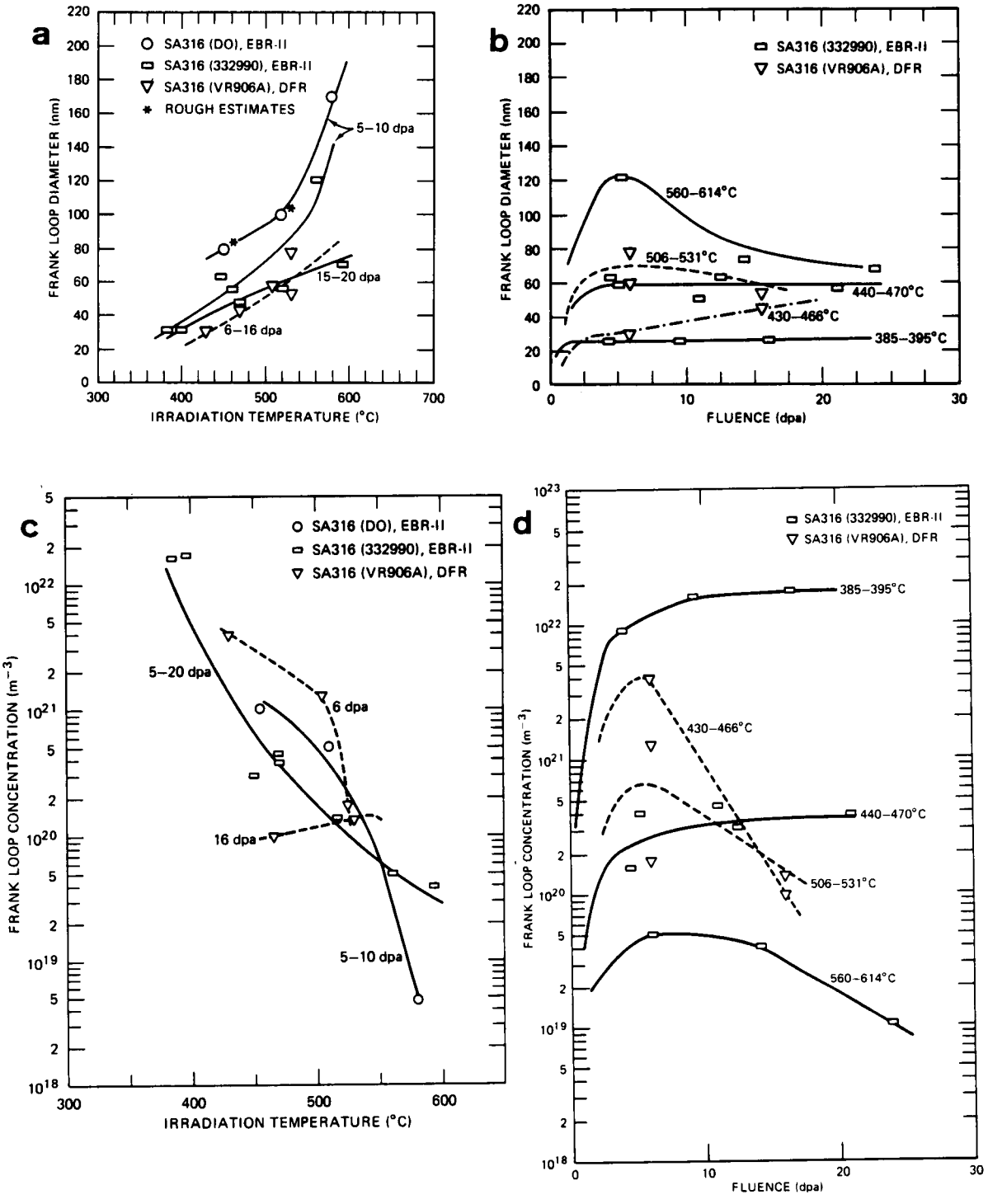

Fig. 6. Frank loop size, loop concentration and total dislocation density are plotted as functions of temperature (a,c,e, respectively) and fluence (b,d,f, respectively) for FBR-irradiated SA 316 from various investigators. References are found in Table 2 and in text.

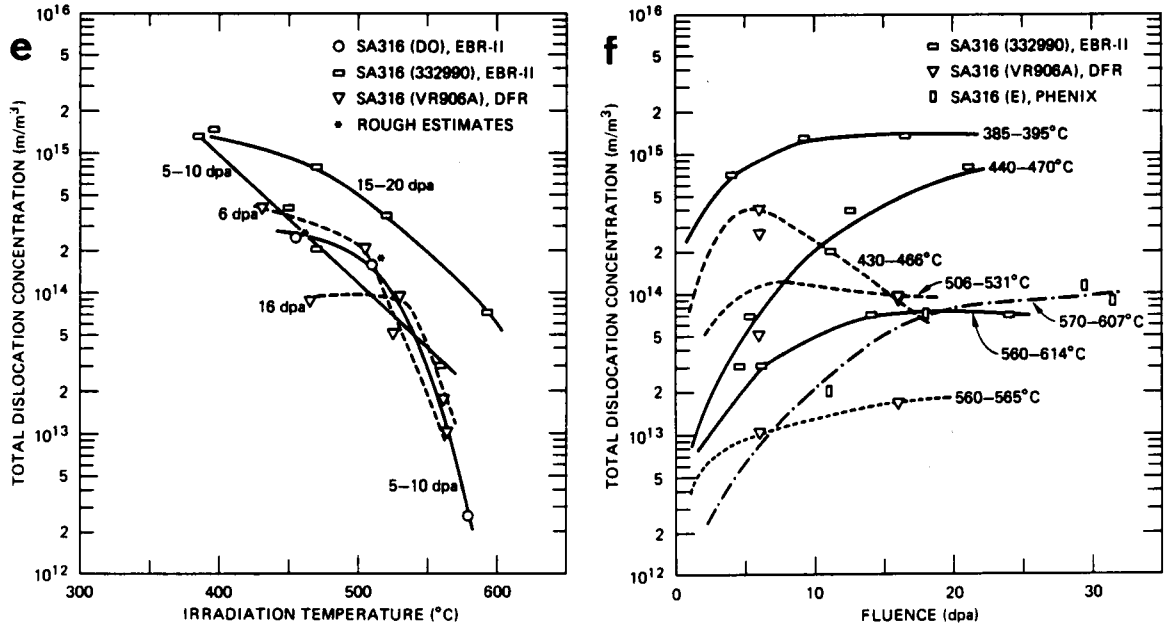

Figure 6 (continued)

increasing fluence below 500 to 550°C, but tend to peak and then decrease with fluence at higher temperature (similar to the behavior of loop size). By contrast, the loop data of Barton et al. strongly peaks and then decreases with increased fluence below 500°C. Generally, then, loop nucleation either reaches a steady state or tends to decrease with increasing fluence and can be quite variable from heat to heat. Loop nucleation tends to decrease with increasing temperature. Together with the stability of the dislocation network that results from their unfaulting, both nucleation and growth behavior of loops influence the total dislocation density.

The total dislocation density is also a strong function of temperature, particularly above 500 to 550°C [Fig. 6(c)], tending to decrease with increased temperature. Compared to Fig. 6(a,b), the

decreased loop nucleation at higher temperature dominates the behavior of the overall dislocation structure, in contrast to the increased size of loops. The fluence dependence of total dislocation concentration [Fig. 6(b)] also most strongly reflects the fluence dependence of loop nucleation. The total dislocation density increases and tends to saturate with increasing fluence for the Brager and Straalsund and LaNauor et al. data, but the saturation levels depend on temperature. The saturation level appears to be ~7 to 14 × 10^{14} m/m^3 below 500°C and ~7 to 10 × 10^{13} m/m^3 above 550°C. The data of Barton et al. in Fig. 6(f) appear to saturate with fluence at ~1 × 10^{14} m/m^3 at ~500°C, but peaks and then decreases at ~450°C. The total dislocation density data of Barton et al. at ~560°C saturates [Fig. 6(f)] at very low levels of ~1 to 2 × 10^{13} m/m^3, apparently because loop formation decreases dramatically [Fig. 5. p. 26)]. It appears, in summary, that total dislocation density most strongly reflects the temperature and fluence dependence of loop nucleation and growth up to the point of unfaulting. The dislocation concentration therefore represents the dynamic balance between loop nucleation, growth, and unfaulting to generate a dislocation network and mutual annihilation of dislocation lines to eliminate the dislocation network; it should be sensitive to irradiation parameters that affect these.

The temperature and fluence dependence of dislocation evolution are critically important to rate theory descriptions of swelling.[118,119] The same rate theory approach can also be used to describe loop nucleation and growth,[120-126] as well as loop unfaulting to form dislocation

networks.[127] Hayns[123] and Ghoniem and coworkers[124-126] find trends similar to those observed for the loop data in Fig. 6(a,b,c,d,e) — namely that loop size and concentration saturate with fluence and that loop concentration decreased while loop size increased with increased temperature. The calculations of Hayns, however, predict loop densities that are low compared to the data and have a very shallow temperature dependence for the loop concentrations, in contrast to the steeper dependence shown in Fig. 6(a) above 500°C. Ghoniem and Scharafat[125] agree reasonably well with the observed dependence of loop concentration on temperature, consistent with Fig. 6(c), although their loop concentrations are very low (possibly due to short irradiation times). Garner and Wolfer[127] include unfaulting of loops and recovery processes in their description of dislocation network evolution work and they find a total dislocation density that saturates at $\sim 6 \times 10^{14}$ m/m^3 which is independent of temperature. Although they fit the data presented by Brager et al.,[128] their contention is clearly at odds with all the data presented in Fig. 6(f), including the earlier data of Brager and Straalsund.

Next, we examine the evidence for any effects of helium on dislocation microstructure. To date the only neutron data available comes from helium preinjected SA 304 irradiated in EBR-II by Bloom and Stiegler[45] and Harkness et al.[46] Bloom and Stiegler found that preinjected helium (20 at. ppm) increased the loop concentration while decreasing the loop size compared to uninjected material. Harkness et al. found similar results for preinjection of ~100 at. ppm, noting that loop size was about half and loop concentration twenty times greater than uninjected material.

Much more data on the effects of helium on dislocation evolution are available on austenitic alloys subjected to ion irradiation. Low levels of helium (5—20 at. ppm) were often preinjected for ion and electron simulation studies of void swelling for FBR application,[129] but higher levels and more variations in gas injection methods have been achieved recently in support of the MFE program.[32,33,130,131] There is generally very little effect of helium on the dislocation evolution in high-purity austenites, unless large amounts of helium are cold preinjected into the samples,[33,34,132] because these alloys form dislocation networks with very few loops. Choyke et al.[133] find little change in total dislocation density in SA 304 for various modes of helium introduction, but find the Frank loop fraction to increase with increased helium content, the most dramatic increases occurring after cold preinjection. Williams[129] finds no significant effect of 10 at. ppm cold preinjected helium on the development of dislocations in SA 316 for low fluence (<2 dpa) irradiation with C^{2+} and Ni^{6+} ions. The data of Wood et al.[134] are in good agreement with Ayrault et al.[135] who show no effect of helium on total dislocation development of the same heat of SA 316 under dual-ion irradiation at 5 to 15 at. ppm He/dpa. Ayrault et al. show the dislocation density to increase at lower fluence, but then to saturate with fluence at the same concentration found at 5 to 15 at. ppm/dpa. They find that Frank loop development is sensitive to helium injection mode or rate. The strongest effect of helium on loop refinement and stability is found for cold helium preinjected titanium-modified austenitic steels.[135,136] In these cases, the helium tends to

drastically refine the scale of loop nucleation and prolong loop stability to high fluences (~70 dpa).

Finally, it is appropriate for this work to consider data on the effects of thermal aging on helium preinjected material. The first such study was undertaken by Barnes and Mazey[137] as they initially sought to simulate and study low-temperature neutron damage in copper. Low-temperature α-particle bombardments generally produce "black-spot" loop damage together with the gas injection. They found the very fine loops to grow, to coarsen, and to eventually form a dislocation network as bubbles became visible in the matrix. Later, work on helium preinjected SA 316 by Mazey and coworkers[42,43] revealed similar results, with faulted loops growing into a dislocation network at 600 to 750°C. They concluded that helium was trapped in vacancies, allowing interstitials to cluster and form loops, and that the loops grew via vacancy emission to feed bubble growth. Similar observations of loop growth in helium preinjected SA 316 were also made by Smidt and Pieper.[44] Cawthorne and Fulton also observed that the "black-spot" damage produced by low-temperature reactor irradiation grew and coarsened into a Frank loop structure upon postirradiation annealing. However, Stiegler and Bloom[138] and Holmes et al.[139] during postirradiation annealing simply noted unfaulting and recovery of dislocation structures produced in SA 304 via higher temperature reactor irradiation. The growth of small interstitial loops during aging via vacancy emission is initially counter-intuitive, but seems consistent among the data. Such behavior could indicate a nonequilibrium vacancy concentration in the matrix during aging of the helium preinjected samples.

Cavity Microstructure

Cavities are three-dimensional clusters of vacancies and gas atoms whose boundaries approximate free surfaces. Cavities can exist in the matrix or in association with other microstructural features such as precipitates, dislocations, or grain boundaries. Two extreme types of cavities can be defined. One type is a bubble which is nearly stabilized by its internal gas pressure (an over-, under- or equilibrium pressure). The other type is a void, which has an excess of vacancies relative to gas atoms (or is truly gas-free) and grows in response to a supersaturation of vacancies in the lattice. Grain boundaries (high angle, incoherent) allow discrimination between the two types of cavities because grain boundaries are infinite sinks for excess vacancies; equilibrium bubbles are generally found at grain boundaries whereas voids do not exist at grain boundaries in the absence of stress. Literature data and theories on cavities will be discussed first in terms of bubbles, and then voids.

A. Bubbles

After years of inert gas bubble observations in fuels, Barnes and Mazey in 1960–63 conducted the first comprehensive TEM study of helium bubbles in nonfissile metals using helium-preinjected copper.[137,140] This was followed by Vela and Russell in 1965–66, who used neutron-irradiated Cu-B alloys.[141,142] Their classic results established the behavior of bubbles under aging (conditions of no continuous helium supply and no vacancy supersaturation).

Bubbles formed first at grain boundaries and then in the matrix along dislocations. Larger bubbles were found at grain boundaries than in the matrix.[143-149] Bubbles never shrank; instead, once formed, they only grew or coalesced,[147,148] consistent with the helium being insoluble. Bubbles were observed (or suspected) to grow under aging by random (Brownian) migration and coalescence in the matrix or to coalesce along dislocations.[44,143,147,150,151] Rothaut and Schroeder,[152] however, are an exception; they suggested that Oswald ripening was occurring (emission of helium and vacancies from smallest bubbles to feed growth of largest ones). The migration of bubbles can occur via several different mechanisms which reveal several more distinguishing properties of bubbles.

For a gas bubble in mechanical equilibrium, the surface tension restrains the expansion of the gas according to the relationship,

$$p = 2\gamma/r \ , \qquad (3)$$

with p = internal pressure, γ = surface energy, and r = bubble radius, all in self-consistent units.[56] This relationship was demonstrated by Barnes and Mazey[137] as they observed bubbles to coalesce and conserve surface area rather than volume during in situ, pulsed annealing in a TEM. Barnes and Mazey also directly observed bubble migration in the steep temperature gradients induced by their particular annealing situation. They found bubble velocities to be inversely proportional to size, which suggested surface diffusion as the driving force. The experimental bubble growth kinetics data (i.e., $r \alpha t^n$, with t = time and $n \leq 1/2$)

of Smidt and Pieper[44] and Goodhew and Tyler[147] also suggested surface diffusion; however, the data of Walker[151] suggest migration via a volume diffusion mechanism; the data of Cost and Chen[153] and also Goodhew and Tyler (for larger bubbles) suggested a ledge nucleation mechanism. In addition to these mechanisms for free migration, many data sets indicated that bubble migration was either assisted or constrained via a dislocation-bubble drag interaction[137,141,143-150,154,155] and strongly constrained by precipitate particles.[137,143,144] At temperatures of about 0.65 to 0.70 T/T_m or higher, the data indicate unstable ("breakaway") bubbles growth by vacancy absorption without coalescence.

This thesis focuses on the details of bubble growth data for helium preinjected-and-aged SA 316, which correspond to the studies of Mazey and Francis,[42] Smidt and Pieper,[44] and Rothaut and Schroeder.[152] The data on SA 316 of Mazey and Francis are most relevant, with preinjected helium levels of 1, 10, 100, and 1000 at. ppm and aging temperatures from 200 to 1100°C. A schematic plot of the time and temperature dependence of their qualitative loop and bubble observations is given in Fig. 7. The temperature dependence of their bubble sizes and concentrations at 100 at. ppm He is shown in Fig. 8(a). They observed roughly concurrent Frank interstitial loop and bubble growth at ~570 to 750°C but bubble growth alone at higher temperature (Fig. 7), consistent also with the data of Smidt and Pieper and Rothaut and Schroeder. Figure 8(a) shows increased bubbles sizes and strongly decreased concentrations with increased aging temperatures. Bubbles were observed above 570°C for 10 to 1000 at. ppm He, but could only be found at 750°C and above for

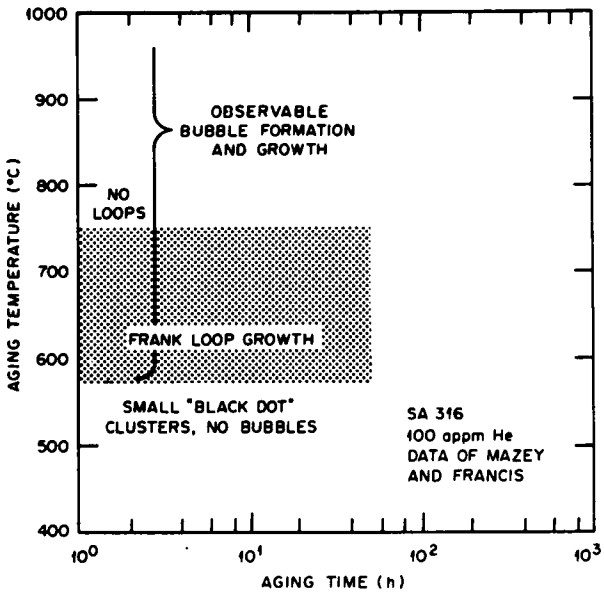

Fig. 7. A plot of qualitative observations of loop and bubble growth as functions of time and temperature for the data of Mazey and Francis on SA 316 stainless steel aged with 100 at. ppm preinjected helium. Data reference found in text.

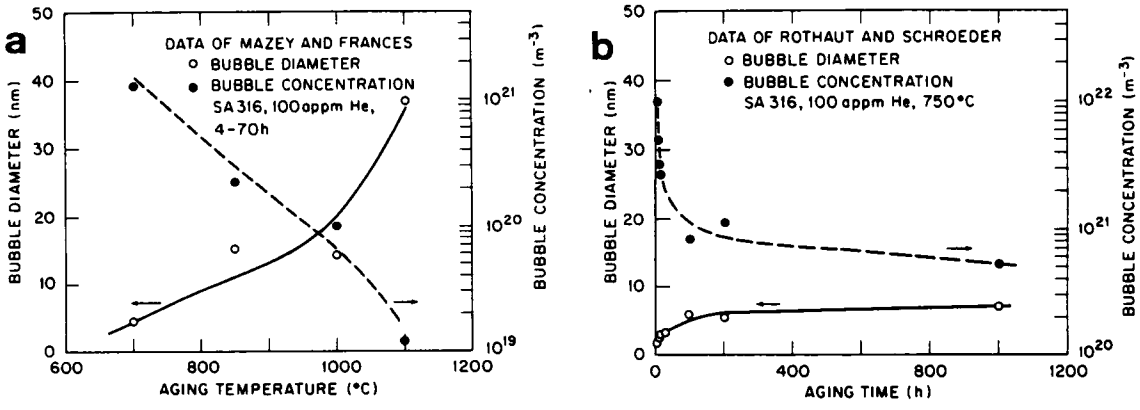

Fig. 8. Plots of bubble size and concentration for aged SA 316 containing 100 at. ppm preinjected helium. (a) As functions of aging temperature after 4 to 70 h from the data of Mazey and Francis, and (b) as functions of time at 750°C from the data of Rothaut and Schroeder.

1 at. ppm. Bubble size was little affected by increasing the amount of preinjected helium from 100 to 1000 at. ppm, but the bubble concentration increased by a factor of 50 to 100, according to the data of Mazey and Francis. The microstructural statistics of Rothaut and Schroeder for SA 316 aged at 750°C with 100 at. ppm preinjected helium are plotted as functions of time in Fig. 8(b). These data show very weak time evolution of bubble size and concentrations after an initially rapid coarsening stage. These data form a base line for the behavior of helium bubbles in SA 316 without displacive irradiation.

Under displacive irradiation, helium atoms can be dislodged from cavities by direct collision by neutrons or PKAs or from disruption of small bubbles and vacancy-helium clusters by cascades.[98,156] Our consideration here does not include fission fragment destruction of bubbles, as observed in fuels.[157-159] Bubbles can also grow via vacancy absorption if a supersaturation exists under displacive irradiation, in contrast to the aging conditions described above with no supersaturation. Early, low-fluence thermal reactor irradiations of austenitic stainless steels, performed in the context of helium embrittlement studies, found no observable bubbles for helium contents of about 50 at. ppm or less (from ^{10}B reactions) at irradiation temperatures of 650°C or less.[15,143,145,160] Bubbles were found at grain boundaries and in the matrix only after postirradiation annealing at higher temperatures. In 1967 Bloom et al.[109] observed small cavities in SA 304 (suspected to be bubbles) after ORR irradiation to moderately low fluences at 454°C. In 1968 Brager and Robbins[161] found bubbles in a 304 stainless steel after

ETR irradiation at 290°C to still higher fluence, and Manley and Rhodes[162] in 1972 found bubbles at irradiation temperatures of 540°C and above in a 20 Cr/20 Ni/Nb austenitic steel after long-time exposure (~40,000 h) in a thermal reactor. Both demonstrated bubble behavior via postirradiation annealing. Robbins[163] and Manley and Rhodes also realized that considerable helium was being produced from the reaction of thermal neutrons with nickel, in addition to that produced from boron (described earlier in the Gaseous Transmutation section).

Bubble observations in FBR-irradiated steels were generally neglected, as attention was focused on void studies. However, Brager and Straalsund[38] noted bubble formation together with voids at 625 to 740°C, and bubbles instead of voids at higher irradiation temperatures for SA 316 in EBR-II. In addition, many early postirradiation annealing studies of FBR-irradiated materials found voids to shrink, leaving tiny helium bubbles.[23,138,139,162] Bubbles have also been observed to develop together with or instead of voids at a variety of temperatures and fluences for type 316 stainless steel irradiated in HFIR in the context of the fusion program.[49,164,165] There is, however, little systematic HFIR data for SA 316, as mentioned earlier. Finally, Thomas and Beeston[112] have recently observed fine cavities, which they believed to be bubbles, after high fluence irradiations (39—44 dpa) in ATR and ETR (also with high helium generation) at temperatures as low as 300 to 350°C.

Numerous dual (ion plus helium) beam or helium-preinjected ion irradiations have also explored regimes of bubble formation under displacive irradiation. However, in general, continuous bubble growth was

not observed. Instead, tiny bubbles (or stable cavities) were often found to form and then to either convert to voids or remain stable, if void formation was suppressed.[32,130-136]

Next, some important aspects of early theoretical work on bubble development are summarized. Greenwood et al.[166] in 1959 were among the first to suggest that vacancy diffusion played a key role in bubble growth (as opposed to mechanical deformation to relieve excess internal bubble pressure) and to suggest the equilibrium relationship of Eq. (3). Early theoretical analyses focused on bubble growth, with little attention to nucleation. Greenwood et al. envisioned bubble growth through vacancy absorption (either from dislocations or grain boundaries with no vacancy supersaturation) in response to gas atom absorption and overpressuring. Many other investigators emphasized growth via bubble migration and coalescence governed by a rate-limiting mechanism. Greenwood and Spreight,[167] Shewmon,[168] and Gruber[169] suggested surface diffusion as controlling the growth rate; Shewmon[168] and Nichols[170] suggested volume diffusion and vapor transport as the limiting factor for very large bubble sizes; and Willertz and Shewmon[171] suggested ledge or facet nucleation as the controlling factor. Speight[172] and Barnes[173] discussed models in which bubbles coalesced either along dislocations or through their dragging action. Willis and Bullough[174] showed theoretically that an elastic interaction could induce bubble coalescence. Common features of early theories were helium flowing into bubbles due to its extreme insolubility and then bubble growth occurring primarily because coalescence events cause an overpressure which is relieved by

vacancy absorption. Goodhew and Tyler[147] have demonstrated overpressing experimentally. The vacancy requirement can be seen from Eq. (3) by solving for the number of vacancies (m) and gas atoms in an equilibrium bubble (spherical) to obtain

$$\frac{m}{n} = \frac{kT}{2\Omega\gamma} r \ , \tag{4}$$

where n = number of gas atoms (assuming an ideal gas), k = Boltzmann's constant, T = temperature, and Ω = vacancy volume. From Eq. (4), a bubble must continue to obtain more vacancies per gas atom to maintain equilibrium as it grows.

Pressure can adequately be described by an ideal gas law for bubble diameters larger than ~100 nm (ref. 173). For smaller sizes, however, Barnes in 1964 pointed out that the ideal gas predicted too many gas atoms or too much pressure compared to a reduced Van der Waals equation of state. Cost and Chen[175] in 1977 showed a more realistic virial equation of state which gave values between the ideal and reduced Van der Waals predictions; they estimated a compressibility greater than one as the parameter to describe deviation from ideal behavior. This work has been extended by recent, parallel work of Wolfer[176] and Brearley and MacInnes,[177] who both used interatomic potentials to describe the behavior of a very densely packed gas. These equations allow better gas accounting for small bubbles. However, even with a more compressible gas, 10-nm-diam bubbles need about ten times more vacancies per gas atom than the one-to-one ratio found in single or di-vacancy helium atom clusters.

The discovery of voids proved that variable vacancy supersaturation did exist at higher temperatures under displacive irradiation. Therefore, more recent theoretical work began treatment of both nucleation and growth of bubbles under such conditions. Bullough and Perrin[178] highlighted several clear distinctions between bubble and void behavior in the presence of vacancy supersaturation. In contrast to voids, which will be considered later, bubbles are stable to shrinkage under compression, but can expand unstably under tension once they become larger than some critical radius. Nolfi and Wiedersich[179] also described stress-free bubble expansion to an underpressured, dynamic "equilibrium" if, after an initial vacancy supersaturation, equal fluxes of vacancies and interstitials eventually impinge on the bubble.

Among the first to investigate dynamic bubble nucleation and growth under displacive irradiation employing an atomistic rate theory approach were Odette and Frei[31] in 1974 and Odette and Langley[180] in 1975. Bubble growth occurred only when these cavities did not convert to voids (bias-driven cavities). Such behavior was found only at very high bubble concentrations. Their calculations assumed two helium atoms and a di-vacancy to the stable nucleus for a bubble. Odette and Langley describe a stress-free critical radius for bubble-to-void conversion as a result of the bubble accumulating gas atoms in a vacancy supersaturation. Gas-driven bubble growth can occur below this limit, but these are very small (<5 nm in diameter) and do not cause significant swelling. For a variable and continuous helium generation rate, bubble concentrations were predicted to increase with increased helium, a

result consistent with the early Mazey and Francis data and with more recent HFIR data. The work of Odette and Langley has been extended recently by Stoller and Odette[35,181] to fit EBR-II and HFIR data on 20%-cold-worked (CW) 316 and to predict fusion first wall swelling behavior. Ghoniem and Takata[98] have also recently included a sophisticated rate theory treatment of bubble formation from the standpoint of the interactions and clusterings of individual point defects and helium atoms. They included the transition between the nucleation and growth stages by continuously monitoring an ensemble of evolving clusters. They assumed the "bubble" nucleus to be a tri-helium interstitial cluster which then attracted vacancies. They included the best picture available in 1980–82 of the several modes of helium atom diffusion (see section on Gaseous Transmutants) and they included various modes of bubble or cluster dissolution under irradiation (as discussed earlier). Ghoniem and coworkers[93] continue to study the atomistics of helium and point defect migration and interactions and to describe the earliest stages of bubble formation. Glasgow et al.[182] also treated the possibility of bubble growth as a function of helium generation and vacancy supersaturation, but for fixed nucleation. They also included Wolfer's[176] equation of state to describe the pressure of the densely packed gas in small bubbles. Finally, theoretical studies of the critical radius have been continued by Hayns,[183] Townsend,[184] and Mansur and Coghlan.[185] In summary, the theoretical treatments consistently predict low swelling and small sizes when bubbles do not convert to voids. Most also agree that gas-driven bubbles are the dominant mode of swelling under displacive

irradiation at about 600 to 650°C or above. We see next that voids behave differently.

B. Voids

Cawthorne and Fulton's[20,21] discovery of voids in 1966–67 in DRF-irradiated SA 316 confirmed earlier conjecture by Greenwood et al.[166] Greenwood et al. indicated that if dislocations preferentially absorbed interstitials, then a vacancy supersaturation would result during elevated-temperature irradiation. They concluded that bubbles would not remain gas-driven but rather would begin to grow into underpressurized cavities in response to condensation of excess vacancies. The ideas of Greenwood et al. seemed a minority opinion among those working on bubble work in the early 1960s, but these ideas became foundational to the theoretical work that followed the discovery of voids in the late 1960s and early 1970s. Few phenomena have captivated or excited the radiation damage community as did void swelling.

As continued evidence for irradiation-induced voids was found in austenitic stainless steels in 1968–71 (refs. 138,139,186) it became obvious that the phenomenon was general. Voids were also found in neutron-irradiated pure metals, first in 1968 in nickel,[187] and then in aluminum,[188–190] copper,[189] molybdenum,[191,192] vanadium,[193] and a host of other metals.[194,195] In fact, to date one of the few metals not to form voids under neutron irradiation is zirconium.[196] In SA 316, voids were found at irradiation temperatures of 350 to 650°C, but investigations of various metals indicated that the phenomenon was general at homologous temperatures of 0.3 to 0.55 T_m (ref. 23). Voids observed due

to quenching and aging,[197] creep,[198] and the Kirkendall effect[199] all preceded the irradiation-induced phenomenon. Subsequent investigation also demonstrated that void formation was not unique to neutron irradiation, but could be found under heavy- and light-ion irradiation,[200-202] high-voltage electron microscope (HVEM) irradiation,[23,203-205] (voids were even found after electromigration[206]) and laser bombardment followed by aging.[207] As many materials were found to swell substantially, it became obvious that such swelling would be performance limiting in service, and some solution to the swelling problem was necessary.[208] Early work indicated that complex alloys swelled less than pure materials and that, particularly for 300-series stainless steels, swelling was quite sensitive to minor compositional changes (or even heat-to-heat variations) and could be reduced by cold working.[3-5,23,189,194,195,208-213] Therefore, efforts became divided into those directed toward solving the engineering problem of void swelling and those directed toward understanding the physics of void swelling. Furthermore, the initial microstructural similarity between ion and electron irradiation to neutron irradiations led many people to use the "simulation" techniques for both basic studies and alloy development screening. The simulation techniques, particularly the ion irradiations, offered a more controlled irradiation environment in which parameters such as temperature, stress, helium generation rate, etc. could be uncoupled or combined and varied in manners not possible under neutron irradiation. These studies were ideal for mechanistic investigations. At much higher damage rates, the "simulation" techniques also satisfied the need for quickly screening

alloys and "predicting" swelling behavior for alloy development efforts to meet the demanding schedule for FBR near-term goals. However, correlations of ion and neutron data, although qualitatively reasonable, were not exact in coincidence of swelling or swelling resistance behavior.[214-216] In high swelling materials, for instance, void formation differences between "simulation" and neutrons irradiations could be accounted for by a simple shift to higher temperature with increased damage rates.[216-218] Complex phenomena such as precipitation reactions, however, did not shift or accelerate to correlate so simply. Thus, while many early ion and electron irradiations were conducted on engineering alloys, ion work in the mid-1970s shifted toward investigating simpler alloys with considerable theoretical modeling support.[218,219] Reactor irradiation experiments, on the other hand, became devoted to investigating and achieving higher fluence data on more swelling-resistant materials as a result of a nationally coordinated FBR materials development program.[19,220] As a result, data rapidly ceased to be accumulated on materials such as SA 316.

In contrast to bubbles, voids grow easily via vacancy absorption generally having much larger growth rates than bubbles would have at the same temperature. Voids tend not to migrate, but grow without apparent saturation (with fluence) and coalesce by impingement at very large sizes.[23,118] As mentioned before, voids were never observed at grain boundaries after stress-free irradiation.[221] Voids were always found to ultimately shrink upon postirradiation annealing, and disappear or leave residual bubbles,[23,138,139,162] although an intermediate coarsening via

Ostwald ripening could precede final elimination.[23] Finally, voids are not observed above about 0.55–0.6 T_m, whereas helium bubbles remain stable until nearly the melting point of most metals. Because the literature is so extensive regarding void formation and swelling, detailed data are reviewed only for neutron-irradiated SA 316.

The collective qualitative observations of many researchers show a systematic progression of cavity phenomena with either increased temperature or fluence (Fig. 9). The SA 316 data are from the same investigations mentioned previously (Dislocation Section,[20,38-40,113-116]), with the addition of observations by Kenfield et al.[222] and Lee et al.[223] (on M2783 heat of SA 316). Symbols are consistent with Figs. 5 (p. 26) and 6 (p. 30) and the steel compositions are again contained in Table 2 (p. 27). The cavity phenomena progress with increasing temperature from tiny matrix bubbles at ~300 to 375°C, to matrix voids plus precipitate-associated voids at ~425 to 625°C, to precipitate voids plus small matrix bubbles from ~625 to 750°C, and finally to small matrix bubbles again above 750°C. The low-fluence ORR data of Bloom et al.[109] on SA 304 (an easy swelling steel) provided a lower temperature limit on cavity formation at 400 to 450°C. However, at much higher fluence, bubble formation is possible as low as 300°C, as found by Thomas and Beeston[112] for SA 348 in ETR and ATR. Cavities will usually become visible at higher fluences, even if they cannot be seen at lower fluences. The matrix plus precipitate-associated void regime shows the greatest fluence dependence. Precipitate-associated voids generally appear first, followed by matrix voids at higher fluence. Next, we examine the quantitative data at ~400 to 700°C.

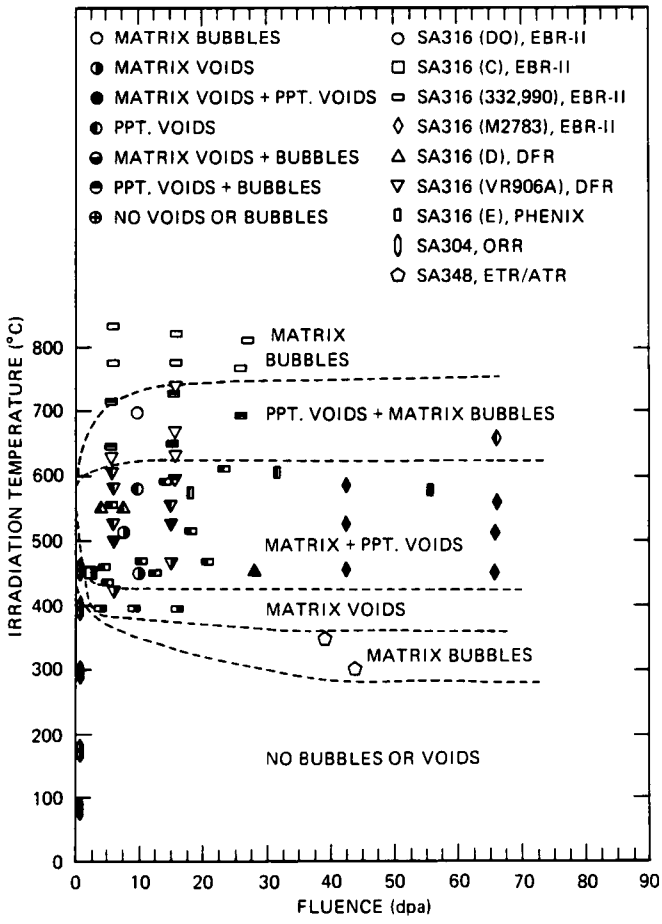

Fig. 9. A plot of cavity character as functions of temperature and fluence for FBR-irradiated SA 316. Regions indicate the transitions from bubble to void back to bubble regimes as temperature increases. Data references are found in Table 2 (p. 27) and in text.

The temperature and fluence dependencies of void diameter, void concentration, and void swelling are shown in Fig. 10 for the SA 316 microstructural data of Stiegler and Bloom,[40] Brager and Straalsund,[38] Kenfield et al.,[222] Barton et al.,[39] and LeNaour et al.[116] The swelling data of Bramman et al.[113] and several microstructural data points by Lee et al.[223] are also included. Figure 10(a) shows that voids get larger as either irradiation temperature or fluence increase; at higher temperatures,

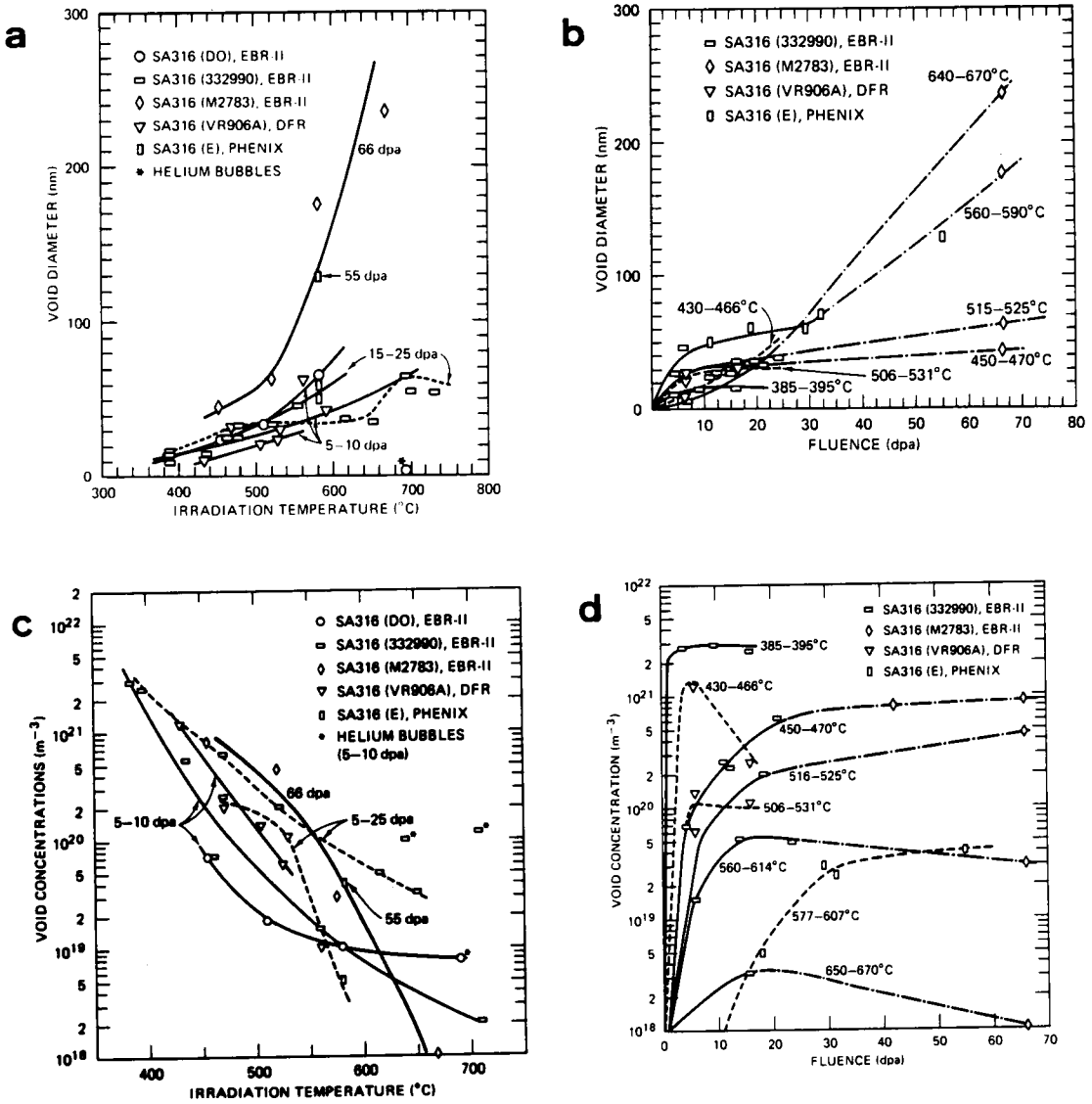

Fig. 10. Void size, void concentration, and total swelling are plotted as functions of temperature (a, c, e, respectively) and fluence (b, d, f, respectively) for FBR-irradiated SA 316 from various investigators. References are found in Table 2 (p. 27) and in text. The high fluence M2783 heat data are connected to the lower fluence 332990 heat data because both are air-melted steels irradiated in EBR-II and the trend curves are reasonable.

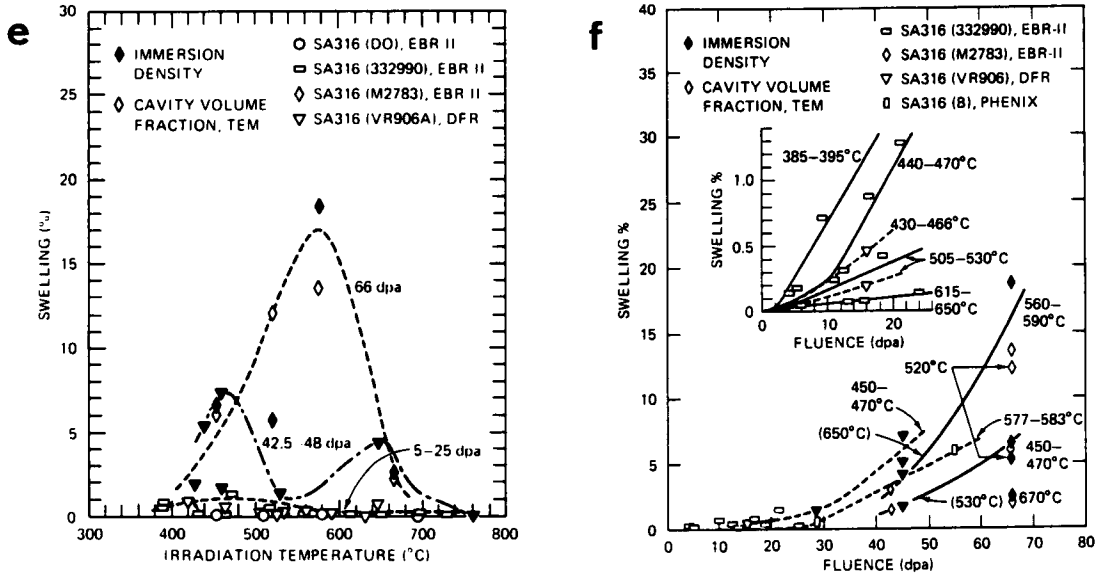

Fig. 10 (continued)

nearly all large voids are attached to precipitates. By contrast, bubbles are very small, even at high temperature. The temperature dependence of void concentrations is opposite to their size dependence. Void concentrations [Fig. 10(c)] decline steeply with increased irradiation temperature, but tend toward higher concentrations with increased fluence, particularly below 550 to 600°C. Fine bubbles are much more concentrated than voids, particularly at higher temperatures.

Macroscopic swelling increases in proportion to the product of void concentration and its averaged volumes. In the simplest cases the swelling (or volume increase) should be related to the macroscopic density change as follows:

$$\Delta V/V_0 = (V_f - V_0)/V_0 = \Sigma/(1 - \Sigma) \ , \qquad (5)$$

where

$$\Sigma = \text{negative fraction density change} = (\rho_f - \rho_0)/\rho_0) \ ,$$

with V_0 = initial volume, ρ_0 = initial density, V_f = final volume, and ρ_f = final density. Void formation usually dominates the volume increase under stress-free irradiation. However, precipitate phases can also cause additional volume changes or they affect matrix lattice parameter through compositional changes. In general, cavity volume fraction (CVF) determined from TEM void statistics, and immersion density (ID) determined by weighing and macroscopic volume determinations, are independent measurements of swelling which should agree, but often do not. Immersion densities are inaccurate at small values of swelling and TEM determinations of swelling are difficult for high swelling due to very large voids (usually requires HVEM). Figure 10(e) therefore shows both CVF and ID swellings at high fluence and CVF swelling at lower fluence as functions of temperature.

At lower fluence [Fig. 10(e)], the swelling data show a flat temperature dependence with a slight peak at about 460 to 480°C. At high temperatures, swelling is low due to decreased void nucleation. Conversely, at low temperatures, swelling is low because void growth is diminished {although nucleation increased [Fig. 10(a,c)]}. The higher fluence data of Kenfield et al.[222] show a temperature dependence strongly peaked at ~580°C. The large peak in this temperature range appears to be due to additional void growth with little increase in nucleation as fluence increases. The ID data of Bramman et al.[113] at 42 to 48 dpa

[corrected to IAEA dpa calculations from half-Nelson dpa by a factor of 1.15 (ref. 224)] show two swelling peaks with increased temperature, one at ~450°C and one at ~650°C. Comparison of the Bramman et al. data with that of Kenfield et al. demonstrates how wide the heat-to-heat variation of swelling behavior can be for the range of steels included in this work.

Figure 10(b,d,f) illustrates the fluence dependencies of microstructural and swelling data. In Fig. 10(b), void growth is initially rapid at most temperatures up to about 10 to 15 dpa, and then becomes slower and temperature dependent, except at the highest temperatures. Except for the observations of Barton et al.[39] at 430 to 460°C, all data show void growth to nearly saturate with fluence below about 525 to 530°C. At higher temperatures, void growth rapidly ensues after a slow growth transient period of about 20 to 30 dpa. Figure 10(d) shows clearly that void nucleation is also initially rapid and then tends toward saturation with increased fluence (again with the exception of the Barton et al. data at 430 to 466°C).* Nucleation decreases and saturates more slowly as temperature increases; however, the highest temperature data (650 to 670°C) do not indicate saturation, possibly due to coalescence.

The fluence dependence of swelling reflects the combined fluence dependencies of void growth and nucleation. Both total swelling and void microstructural evolutions can be described by an "incubation" or

*This unusual void behavior does correlate, however, with similar unusual behavior in fluence dependence of their Frank loop and total dislocation concentration data in Fig. 6(d and f) (p. 30).

transient regime followed by a regime of nearly linear void growth and rapid swelling increases with fluence.[23,225,226] As Fig. 10(b,d,f) shows, however, the two incubation periods are not coincident, with void formation being essentially complete before swelling develops to the 0.5 to 1% level. Figure 10(f) therefore shows both the low swelling at low fluences (inset) and high swellings at higher fluence. Initial swelling more closely reflects void nucleation than growth, particularly considering the temperature dependence of the fluence curves [Fig. 10(b,d,f)]. The "steady-state" swelling increases with fluence, mainly reflecting void growth after nucleation saturates. Swelling rates were temperature dependent, with lowest swelling rates (~0.05%/dpa) observed at the highest and lowest temperatures and highest swelling rates (~0.7%/dpa) at the peak temperature. At 450 to 470°C, the swelling rate was low due to a lack of void growth, whereas the low rate at 640 to 670°C reflects a lack of nucleation. By contrast, however, Brager and Garner[227] recently reviewed and reported swelling data in SA 316 and indicated virtually no temperature dependence to the steady-state swelling rate at higher fluence.

Very little neutron data exist for the effects of helium on void formation under neutron irradiation. Bloom and Stiegler[45] found an increase in void nucleation and a slight reduction in void size and swelling for EBR-II-irradiated SA 304 with 20 at. ppm preinjected helium compared to uninjected material. Harkness et al.[46] in 1973 found similar results for SA 304 irradiated in EBR-II with a similar amount of preinjected helium, but also found complete suppression of void formation

at 76 and 100 at. ppm preinjected helium. When they aged the preinjected samples to coarsen the helium distribution, however, they then found voids. These results seemed to corroborate the early inference, from void annealing, that helium influenced void nucleation by forming bubbles which then serve as void nuclei. However, the void suppression was quite surprising, but has also been seen for SA 316 preinjected with 110 at. ppm He and irradiated in EBR-II.[165] This suggests a sink strength (concentration) dependence to the nucleation of voids from bubbles.

The only avenue to obtain increased helium to dpa generation rates under neutron irradiation is thermal reactor irradiation with specimens located near enough to the fuel to get sufficient displacement damage from fast fission neutrons. Manley and Rhodes[162] in 1972 found voids at 400°C after long-time (40,000 h) irradiation in a thermal reactor. For HFIR-irradiated type 316 stainless steel, Maziasz et al.[49] in 1975 suspected voids in SA 316 irradiated at ~530 to 555°C. More recent work by Maziasz and Grossbeck[228,229] suggests that voids form among dominantly bubble microstructures at lower temperatures for CW 316 stainless steel in HFIR. However, Brager and Garner[36,37] believe that all the cavities seen in HFIR samples are voids.

Considerable information about helium effects on the cavity microstructure is available from preinjected or dual-beam ion irradiations of austenitic stainless steels. Small (5–20 at. ppm) amounts of helium were often preinjected for void simulation studies on the FBR program,[200,202,214–216,230–235] but higher helium concentrations have

been used in the fusion program.[32,130,236-241] The generally observed effect is that helium increases the overall cavity concentration; however, whether these bubbles (or stable cavities) remain small or become large voids depends on the material and the temperature, amount and mode of helium introduction. Early ion work on SA 316 by Nelson and Mazey[200] showed that void formation did not require the presence of helium, but that helium and oxygen clearly enhanced void nucleation. Keefer and Pard[230] showed both enhanced and accelerated void formation in proton-irradiated (500°C) SA 316 containing cold-preinjected helium (0—28 at. ppm) whereas McDonald et al. observed no effect of overall amounts of helium injected intermittently during nickel ion irradiation of SA 316 at 600°C. By comparison, higher purity stainless steels and type 304 stainless steel easily form voids without helium during ion irradiation.[130,240] Void formation becomes more difficult under ion irradiation without helium in titanium- and niobium-modified steels [e.g., type 321 and FV548 (refs. 43, 242,243)], and even more so in advanced low-swelling titanium-modified austenites such as LS1A (to ~600 dpa) and LS1B (~100 dpa).[135,136] At higher damage rates under HVEM irradiation, helium-free void nucleation is easy, even in FV548 (refs. 244,245). Large amounts of helium can also affect void nucleation and growth. In high-purity austenitic alloys under ion irradiation, unless the helium is cold preinjected, most cavities are voids. If bubbles form and convert to voids, void sizes tend to decrease as cavity concentrations increase; however, overall swelling is often greater than irradiations with no helium.[130,237,238,240] As the He/dpa ratio is

increased for dual beam irradiations of high-purity steels and type 316 stainless steels, void growth further decreases, and now swelling can increase or decrease.[32,237,240] Hot preinjected helium increases or decreases swelling, depending on the amount and temperature of implantation.[32,134,238] Fairly consistent suppressions of void formation and swelling are found when larger amounts of helium are cold preinjected with high concentrations of fine bubbles (stable cavities) forming instead.[32,237,238,241] Virtually no swelling due to voids was observed in SA 316 ion irradiated to ~25 dpa at 625°C with 15 at. ppm cold preinjected helium by Kohyama et al.[240] and to ~70 dpa for SA LS1A with ~112 at. ppm by Kenik.[135] To summarize, helium can either enhance or suppress void formation during ion irradiation, depending on whether bubble nucleation continues or bubbles convert to voids. Overall, the experimental observations on temperature, fluence, and helium dependence of void swelling are reasonably consistent, but difficult to intuitively rationalize without theoretical analysis.

Predicting higher fluence swelling behavior or swelling resistance became immediate needs after the discovery of voids. Traditionally, several approaches have emerged. On a strictly empirical basis, neutron data could be extrapolated, based on "reasonable" assumptions about void behavior at higher fluences or based on some theoretical insight plus correlation with "simulation" data. As a result, a large effort was devoted to theoretical modeling of void nucleation and growth from the accumulation of primary damage products (vacancies, interstitials, and helium atoms). More recently, a new scheme for rationalizing

and predicting swelling results for types 304 and 316 stainless steels has been proposed on the basis of insight obtained from correlating "microchemical evolution" with swelling and microstructural evolution.[246]

Theoretical work on void formation and swelling lagged the experimental work by several years because that community was surprised by the existence of a vacancy supersaturation and had trouble visualizing the physical basis for it,[178,185,245] despite the prediction by Greenwood et al.[166] This portion of the literature survey relies heavily on several key reviews.[23,118,220,221,248-251]

The experimental void formation results clearly suggested a nucleation and growth phenomenon. It was also obvious that dislocation and void developments were somehow correlated. Although some early theoretical work involved solving diffusion equations to a single cavity,[178,247] by far the most useful and lasting theoretical modeling resulted from application of the chemical reaction rate theory formalism to void swelling by such workers as Harkness and Li,[186,221] Wiedersich,[252] Brailsford and Bullough,[119] and Fisher and Williams[253] in 1969 to 1972. Most early work treated void growth in more detail than void nucleation, although as we shall see shortly, the same rate theory approach can be used for both. Rate theory ties the various point defect generation and loss terms into conservation equations for vacancies and interstitials of the form

$$G_v - RC_vC_i - K_vC_v = \frac{\partial C_v}{\partial t} \quad , \tag{6}$$

and

$$G_i - RC_vC_i - K_iC_i = \frac{\partial C_i}{\partial t} \quad , \tag{7}$$

where the subscripts v and i denote interstitials and vacancies, respectively, G's the effective point defect generation rates per unit volume, C's the concentration of point defects, K's reaction rate constants for various point defect sinks, and R the coefficient of recombination (all after the notation of Mansur[118]). These equations must include additional terms for the ion or electron irradiation case, but are adequate to describe neutron irradiations. These equations describe a continuum in which point defect concentrations, generation, and the various sinks are uniformly distributed spatially, and if the time derivatives on the right-hand side are set to zero, they describe a quasi-steady state. The generation rates of vacancies and interstitials from the primary damage state are equal (hence $G_i = G_v$); however, since there are equilibrium thermal vacancies and essentially no thermal interstitials, $C_v > C_i$. The RC_iC_v term couples Eqs. (6) and (7) so that they must be solved simultaneously. The sink terms sum all individual sink types for a particular defect (i.e., $K_v = \sum_j K_v^j$, where j denotes sink types such as bubbles, voids, dislocations, precipitate particles, etc.; likewise for K_i) and reflect the diffusion of the point defects and the sink strengths as follows (for vacancy sinks):

$$K_v^j = S_v^j D_v = \left[\sum_{r=o}^{\infty} N_v^j(r) s_v^j(r) \right] D_v \quad , \tag{8}$$

with

$$s_v^j = g_v^j Z_v^j m_v^j \quad , \tag{9}$$

where D_v is the diffusion coefficient, S_v^j and s_v^j are total and individual sink strength of the j-th type sink, respectively. $N_v^j(r)$ is the concentration of the j-th type sink of radius, r, g^j is the geometric parameter (usually describing the surface area of the sink), Z^j is the sink capture efficiency (ratio of real sink absorption of defect current to that of perfect, ideal sink) and m^j is the multiple sink correction factor to reflect the interaction with the sinks in the system. These equations contain the physics and reflect the history of the development of void growth theory.

From Eqs. (6) and (7) it is obvious that if all defects flowed equally to all sinks, they would annihilate or recombine and there would be no net swelling. Therefore one sink (usually assumed to be the dislocation) had to be biased (or have a greater efficiency for interstitials than vacancies) to allow a vacancy supersaturation to condense preferentially at neutral or unbiased sinks such as voids.[178,186] In 1971, Harkness and Li[221] showed (from the work of Ham[254] in 1959) that preferential attraction of interstitials over vacancies to dislocations resulted from the larger misfit strain and higher mobility of the interstitial, giving the dislocation a larger capture radius for interstitials. Bias work for dislocations was extended by Wolfer and Ashkin[255] in 1976. With the biased flow of interstitials to dislocation, the flow of generated vacancies partitioned to voids can be determined from

Eqs. (6–8), and with some simplifying assumptions, swelling due to void growth can be obtained as a function of fluence. Obtaining the temperature dependence of swelling is more difficult. Harkness and Li[186,221] first calculated the temperature dependence of swelling (a peaked maximum), but explained it through the temperature dependencies of void and loop nucleation rather than void growth. Wiedersich[252] explained the temperature dependence as the combined temperature dependencies of the vacancy supersaturation (decreasing with increasing temperature) and the fraction of point defects annihilating at sinks (a peaked maximum near peak swelling temperature). Brailsford and Bullough[119] calculated a separable temperature dependence factor into their swelling as a function of fluence equation; it cut off swelling at lower temperature, mainly due to recombination, and at higher temperature, due to thermal vacancies overwhelming the supersaturation (similar to Wiedersich's explanation). Hayns,[256] however, more recently pointed out that bulk recombination is also important in limiting swelling at higher temperatures for temperature dependent sink concentrations (as the data show).

Precise swelling kinetics were a result of assumptions about void nucleation mechanisms as well as mechanisms limiting growth, as pointed out by Claudson et al.[247] in 1969. In growth theory, if voids are good sinks for point defects, then they should accept defects as fast as they diffuse to them and their growth kinetics will be volume-diffusion limited. Most early work assumed diffusion-controlled kinetics[178,186,221,252,253,257] except for Claudson et al.,[247] who assumed a particular surface reaction as limiting. Mansur et al.[258]

later extended rate theory to include both surface reaction-limited void growth (deduced for the SA 316 data of Brager and Straalsund[38]) and void growth due to coalescence by impingement. Fisher and Williams[253] showed that the swelling kinetics changed as the dislocation evolution changed from loop growth to a constant dislocation density to a recovering dislocation structure. Swelling kinetics for various combinations of sink domination, limiting defect supply mechanisms, and dislocation evolution are summarized in Table 3, taken from the review by Mansur.[118] For a given recombination and dislocation regime (i.e., constant temperature), Mansur describes a Q factor that gives the ratio of the dislocation and cavity sink strengths, to indicate which sinks dominate and which regions of swelling kinetics are obeyed, as shown in Fig. 11. Most steels progress from $n > 1$ to $n \sim 1$ with increasing fluence [Fig. 10(f)] in reactor, but $n < 1$ behavior is possible if cavities become the dominant sinks.[131,165,237,259-261] Several more recent contributions to growth theory include the multiple sink correction,[262] the effects of impurity atoms enhancing point defect recombination,[263,264] the effects of precipitate particles as either additional sinks[119,226,252,263,265,266] (usually to suppress void swelling) or point defect collectors for attached voids[265-267] (to enhance void swelling). Mansur et al.[268] have also introduced a more realistic picture of primary defect generation into rate theory than the homogeneous generating of mono-defects usually assumed. Yoo[269] and Ghoniem and coworkers[270-272] deviate from the normal steady solutions of Eqs. (6) and (7) to obtain time-dependent solutions capable of treating transients. Wolfer et al.[249] have also overcome

Table 3. Fluence Exponents of Void Growth for Limiting Cases and Different Mechanisms of Point Defect Absorption at Void[a]

Dominant Sink	Recombination Importance	Value of n in $\Delta V/V \propto (dpa)^n$ for Each Model: Dislocation Loop Growth	Constant Dislocation Density	Dislocation Mutual Annihilation
		Both Defects Diffusion Controlled		
Dislocation	Minor	6/7	3/2	3
Dislocation	Dominant	3/2	3/2	3/2
Void	Minor	6/5	3/4	0
Void	Dominant	2	1	$\Delta V/V \propto$ in dpa
		Both Defects Surface Controlled		
Dislocation	Minor	6/5	3	6
Dislocation	Dominant	3	3	3
Void	Minor	6/7	3/5	0
Void	Dominant	2	1	$\Delta V/V \propto$ in dpa
		Interstitial Surface-Controlled, Vacancy Diffusion Controlled		
Dislocation	Minor	6/7	3/2	3
Dislocation	Dominant	3/2	3/2	3/2
Void	Minor	6/7	3/5	0
Void	Dominant	2	1	$\Delta V/V \propto$ in dpa

[a]Taken from review by L. K. Mansur, Nucl. Technol. 40 (1978) 5–34.

the normal nucleation difficulties of growth theory by melding together a hierarchy of rate equations through the Forker-Plank formalism to obtain a smooth transition from nucleation to growth.

While early theory work viewed helium as helpful or necessary to void nucleation,[119,221] most imagined the small amounts of helium simply drained innocuously into growing voids.[257] Although adequate for FBR application, the question is opened at the higher helium-generation rates expected for fusion reactor conditions. Yoo and Mansur[273] and

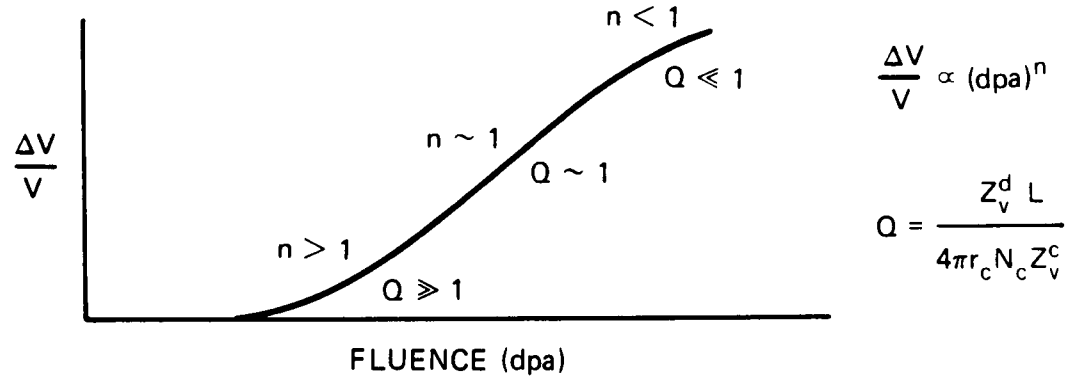

Fig. 11. A schematic representation of the swelling-fluence relationships possible as the balance between total dislocation and cavity sink strength changes. The terms are defined as follows: n = fluence exponent, Q = sink strength ratio, Z_c^d = capture efficiency of dislocations for vacancies, L = dislocation density, r_c = average cavity radius, N_c = cavity concentration and Z_v^c = capture efficiency of cavities for vacancies. Most materials progress from n > 1 to n ~ 1 as fluence increases under neutron irradiation. Taken from L. K. Mansur, Nucl. Technol. 40 (1978) 5–34.

Glasgow et al.[182] partition generated helium into growing voids and calculate its effects on swelling at various temperatures for nickel and type 316, respectively. Yoo and Mansur found no effect of helium on the void swelling regime, without altering the bias; they did find a slight extension of the higher temperature cutoff for voids and then higher temperature swelling due to helium bubbles. Glasgow et al. similarly found no effect of helium on biased void swelling, but then did find negligible swelling due to bubbles if they reduced the bias. Both growth theory treatments assume constant void densities, whereas helium usually increases void nucleation. The critical radius concept forms a bridge between nucleation theory and purely growth theory.

If bubbles are nuclei for voids (complex alloys, reactor damage rates), void nucleation can be treated by calculating the critical size at which the bubbles grow rapidly (diffusion-controlled kinetics) in response to the vacancy supersaturation and do not require helium to prevent vacancy emission (see similar critical radius discussion in Bubbles Section). One can either assume an initial distribution of tiny bubbles or evolve clusters via a nucleation theory, which will be considered next. The first researchers to consider conversion of a stress-free bubble to a bias-driven void was Sears[257] in 1971, using a diffusion cell rather than a rate theory-effective medium approach and an ideal gas law with helium generation typical of FBR irradiation for aluminum. Odette and Langley[180] in 1975–76 described a similar critical radius, but derived it using a rate-theory approach, continuous helium partitioning to all cavities and clusters in an evolving microstructure (using numerical techniques), and a variety of helium generation rates. Work on developing analytical rate theory expressions for or calculating variable dependencies of the critical radius has continued with Hayns[183] using an ideal gas, and Townsend[184] and Mansur and Coghlan[185] using a van der Waals gas law. The critical radius usually becomes larger with increased temperature and smaller with increased internal gas pressure. Odette and Langley included the important effect of increased bubble nucleation (and hence increased sink strength) which decreased the vacancy supersaturation and decreased both the swelling rate and conversion of bubbles to voids; they predicted lower swelling for a fusion reactor than an FBR if the helium induced sufficiently high bubble

concentrations. By contrast, however, extension of this work by Stoller and Odette[35,181] predicts more swelling in a fusion reactor than an FBR if intermediate bubble concentrations develop and these easily convert to voids in the matrix and at precipitate particle interfaces. These divergent (but legitimate) possibilities for void development and swelling bring the focus to the nucleation stage of the cavity microstructure.

The void nucleation problem was much more difficult than growth theory. However, growth theory did demand some input regarding cavity concentrations, either from simple assumptions, experimental data, or from a nucleation theory involving atomistic interactions and clustering. Harkness and Li[221] modeled void nucleation as occurring in the vacancy-rich cores of displacement cascades (possibly stabilized by helium) and then used homogeneous thermodynamic nucleation, with adjustable parameters (a temperature-independent vacancy cluster formation constant and the surface energy) fitted to their experimental data. The void nucleation rate is then the number of critical nuclei times their frequency of promotion past some critical size for stability (they found radii of ~0.1 nm). They obtained the strong temperature dependence of nucleation found in the data and predicted saturation of void densities with fluence, also as found in the data. They, however, found strong coupling to dislocation loop development and sensitivity to parameters poorly known (i.e., surface energy) and were thus unable to proceed in the absence of data. However, they pointed out that a vacancy supersaturation (and hence a bias) was as or more important for nucleation than it was for void growth. The initial nucleation work of Russell[274]

and Katz and Wiedersich[275] in 1971 used a rate theory approach to describe void formation from interaction and clustering of dilute, homogeneous supersaturations of vacancies and insterstitials. A great difficulty compared to classical nucleation of precipitates from a supersaturation was the presence of vacancies and interstitials (matter and anti-matter) that could not form embryos unless a quasi-equilibrium distribution was imposed (as by Katz and Wiedersich[275]). Many researchers[119,195,257] had discussed the improbability of void nucleation without helium (Sears,[257] for instance, showed a critical radius of 2 nm without helium); in 1972 Russell[276] (without considering interstitials) and Loh[277] (considering interstitials following Katz and Wiedersich) included helium by nucleating voids on single, immobile helium atoms trapped in vacancies. In 1973, Katz and Wiedersich[278] also included nucleation on single and clustered gas atoms immobilized in vacancies, and in 1974 Wiedersich et al.[279] also included helium emission from clusters via interstitial absorption. In 1976, both Russell[280] and Wiedersich and Katz[281] allowed mobile gas to both impinge and be emitted from the clusters and, together with Wiedersich and Hall[282] in 1977, allowed helium re-emission from single vacancies and clusters. Singh and Foreman[283] in 1975 also allowed the normally stationary clusters to migrate and coalesce during the nucleation stage, similar to earlier bubble growth theory. The above work showed helium to tremendously enhance void nucleation at the low helium generation rates typical of FBRs (~0.1–0.5 at. ppm/dpa), particularly at lower temperatures. Wiedersich and Katz[281] showed increased helium generation to increase

higher temperature void nucleation until the point at which the increased cluster density contribution to the sink strength suppressed the vacancy supersaturation (similar to Odette and Langley[180]). The difficulty associated with knowing when to terminate nucleation could be solved by coupling to growth theory as suggested by Wolfer et al.,[249] or via a unified theory of all relevant processes into a master differential equation analyzed with a nodal line/critical point formalism in reaction path–cluster size space, as suggested by Russell.[284] Finally, it is also clear that impurity segregation to void embryos (vacancy clusters) enhances nucleation similar to the effects of helium. Beeler and Beeler[285] showed that voids nucleated from cascades were stabilized against dissociation by impurity segregation. Wolfer and coworkers[286-288] have also shown that tiny voids surrounded by a solute shell (most probably due to radiation-induced solute segregation) can be biased against interstitials compared to bare voids.

Despite the abundance of work on cavity nucleation relevant to FBR-irradiation conditions, very little work had explored cavity nucleation at the higher helium generation rates expected for fusion reactor conditions. Odette and Frei[31] were first in 1973–74 with a heirarchy of rate equations describing the diffusion and clustering of substitutional helium (remember that others considered these immobile), integrated numerically to evolve a bubble microstructure (anything larger than two helium atoms plus two vacancies). This was then coupled to a void nucleation model (following Russell and Katz and Wiedersich[276,278]) and a void growth model. They were among the first to calculate final void

and bubble concentrations for EBR-II irradiation conditions, not to mention fusion or HFIR, and the first to couple nucleation (without a data fit) to growth theory. Odette and Frei found the EBR-II microstructure to be void dominated, the fusion condition to be bubble dominated, and the HFIR case to be intermediate with both bubbles and voids (the reported helium generation per dpa for HFIR irradiation was too low at that time[49,164]). Many nucleation reviews have neglected this work.[284,289]

More recently, Hall[290] has considered partitioning of the helium to various traps available in the primary damage state for high helium generation. Singh and Foreman[289] calculate void densities as a function of helium for a hierarchy of rate equations for helium-vacancy reactions and clustering (mobile clusters, but no cluster destruction) and obtain the square root dependence of void concentration on helium content often observed experimentally.[33] In 1980, Ghoniem[291] attempted "microvoid" nucleation for fusion conditions with a heirarchy of rate equations describing vacancy clustering, but he encountered problems without helium stabilization. In 1982, Ghoniem and Takata[98] (as mentioned previously in the Bubbles section) have presented the most sophisticated picture of void nucleation to date; they simultaneously monitored a large hierarchy of rate equations and allowed interaction of vacancies and helium atoms to form clusters (including detailed partitioning of helium throughout the microstructure and including helium and tiny cluster resolution possibilities). They also provided a smooth transition from bubble nucleation to void growth by monitoring helium partitioning and

distinguish between bubble- and void-like cavities on the basis of internal pressure. They found void nucleation almost directly at lower temperature (480–550°C), but found bubble formation to precede voids at ~650°C. They also predict swelling and microstructures which compare reasonably with the early HFIR SA 316 data of Maziasz et al.[49] Ghoniem and coworkers[93,97] are continuing to evolve a nucleation and growth model similar to the nodal line/critical point scheme of Russell,[289] but including the most complete picture of helium-point defect reactions and clustering atomistics currently available.

In summary, the theoretical work has been extensive and has contributed great insight into the underlying physics of microstructural development during irradiation. However, more work is needed to understand completely neutron irradiation results, particularly for more complex and swelling-resistant alloys. Areas identified in recent critical reviews[118,219,249] which need both better experimental characterization and better conceptual and mechanistic incorporation into the theoretical framework are dislocation evolution, the effects of radiation-induced solution segregration (RIS), and precipitate evolution under irradiation. The low fluence evolution of the cavity structure is most essential for nucleation studies.

Finally, we will consider some ways in which RIS effects are being incorporated into the picture of void formation and swelling. According to the mechanistic classifications of Mansur et al.[265] RIS can have direct (impurity layer or shell formation) effects, indirect effects

(by changing the sink concentrations or their point defect capture efficiencies) or mediated (changing diffusion coefficients or depleting solute trap-recombination sites in the matrix) effects on void formation and growth. Although many effects of RIS could be envisioned [see, for instance, Odette, 1979 (ref. 251)], the only RIS effects incorporated into rate theory were the enhancing effects of solute shells or layers on void nucleation[286-288] or the depletion of solute traps in the matrix[263,292] prior to about 1980 (Mansur[292] treats the possibility of RIS changing the bias and its effect on swelling without specifying how it changes the bias). In 1976, Venker and Ehrlich[293] suggested a correlation that related the increased concentration of a fast diffusion minor solute (like Si and Fe) to lower swelling via a reduced vacancy concentration (caused by faster moving vacancies to counterbalance faster moving solutes). In 1978 Marwicks[294] further suggested a coupled effect whereby the fast diffusing major species (i.e., Fe in Fe-Ni) induces enrichment of the slow diffusing species (Ni) at a void, which in turn hinders further flow of vacancies through an opposing Kirkendall vacancy flux. However, Rothman et al.[295] refutes the contention of Venker and Ehrlich by showing that their quoted data for diffusion coefficients of iron, nickel, and chromium as functions of silicon content were wrong. However, Garner and Wolfer[296] have used nucleation rate theory (early Katz and Wiedersich[275] type without helium) to extend Venker and Ehrlich's suggestion, and showed reduced nucleation rates as concentrations of fast diffusing species increased (like Si in Ni).

An entirely different connection between RIS effects and void formation and swelling was offered in the "microchemical evolution" model, as summarized in a recent review by Garner.[246] This model is based on the correlated, coincident observations by Brager and Garner of (a) large volumes of precipitate phases highly enriched in nickel and silicon (this will be treated further in the next section on Precipitation and Microcompositional Development), (b) reductions of matrix concentrations of silicon and especially nickel, and (c) substantial void formation and swelling.[297-300] A relationship has been developed relating the average matrix content (C_{Ni}) and the onset of "steady-state" void swelling to a critical nickel level as follows:

$$C^{*}_{Ni} = C^{0}_{Ni} - 3(C_{Si} + C_{c}) \quad , \qquad (10)$$

where C^{0}_{Ni}, C_{Si} and C_c are initial concentrations of the indicated elements (in atomic percent). A schematic of this "microchemical-evolution" correlation with swelling-fluence behavior is shown in Fig. 12, from Garner.[301] The data often used to support this correlation are given in Fig. 13 (correlation of void formation and matrix nickel content in SA and CW 316 from Brager and Garner[300]). Several features of the model are that C^{*}_{Ni} is ~9% (unclear whether weight or atomic percent), which represents a saturation state (independent of microstructural evolution path or temperature) that instantaneously and locally launches the material into steady-state void swelling. Brager and Garner correlate C^{*}_{Ni} with the microstructural onset of void formation;[299,300] some suggested underlying physical reasons are diffusion coefficients or sink

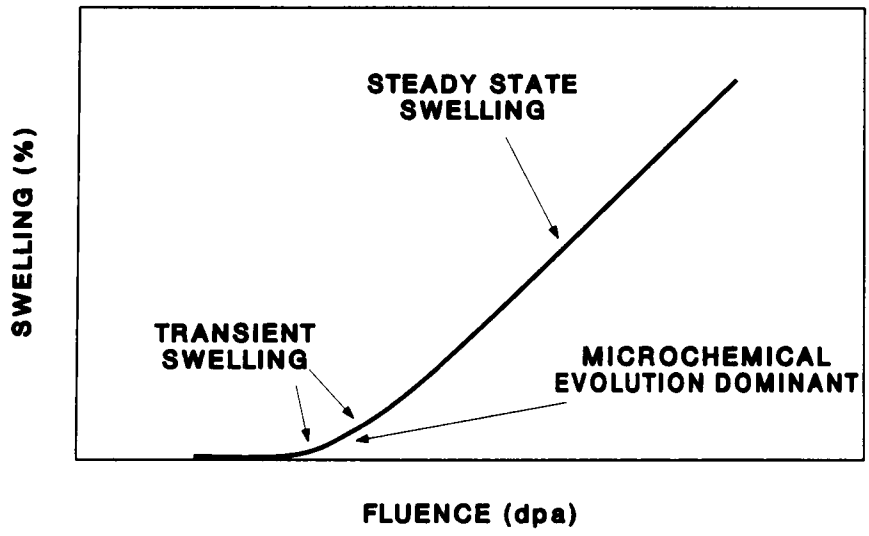

Fig. 12. A schematic of the correlated relationship between microchemical evolution and macroscopic swelling behavior, as envisioned by Garner (reference found in text).

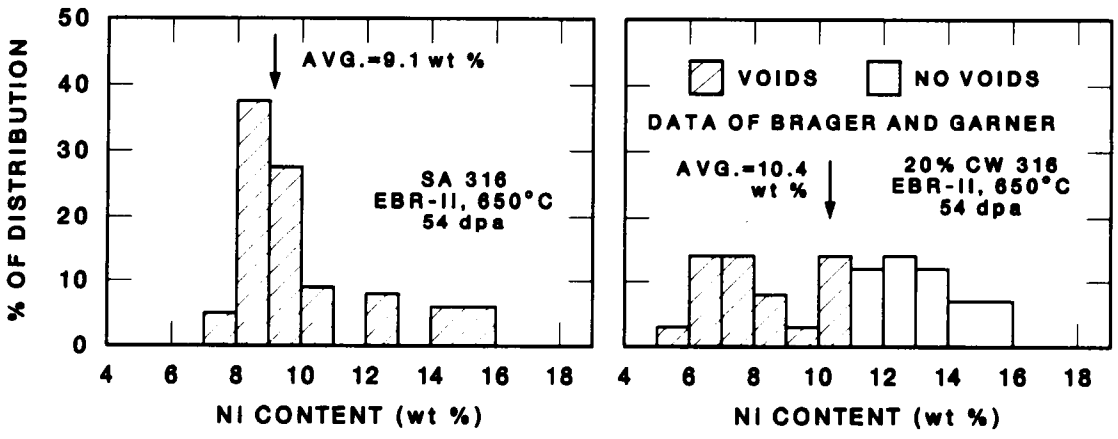

Fig. 13. Correlation of matrix nickel content and the presence or absence of voids in type 316 stainless steel, after EBR-II irradiation to the conditions indicated, from the data of Brager and Garner (data reference found in text).

capture efficiencies altered via RIS.[302] This model apparently gets support from the work of Porter[303,304] and Thomas,[305] mixed support from Le Naour et al.,[116] and very little support from Brun et al.[306] Since many researchers find that nickel segregates to voids,[116,235,300,304-307] it is curious that void formation should correlate spatially with nickel depletion (see Fig. 13). Several recent data suggest that nickel segregation to voids was the major cause of matrix nickel depletion, with precipitate effects being minor.[116,306,308] If this is the case, then the nickel depletion may be the result rather than the cause of void growth, particularly since the void microstructure is established well before appreciable swelling is found or C^*_{Ni} ≈9% is reached [correlate Fig. 10, p. 51, with Fig. 12). It is also stated that "microchemical evolution" was not much affected by increased helium generation, and should therefore be similar for fusion and FBR irradiations of type 316 stainless steel.[36,37,227] However, analysis of the same data by Maziasz and coworkers[33,131,165,259] leads to very different conclusions and interpretations, some of which are addressed later by data in this thesis.

Precipitation and Microcompositional Development

Precipitation generally results from chemical reactions in the solid state which relieve supersaturation of a least one of the reactants. In concentrated, multicomponent solid solutions like type 316 stainless steel, many elements and several different phases can be involved in the precipitation process. Without irradiation, as generally reflected by LeChatelier's principle, the system progresses irreversibly from a highly nonequilibrium state, either directly or

indirectly (through a sequence of metastable phases), to an equilibrium distribution of stable phases. However, unlike gas or liquid reactions, the precipitate phase is not simply removed from the system; the volume misfit, crystallographic orientation, and interfacial structure are additional factors of the new phase that inhibit its formation and growth in the solid state. Without irradiation, normal diffusion supplies the reactants until either equilibrium is reached or the driving force becomes too small. Under irradiation, however, the system can either be driven toward equilibrium or toward a new, very unnatural steady state, depending on the peculiar unmixing action of RIS. During thermal aging, microcompositional development simply depletes the elements from the matrix which enrich the precipitates (generally carbon, silicon, molybdenum, and chromium in type 316 stainless steel). However, under irradiation, microcompositional development often differs and depends upon the combined effect of RIS, which occurs at all point defect sinks including precipitate particles.

A. Radiation-Enhanced Diffusion and Induced Solute Segregation

Diffusion in the solid state is interesting conceptually because even though lattice sites are frozen into the crystal, atom and point defect positions are not, and appreciable migration can occur at higher temperatures. Diffusion in multicomponent alloys, despite difficulties, can generally be measured experimentally in terms of bulk solute redistribution, and explained theoretically on the basis of atomistic processes (for example, see rate theory model by Damask and Dienes,[309] or random alloy model by Manning[310]). Enhanced diffusion was among the

first effects of radiation to be studied [early 1950s (refs. 311,312)]; it seemed reasonably explained by the increased point defect concentrations produced under irradiation. An enhanced diffusion coefficient for solutes, including both vacancy and interstitial contributions to migration, can be expressed from equations similar to Eqs. (6) and (7) (pp. 59,60) (refs. 313–315). Many reviews of thermal diffusion are available (see, for example, refs. 316–318). In an ideal binary solution, thermal diffusion lowers the free energy of the system by eliminating concentration gradients (Fick's first law). In 1948, Darken included the thermodynamics of nonideal solutions into the diffusion coefficient description to relate chemical to tracer diffusion.[319] He found that endothermic solutions would mix more easily and exothermic solutions would resist mixing, compared to ideal solutions. Diffusion to create compositional gradients, as in spinodal decomposition, can occur if the nonideality is sufficient to make the diffusion coefficient negative.[320] In general, irradiation will cause more diffusion to occur earlier and at lower temperatures than during aging. However, the quantitative enhancement also reflects point defect recombination and sink annihilation probabilities and hence must include radiation-induced microstructural considerations.[314] By far, the greater conceptual problem for the irradiation effects community has been the phenomenon of RIS.

Anthony, in 1971 (ref. 321), first anticipated the enrichment of slow diffusing solutes at the expense of fast diffusing solute depletion caused by supersaturated vacancy fluxes flowing to a void (inverse-Kirkendall effect[322,323]) and the enrichment due to vacancy-solute

binding and dragging effects. Okamoto and Wiedersich,[324] in 1974 first suggested enrichment at sinks due to binding of solutes to interstitials which form mixed dumbbells on the basis of solute misfit size (undersized atoms binding, oversized atoms not). The experimental evidence came from Okamoto and coworkers[324-325] in 1973–74 using a Fe–18Cr–8Ni–1Si austenitic steel. They first found strain effects around voids leading to irradiation-induced precipitation (RIP) during electron irradiation and then found silicon and nickel enrichment at ion-bombarded surfaces [detected by Auger electron spectroscopy (AES)]. Direct observations of RIS at individual sinks in Fe-Ni-Cr-based alloys followed, utilizing analytical electron microscopy (AEM). The first such observation was silicon enrichment at Frank loops by Kenik[326] in 1976, followed by observations of nickel enrichment at voids by Marwick et al.[307] in 1978. Further evidence continued to accumulate for RIS depletion of chromium[327,328] and for enrichment of phosphorus[329] at ion-bombarded surfaces of type 316 stainless steel. Little, however, is currently known about the RIS behavior of carbon, manganese, titanium, or vanadium in stainless steels.

Equilibrium (or Gibbsion) and nonequilibrium thermal solute segregation can occur without irradiation or precipitation. Equilibrium segregation of low solubility impurities will occur through their diffusion to grain or interphase boundaries[330-332] (if the boundary energy is lowered) and will favor the highest energy (largest structural misfit) boundaries.[333] Nonequilibrium segregation can occur if solutes bind strongly to and migrate with vacancies.[334,335] Impurities like

phosphorus and sulfur (and to a lesser extent carbon and nitrogen) are often highly enriched at surfaces and boundaries in steels during high-temperature aging due to equilibrium segregation.[333,336,337] Manganese enrichment has also been observed in dilute iron-base alloys[338] and was attributed to the vacancy drag mechanism. Carbon segregates to dislocations (Cottrell atmosphere effect), and together with other solutes like titanium and niobium, to stacking faults (Suzuki effect).[339-341] Silicon also apparently can segregate at carbide interphase boundaries (possibly due to its rejection by the carbide) in aged, low alloy steels.[342]

In contrast to thermal segregation, RIS is a quasi-steady-state balance between solute in-flow coupled to the irradiation-produced defect fluxes and backflow due to normal diffusion to eliminate gradients. Hence, RIS effects at sinks can reverse if irradiation ceases while the temperature is maintained, or if point defect fluxes to sinks are interrupted. The four basic mechanisms coupling solute flows to the point defect fluxes are inverse-Kirkendall and solute drag mechanisms for both the vacancy and interstitial fluxes. Figure 14 shows typical composition profiles at irradiated surfaces for type 316 stainless steel and related pure alloys taken from Sethi and Okamoto.[328] Despite variable alloy composition, flux, fluence and temperature dependencies, chromium and molybdenum are generally observed to deplete while nickel, and especially silicon, enrich at surfaces (neutral sinks). Theoretical work on RIS provides the insight to relate these changes to atomistic behavior, as demonstrated in several recent reviews by Wiedersich, Okamoto, and coworkers.[343-346] Both theory (defect configuration[347])

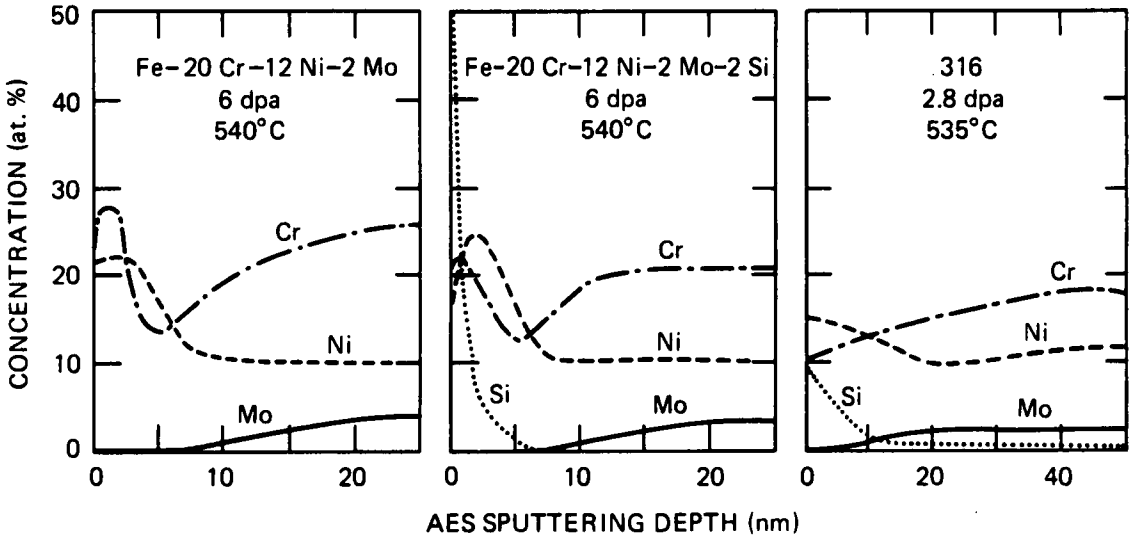

DATA OF SETHI AND OKAMOTO

Fig. 14. Auger electron spectroscopy (AES) compositional profiles of ion-bombarded surfaces as functions of sputtering depths for the irradiation conditions and alloys indicated. Data reference is found in text.

and experiments[348-350] in nickel alloys generally confirm that undersized solutes bind and migrate strongly to sinks with interstitial defects (I-S complexes), whereas oversized solutes do not. Table 4 contains the size-misfit information for substitutional solutes in type 316 stainless steel and shows that only nickel and silicon are undersized, consistent with their strong enrichment in Fig. 12 (p. 74). The original work of Anthony[321] as well as later theoretical work indicated that fast diffusing solute should move against a vacancy flux and deplete at sinks. Table 4 also contains diffusion data for solutes in alloys similar or related to type 316 stainless steel; it shows that chromium and molybdenum diffuse faster than the solvent iron atoms. Nickel is the slowest and silicon the fastest diffusing substitution solutes. Nothing

Table 4. A Summary of Solute Information Relevant to Radiation-Induced Solute Segregation and Austenite Stability in Type 316 Stainless Steel

Size Factor[a]		Austenite Stability		Volume Diffusion Data (~600°C)
Oversized (% volume dilation)		Stabilizers (Nickel Equivalents, wt %)		Diffusivity (m^2/s or Relative Order)
				Alloy System — Fe–17 Cr–12 Ni
Cr	+4.8	Ni	1[c]	$D_C^* \sim 5 \times 10^{-15}$ (* = tracer)[e]
Mo	+35.9	Mn	0.5	
Mn	+3.4	C	30	$D_{Fe}^I \sim 7 \times 10^{-22}$ (I = intrinsic)[f]
Ti[b]		N	30	
				$D_{Cr}^I \sim 2 \times 10^{-21}$[f]
		Destabilizers (Chromium Equivalents, wt %)		$D_{Ni}^I \sim 8 \times 10^{-22}$[g]
Undersized		Cr	1[c] 1[d]	Alloy Systems — Fe–15 Cr–20 Ni; Fe–15 Cr–45 Ni; Fe–20 Cr–45 Ni
Ni	–3.2	Mo	1 1.8	
Si	–2.7	Si	1.5 1.6	$D_{Cr}^I > D_{Fe}^I > D_{Ni}^I$[h]
		Nb	0.5 1.7	
		Ti	--- 2.4	Other Steels and Iron-Base Alloys
				$D_{Mo}^* > D_{Cr}^*$[i] ; $D_{Si}^* > D_{Mo}^* > D_{Mn}^*$[j]

[a]Primarily based upon partial molar volumes determined from the composition dependence of the immersion density of substitution solutes from data by J. L. Straalsund and J. F. Bates, Met. Trans. 5 (1974) 493.

[b]A. D. Marwick, R. C. Pillar, and P. M. Sivell, J. Nucl. Mater. 83 (1979) 35.

[c]Equivalence determined from ability to produce delta ferrite in welds of austenitic stainless steel [C. J. Long and W. T. DeLong, Welding J. 52 (1973) 281–285].

[d]Equivalence determined from ability to produce sigma or chi phase in austenitic stainless steel after aging [F. C. Hull, Welding J. 52 (1973) 104–105].

[e]R. A. Perkins and P. T. Carlson, Met. Trans. 5 (1974) 1151.

[f]R. A. Perkins, R. A. Padgett, Jr., and N. K. Tunali, Met. Trans. 4 (1973) 253.

[g]R. A. Perkins, Met. Trans. 4 (1973) 1665.

[h]S. J. Rothman, L. J. Nowicki, and G. E. Murch, J. Phys. F. 10 (1980) 383–398.

[i]P. J. Alberry and C. W. Haworth, Met. Sci. 8 (1974) 407.

[j]M. A. Krishtal and A. M. Morova, Uch. Zap. Tul. Gos. Pedagog. Inst. Fiz.-Tekin Nauki, 1 (1967) 93 (in Russian).

definite can be inferred for manganese. Of the four possibilities, the two dominant RIS mechanisms appear to be I-S complex migration and vacancy-inverse Kirkendall (V-IK) effects. The V-IK mechanism would clearly lead to chromium and molybdenum depletion at sinks, consistent with the experimental results (Fig. 12, p. 74). The two mechanisms together would cooperatively lead to nickel enrichment at sinks, but would oppose each other for silicon, as I-S complex migration causes enrichment and V-IK causes depletion. Further understanding of RIS depends on theoretical studies which couple the various diffusion possibilities to a rate-theory approach for obtaining actual irradiation parameter dependencies and enrichment or depletion profiles at sinks.

Wiedersich et al.,[351] in a simpler theory, and Johnson and Lam,[352,353] in a more rigorous treatment, in 1976–78 coupled the solute-diffusion mechanisms to rate-theory point-defect conservation equations for dilute binary alloys [similar to Eqs. (6) and (7) (pp. 59,60) but without defect partitioning to sinks] with an additional solute conservation equation. Johnson and Lam were the first to include the interstitial-drag mechanism. They showed RIS had a general temperature dependence similar to void swelling (0.3–0.7 T_m at 10^{-6} dpa/s; peak near 0.5 T_m), but with a peak slightly below the peak swelling temperature. Bulk recombination eliminates RIS at low temperature and back-diffusion overwhelms it at higher temperatures. Several important features are that migration of I-S complexes produces much stronger enrichment effects than do the vacancy mechanisms, and I-S dominates even if the V-IK effect opposes it (as for silicon). Long-range diffusion and

defect survival are essential for substantial solute redistribution, and RIS will occur as long as significant fractions of the defects are flowing to and being annihilated at sinks (even with no bias in the system). In general the sinks need to be stationary (not mobile, like climbing dislocation network) and larger sinks (i.e., voids[353]) experience greater RIS effects (either enrichment or depletion). Wiedersich et al.[352] have shown that these general results extend to concentrated binary solutions. Marwick[294] has included a non-ideal thermodynamic correction (after Darken[319]) to the V-IK mechanism of RIS, and Wolfer et al.[301] include some effects of basic materials parameters being composition dependent. Lam et al.[355] further extend the theory to concentrated ternary Fe-Ni-Cr alloys and found correspondence to the binary model as well as a good fit to ternary RIS data. However, it still remains for RIS theory to be coupled to or studied in realistic irradiation-produced microstructural development to demonstrate, for instance, a sensitivity to sink strength, or helium, as suggested by the data of Maziasz.[165]

B. Thermal Precipitation

The various alloying elements present in type 316 stainless steel easily dissolve in the austenite at temperatures of ~1000°C and above, but several become highly supersaturated below about 900°C. A quaternary phase diagram, calculated by Shoa and Macklin[356] for SA 316 aged at 650°C is shown in Fig. 15. The austenite is unstable and decomposes either to an equilibrium amount of σ phase or segregates chromium and

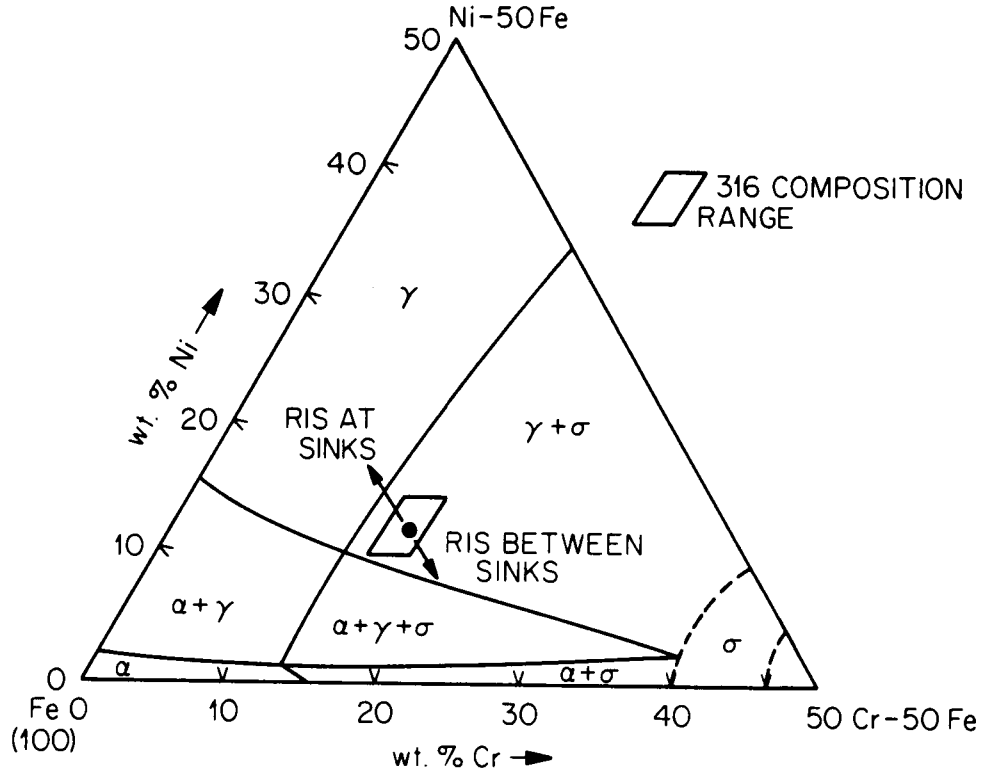

Fig. 15. An Fe-Cr-Ni-X quaternary phase diagram calculated for type 316 stainless steel for aging at 650°C by Shoa and Macklin [Met. Trans. **10A** (1979) 585–590)]. X refers to the other elements present and they are evaluated as chromium or nickel equivalents for their effect on the phase diagram. Arrows are also included to indicate the directions in composition space of microcomposition evolution due to RIS effects occur at or between sinks under irradiation.

like elements into other phases in order to produce a more stable austenite. The Hume-Rothery rules for alloying indicate that solubility is unfavorable if: (a) atomic sizes differ by more than ~15%, (b) the electrochemical nature (i.e., positive or negative ionization), is different, or (c) there is too great a difference in valence or degree of ionization between solute and solvent. These rules are consistent with the considerable solubilities of chromium, nickel, and manganese and

the more limited solubilities of carbon, molybdenum, and silicon in austenitic iron (see Table 4 and ref. 357). Silicon and molybdenum, together with chromium, will also tend to form various intermetallic phases with iron on the basis of electrochemical behavior, atomic size, or electron concentration (i.e., characteristic structure as a function of electron/atom ratio). Carbon supersaturation will tend toward covalently bonded compounds with chromium, molybdenum, and iron. The next problem is characterizing and understanding the various phases which form in type 316 stainless steel.

Thin-foil TEM studies of precipitation in steels are difficult and only began in about 1959—1963 (see, for example, refs. 339, 358—361); prior studies relied upon either metallography or TEM of extraction replicas. Before the mid-1960s most crystallographic phase identification was done by x-ray diffraction from bulk precipitate extractions or by electron diffraction (in TEM) on extraction replicas. Prior to the early- to mid-1970s, limited compositional information on various phases in steel was only available through x-ray microprobe analysis (on ~0.5-μm-sized particles or larger) or through bulk chemical techniques on extracted residues. Today, eucentric tilting, improved probe forming, diffraction and imaging capabilities as well as quantitative compositional analysis of tiny particles using x-ray energy dispersive spectroscopy (XEDS) or electron energy loss spectroscopy (EELS) allow much better phase identification and characterization in modern AEMs.[362] The remainder of this section will highlight the identity and nature of the phases found in type 316 stainless steel or related alloys, describe

the temperature- and time-dependent precipitation data in aged SA 316, and summarize the theoretical and modeling framework available for understanding thermal precipitation.

The precipitate phases generally found in thermally aged SA 316 are $M_{23}C_6$ (τ) and M_6C (η) carbides and the Laves, σ, and χ intermetallics.[9-11,363] MC carbides can form if small amounts of reactive or refractory metals like titanium or niobium are added. Several additional phases, not normally found in type 316 stainless steel but found in other alloys during aging, are also important because they can form in irradiated type 316. Phosphides of the Fe_2P (also containing Ti and traces of As[364]) and Cr_3P types can be found during aging in type 321 and phosphorus modified 18Cr-10Ni-Fe (ref. 365), respectively. The G and γ' phases are also not present in aged type 316, but can be found after aging in silicon-modified 316s (ref. 366), or higher nickel austenites (< ~25 wt % Ni) (ref. 41), respectively. Laves, σ, and χ generally form in iron-based alloys containing silicon, molybdenum, and chromium. The relatively stable cementite (Fe_3C) carbide gives way to a host of complex alloy carbides involving chromium and molybdenum as these solutes become more concentrated in the steel.[367-369] Increased chromium favors progression toward $M_{23}C_6$ (τ), whereas increased molybdenum favors M_6C (η) and eventually M_2C. Williams and coworkers[366,370] showed that increased nickel or decreased chromium shifted the carbide balance from $M_{23}C_6$ (τ) toward M_6C (η) and that increased silicon and decreased carbon shifted the phase stability from $M_{23}C_6$ (τ) toward the G phase. The phases change in response to alloy compositional changes

because most of these, particularly the carbides, apparently have distinct compositions and solubility limits rather than broad ranges of solubility like the austenite. The basic nature of the phases themselves is therefore important to understanding the precipitation response of type 316 stainless steel.

The following portion depends heavily on several more extensive reviews.[9-11,41,371-373] Information for the individual phases can be found in Table 5 and can be summarized as follows:

(a) $M_{23}C_6$ (τ) — A complex carbide with a face-centered-cubic (fcc) structure. The crystal structure was first characterized by Westgren,[374] having 92 metal atoms per unit cell. This phase occurs in many aged steels.[9-11,361,363,364,367,369,375-377] It has a positive misfit volume (~ +10%) and normally contains ~14 Mo—65 Cr—16 Fe—4 Ni (all in weight percent). It is highly enriched in molybdenum and chromium and strongly depleted in iron, silicon, and nickel relative to the 316 matrix. Campbell et al.[367] refer to this phase as kappa carbide, but Stadelmeier calls it tau carbide.[372]

(b) M_6C (η) — A complex carbide with a diamond-cubic structure. The 96 atom unit cell structure was also determined by Westgren;[378] this phase occurs in many aged lower carbon steels.[9,11,362,366,367,369,375,377] The structure can also be half filled with carbon ($M_{12}C$) or unfilled (M_5Si);[371,377,379] this phase was first identified in aged type 316 by Maziasz[380] and Bolten et al.[381] This positive misfit (+10%) phase has the composition 7 Si—23 Mo—31 Cr—11 Fe—25 Ni and is highly enriched in molybdenum and silicon and moderately rich in chromium and nickel

TABLE 5. GENERAL CRYSTALLOGRAPHIC AND COMPOSITIONAL INFORMATION ON PHASES FOUND IN TYPE 316 OR RELATED ALLOYS DURING AGING OR NEUTRON IRRADIATION

PHASE	CRYSTAL STRUCTURE[a]	LATTICE PARAMETER (nm)[b]	SOLUTE ATOMS PER UNIT CELL[c]	VOLUME MISFIT OF PHASE[d]	ELEMENTAL PARTITIONING ENRICHMENT/DEPLETION[e]
γ	CUBIC, Fm3m, A1	a_o = 0.36	4	–	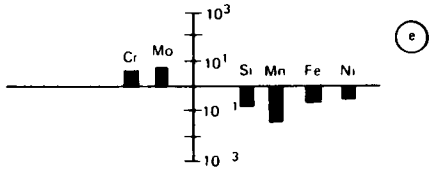
$\tau(M_{23}C_6)$	CUBIC, Fm3m, $D8_4$	a_o = 1.06	92	0.1	
$\eta(M_6C)$	CUBIC, Fd3m, $E9_3$	a_o = 1.08	96	0.1	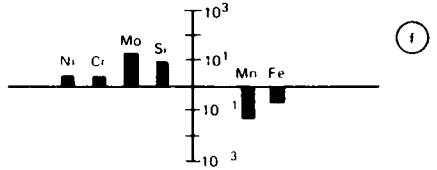
LAVES(A_2B)	HEX., $P6_3/mmc$, C14	a_o = 0.47 (c_o/a_o = 0.77)	12	−0.05	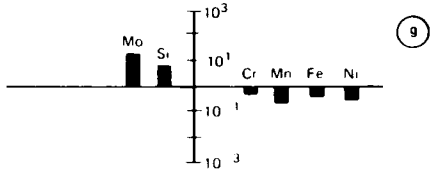
σ(AB)	TET., $P4_2/mnm$, $D8_b$	a_o = 0.88 (c_o/a_o = 0.52)	30	~0	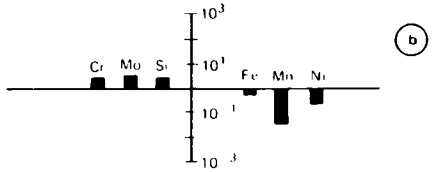

Table 5 (Continued)

χ	CUBIC, I43m, A12	a_o = 0.89	58	0.05	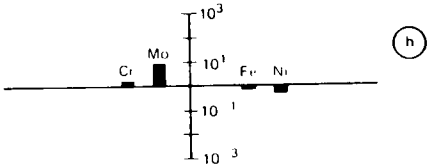
MC	CUBIC, Fm3m, B1	a_o = 0.43	4	0.7	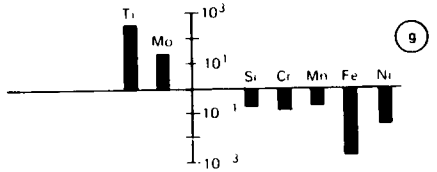
M_2P	HEX., P321, C22	a_o = 0.6 (c_o/a_o = 0.6)	6	−0.4	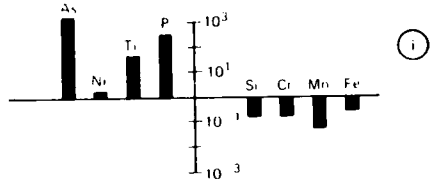
Cr_3P	TET., $I\bar{4}$, S_4^2	a_o = 0.92 (c_o/a_o = 0.5)	32	~0	NOT AVAILABLE

Table 5 (Continued)

$\gamma'(M_3Si)$	CUBIC, Pm3m, $L1_2$	a_o = 0.35	4	−0.1	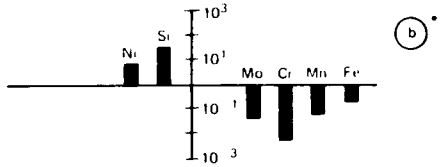
$G(M_6Ni_{16}Si_7)$	CUBIC, Fm3m, A1	a_o = 1.1	116	0.05	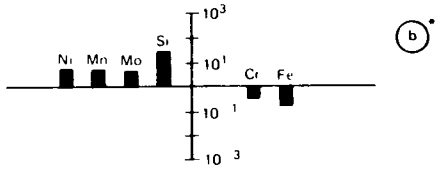

[a]FOR EACH PHASE (LATTICE SYSTEM, SPACE GROUP, STRUCTURE TYPE) WHERE LATTICE SYSTEMS IS THE BRAVAIS LATTICE TYPE – SPACE GROUP IS GIVEN BY THE SHORT FORM OF THE POINT GROUP SYMMETRY ELEMENTS IN THE HERMANN-MAUGUIN SHORT NOTATION; STRUCTURE TYPE IS THE STRUKTURBERICHT NOTATION FOR THE ELEMENT OR PURE COMPOUND THAT IS THE PROTOTYPE STRUCTURE FOR THAT CRYSTAL CLASS, C. J. SMITHELLS, Ed., *METALS REFERENCE BOOK*, 5th ed., BUTTERWORTHS, LONDON, 1976, pp. 108–77.

[b]E. H. LEE, P. J. MAZIASZ AND A. F. ROWCLIFFE, "THE STRUCTURE AND COMPOSITION OF PHASES OCCURRING IN AUSTENITIC STAINLESS STEELS IN THERMAL AND IRRADIATION ENVIRONMENTS," pp. 191–218 IN CONF. PROC. *PHASE STABILITY DURING IRRADIATION*, eds. J. R. HOLLAND, L. K. MANSUR AND D. I. POTTER, THE METALLURGICAL SOCIETY OF AIME, WARRENDALE, PA (1981).

[c]THE TOTAL NUMBER OF ATOMS PER UNIT CELL OF THE STRUCTURE MINUS THE NUMBER OF INTERSTITIAL CARBON OR NITROGEN ATOMS (IF ANY).

[d]FRACTIONAL DIFFERENCE BETWEEN VOLUME PER SOLUTE ATOM IN NEW PHASE COMPARED TO ORIGINAL AUSTENITE. + MEANS MORE VOLUME IN NEW PHASE THAN ORIGINAL AUSTENITE.

[e]THE PARAMETER IS THE CONCENTRATION OF AN ELEMENT IN THE NEW PHASE COMPARED TO THE ORIGINAL CONCENTRATION IN THE AUSTENITE. NUMBERS GREATER THAN ONE INDICATE ENRICHMENT AND VALUES LESS THAN ONE SIGNAL DEPLETION. PHASE IS FORMED DURING AGING UNLESS OTHERWISE INDICATED.

[f]P. J. MAZIASZ, SCRIPTA MET. 13(1979), 621–626.

[g]P. J. MAZIASZ, "HELIUM TRAPPING AT Ti RICH MC PARTICLES IN Ti-MODIFIED AUSTENITIC STAINLESS STEEL," pp. 477–492 IN CONF. PROC. *PHASE STABILITY DURING IRRADIATION*., eds. J. R. HOLLAND, L. K. MANSUR AND D. I. POTTER, THE METALLURGICAL SOCIETY OF AIME, WARRENDALE, PA (1981).

[h]B. WEISS AND R. STICKLER, MET. TRANS. 3(1972), 851–866.

[i]J. BENTLEY AND J. M. LEITNAKER, "STABLE PHASES IN AGED TYPE 321 STAINLESS STEEL," pp. 70–91 IN *THE METAL SCIENCE OF STAINLESS STEELS*, eds. E. W. COLLINGS AND H. W. KING, THE METALLURGICAL SOCIETY OF AIME, NY (1979).

[*]COMPOSITIONS FROM PHASES PRODUCED UNDER EBR II IRRADIATION, BUT PHASES ARE FOUND THERMALLY AS WELL.

compared to the 316 matrix. Maziasz highlights identification difficulties when M_6C (η) is found with tau phase and the potential confusion when this phase is called H phase (or omega[367]) or when Laves is called eta.[9]

(c) Laves — An intermetallic Fe_2Mo type phase, named after its discoverer.[381] Laves has a nearly ideal hexagonal-close-packed (hcp) structure, 12 metal atoms per unit cell, and a slightly negative misfit relative to the austenite. Although primarily found in molybdenum-containing steels,[9-11] Laves phase is definitely stabilized by incorporation of silicon,[382] but tends not to be found in higher nickel austenites.[383] The thermal composition is 5 Si—43 Mo—13 Cr—33 Fe—6 Ni and the phase is highly enriched in molybdenum and silicon but depleted of all other elements compared to the 316 matrix.

(d) σ — An intermetallic (Fe,Cr,Mo) compound, first found in Cr-Fe alloys by Bain and Griffiths.[384] It has a body-centered-tetragonal (bct) structure with 30 atoms per unit cell and essentially no misfit with austenite matrix. The thermal composition is 1.4 Si—6 Mo—37 Cr—50 Fe—5 Ni and the phase is enriched in silicon, molybdenum, and chromium and depleted of nickel and iron relative to the 316 matrix.

(e) χ — A complex intermetallic compound, first detected in molybdenum-containing steels by Andrews,[385] with a body-centered-cubic (bcc) structure having 52 atoms per unit cell and a slightly positive misfit with the austenite matrix. It is often found in molybdenum- and titanium-containing steels and appears more readily in type 316s with higher silicon and lower carbon.[9,386-388] The composition in type 316

is 22Mo—21Cr—52Fe—5Ni (AEM measurements of silicon content were not made) and the phase is primarily molybdenum-enriched relative to the 316 matrix with a smaller chromium enrichment and nickel and iron depletions.

(f) MC — An fcc carbide, not generally found in type 316 unless titanium or niobium, is added. This phase has the largest positive misfit of the phases found in steels which makes vacancy absorption important to its formation.[340,389] It is among the most finely distributed and yet most stable phases in steel.[306,364,374,390] Only recently has AEM revealed large molybdenum concentrations (and subsequent stoichiometry effects) in small particles of titanium-rich MC.[389,391] A very important feature of these carbides is that they are strongly depleted of the Fe, Mn, Cr, Ni, and Si present in the austenite matrix.

(g) M_2P — A complex phosphide compound usually formed with iron or chromium. The same phase structure is also found in Fe-Cr arsenides,[392] titanium-rich phosphide-arsenides,[364] and Ti-Mn silicides.[393] A nonideal hexagonal structure with 6 metal atoms per unit cell and a considerable negative volume misfit (the largest among the phases). The phase was found recently in type 321 stainless steel aged for ~17 years at 600°C by Bentley and Leitnaker.[364] They found the phase composition to be 7P—27Ti—4Cr—27Fe—17Ni—18As with As, P, and Ti being tremendously enriched, Ni slightly enriched, and the other elements depleted relative to the austenite.

(h) Cr_3P — A phosphide with a tetragonal structure, 32 atoms per unit cell, and almost no volume misfit with the matrix. This phase was observed by Rowcliffe and Nicholson[365] in a high P, low C, 18Cr—10Ni

steel, and it has the same thin lath or rod morphology (parallel to $\langle 001 \rangle_\gamma$) as found for Fe_2P (ref. 364). No chemistry is available.

(i) γ' — An ordered fcc, A_3B intermetallic compound that often has almost the same lattice parameter as the austenite with little or no misfit. $Ni_3(Al,Ti)$ was first found by Taylor and Floyd[394] in nickel base alloys, but Ni_3Si and Ni_3Fe are also found in nickel alloys.[395,396] Although not found in aged type 316s, the phase does form under irradiation with the composition 20 Si—(10 to 20) Fe—(60 to 70) Ni and is highly enriched in silicon and nickel and strongly depleted of the other alloying elements.

(j) G — A complex silicide, first identified by Beattie and Ver Snyder[397] and later found to have an fcc, $M_6Ni_{16}S_7$ structure, where M can be Ti, Nb, or Mn or Cr.[398,399] It has 116 atoms per unit cell and $a_0 \sim 1.1$ nm and can be very difficult to distinguish, on the basis of diffraction, from τ and η carbides. This phase is generally found after aging in high silicon and low carbon austenitic steel[366,400] but not in lower nickel or higher molybdenum steels.[370] The composition (after irradiation in 316 + Ti) is 16Si—6Mo—2Ti—8Cr—8Mn—12Fe—48Ni and it is very rich in silicon, nickel, manganese, and molybdenum, and depleted of chromium and iron relative to the matrix.[41,306]

In summary, the phases formed in aged type 316 are solute rich and solvent (Fe) poor to varying degrees and differ discernibly in structure and composition. In general, all phases are enriched in molybdenum and, except for τ and χ, are found to be quite rich in silicon. Only τ, η, and, σ have significant chromium enrichment and only η is found to be

rich in nickel. These phases also have small or negligible volume misfit. The precipitation response also depends upon the aging time and temperature in SA 316.

The most complete characterization of precipitation in aged SA 316 was done by Weiss and Stickler[9] in 1972, for temperatures ranging from 400 to 900°C at times between 0.17 to 3000 h. The various phases formed as functions of time and temperature are mapped in a phenomena plot in Fig. 16 and the composition of the steel is found in Table 2 (p. 27). Spruiell et al.[10] also examined precipitation in aged SA 316

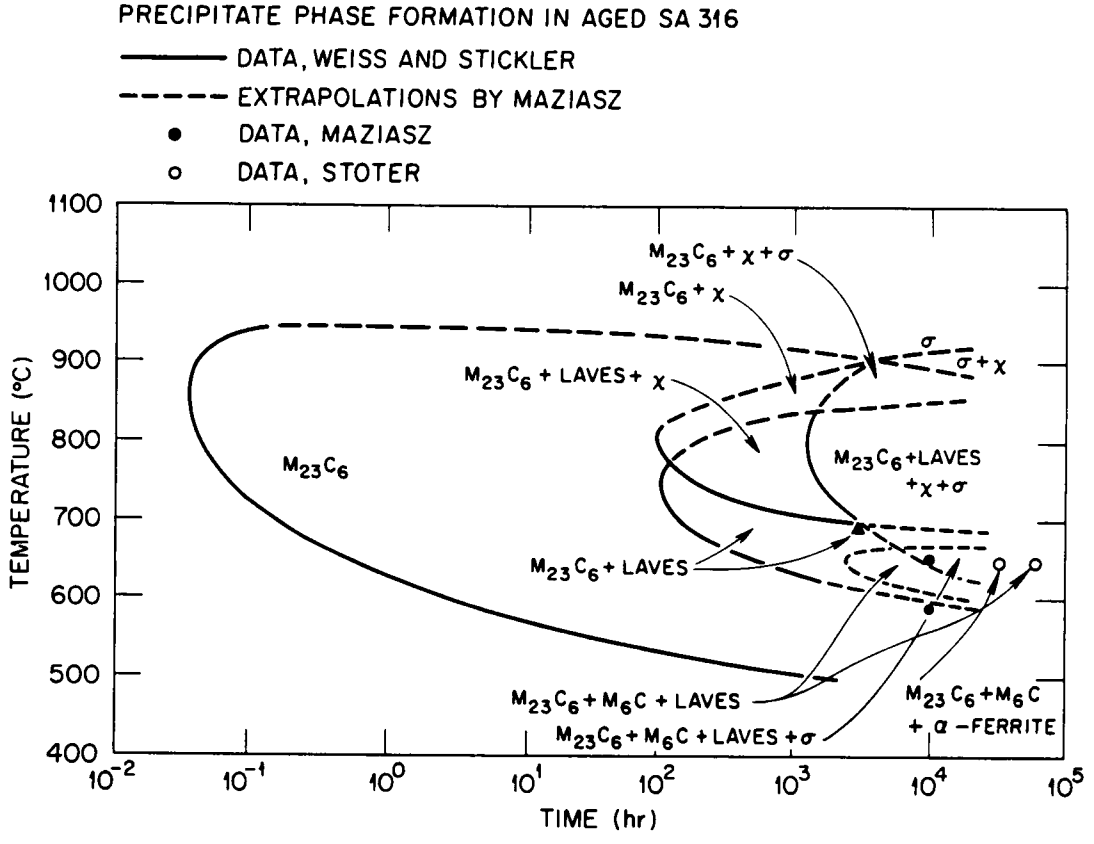

Fig. 16. A plot of precipitate phase formation as functions of time and temperature for precipitation in aged SA 316. The diagram is a composite of various work and data references are found in text.

(heat 332990, Table 2, p. 27) and found good agreement with Weiss and Stickler. Spitznagel and Stickler[386] further examined the precipitate volume fractions and their effect on sample density as functions of aging time and fabrication process (air as opposed to vacuum melt) for SA 316. All of this work, however, was done prior to the application of AEM to aged SA 316. More recently, Maziasz,[379,401] Bolten et al.[380] and Stoter,[363] employing AEM, found the M_6C (η) phase after aging 10,000 h or more at 650°C; η was suspected, but never found, by Weiss and Stickler. Maziasz[401] also found σ phase at 650°C (the lowest reported temperature in SA 316 to date) and Stoter found the transient presence of α-ferrite after 28,000 h at 650°C. First, consider the temperature dependence of the phases after long-term aging. In general, no precipitation is found below 500°C, and $M_{23}C_6$ (τ) can be found from about 500 to nearly 900°C. M_6C (η) appears in the narrow range between 600 to 700°C. Laves occurs from above 600°C to about 850°C and χ from about 700 to near 900°C. Sigma can be found from about 900°C to as low as 650°C. There is definitely an upper temperature cutoff to the stability of these phases because Bolten et al. and Stoter observed that the $M_{23}C_6$ (τ) plus M_6C (η) plus Laves precipitates formed after 60,000 h at 650°C, completely dissolved after reannealing for 1 h at 1050°C. Microstructurally, within a given phase field, the distribution of particles coarsens as temperature increases. σ and χ phases present at the higher temperature are much coarser than the Laves, $M_{23}C_6$ (τ), and M_6C (η) phases which are stable at lower temperatures. There is, however, very little quantitative TEM on sizes or concentrations. The maximum volume

fraction of precipitation (as determined by bulk extractions) occurs at about 800°C, where the kinetics for the various phases appears maximum (Fig. 16). There is little evidence for temperature dependence of the phase compositions, except for Laves. Williams,[402] using AEM, showed Laves to decrease slightly in nickel and chromium concentrations while increasing in molybdenum and iron as aging temperature increased in the 650 to 750°C temperature range.

The time dependence of the precipitation in aged SA 316 reflects the kinetics and interactions of the various individual phases, and particularly the metastability of $M_{23}C_6$ (τ) in this alloy. $M_{23}C_6$ (τ) is the first phase to form in aged type 316 stainless steel, requiring only minutes to precipitate at 800 to 900°C (see Fig. 16). It nucleates first at grain boundaries, then at twin boundaries, and finally along matrix dislocations. Tau's formation kinetics are definitely enhanced by increased matrix carbon content or by increased dislocation densities in cold-worked material.[9,10] In type 304, $M_{23}C_6$ forms and remains stable after several thousand hours aging at 725°C (ref. 386). However, at longer times in SA 316, $M_{23}C_6$ stability is reduced by the formation of the Mo-Cr intermetallic phases. In low carbon heats of type 316 stainless steel, Weiss and Stickler[9] and Spitznagel and Stickler[386] find dissolution of $M_{23}C_6$ (τ) following formation of σ and χ after longer times at ~800°C. For similar aging of high-carbon type 316 stainless steel, $M_{23}C_6$ (τ) remains stable and intermetallic phase formation is retarded; however, Stoter[363] at 650°C finds dissolution of $M_{23}C_6$ (τ) together with increased M_6C (η) precipitation upon formation

of Laves phase between 28,000 and 60,000 h. Many investigators[376,376] find $M_{23}C_6$ (τ) to form and then to subsequently dissolve at the expense of M_6C (η) formation in other steels; they conclude that $M_{23}C_6$ (τ) is not a stable phase. Specific times, temperatures, and volume fractions associated with this effect are sensitive to alloy composition. Many of the stable phases in type 316 stainless steel also appear to nucleate sympathetically on $M_{23}C_6$ (τ) phase particles, making their microstructures and kinetics quite dependent on formation of that phase.

There is little quantitative TEM data on the complex nucleation and growth of the various phases in SA 316. All the phases appear heterogeneously nucleated. Lewis and Hattersley[361] and Beckitt and Clark[341] described the evolution of $M_{23}C_6$ (τ) in various aged austenitic stainless steels. These particles are found after short times at 700 to 750°C along dislocations; they induce new dislocations as they grow which in turn serve to nucleate more particles. Small $M_{23}C_6$ particles later impinge or sinter to form the larger, more complex particles. There are no systematic data on the time evolution of either the matrix or the precipitate phase compositions during thermal aging.

The nonequilibrium phase decomposition, even in a complex alloy like type 316 stainless steel, can be considered in terms of an equilibrium end point and a natural (irreversible) path toward it. Continuum thermodynamics determine the stable phases and their equilibrium amounts, distributions, and morphologies. However, thermodynamic plus kinetic considerations determine the actual microstructural evolution,[403] with the additional complexity of transient metastable phases. Although

nucleation and growth occur, it is unclear whether or not coarsening also occurs in type 316 stainless steel after long-time aging. Unique features of solid-state reactions are the roles that both volume misfit and interfacial structure play in nucleation,[404-406] and the role that the latter plays in growth.[407,408] These generally represent additional barriers that work against the free energy of formation driving the reaction. Extensive review of nucleation and growth theories can be found by Christian, Russell, and Aaronson et al.[403,406-409] While most theory is for homogeneous nucleation, the phases in steel clearly appear to be heterogeneously nucleated, either at dislocations, grain or twin boundaries, or sympathetically at the interfaces of other phases. A stable phase will not be present if it cannot nucleate, and the formation of metastable phases in type 316 stainless steel instead would indicate that they nucleate more easily than the stable phases (several phases may compete to nucleate). A precipitate particle (like the voids discussed earlier) will grow when it becomes larger than some critical sized nucleus; this critical nucleus is usually determined by optimizing size and shape to minimize strain and interfacial energies.[405,406,408] Pre-precipitation phenomena such as segregation or formation of Guinier-Preston (GP) zones can strongly influence heterogeneous nucleation. In general, the microstructural location and crystallographic habit will be determined by the nucleation stage of the precipitation.

Growth of the second-phase particles in SA 316 appears to be thermally activated and will occur monotonically until either the supersaturation driving the reaction diminishes, some barrier is encountered,

or dissolution occurs either due to coarsening (i.e., Oswald ripening) or due to transient metastability. The interfacial structure plays an important role in the kinetics and morphology of particle growth. Most investigators imagine some point early in the nucleation when the interphase boundary is coherent (registry of atoms and planes) with the matrix. However, if crystal structure, misfit strain (and possibly composition and bonding nature) are sufficiently different between the phases, coherency will be lost. The interface will then be semicoherent, with either a dislocation structure or possibly coherency strains (depending upon sharpness or boundary thickness[404]), or will have mixed regions of disorder and coherency,[407,408] or will be incoherent (but not necessarily structureless). Coherent and semicoherent interfaces are sessile and atomic attachment to the interface usually controls the kinetics of growth. Incoherent or disordered interfaces are glissile, however, and growth will be either bulk diffusion controlled or controlled by short circuit diffusion paths (along dislocations or twin or grain boundaries). These considerations at the various growing interfaces will determine the basic particle morphologies described by Aaronson et al.,[408] which are plate, needle, lath, or equiaxed shapes. The phases in type 316 stainless steel do fall into these categories; however, the same phase can have a variety of morphologies, usually depending on specific crystallographic habit.[401] Interfacial TEM characterizations or plots of atomic matching indicate semi-coherency for $M_{23}C_6$ (τ) in aged austenitic steel.[341,361,409] The situation is unknown for the other phases and at least several may be incoherent.

Thermodynamics play the dominant role in determining which stable or metastable phases form and, through chemical reactions and elemental solubilities of each phase, in determining microcompositional repartitioning. Even in nonequilibrium decomposition, the phases formed must at least lower the free energy of the mixed, but highly supersaturated solid solution. The free energy of mixing (ΔG^m_γ, γ denoting the austenite phase) is related to the activities of the various solutes by the equation

$$\Delta G^m_\gamma = RT \sum_{i=A}^{N} \ln a_{i,\gamma} \quad , \tag{10}$$

where R is the gas constant and $a_{i,\gamma}$ is the activity of the i-th component in an N component solution.[410] For nonideal solutions, a large, negative (exothermic) enthalpy of mixing for a given solute favors unmixing into a solute rich compound and solute-poor solution. However, the unmixing may involve the reaction of several solutes rather than the solvent, as in the case of $Cr_{23}C_6$ (τ), which can be expressed as the reaction

$$23 \text{ Cr (dissolved in } \gamma) + 6 \text{ C (dissolved in } \gamma) \rightarrow Cr_{23}C_6 \quad , \tag{11}$$

where, if equilibrium is reached, then,

$$\Delta G^0 (Cr_{23}C_6) = - RT \ln \left[\frac{1}{(a_{Cr,\gamma})^{23} (a_{C,\gamma})^6} \right] , \tag{12}$$

where ΔG^0 ($Cr_{23}C_6$) is the free energy of formation of that phase in the standard state (metallic chromium reacting with graphite). The $Cr_{23}C_6$ phase is assumed insoluble ($a_{\tau,\gamma} = 1$), but supersaturated solutes can have $a_{i,\gamma} > 1$. Equation (12) describes the equilibrium activities

that the system is progressing toward as it lowers the austenite concentrations of solutes in order to form the stable amount of that phase. However, if the activities further decrease, say by formation of a second or third phase in multiphase sequence, the new phase can become unstable and dissolve. Solutes other than the major reactants can be involved in several ways that also cause repartitioning between the austenite and new phase accordingly. Firstly, other solutes may also participate in the precipitation reaction as substitutes for the major reactants or as surface catalysts. Chang and Najock,[411] for example, describe the solubility of Mo_2C in $Cr_{23}C_6$ for the complex $M_{23}C_6$ carbide and the substitution of molybdenum for chromium in that phase accordingly. Figure 17(b) depicts precipitate enrichment schematically, with

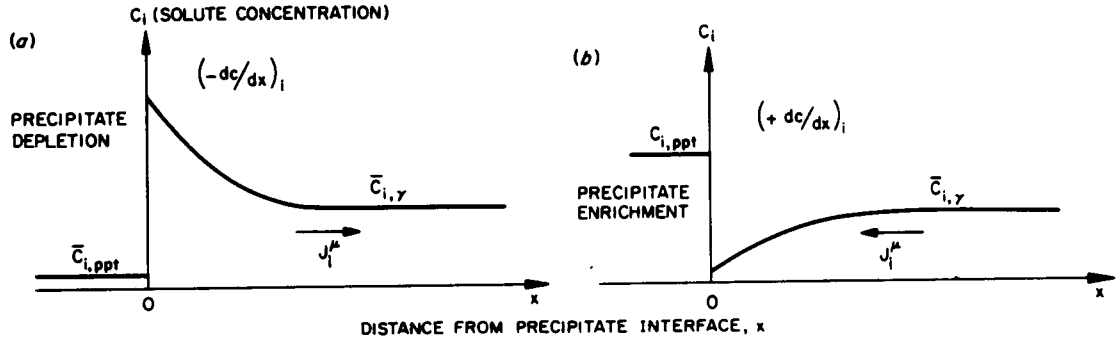

Fig. 17. A schematic of solute depletion (a) and enrichment (b) in precipitate phase particles during thermal aging and the associated concentration profiles (dc/dx) and solute flow directions (j_i^{μ}) needed to accomplish this during particle growth. Solute enrichment will occur for reactants in the phase formation or because elements are catalysts or are more soluble in the new phase than in the surrounding matrix. Depletion usually occurs due to low solubility in the new phase.

matrix solute depletion and flow toward the interface. Secondly, because a new phase exists, equilibrium demands that chemical potentials of other elements be equal in the two phases (i.e., $\mu_{Si,\tau} = \mu_{Si,\gamma}$). However, when there are differences in solution character (ideal, nonideal) or in solubility limits between the two phases, the elemental concentrations will be unequal at the interphase boundary (see Fig. 17). Generally, elemental insolubility in the new phase will cause solute depletion in the phase and hence buildup ahead of and diffusion away from the advancing interface [Fig. 17(a)]. Such behavior is inferred for silicon at carbides in steel by Yoshida.[342] Solute partitioning across the interface can slow down diffusion-controlled growth, if it must be accomplished before the interface progresses. Such segregation may also strongly influence sympathetic nucleation of other phases at these boundaries [i.e., Laves and M_6C (η) at $M_{23}C_6$ (τ) boundaries[165,363,390]]. As we shall see under Irradiation, forced incorporation of insoluble elements can also destabilize a phase by reducing the free energy of formation in Eq. (12).

C. Precipitation Under Irradiation

Arkell and Pfeil[412] in 1964 first observed precipitation via TEM in neutron-irradiated steel. They interpreted their findings as an enhanced thermal effect, consistent with the prevailing theoretical understanding and expectations at that time, as reviewed by Brinkman and Wiedersich[413] in 1964–65. Enhanced diffusion was expected to accelerate thermal processes like precipitation. Despite Anthony's work[321] on RIS in 1971, this view prevailed until about 1972–74. Many studies neglected

precipitation. For example, Cawthorne and Fulton[20] in reporting their discovery of large Frank loops and radiation-induced voids, failed to mention precipitation, despite copious TEM evidence for it in their micrographs. In 1972–74, however, irradiation-induced phases (RIP) were found by Okamoto et al.[325] in 1 MeV electron-irradiated 18 Cr–8 Ni–1 Si stainless steel, by Brager and Straalsund,[38] and Brown[414] in FBR-irradiated SA 316, and by Williams et al.[415] and Sikka and Moteff[416] in tungsten-rhenium alloys irradiated in EBR-II. Only Williams et al. and Sikka and Moteff identified their RIP; in W–25 Re they found χ phase under irradiation instead of the normal σ phase expected during aging. These workers and Brager and Straalsund found these phases to dissolve upon postirradiation annealing, a critical test for an RIP. By contrast, postirradiation annealing increased the amount of precipitation found by Arkell and Pfeil, substantiating their claim of an irradiation-enhanced phenomena. Okamoto and coworkers first suspected a link between RIP and RIS.[324,325]

The identification of RIPs continued for FBR-irradiated stainless steels. In 1977–78, Cawthorne and Brown[417] and Brager and Garner[297] discovered γ' (Ni_3Si type) in type 316 stainless steel and Thomas[418] found G phase in 1978 in the titanium-modified LS1 austenitic stainless steel. Brager and Garner, and Thomas first presented XEDS composition information, showing that the γ' and G phases were highly enriched in nickel and silicon, making quite obvious the connection with RIS. Moreover, Brager and Garner found no γ' for control specimens aged for 15,000 h at the irradiation temperature[297] and further found γ' to disappear upon

postirradiation annealing also at the irradiation temperature for several thousand hours.[298] It indeed did appear that after high fluence irradiation, nearly all the phases and matrix regions around voids were enriched with silicon and nickel (and possibly carbon), sufficient in some cases to cause the remaining austenite to transform to α-ferrite during irradiation [304,419-421] (see Fig. 15, p. 84) (or possibly to martensite upon cooling from the irradiation temperature[422]). Brager and Garner in 1978 also found the nickel- and silicon-rich "$M_{23}(C,Si)_6$," to be a major phase under irradiation.

For years, many studies[4,38-40,49,113,114,222] had previously identified the blocky, cubic epitaxial carbide formed in type 316 stainless steel after FBR irradiation as $M_{23}C_6$ and simply assumed it to be similar to the thermal phase. Clearly it was not an RIP. Moreover, because this phase was nickel- and silicon-poor during aging (see Table 5, p. 88), Brager and Garner's findings meant that either (a) the phase was a compositional variant formed rich in these elements under irradiation, or (b) the phase formed initially poor in these elements and then became progressively richer by absorbing them at higher fluence. Brager and Garner chose the latter interpretation, terming it an "infiltration-exchange" process.[246,298-300] The same explanation was applied to Laves phase in CW 316, found to be nickel-rich and molybdenum-poor after EBR-II irradiation compared to the thermal phase.[298] These observations and concepts were foundational to the "microchemical-evolution" model used by Brager and Garner to explain void swelling (as discussed previously in the subsection on that topic).

However, perceptions about the nature of precipitation under neutron irradiation began changing in 1979 when Maziasz and Williams and Titchmarsh found the M_6C (η) phase in neutron-irradiated type 316 and FV548 steels,[380,401,424,425] concurrent with its identification in aged type 316 (refs. 380,381,401). These observations were important because the phase was found to be similarly nickel- and silicon-rich under aging and under irradiation.[380] Subtle diffraction differences separate identification of M_6C (η) from $M_{23}C_6$ (τ) (refs. 41,380,381,424,425), but careful compositional study of the $M_{23}C_6$ (τ) phase showed it to be similarly nickel- and silicon-poor under HFIR or EBR-II irradiation and under aging.[41,165,380,389,424] These findings challenged prior identifications of "$M_{23}C(C,Si)_6$" and strongly suggested that instead, the dominant carbide under neutron irradiation was M_6C (η), as emphasized by several reviews.[41,373,402] Brager and Garner indeed hinted at the possibility of the diamond cubic M_6C phase,[298] and later with Yang identified it,[426] but they continued to also identify the nickel- and silicon-rich $M_{23}C_6$ (τ) phase under irradiation.[36,37,426,427] Recent accurate work of Williams,[402] identifying nickel- and silicon-rich M_6C (η) and nickel- and silicon-poor $M_{23}C_6$ (τ) in SA 316 irradiated from ~400 to 600°C to ~50 dpa (IAEA dpa) further refutes the "$M_{23}(C,Si)_6$" identification and the "infiltration-exchange;" however, recent work by LeNaour et al.[116] supports these. Laves phase can be compositionally altered by irradiation, but the MC phase is always compositionally identical for irradiation compared to aging.[41,165,373,389,402]

Several new ideas stemmed from the data which constrasted with that of Brager and Garner. It seemed possible that the phases occurring in aged steels had distinct and different elemental compositions and solubility limits which were preserved under irradiation; they then formed under irradiation based on their compatibility with RIS (and/or point defect-misfit interactions[41,165,366,373,389,390,402]). This led Lee et al.[41] to classify the various phases as follows: (a) Thermal phases whose formation is enhanced [M_6C (η), Laves] or retarded [MC, $M_{23}C_6$ (τ), and possibly σ, χ] under irradiation, but whose compositions are essentially unaltered, (b) irradiation modified phases which form under aging and are stable under irradiation but are compositionally altered by the effects of RIS [Laves, M_6C (η) at low temperatures[402] and possibly the Fe_2P phase], and (c) phases induced to form in a particular steel by irradiation, mainly by RIS effects, which do not form during aging (G, γ', and often Fe_2P phases). Several visualize RIS as the key to precipitation under irradiation, changing the matrix composition around sinks to create "microalloy" regions.[165,251,373,402] (see Fig. 15, p. 84). Phases then form in these "microalloys" as if they were bulk alloys being aged at the irradiation temperature. In fact, Williams and co-workers[366,370] proved this by making alloy modifications to simulate in bulk the RIS effects occurring at sinks; they then found the same M_6C (η) and G phases found only under irradiation in the original alloy. Yang et al.[426] offer an additional phase classification of (d) phases transformed either crystallograpically [$M_{23}C_6$ (τ)] or compositionally [Laves, $M_{23}C_6$ (τ)] through the "infiltration-exchange"

mechanism. Lee et al.,[41] Maziasz,[165] and Williams and coworkers,[373,402] however, argue against this last classification on the basis of detailed experimental evidence. The current controversy remains unresolved and requires more careful data, particularly from comparison of the same heat of type 316 stainless steel, both irradiated and thermally aged. The remainder of this section will summarize the available temperature, fluence, and helium-dependent data for neutron-irradiated SA 316 and will summarize the current theoretical understanding of precipitation under irradiation.

The authors, who investigated cavity and dislocation microstructures in FBR-irradiated SA 316 prior to 1978, included far less information on precipitation (the same authors cited in the Dislocation and Cavity Microstructural sections[38-40,113,116,222,223]). Their qualitative phase or general precipitation observations, together with the recent observations of Williams (also on heat VR 906A[402]), are included as functions of temperature and fluence in Fig. 18. Symbols used are consistent with those used previously in Figs. 5 (p. 26) and 9 (p. 51) and steel compositions are found in Table 2 (p. 27). Precipitation is generally classified as carbides [these could include either $M_{23}C_6$ (τ), M_6C (η) or G phase], rod or acicular phase particles (this peculiar phase is tentatively identified as the Fe_2P type,[41] with rod axis parallel to $\langle 001 \rangle_\gamma$) or Laves phase. Their observations are taken at face value with no attempt to re-interpret. In addition to the confusion about the nature of the carbide phases, no authors had identified Laves phase in SA 316 under FBR irradiation[401] prior to 1978. However,

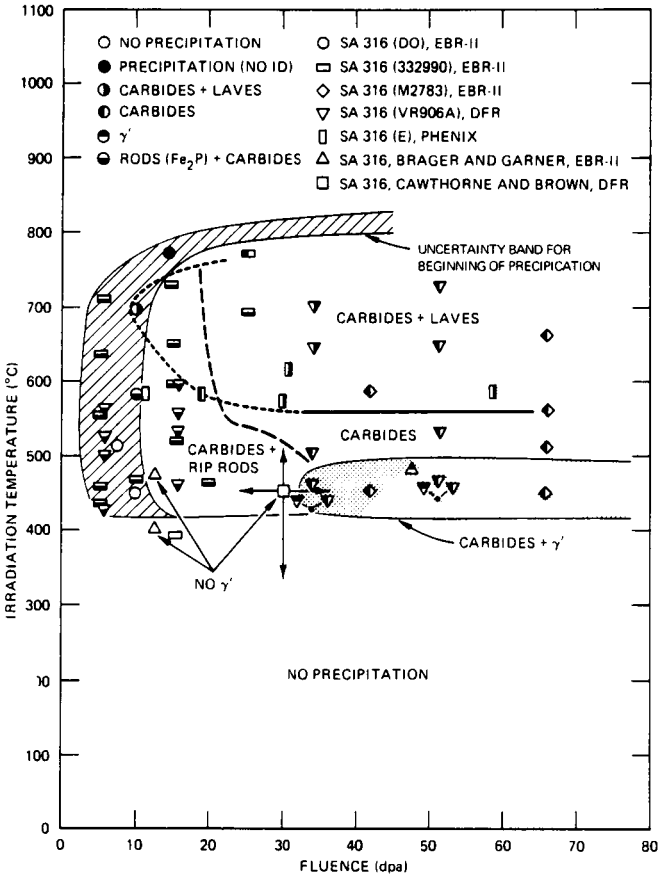

Fig. 18. A plot of various precipitation phenomena as functions of temperature and fluence for FBR-irradiated SA 316. General phase stability regions and transition regions are indicated. Data references are found in Table 2 (p. 27) and in text.

Maziasz,[401] LeNaour et al.,[116] and Williams[402] confidently identified Laves at temperatures of about 600°C and above. Therefore, some fraction of the previous observations on coarse rod, acicular, or wing-shaped particles probably includes Laves phase. The most confident phase identification to date is that of γ', from re-examination of many samples following its discovery by Cawthorne and Brown[417] and Brager and Garner,[297] and from more recent information by Lee et al.[223] and by Williams.[402]

Precipitation in FBR-irradiated SA 316 seemed absent below about 400 to 425°C (see Fig. 18), but a variety of phases were found at higher temperatures. At fluences of about 10 dpa or less, precipitation from ~425 to 700°C tended to be a mixture of carbide types [$M_{23}C_6$ (τ), M_6C (η), and/or G phase] and acicular needles, based mainly upon the data by Brager and Straalsund[38] and Barton et al.[39] Apparently Bloom and Stiegler[40] observed no precipitation below ~550°C and LeNaour et al.[116] observed none at ~580°C. Maziasz identified $M_{23}C_6$ (τ) and Laves at 700°C after 13 dpa, but observed no acicular needles.[401] At intermediate fluences, Laves and carbides were observed above ~550°C, and the large acicular rods observed by Brager and Straalsund and Barton et al. may also be Laves phase. At fluences higher than ~30 dpa, γ' and a small fraction of carbides were observed from about 425 to 500°C, with at least carbides from ~500 to 550°C and carbides plus Laves above ~550°C. Despite careful work on the other phases, Williams[402] at higher fluences does not identify or confirm the absence of the acicular needles; these were definitely seen in the same heat of SA 316 irradiated to lower fluences in DFR by Barton et al. This point is important because the acicular needles may well be a transient phase that persists longer as the irradiation temperature is lowered. The observations of Kenfield et al.[222] indicate at least carbide precipitation from 450 to 650°C at 66 dpa. Precipitation appears enhanced by about 100°C for SA 316 under irradiation compared to aging, but little else can confidently be said about shifts of individual phase regions.

Once the phases formed, they appeared to remain stable with increased fluence under irradiation, except possibly for the acicular needles. At temperatures below about 550°C, carbide and acicular needle-type phases formed after a few dpa; at temperatures below 475 to 500°C, γ' followed after about 30 dpa. Above 550°C, carbides and acicular needles again formed rapidly; Laves then followed after 20 to 30 dpa at 600°C and after ~10 to 12 dpa at 700°C. The acicular needles again may only be an early, transient phase. The kinetics of the carbides in SA 316 seem sluggish for temperatures above 525 to 550°C, because they need anywhere from 1000 to 3000 h (using an exposure time conversion of ~300 h/dpa) to form under irradiation, as compared to minutes to several hours during aging [cf. Figs. 16 (p. 94) and 18]. The kinetics of Laves phase also seems slightly retarded by irradiation. Precipitation appears particularly sluggish in the heats of steels examined by Bloom and Stiegler[40] and LeNaour et al.[116] below 600°C.

Only Brager and Straalsund[38] and Bloom and Stiegler[40] included quantitative microscopy on precipitation. Brager and Straalsund reported carbide particle concentrations of about 10^{22} particles/m^3 from 400 to 700°C. They qualitatively noted that precipitate size increased with increasing irradiation temperature and found the maximum precipitate volume at 600 to 700°C. Bloom and Stiegler found carbide concentrations about four orders-of-magnitude lower than Brager and Straalsund from 580 to 700°C. Bloom and Stiegler noted that acicular needles were much more finely distributed than the carbides at ~580°C (about a factor of 30);

however, Laves particles (as identified in the same sample by Maziasz[401]) were found much coarser than carbides at ~700°C (a factor of 10).

Except for the "infiltration-exchange" type compositional change of $M_{23}C_6$ (τ), there is no systematic fluence dependent compositional information on any of the phases found in FBR-irradiated SA 316. Only Williams[402] reported temperature dependencies for the compositions of M_6C (η) and Laves phase. Compositionally, both phases reflect the temperature dependence of RIS. Both phases exhibited significant nickel decreases and molybdenum increases with increased irradiation temperature. Silicon contents were fairly constant functions of temperature for both phases and iron content was also quite constant for M_6C (η). Iron content increased with increased temperature only for Laves, while the chromium concentration decreased for both phases.

An effect of helium on precipitation in type 316 stainless steel under neutron irradiation was first suggested by Maziasz in 1978–79, based upon comparison of observed HFIR data with a composite of published EBR-II data.[401] Kenik[135] and Choyke et al.[133] presented even clearer evidence for precipitation sensitivity to helium in austenitic stainless steels under ion irradiation, with the effect varying with changes in mode and amounts of injected helium. Such an effect of helium on solid state chemical reactions was initially puzzling, because helium is a chemically inert gas. However, Odette[251] suggested in 1979 that such effects could occur if the helium-induced cavity sink strength changed sufficiently to affect RIS. Under ion irradiation, the phase

balance in most cases shifted away from RIP phases (acicular needles and G) toward either thermal phases, like MC and M_6C (η), or toward no precipitation at all, as the amount of helium and/or degree of microstructural refinement increased.[33,131-133,135,136,428,429] Maziasz and coworkers[33,131,165,401,424] found similar results under neutron irradiation, comparing data for CW 316 irradiated in EBR-II and HFIR. In particular, comparing the compositions of Laves phase among aged, EBR-II irradiated and HFIR irradiated samples of the same steel, the nickel content was much lower in HFIR than for Laves in EBR-II and similar to aging.[131,165] These data clearly demonstrate the transition from RIP to radiation-enhanced thermal precipitation as RIS is suppressed by increased helium generation/microstructural refinement. These data, however, are also the subject of controversy, as Brager and Garner, for comparison of the same samples,[36,37] claim that helium does not affect either RIS or precipitation. Finally, Maziasz[165] also observed suppressed RIS/RIP due to helium preinjection (110 at. ppm) which increased bubble concentrations for SA 316 irradiated at 625°C to ~8.4 dpa in EBR-II.

Radiation damage theory focused little attention on phase stability under irradiation prior to 1976—1977 (refs. 430, 431); afterwards, however, efforts increased, culminating in several conferences and books devoted to the subject in 1978—1979 (refs. 432—434). This portion of the literature survey relies heavily on reviews by Hudson,[430] Russell and coworkers,[435-437] Martin and coworkers,[438,439] and Wilkes.[440] In 1972, Nelson et al.[441] combined the effects of cascade dissolution

together with those of enhanced diffusion into a simple theory, representing the state of knowledge for the effects of irradiation on phase stability at that time. However, the discovery of RIPs both in engineering and in simple alloys prompted much more work in 1975–1977 to incorporate the effects of RIS and point defect supersaturations into the theoretical study of phase stability under irradiation.[442-444] Irradiation can lead either to a true equilibrium state, unattainable under aging, or to the establishment of a driven, nonequilibrium steady state. To treat the irreversible thermodynamics of phase stability under irradiation, most researchers use the atomistic approach and describe the kinetics in a dynamic steady state.[435-439] However, several investigators employ a continuum thermodynamics approach instead to describe a static steady state of minimized potential functions.[440,445,446] Predictions match better with experimental observations through the kinetic approach. Most theoretical work on phase stability under irradiation deals with the ordered γ' phases in binary nickel base alloys and with ion or HVEM irradiation. Nevertheless, the general principles and various mechanisms affecting precipitation under irradiation can apply to the phases found in SA 316. With an emphasis toward recognizing the mechanisms on the basis of AEM data, we will consider their effects on A-type observables, relating to phase identity and nature (i.e., crystal structure and composition), or B-type observables relating to microstructural characteristics of a given phase (i.e., particle size, concentration, shape, or volume fraction). Most of the theoretical work deals with FBR-type conditions and does not extend to fusion conditions.

Also, despite much conjecture, there has been no quantitative theoretical work on compositional changes of precipitate phases under irradiation.

The mechanisms affecting phase stablility under irradiation may be summarized as follows:

(a) Radiation Enhanced Diffusion — This effect (reviewed in Part A of this subsection) has long been identified as the primary cause of radiation-enhanced thermal precipitation. Enhanced diffusion can also be involved in RIP or radiation-modified precipitation, as well as ordering or reordering and precipitate coarsening under irradiation.[431,440,447] Despite the predominance of radiation-induced phenomena, this mechanism is supported by observations of MC precipitation in steels during lower temperature neutron irradiation,[390,412,448] enhanced precipitation of θ' in HVEM-irradiated Al—4% Cu,[449] and accelerated thermal precipitation in type 316 stainless steels when helium effects suppress RIS under neutron irradiation.[131,165] This mechanism affects both A- and B-type observables.

(b) Displacement Cascade-Induced Dissolution, Disordering, and Mixing — A unique and often destabilizing factor for precipitation in an irradiation environment compared to thermal aging.[413] The effects of cascades on precipitate particle stability are shown schematically in Fig. 19(a). Cascades can destroy crystallinity in the unstructured regions of their cores and cause disorder or mixing and stirring in the larger recombination zones which surround the core.[440,441,450] Cascade effects often depend on precipitate size and irradiation temperature. First, consider lower irradiation temperature. For small, incoherent

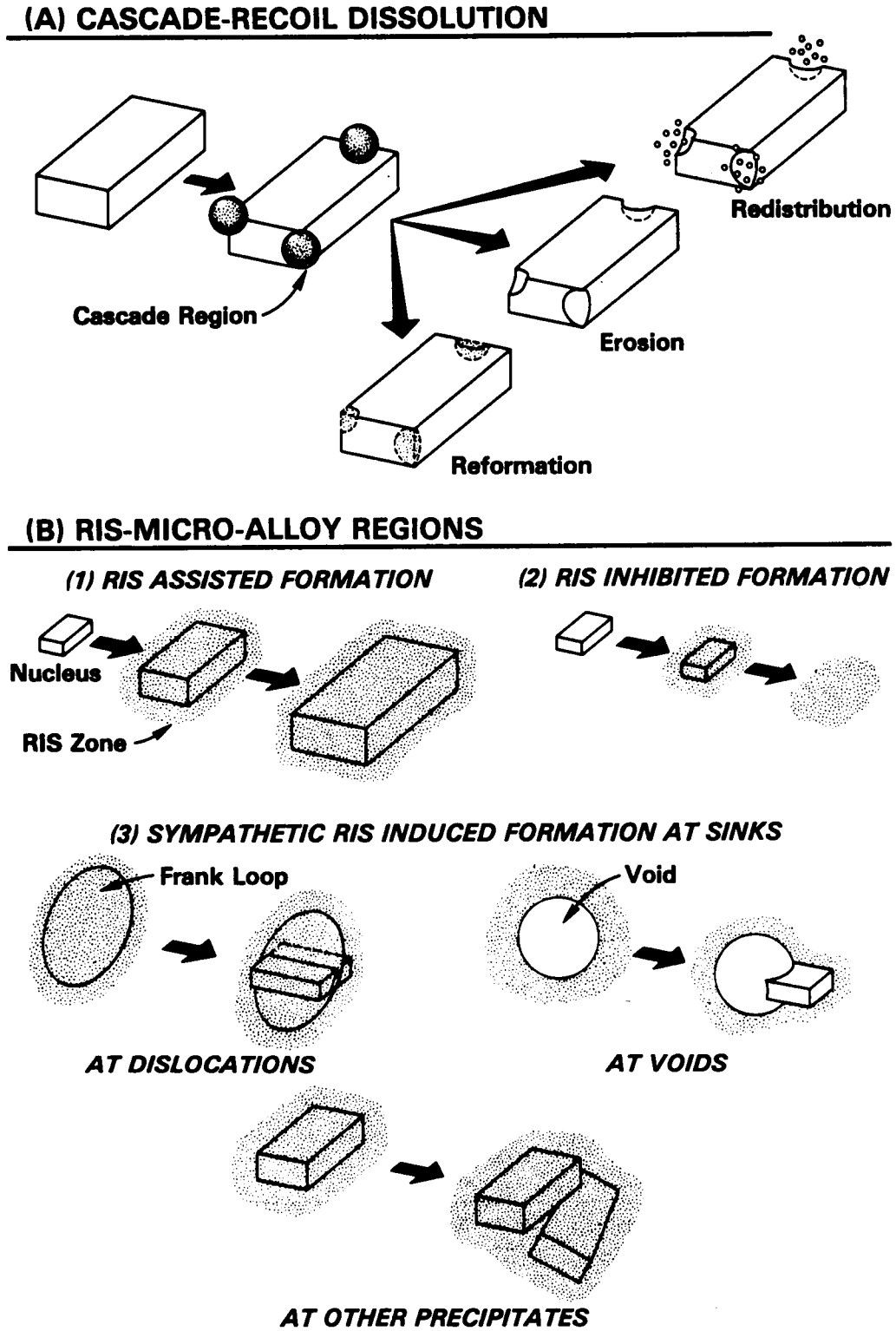

Fig. 19. Schematic conceptual representation of how the mechanisms of (a) cascade recoil dissolution and (b) formation of micro-compositional regions due to RIS affect phase stability under irradiation.

particles, destruction can occur if the particle is encompassed by the cascade.[441] For similar larger particles, dissolution can occur due to both the cascade and its disordering zone. Cascades can progressively spall or erode larger incoherent particles [Fig. 19(a)] and even cause the matrix to disorder or become amorphous.[440,451] Dissolution of incoherent particles usually affects B-type observables. Secondly, consider higher temperatures where diffusion is possible. Small particles can re-form in the solute-rich region following dissolution and larger particles can either heal their cascade damage by re-forming the original particles or by redistributing them as much smaller particles [see Fig. 19(a)]. The latter two effects require that the adjacent matrix remain supersaturated in order to re-precipitate the same phase. Redistribution of larger particles as smaller ones has recently been observed for ThO_2 particles in nickel,[452] MC in stainless steel,[429] and in many cases of γ' in nickel-based alloys.[453,454] This case has also been studied theoretically by Frost and Russell.[450]

Chow and Ghoniem[455] have also extended the precipitate dissolution studies to include the higher energy cascades expected in fusion reactor environments. Cascades can affect both A- and B-type observables at higher temperatures, particularly if cascade mixing or redistribution and re-formation dilute the precipitate composition. Finally, Vaidya[456] observed that ordered particles with coherent or semi-coherent (and hence sessile) interfaces can lose coherency to become disordered and glissile, aiding dissolution.

(c) Radiation-Induced Solute Segregation — This effect of irradiation (whose various mechanisms were also reviewed in Part A of this subsection) is the principal cause of irradiation-modified or irradiation induced precipitation. Quantitative theory has been applied to the RIP of ordered and coherent γ' formation (constant stoichiometry) in undersaturated binary nickel alloys.[346,348,352,353,438,442,444,454] RIS simply occurs at sinks (affecting type-B observables) and triggers precipitation when the local solubility limit is exceeded. Figure 20 represents schematically enrichment/depletion couplings between precipitate solute level, matrix solute gradients, and diffusion directions; the case for RIP in binary alloys would be Fig. 20(b), with solute flow up the concentration gradient to produce enrichment in the precipitate. Martin and coworkers[438,439] also describe homogeneous RIP of γ' type phases resulting from diffusional instabilities in defect supersaturated solutions caused

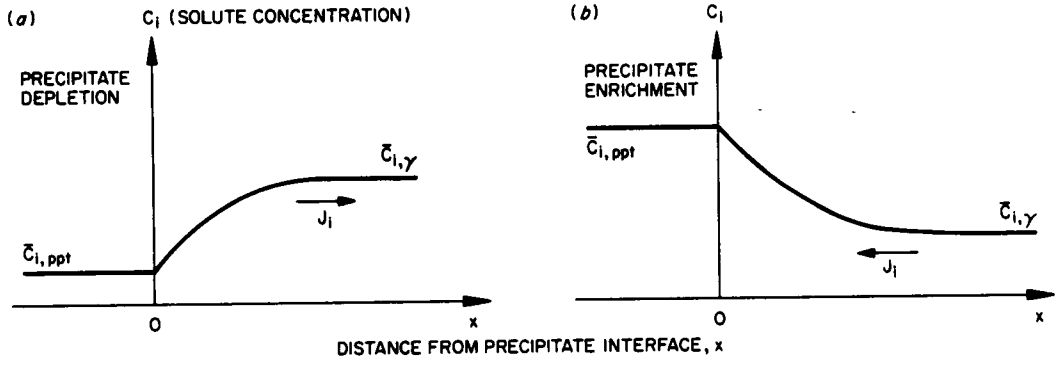

Fig. 20. A schematic of (a) solute depletion and (b) solute enrichment induced in precipitate particles by RIS during irradiation. Also included are the RIS-induced matrix gradients necessary to accomplish this. Solute flows in both cases are up the compositional gradients, just the opposite of the behavior found during thermal aging (see Fig. 17, p. 101).

by recombination due to solute concentration fluctuations. As point defects flow to an area of enhanced recombination, coupled RIS amplifies the solute fluctuations (almost analogous to spinodal decomposition), leading to precipitation. RIS toward and away from sinks is also involved in the redistribution of γ' and its altered coarsening kinetics [altered relative to the classic theory for Lifshitz and Slyozov[457] and Wagner[458] (LSW theory) for diffusion-controlled coarsening] in supersaturated (and sometimes preirradiation aged) nickel-based binary and superalloys.[447,453,454]

For the behavior of the complex, incoherent phases found in irradiated steels, several different conceptual models are derived from the data.[41,165,246,251,343,366,373,402] Brager and Garner suggest that phases form either as nickel- and silicon-rich (i.e., RIPs such as γ' or G phases) or become progressively enriched in these elements (via the "infiltration-exchange" across static interphase boundaries) due to RIS.[246,298,299] Different concepts are advanced, however, from the data of Maziasz, Lee and coworkers,[41,165,380,424,429] and Williams and coworkers;[366,370,373,402] several of these are illustrated schematically in Fig. 19(b). Thermal phase formation may be enhanced or retarded, depending upon whether the solute enrichment/depletion characteristics of the phase couple positively or not with the enrichment/depletion effects of RIS, respectively.[165] Figure 20(a) illustrates the positive interfacial coupling obtained when RIS causes depletion of a solute which the precipitate rejects [contrast the manner in which depletion occurs under aging, Fig. 17(a), p. 101]. If the thermal phase nucleates

and couples positively with RIS [i.e., M_6C (η) phase], the compositional zone developed by RIS due to the precipitate functioning as a sink will aid growth [as shown in Fig. 19(B.1)]. Conversely, if the thermal phase nucleates, but couples negatively with RIS (i.e., $M_{23}C_6$, MC), it can dissolve as forced in-diffusion or cascade mixing of incorporate insoluble elements into the phase [as shown in Fig. 19(B.2)]. For irradiation-modified phases, RIS can oppose gradients being established by the chemical potential of elements in the phase, producing enrichment/depletion gradient couplings intermediate to those illustrated in Figs. 17, p. 101, and 20 [i.e., molybdenum in M_6C (η) and Laves]. Finally, heterogeneous nucleation of parasitic RIPs usually depends on sympathetic sinks (loop, void, or other precipitate particles), which possibly establish the RIS-microalloy beforehand and sustain particle growth [Fig. 19(B.3)].[165] Obviously, RIS can affect both A- and B-type observables.

(d) Point Defect Effects — Excess concentrations of vacancies and interstitials can exist in both the matrix and the precipitate phase under irradiation. These can be regarded as "chemical-components," mixed into either the matrix or precipitate phases, which can alter their free energies under irradiation.[443,459,460] However, such effects on stability are regarded as small.[440] The review of thermal precipitation highlighted the need for phases to either absorb or emit vacancies in proportion to their volumetric misfit (i.e., vacancy absorption for oversized misfit). Russell and coworkers[436,437,443] considered the nucleation stability of incoherent precipitates under irradiation with various misfits (the same nodal line/critical point formulation

used by Russell for void nucleation[284]) in a vacancy supersaturation. They concluded that oversized phases were stabilized while undersized phases were destabilized under irradiation. However, of the three phases in steel with positive misfits of 10% or more (see Table 5, p. 88), only M_6C (η) appears to be stable under a variety of irradiation conditions. Vacancy supersaturation certainly benefits the highly oversized MC phase,[389,461] but both MC and $M_{23}C_6$ (τ) apparently depend much more upon the suppression of RIS for stability.[165,389,390,428,429] By contrast, several of the phases induced or enhanced in steels by irradiation, like Laves, acicular Fe_2P rods and γ' (Ni_3Si) have negative misfits. It seems strange that the stabilizing effect of excess interstitials on these phases would be ignored. Although the supersaturated population of interstitials at any point in space and time is negligible, due to their extreme insolubility and high mobility, the overall <u>accumulation</u> at sinks must balance the vacancy production under irradiation (similar to the situation for loops and voids). In fact, it has been suggested that the precipitates may be biased sinks during growth, either on the basis of their misfits, or because they have a "chemical" component to their bias, due to a strong phase enrichment of elements that migrate interstitially, like nickel and silicon.[389,390] For the most part, point defect effects have been considered only for type A observables, with the possible exception of volume fraction for type B.

The perspective then is that the conceptual and theoretical modeling has advanced much farther for thermal precipitation than for phase instability under irradiation. Very little modeling applies

directly to precipitation in type 316 stainless steel under irradiation. Except for several ideas about RIS dilution or suppression due to increased cavity sink concentrations,[131,165,251] there are no formal theoretical expectations for helium effects on precipitation. It does appear that for the mechanisms considered, RIS dominates the phase behavior in steels under irradiation. In comparison to the dearth of information on cavity and dislocation evolution, the area of phase stability in irradiated steels requires more consistent experimental characterization.

Summary of Literature Survey

Primary Damage

A. Vacancies and Interstitials

Fission and fusion neutron energy spectra overlap; only small fractions of the overall fusion PKAs are produced by neutrons above 10 to 14 MeV. Higher energy cascades tend to split into subcascades which are then similar to fission cascades (~25–35 keV). Therefore, dpa is a good measure of defect production. Above 0.2 to 0.3 T_m, however, primary damage does not directly survive; defect production (dpa) is only one of the factors governing evolution of the secondary damage structure.

B. Gaseous Transmutants: Helium and Hydrogen

Helium appears more important than hydrogen, judged from its effects on cavity nucleation and from its strong interaction with point defects, particularly vacancies. Inert, insoluble helium atoms migrate

easily as interstitial defects, but can also be strongly trapped in vacancies. A balance between these two migration modes determined how helium atoms influence secondary damage evolution. Helium production is very low in EBR-II and very high in HFIR, due to reactions of thermal neutrons with nickel; it is intermediate for fusion, due to reactions of 10 to 14 MeV neutrons with all atoms.

C. Solid Transmutants: Manganese and Vanadium

These are negligible in EBR-II. Production of both transmutants is slight during fusion irradiation. HFIR irradiation depletes manganese, whereas vanadium is first produced and then burned out. Resulting compositional changes for austenitic steels irradiated in HFIR vary within the solubility limits for these elements in the austenite; there is currently no evidence for dramatic effects of these compositional changes on secondary damage evolution.

Secondary Damage

A. Dislocations

Below ~300°C, "black-dot" loops are the result of frozen-in cascade (vacancy) damage; larger Frank loops are agglomerates of mobile interstitials. During FBR irradiation at 400 to 625°C, Frank loops grow and unfault to feed network formation. Dislocation network evolution strongly reflects the temperature and fluence dependence of loop formation. Preinjected helium refines the scale of the loop microstructure; simultaneously co-generated helium apparently has little effect on the dislocation evolution during irradiation. Surprisingly, interstitial loops grow in helium-preinjected SA 316 during thermal aging.

B. Cavities

1. Bubbles — These are cavities with surface tension balanced by internal gas pressure. Helium bubbles form by agglomeration of vacancies and gas atoms with or without irradiation; bubbles can easily exist at dislocations, grain, or interphase boundaries. During thermal aging, small bubbles migrate and coalesce to grow. Under displacive irradiation, they can also accumulate vacancies and grow as voids, if they exceed a critical size. In FBR-irradiated SA 316, bubbles are the usual matrix cavities found at the lowest (300–350°C) and highest (700–750°C) temperature. However, bubbles are often mixed with voids at intermediate temperatures. Increased helium generation increases bubble nucleation. Theoretical work has been done on bubble growth, but the current focuses are on atomistic reactions and clustering kinetics to describe bubble nucleation.

2. Voids — In contrast to bubbles, these cavities are either purely vacancy clusters or considerably underpressurized with gas. They grow or remain stable when the influx of vacancies is greater than the vacancy re-emission rate. Voids are not found at grain boundaries without stress. Voids generally form under displacive irradiation from ~350 to 700°C. The phenomenon progresses from matrix voids to precipitate-associated voids as irradiation temperature increases. Void swelling in SA 316 usually peaks at 575 to 625°C under FBR irradiation. Increased helium generation can increase or decrease void swelling, depending upon the balance between bubble and void nucleation. Theory for void growth is well established and work continues, coupling void

growth to dislocation, precipitation, and RIS evolutions. However, void nucleation theory remains difficult; currently, void nucleation is treated either by considering the conversion of pre-existing distributions of embryonic bubbles to voids as they exceed their critical radii or by evolving clusters through atomistic interaction kinetics.

C. Precipitation and Microcompositional Development

1. Radiation-Enhanced Diffusion and -Induced Solute Segregation — Thermal diffusion occurs above about 400 to 500°C; irradiation can enhance or accelerate thermal diffusion. Elements like S, P, C, Ni, or Si can segregate to grain or interphase boundaries via thermal diffusion to achieve equilibrium. Irradiation, however, can induce different segregation as various elements coupled to point defect fluxes impinge upon sinks. Various RIS mechanisms lead to Si and Ni buildup and Cr and Mo depletion at sinks in SA 316. Current RIS theory can treat general segregation in concentrated ternary alloys, but is not yet coupled to the complex sink evolution found in SA 316 under irradiation.

2. Thermal Precipitation — In general, $M_{23}C_6$ (τ), M_6C (η), Laves, χ, and σ phases precipitate in aged SA 316 at 550 to 900°C to relieve supersaturations of Si, Mo, Cr, and C. $M_{23}C_6$ generally forms first. Other phases form subsequently at longer times at 650°C, and then $M_{23}C_6$ can become unstable. These phases are crystallographically and compositionally distinct. All of the thermal phases are Mo-rich and Fe-poor, but vary in their affinities for Si, Cr, and Ni. They nucleate heterogeneously, coarsening with increased temperature; maximum precipitation occurs at ~800°C. Although thermodynamic and kinetic theories

apply generally to precipitation in SA 316, little specific work for this case has been done.

3. Precipitation under Irradiation — Only recently (1978–79) have irradiation effects on precipitation been realized in SA 316. These effects are: (1) enhanced or retarded formation of thermal phases, (2) modified compositions of thermal phases, and (3) induced precipitation of other than thermal phases. Cascade dissolution, point defect–phase misfit interactions, and RIS are mechanisms that affect precipitate formation under irradiation. However, RIS seems to have the strongest influence. RIS causes new "microalloys" to form around sinks; compatible phases then form in these new, compositionally altered regions. Enrichments of Ni and Si (and Mo, Cr depletions) due to RIS tend to favor M_6C (η) and Laves formation, while retarding formation of $M_{23}C_6$ (τ), σ, and χ phases in type 316 stainless steel. RIS can also induce the Fe_2P, Ni_3Si (γ'), and G phases to form. Precipitation occurs in EBR-II above ~400°C and tends toward radiation-induced and -modified phases from about 400 to 650°C. Precipitation becomes nearly thermal at higher temperatures. Helium, thus far, has been found to almost completely suppress the effects of RIS on precipitation under irradiation. Little of the general theoretical work on phase stability under irradiation to date applies directly to the specific phase evolution found in SA 316.

CHAPTER III

EXPERIMENTAL

Specimen Preparation

Sheet and rod stocks were fabricated from the DO-heat of SA 316, whose composition is given in Table 6. In general, the material was 50% cold worked either into stock of ~4-mm-diam rod or by swaging 0.254-mm-thick sheet (by rolling), from which specimens were machined or punched, respectively. Drawings of the buttonhead HFIR-CTR specimens machined from rod stock, and of the sheet tensile (SS-2) specimens punched from sheet stock are shown in Fig. 21(a,b), respectively. Control specimens for thermal aging were also cut from the rod stock (~50 mm long). Specimen materials were finally solution annealed for 1 h at 1050°C in high purity argon.

Table 6. Composition of DO-Heat Type 316 Stainless Steel

Element	wt %	Element	wt %
Cr	18.0	Ti	0.05
Ni	13.0	P	0.013
Mo	2.58	S	0.016
Mn	1.9	N	0.05
Si	0.8	B	>0.0005
C	0.05	Fe	Bal

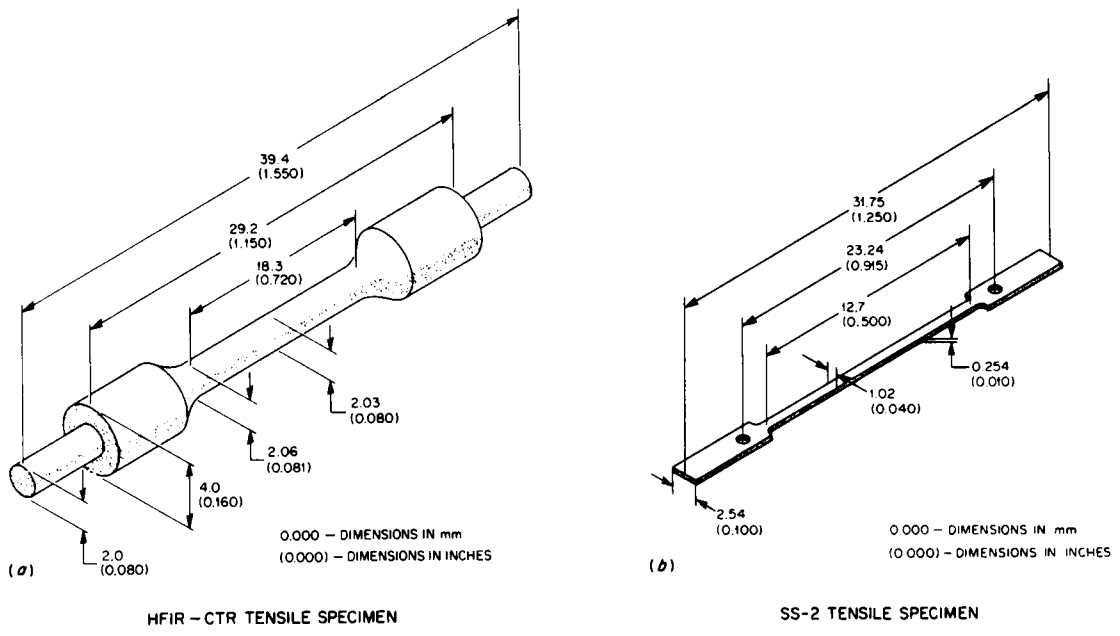

Fig. 21. Drawings and dimensions of tensile specimens which were irradiated and then sectioned to obtain TEM specimens. (a) Buttonhead specimens irradiated in HFIR and (b) sheet specimens irradiated in EBR-II.

Exposure Environments

Helium Preinjection

Several SS-2 tensile specimens of SA 316 were preinjected with ~110 ± 23 at. ppm He* along the gage sections using the Oak Ridge Isochronous Cyclotron (ORIC). The irradiation assembly is shown in Fig. 22. Specimens were irradiated at ~20°C with a 60 MeV (9.6 pJ) alpha particle beam at a current of 5 μA; an energy degrader wheel was used to produce a uniform through-thickness distribution of helium.[462]

*Helium measured using fusion mass spectrometry by H. Farrar at Atomics International, Division of Rockwell International, 1976.

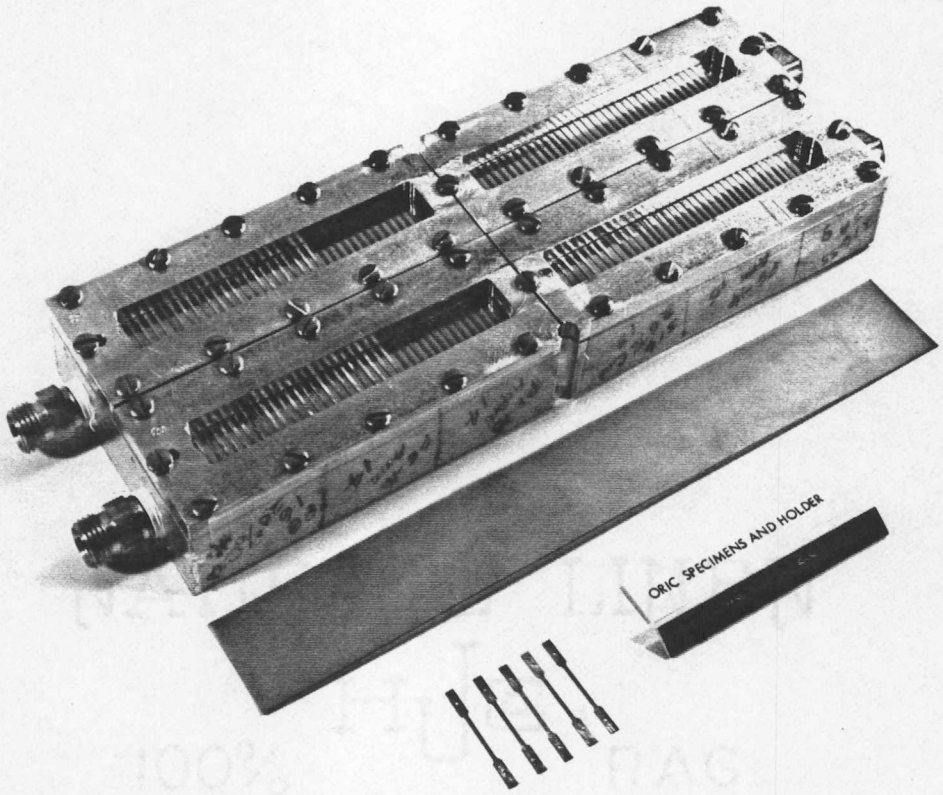

Fig. 22. Specimens and target assembly used for helium preinjection in ORIC. (a) Water-cooled sample holder and target, with SS-2 specimen loaded, (b) initial sheet material, and (c) SS-2 specimen punched from sheet.

Thermal Aging

Pieces of rod stock of SA 316 were aged at 275, 375, 475, 560, 600, 700, 800, and 900°C for 2770 and 4400 h. Similar specimens were also aged at 650°C for 100 h and at 600 and 650°C for 10,000 h. Helium preinjected SS-2 specimens were sectioned into several pieces along the gage; these were also aged, together with similar uninjected pieces, for 1000 h at 400 and 600°C and 10,000 h at 400, 500, 600, and 700°C. The samples were usually wrapped in tantalum foil and sealed in quartz tubes,

which were evacuated and back-filled with high purity argon. These tubes were then aged in air furnaces, controlled to ±10°C or less.

EBR-II Irradiations

Low fluence TEM wafers of SA 316 were cut from the gage sections of untested SS-2 tensile specimens [as shown in Figs. 21(b) and 22], irradiated in experiment X-264 in 1976–77. The experimental subassembly was irradiated in row 7 to a fast fluence of 1.6×10^{26} n/m^2 (E > 0.1 MeV), which produced about 8.4 dpa (at ~$0.4–0.6 \times 10^{-6}$ dpa/s) and 5 at. ppm He, at temperatures of 500 and 625°C. The 500°C temperature was achieved by thermally isolating a sodium-filled subcapsule (via a helium gas gap) from reactor coolant sodium to allow gamma heating. The 625°C temperature was obtained by locating a sodium-filled subcapsule next to a heat pipe of about the same temperature. Helium preinjected and uninjected specimens were adjacent to each other in each subcapsule.

Higher fluence TEM wafers (~0.25–0.50-mm thick) were obtained from SA 316 material irradiated in experiment X-100, irradiated in row 2 of EBR-II (about 1970–73).[463] A typical holder with buttonhead tensile specimens is shown in Fig. 23. Several wafers were cut from a holder irradiated at ~525°C to 5.6×10^{26} n/m^2 (E > 0.1 MeV) to produce ~31 dpa and ~19 at. ppm He. Other wafers were sectioned from the shoulder of an untested tensile specimen irradiated at ~630°C to 6.6×10^{26} n/m^2 (E > 0.1 MeV), producing ~36 dpa and 22 dpa. Damage rates ranged from 1 to 1.25×10^{-6} dpa/s. Irradiation temperatures reported are averages between initial design and final temperatures; irradiation temperatures

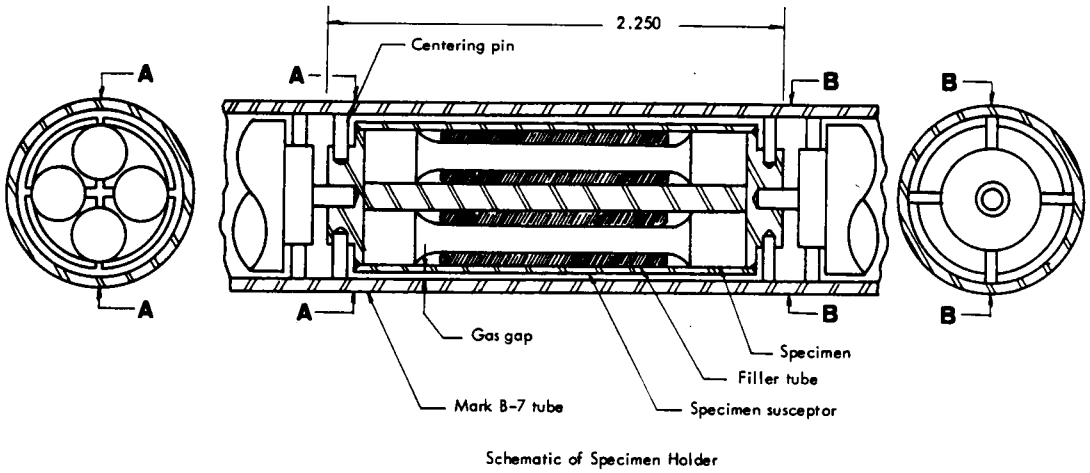

Fig. 23. A schematic drawing of a specimen holder and buttonhead tensile specimens used in EBR-II X-100 materials irradiation experiment.

progressively increased as differential swelling increased the gas gap during the irradiation history[40] (e.g., 500°C start/550°C finish for an average of about 525°C).

HFIR Irradiation

Lower fluence TEM wafers were obtained from buttonhead tensile specimens irradiated in HFIR-CTR-16 at reactor ambient coolant temperature (55°C),[464] and from HFIR-CTRs-9 through 13, irradiated at 325 to 640°C (1977). Neutron fluences produced 5.3 to 17.8 dpa and 180 to 1020 at. ppm He. Some TEM wafers were cut from the shoulders of tensile tested buttonhead specimens (generally tested 75—100°C below their irradiation temperatures) of the type shown in Fig. 21(a); other wafers were cut from shoulders or gages of untested specimens. The exact exposure parameters and specimen conditions are detailed for each sample in Table 7. Experimental assemblies were irradiated in the radially

Table 7. Exposure Parameters for SA 316 (DO-Heat) Specimens Irradiated in HFIR

Specimen Identification	Irradiation Temperature, °C		Neutron Fluence (E>0.1 MeV) (10^{26} nm^2)	Helium Content[c] (at. ppm)	Displacement Damage[d] (dpa)	Exposure Time (h)	Experiment	TEM Wafer Location	Specimen Condition
	Original Calculated[a]	Revised[b]							
A-13	55	55	0.9	270	7.8	2,752	CTR-16	Shoulder	Tensile tested[e]
A-12	285	325–350	0.64	180	5.3	2,770	CTR-13	Shoulder	Untested
A-11	375	425–450	1.1	380	9.2	2,770	CTR-13	Shoulder and gage	Untested
A-7	375	425–450	1.7	740	14.3	4,400	CTR-9	Shoulder	Tensile tested[f]
A-9	465	515–540	1.4	600	12	4,400	CTR-9	Shoulder	Tensile tested[f]
A-3	475	525–550	2.18	1020	17.8	4,400	CTR-9	Shoulder	Tensile tested[f]
A-10	565	615–640	1.3	440	10	2,770	CTR-13	Shoulder	Tensile tested[f]
A-6	565	615–640	2	880	16.6	4,400	CTR-9	Shoulder	Tensile tested[f]
DO-19	480	530–555	6.1	3000	47	12,800	SS-5	Gage	Untested[g]
DO-15	530	580–605	8.3	4000	64	16,200	SS-2	Gage	Tensile tested[f]
DO-2	550	600–625	6.2	3000	47	16,200	SS-2	Gage	Untested
DO-10	575	625–650	4.2	2000	33.5	7,800	SS-4	Gage	Untested
DO-17	680	730–755	6.9	3300	53	12,800	SS-5	Gage	Tensile tested[h]
DO-7	680	730–755	8.4	4140	68.5	16,200	SS-2	Gage	Tensile tested[f]

[a]Based on two-dimensional heat transfer calculations.

[b]Revised upwards by +50 to 75°C based on microstructural comparison with samples whose temperatures had been measured via melt capsules (see P. J. Maziasz, pp. 54–97 in ADIP Semiann Prog. Rept. Sept. 30, 1981, DOE/ER-0045/7. and M. L. Grossbeck and K. C. Liu, Nucl. Technol. **58**, 538–47 (1982).

[c]Calculated from empirical equation based on fusion mass spectrometry measurement of selected samples (see Wiffen et al., "The Production Rate of Helium During Irradiation of Nickel in Thermal Spectrum Fission Reactors," to be published in Journal of Nuclear Materials.

[d]Calculated from total flux (see Gabriel, B. L. Bishop, and F. W. Wiffen, "Calculated Irradiation Response of Materials Using Fission Reactors (HFIR, ORR, and EBR-II) Neutron Spectra," ORNL-TM-6367 (August 1977). It also includes displacements due to recoils from helium production (see L. R. Greenwood, pp. 66–86 in ADIP Semiann Prog. Rept. Mar. 31, 1982, DOE/ER-0045/8).

[e]Tested at 35°C.

[f]Tested at 75 to 100°C below revised irradiation temperature.

[g]Specimen was bent, apparently due to excessive swelling of the gage section.

[h]Tensile tested at 575°C.

symmetric peripheral target positions (PTPs) located at the outside of the HFIR flux trap, adjacent to the fuel. Damage rates varied from 0.5 to 1.1 × 10^{-6} dpa/s with position above and below reactor midplane. Previously calculated irradiation temperatures were corrected upwards by +50 to 75°C, based upon more recent information that γ heating rates were higher than assumed.[465,466] Figure 23(b) shows that temperature was approximately constant in gage and shoulder, and that assumption was checked and verified microstructurally for specimen A-11 (Table 7). Previous work on similar specimens has shown that postirradiation tensile testing does not perturb the as-irradiated microstructure in the shoulder section of these tensile specimens.[465]

Higher fluence TEM samples were obtained from buttonhead tensile specimens irradiated in experiments HFIR-SS-3 through -7 (1969–71) at 530 to 755°C and neutron fluences producing 33.5 to 68.5 dpa and 2000 to 4140 at. ppm He. Irradiation conditions were very similar to HFIR-CTR-9 through -13, except that temperatures remained uniform only near the central region of the gage [see Fig. 24(a)]. TEM wafers therefore had to be cut from gage sections; some of these specimens had been tensile tested, others had not, as indicated in Table 7. Specimen DO-19 was apparently bent during irradiation due to swelling, and possibly creep, in the gage (also noted in Table 7).

Specimen Examination

Immersion Density

Immersion density changes were measured for the high fluence EBR-II samples and for the tensile specimens irradiated in HFIR. Specimens

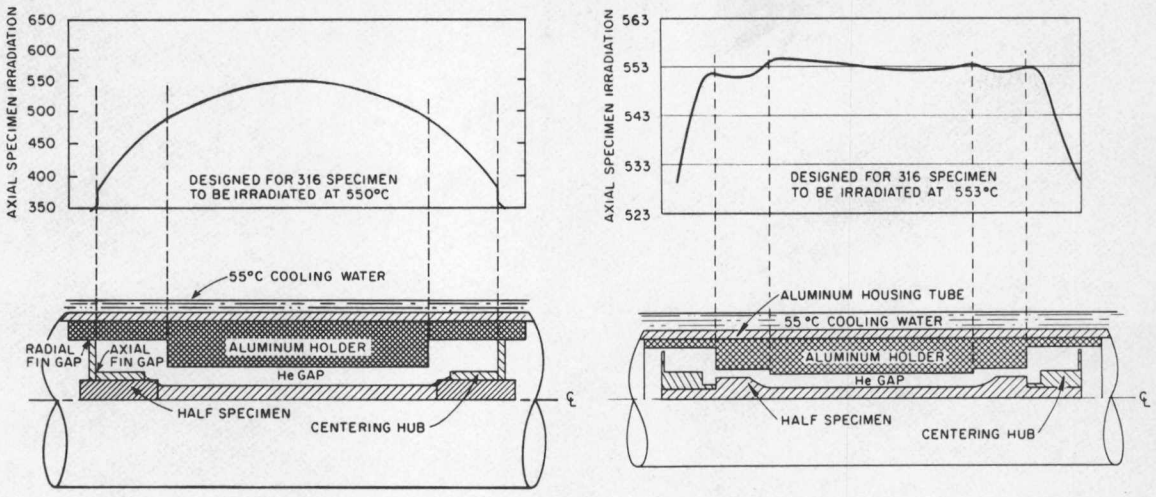

Fig. 24. Calculated axial temperature distribution for (a) specimens irradiated in earlier HFIR experiments (SS-2 through -8) and (b) specimens irradiated in later HFIR experiments (CTR-9 through -13). The later specimens were redesigned to allow a nearly constant temperature profile from gage to shoulder.

from HFIR-SS-3 through -7 were electropolished prior to measurement, and then measured in water wetted with photoflow.[164] However, the temperature distributions in and mass fraction represented by the shoulders [see Fig. 24(a)] make these measurements suspect with regard to representing swelling of the control gage region. Densities of specimens from HFIR-CTR-9 through -13 were measured in water or ethyl phthalate, with liquid density calibrated against a quartz standard.[467] The latter are considered more reliable because temperatures were uniform through the shoulder and gage [Fig. 24(b)].

Conventional Transmission Electron Microscopy (CTEM)

Wafers cut from thermally aged materials, about 0.25 to 0.5-mm thick, were thinned to electron transparency via either a two-stage

dimpling and electropolishing technique,[468] or (more recently) an automatic Tenupol electropolishing technique. The earlier two-stage technique employed solutions of perchloric acid in ethanol. More recent two-stage and automatic Tenupol electropolishing utilized sulfuric acid in methanol (12.5 vol % acid) at temperatures of 0 to 10°C or below.

Reactor-irradiated specimens were thinned using similar polishing techniques; however, the polishing units were shielded or set up remotely to afford protection from high energy gamma emission of the radioactive specimens. Specimens irradiated in EBR-II had low activities of 10 to 100 mR/h or less, whereas HFIR-irradiated wafers of type 316 stainless steel had activities of ~10 R/h or more at contact, and were extremely difficult to handle.

Specimens were examined in CTEM using JEM 100C and 100CX (120 keV), Philips EM400 (100–120 keV), and Hitachi 1 MeV electron microscopes. Magnifications were calibrated nearly every session with a standard grid. Thicknesses were measured via either stereomicroscopy, generally using g_{111} or g_{200}, $S > 0$ dislocation contrast or $S \gg 0$ kinematical cavity (underfocused) contrast or via counting the number of dynamical thickness fringes (using g_{111} or g_{200}, $S = 0$).[469–471]

Cavity statistics (d_c — cavity diameter and N_c — cavity concentration) and size distributions were obtained using a Zeiss particle analyzer. Cavities were observed in kinematical, underfocused (bright center surrounded by dark Fresnel fringe) contrast; small bubble sizes (2–8 nm in diameter) were measured to the inner diameter of the first

dark Fresnel fringe.[104] Sizes of multimodal distributions were determined separately (e.g., matrix bubbles, matrix voids, precipitate-associated voids); total swelling volume fractions were obtained by summing the individual components of swelling. Cavity volume fraction (CVF) was converted to volume swelling (S_V) via the relationship,

$$S_V = \frac{CVF}{1 - CVF} \cdot \qquad (13)$$

Equation (5) (p. 52) also relates S_V to the measured immersion density change (Σ). In samples with significant grain boundary cavitation and swelling (HFIR, high fluences and temperatures), the contribution of those cavities to total swelling was calculated by measuring the cavitation per unit area of grain boundary and multiplying by the area of grain boundary per unit volume of sample, obtained from metallographic measurements of average grain size[472] (30–50 μm for DO-heat 316).

The dislocation analysis involved measuring the dislocation network concentration and loop statistics, as well as characterizing "black dot" loop damage in samples either preinjected with helium or irradiated at low temperatures in HFIR. Dislocation networks were measured in regions 100 to 200 nm thick, using g_{111} or g_{200} two-beam, $S > 0$ diffraction conditions, similar to the work of Barton et al.[39] Network concentrations (Λ, m/m^3) were measured by counting intersections between the dislocation structure and a set of concentric circles scribed onto a transparent overlay. Factors of 1.5 (g_{200}) or 2.0 (g_{111}) were used to account for invisibilities, assuming an isotropic, random distribution of <110> type Burgers vectors. Frank interstitial loops were imaged separately via

high resolution dark field using the <111> satellite streaks near g_{200} reflections.[473] Loop statistics (d_L — loop diameter and N_L — loop concentration) and size distributions were then measured on the Zeiss particle size analyzer, often on several different {111} planes.

"Black-dot" loop sizes were measured using weak beam dark field (WBDF) imaging, with g_{200} and g/3g diffracting conditions. The defects were identified as planar loops if the dynamical black-white (BW) images did not rotate with rotation of the diffracting vector (g). Loop habit plane and invisibility criteria to determine b (SF/RH, perfect crystal convention) were used to determine loop character; the sense of BW contrast vector with g (parallel or anti-parallel) was used to determine the nature of small loops (vacancy, interstitial).[470-472] Small loops were also imaged in 2½ D to rapidly test for a mixture of Burgers vectors of natures.[474,475] The natures of larger Frank loops were determined using $g \cdot b = \pm 2/3$ for strong/weak fault contrast combined with inside/outside dislocation image contrast.[471]

Precipitate analysis involved phase identification and determination of crystallographic habit and particle statistics (d_p — particle diameter or size parameter, assuming shape factor, and N_p — particle concentration). Extraction replicas were used in some cases to help determine average particle size and relative phase fractions (see Analytical Electron Microscopy, next section). Total precipitate volume fractions (PVFs) were estimated in-foil, using either bright field or dark field imaging of the precipitate. Crystallographic data for phase identification and habit determination [orientation relationships (OR)] were

obtained by tilting between several low index zone axis patterns (ZAPs) of the precipitate phase and/or the matrix (aided tremendously by the eucentric tilting capability of modern microscopes). Both selected area diffraction (SAD) and convergent beam diffraction (CBD) techniques were employed for in-foil and/or replica analysis.

At best, the errors in accuracy should be similar to those of Barton et al.[39] N_c, N_d, N_p, and CVF are estimated to be accurate to ±30% of the reported value, d_c to be ±10%, d_L to be ±25%, and Λ and PVF to be ±100%. Precision should be better than accuracy in these experiments. Deviations reported for these data reflect the scatter from multiple measurements and hence relative precision rather than absolute accuracy.

Analytical Electron Microscopy (AEM)

AEM was performed on the JEM 100CX and Philips EM400 electron microscopes equipped for x-ray energy dispersive spectroscopy (XEDS) with Kevex and EDAX units, respectively. Quantitative XEDS was performed in-foil to obtain matrix compositional information (excluding HFIR samples) and occasionally for larger, thinned precipitate particles. Quantitative XEDS for most precipitate phase particles was performed on carbon extraction replicas, particularly for irradiated specimens. Compositional information on the smallest precipitate phase particles could only be performed on the EM400, with a field emission gun that yields high probe currents at very small probe sizes.[476] Microscopes had been optimized for XEDS by Bentley et al.[477] to minimize contamination and

background x-ray detection (in-hole counts); beryllium specimen holders, gimbals, and grids were used to further reduce background x-ray emission. Figure 25 illustrates how the background (in-hole) XEDS spectra is much less for a replica than for a thin film prepared from the same material.

The particular replica technique used in this work was developed to obtain matrix-free precipitates from type 316 stainless steel and to reliably produce large pieces of replica for easy retrieval when working with the very radioactive solutions and cumbersome shielding necessary for the HFIR specimens. Figure 26 illustrates the technique schematically. Samples were cleaned via electropolishing [Fig. 26(a)] in a solution of perchloric acid and ethanol (5 vol % acid), followed by light electrolytic etching to obtain surface relief and bare precipitate

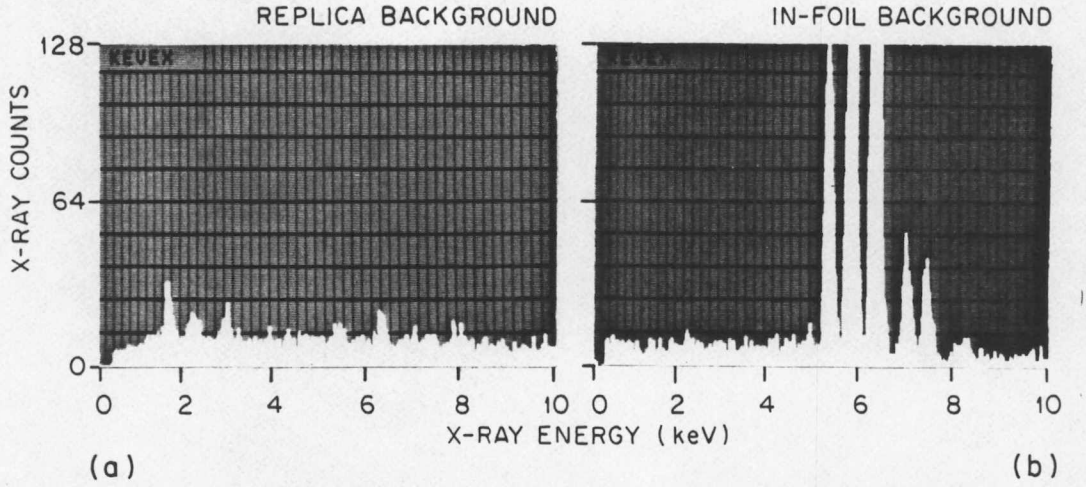

Fig. 25. A comparison of (a) replica film and (b) thin foil in-hole background XEDS spectra for these specimens prepared from SA 316 stainless steel irradiated in EBR-II at 630°C to 36 dpa.

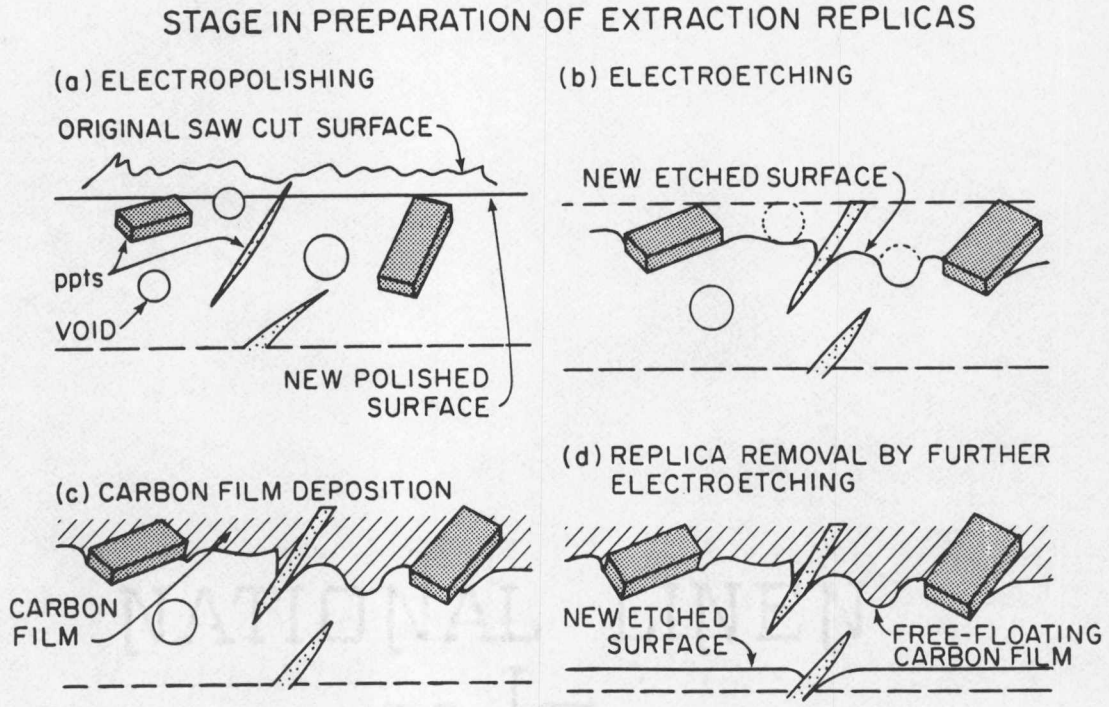

Fig. 26. A schematical representation of the extraction replica process illustrating (a) surface cleaning via electropolishing, (b) surface relief attained via light electroetching, (c) carbon film deposition, and (d) replica removal via further electroetching.

particles [Fig. 26(b)], using hydrochloric acid in methanol (10 vol % acid). Both processes were performed at −10 to −30°C. Electron transparent (50–200 mm thick) carbon films were then deposited [Fig. 26(c)] and then removed by further electroetching [Fig. 26(d)]. Before the final etch, the backs of the samples were painted with microstop to enhance etching underneath the carbon film. Large, continuous films 7 to 15 mm^2 were produced; the films preserved clear imprints of voids and grain boundaries and their associated precipitate particles (see Figs. 27 and 28). Generally, from two to eleven individual particles were analyzed for each phase on each replica.

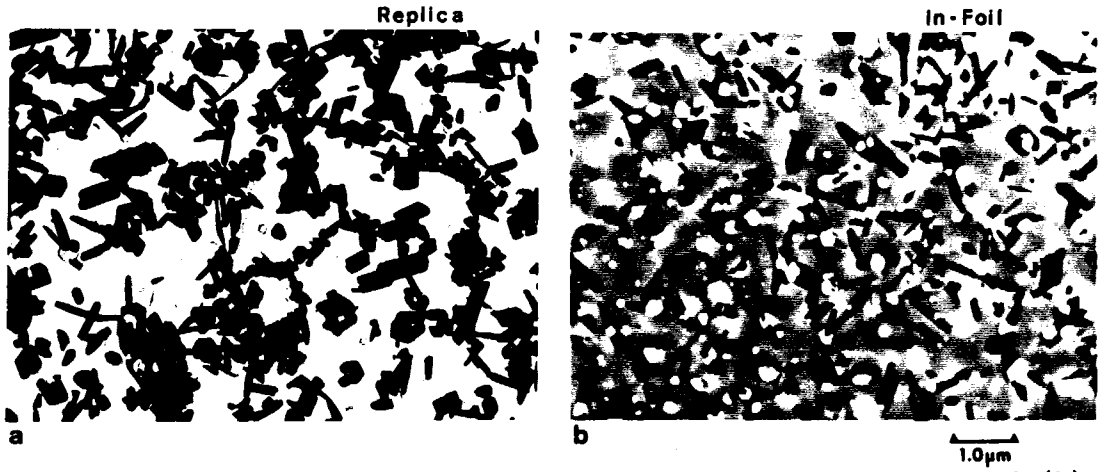

Fig. 27. Comparative TEM of (a) an extraction replica and (b) a thin foil produced from SA 316 irradiated in EBR-II at 630°C to 36 dpa. Note the exact correspondence of precipitate particle shapes and sizes between the replica and thin foil. The particles on the replica are matrix-free and spaced far enough apart for easy XEDS analysis. Also note that association between precipitates and voids is preserved on the replica as well.

Broad beams were also used to obtain XEDS spectra which blended hundreds to many thousands of precipitates into an averaged spectrum in proportion to their relative abundance.[478] The averaged spectra directly represent the overall effect of precipitation on matrix composition (assuming the total precipitate fraction is known); the broad beam spectra can also be deconvoluted to estimate relative phase fractions, if the individual phase compositions are known.

The XEDS data were recorded using a PDP 11/34 and analyzed using an ORTEC-EEDSII computer/multichannel analyzer (both by Digital). Quantitative compositional information for elements heavier than silicon was obtained employing the standardless analysis technique (and absorption corrections, where appropriate) with computer programs developed by

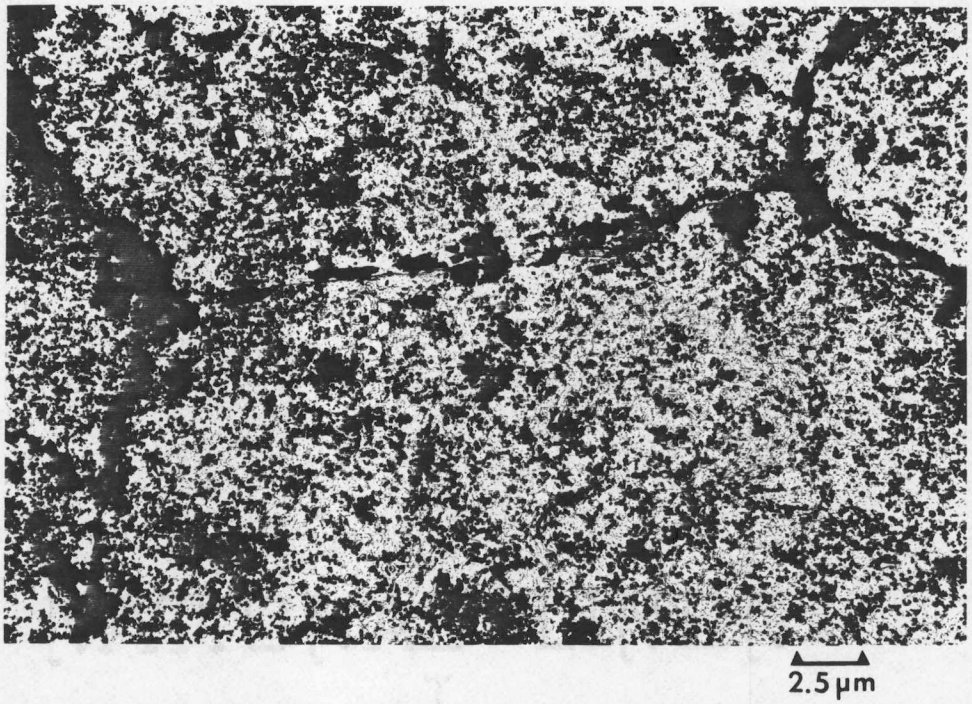

Fig. 28. A low magnification TEM photomicrograph of a replica produced from SA 316 irradiated in EBR-II at 500°C to 31 dpa to illustrate the preservation of grain boundary imprints and precipitate association. This makes analysis of matrix and grain boundary phases separable.

Zaluzec.[479,480] Each peak contained 100 to 100,000 counts, giving statistical significance of ±10 to ±0.3%, respectively, of the reported weight percent. Relative accuracy among various samples is probably better than absolute accuracy of any given compositional measurement.

CHAPTER IV

RESULTS

Data are presented in five major sections, dealing with uninjected and helium-preinjected thermally aged SA 316, with uninjected and preinjected material irradiated in EBR-II, and with HFIR irradiated material. Each section begins with a perspective on the new data and key results, and then is further subdivided to present detailed data on dislocation, cavity, and precipitation components of the microstructural development. Subsections treat temperature and fluence dependencies. More attention is paid (in terms of figures and micrographs) to the newer precipitation data. Each subsequent section relates to preceding sections in order to highlight the effects of irradiation and/or helium on various phenomena.

Thermally Aged SA 316

The perspective from the literature survey is that SA (DO-heat) 316 is more prone toward formation of intermetallic phases, and less toward precipitation of carbides, than heats of steel investigated by others. Quantitative microstructural data on dislocation and on precipitate evolution are new, as are quantitative AEM data on χ phase and on the silicon contents of the various phases.

Dislocation Evolution

Dislocation network concentrations were low (<1 to 5 × 10^{12} m/m^3) at 400 to 500°C and at 900°C, but increased, as precipitation developed

at intermediate temperature, and then peaked (by a factor of 5 to 10) at 550 to 700°C (Fig. 29 and Table 8). Micrographs in Fig. 30 suggest that dislocations were being generated during precipitate particle growth. Such dislocation generation would be consistent with progressive particle nucleation and clustering, as observed here and by others.[341,361]

Precipitation

A. Microstructural Data

Precipitation of various phases occurred upon aging SA (DO-heat) 316 at 560 to 900°C for 2770 h or longer (Fig. 31). Phase identification and quantitative microstructural data are also found in Table 8.

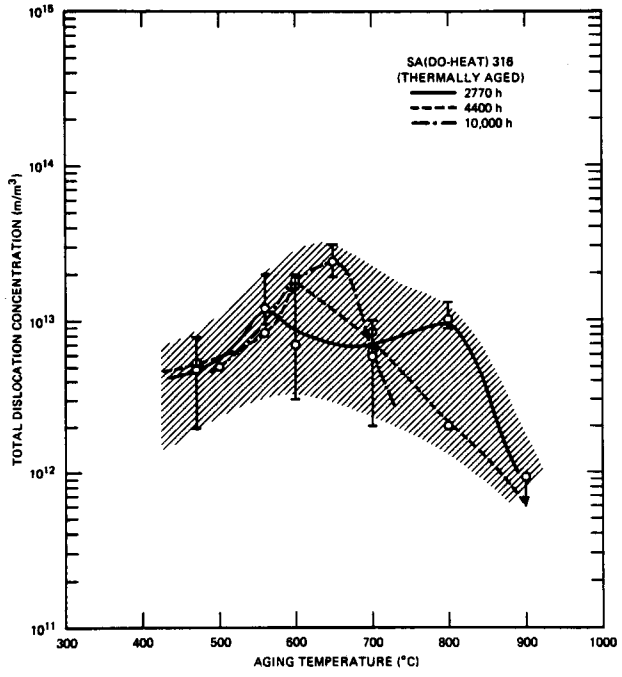

Fig. 29. Total dislocation network concentration (Λ) plotted as a function of aging temperature for SA (DO-heat) 316. Quantitative TEM data can be found in Table 8.

Table 8. Dislocation and Precipitate Microstructural Data on Thermally Aged SA 316

Aging Conditions				Precipitate Data (Matrix)			
Temperature (°C)	Time (h)	Dislocation Concentration (m/m^3)	Phases	Size[a] (nm)	Total Concentration (m^{-3})	Fraction, % Relative	Fraction, % Total Volume
470	2,770	$4.8\pm3 \times 10^{12}$	None				
470	4,400	$0.3-1 \times 10^{12}$	None				
500	10,000	Similar to above	None				
560	2,770	$1.2\pm0.8 \times 10^{13}$	$M_{23}C_6$ (τ)	70[b] 175[c]	1.9×10^{18}	100	0.017
560	4,400	$8.4\pm8 \times 10^{12}$	τ	58[b] 255[c]	3.2×10^{18}	100	0.025
600	2,770	$7\pm4 \times 10^{12}$	τ	80[b] 300–620[c]	5×10^{18}	100	0.34
600	4,400	$1.7\pm1.7 \times 10^{13}$	τ	88[b] 420[c]	5.4×10^{18}	100	0.47
600	10,000	$1.85\pm0.6 \times 10^{13}$	τ	90[b] 450±300°C	9×10^{18}	100	1±0.7
650	100	6.9×10^{12}	None				
650	10,000	2.4×10^{13}	τ+M_6C(η)+Laves+σ[d]	100–400[b] 2000[c] 1600(160)[e]	7×10^{18}	τ – 12 η – 18 Laves – 70	3.2
700	2,770	$6\pm4 \times 10^{12}$	τ+η+Laves+σ^d+χ	160–400[b] 2000–4800[c] 2000(145)[e]	8×10^{18}	τ – 22 Laves – 78	1.7
700	4,400	$8.5\pm6 \times 10^{12}$	τ+η+Laves+σ^d+χ	Similar to above	1.1×10^{19}	Similar to above	2.3
700	10,000	6.2×10^{12}	τ+Laves+σ^d	Similar to above			
800	2,770	$1\pm0.3 \times 10^{13}$	τ+Laves+χ+σ^d+Al-rich phase	450 (by 80) (by 300)[f] 1140 (by 150 (by 470)[f]	1.9×10^{18}	Primarily χ	3.2±2
800	4,400	2×10^{12}	Same as above	Somewhat coarser than above	1.5×10^{18}	Primarily χ	7.2
900	2,770	$<10^{12}$	σ	2–25 μm	$<<5 \times 10^{17}$	100	1–3%
900	4,400	$<10^{12}$	σ	Similar to above		100	Similar to above

[a]Maximum linear dimension (typical shapes for other dimensions can be seen in Appendix A).

[b]Blocky or platelike morphologies.

[c]Rod or lath-shaped $M_{23}C_6$(τ).

[d]σ phase is nearly always found on grain boundaries. It is not included in total volume fraction of matrix phases, except at 900°C where it is the only phase present.

[e]Laves lath or rod-shaped particles. Number in parentheses is the width of the laths. These are typically 40 to 80 mm thick.

[f]Particles include χ, Laves, and $M_{23}C_6$ (τ) phases. All dimensions are given. Numbers in parentheses are thickness followed by width.

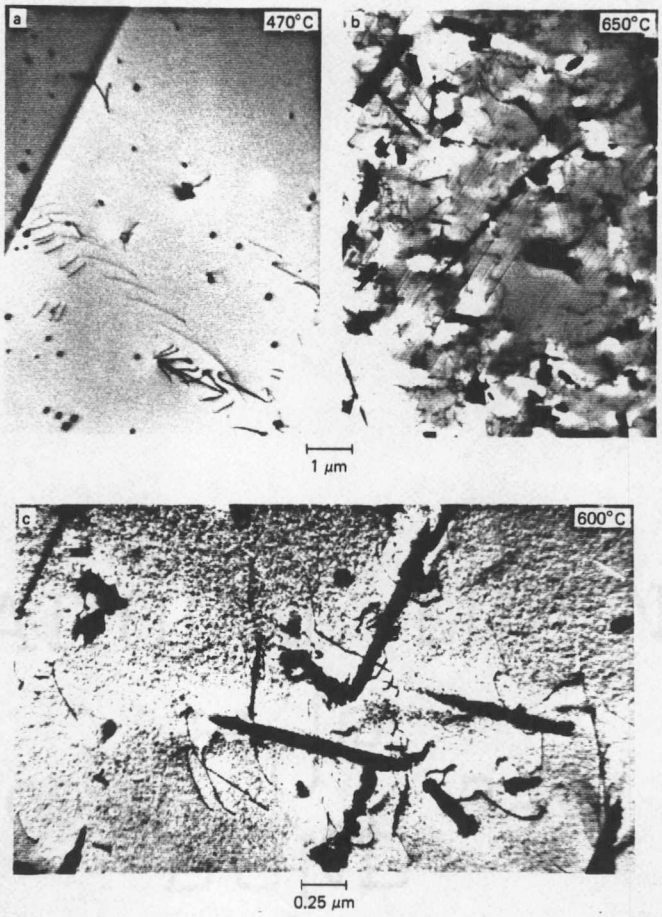

Fig. 30. Micrographs showing the dislocation contents and configurations in SA (DO-heat) 316 aged at (a) 470°C for 4400 h (no precipitation), (b) 650°C for 10,000 h ($M_{23}C_6$, M_6C, and Laves precipitation) at lower magnification, and (c) 600°C for 10,000 h ($M_{23}C_6$ precipitation) at higher magnification. Dislocation tangles around particles and clustered precipitate nucleation suggest dislocation generation during precipitate particle development.

Precipitation was not observed after 100 h at 650°C and therefore carbide precipitation appears sluggish for SA (DO-heat) 316 compared to work by Weiss and Stickler.[9] The dominant phase was $M_{23}C_6$ (τ) at 560 to 600°C, but then progressed to Laves at 650 to 700°C, to χ at 800°C, and finally to σ at 900°C with increased aging temperature (see Fig. 32).

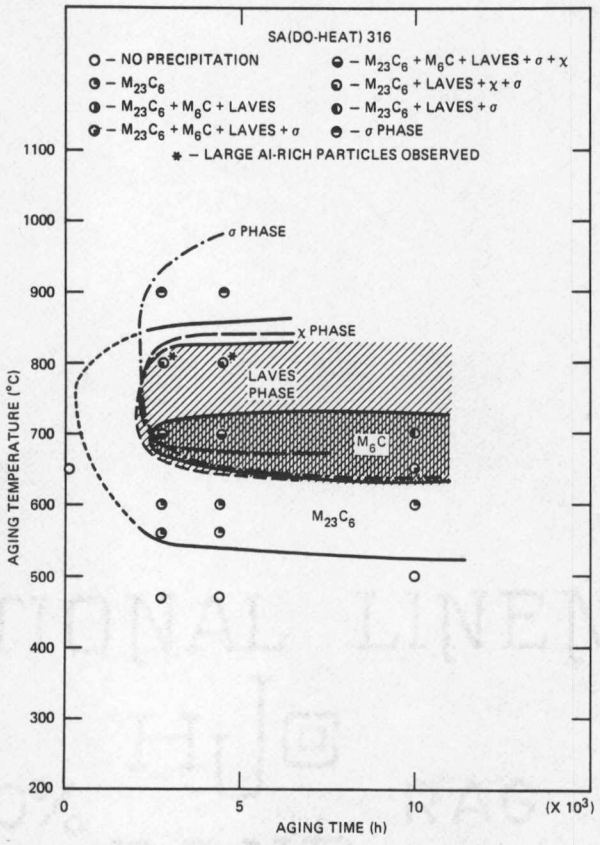

Fig. 31. A plot of precipitate phase formation (grain boundary phases included) as functions of aging time and temperature for SA (DO-heat) 316. Phase identification for each sample can also be found in Table 8. Large aluminum-rich particles are found only at 800°C. This is an air-melted heat of steel, probably killed (deoxidized) with aluminum.

Small amounts of M_6C (η) were found at 650 and 700°C, and small amounts of intergranular σ phase were found at 650 to 800°C. The amount of precipitation (PVF) was maximum at 800°C, as others also find.[9,386] More σ and Laves were found here than found by others,[9,10,363] implying that the SA (DO-heat) 316 is more prone toward intermetallics and less stable toward carbides than other heats of steel.

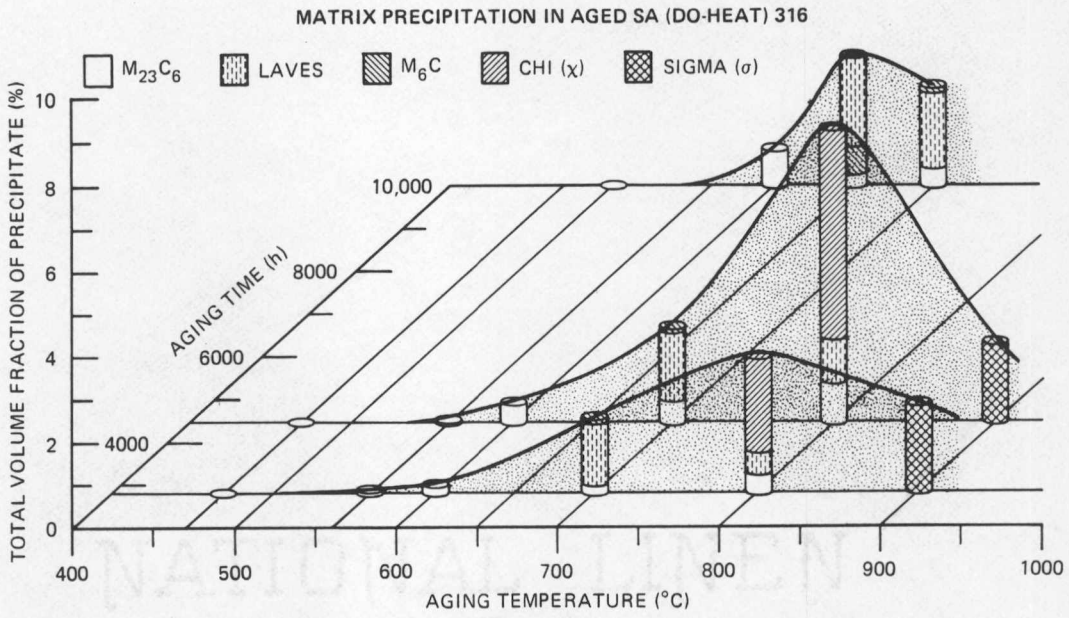

Fig. 32. A plot of relative and total phase volume fractions for matrix precipitation as functions of aging temperature and time for SA (DO-heat) 316. Data are also shown in Table 8. Peak precipitation was found at ~800°C.

Precipitate nucleation peaked at 650 to 700°C, but particle growth increased monotonically with temperature (see Figs. 33 and 34). Particle growth outweighs decreased nucleation to produce maximum precipitation at 800°C (Figs. 32 and 34). Many morphological variants of different phases are illustrated in Appendix A, and some of their correlated crystallographic habit relationships are displayed in Appendix B. $M_{23}C_6$ exhibits many morphologies, all having epitaxial crystal habits, whereas Laves exhibits distinctly coupled morphology/crystal habit pairs.

The most significant time dependencies noted were the rapid increase in precipitate volume fraction (PVF) at 800°C [mainly due to

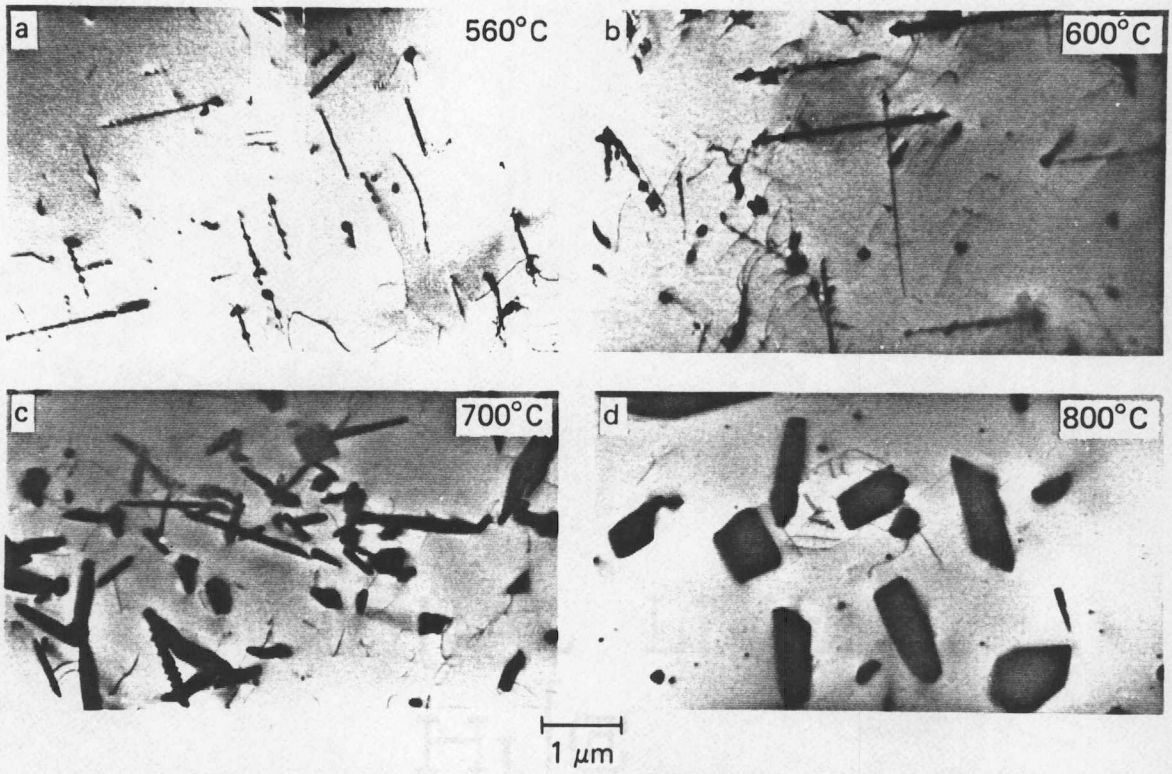

Fig. 33. Microstructures illustrating intragranular precipitate coarsening with increasing temperature for SA (DO-heat) 316 aged for 4400 h. (a) 560°C, $M_{23}C_6$, (b) 600°C, $M_{23}C_6$, (c) 700°C, $M_{23}C_6$ + Laves + M_6C, and (d) 800°C, $M_{23}C_6$ + Laves + χ.

coarsening (Fig. 32)], and the moderate increases in particle concentrations (N_p) at and below 700°C [Fig. 34(b)]. Figure 35 illustrates the sluggish nucleation of $M_{23}C_6$ at 560°C.

Precipitate particles nucleated in clusters at 700°C and below (see Figs. 33 and 36). At lower temperatures, many $M_{23}C_6$ particles emanated from TiN particles, but at 650 to 700°C, Laves and M_6C clustered around central $M_{23}C_6$ particles (similar to observations of Stoter[363] at 650°C). Nucleation of these phases is therefore heterogeneous, and probably sympathetic as well.

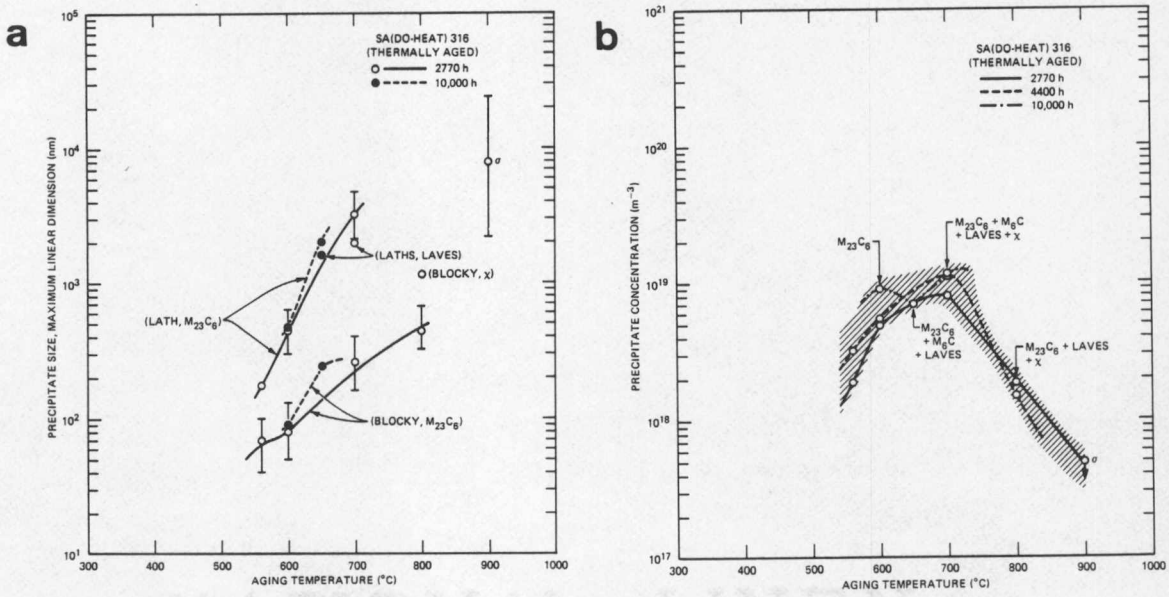

Fig. 34. (a) Phase particle size (d_p), represented by the maximum linear dimension, for various morphological variants, and (b) total precipitate concentrations (N_p) are plotted as functions of aging temperature for several different aging times. Data can also be found in Table 8. The shapes of morphological variants are schematically illustrated in Appendix A, with supporting TEM evidence.

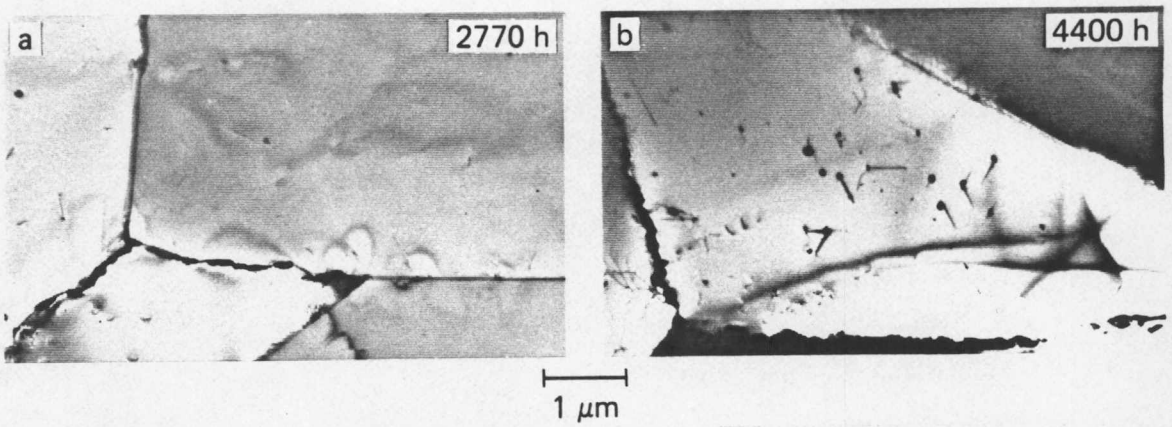

Fig. 35. Progressive nucleation of $M_{23}C_6$ (τ) as time increased for SA (DO-heat) 316 aged at 560°C for (a) 2770 h and (b) 4400 h.

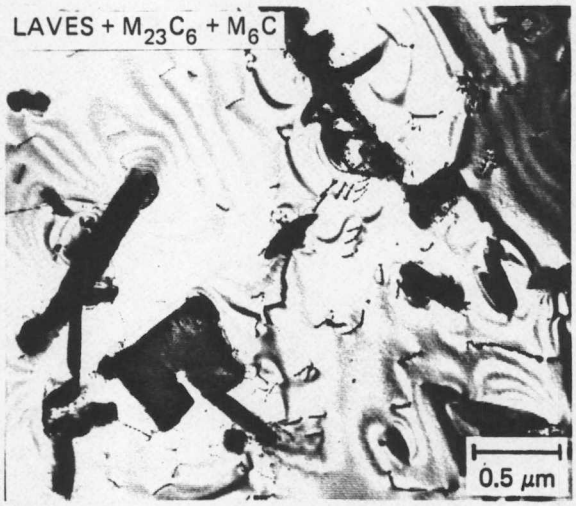

Fig. 36. SA (DO-heat) 316 aged for 10,000 h at 650°C to illustrate clustered nucleation of particles about common centers. These common centers are mainly $M_{23}C_6$ (τ) particles surrounded by Laves and/or M_6C (η) particles, suggesting sympathetic nucleation of the latter two at the former.

B. Microcompositional Data

The phases were all enriched in molybdenum and chromium (except for Laves) relative to the matrix. They were all depleted in nickel [except for M_6C (η)] and iron (Table 9 and Fig. 37). These results are consistent with data of others.[9,41,363,380,402] Laves and η were richest in silicon, while σ and χ had near matrix levels of silicon; $M_{23}C_6$ (τ) was usually depleted of silicon. Relatively, η had the highest nickel and silicon contents, τ the highest chromium level, and Laves the highest molybdenum concentration, while σ and χ contained the most iron. These same trends are also reflected in the broad beam averaged composition of the overall precipitate, as shown in Fig. 38. The chromium level dropped as Laves began to dominate the τ phase with increased temperature (see Fig. 32, p. 147), and molybdenum and iron concentrations

Table 9. XEDS Compositional Information for Matrix and Precipitate Phases in Thermally Aged SA 316

Aging Temperature (°C)	Aging Time (h)	Phases Analyzed (Number of Spectra)		Composition[a] (wt %) Si	P	Mo	Ti	V	Cr	Mn	Fe	Ni
				Precipitate Phase Analyses[b]								
560	2,770	[3]	$M_{23}C_6$(τ)	0.1(±0.1)	0.3(±0.3)	13.3(±3.5)	0.2–2.0	0.4(±0.4)	64.8(±2)	3(±0.4)	15(±3)	2.2(±0.2)
		[2][c]		0.1(±0.1)	0.3	10(±1.7)	0.3	0.3	64.6(±2)	3.3(±0.3)	18.2(±3)	2.8(±0.2)
600	2,770	[4]	τ	0.3(±0.2)	0.4(±0.3)	12(±1.5)	2	0.8	65(±3)	3.7(±0.5)	14(±0.8)	3(±0.3)
		[2][c]		3(±0.3)	0.5	19.6(±1.5)	1	0.7	47(±3)	3	14.4(±0.1)	11(±0.6)
600	10,000	[4]	τ			16(±2)	0.8		66(±2)		15(±2)	2(±1)
		[3][c]		0.1		8.8(±0.8)	0.5		65(±5)		22(±5)	3.5(±0.5)
650	10,000	[4]	τ	0.7(±0.7)	0.2	14(±4.5)	0.3	0.4	64(±8)	2.8	14(±3.8)	3.3(±0.4)
		[5]	M_6C (η)	7.4(±1.4)	0.6	24(±10)	1.7	1.8	30(±8)	1.3	8(±5)	24(±5)
		[9]	Laves	5.7(±1.4)	1	37(±15)	0.5	0.3	13.7(±3.6)	1.4	32(±5)	5.3(±1)
		[2]	σ[d]	1.5(±0.1)		6.5(±0.5)	0.2	0.2	34.5(±0.5)	2.8	49(±1)	5(±0.1)
		[5]	Broad beam analyses	4.8(±0.2)	1	34.5(±3.5)	0.3	0.5	22.3(±2.5)	1.5	26.6(±2.5)	9(±0.5)
700	2,770	[2]	τ	1.4(±0.8)	0.6	17(±4)	1.5	1	60(±12)	1.9	13.5(±1.4)	4.8(±3.7)
		[2][c]	τ	0.7(±0.1)	0.3	12.7(±1)	0.3	0.6	60(±0.5)	2	19(±0.5)	3.9(±0.2)
		[2][c]	η	4.5(±2)	0.2	20	0.3	2.1	31(±3)	1.6	13(±0.3)	27(±4)
		[3]	Laves	5(±0.2)	1.1	39(±0.6)	0.4	0.1	14(±1.6)	1.4	34.3(±1.3)	5.4(±0.5)
		[3]	Broad beam analyses	3.5(±0.3)	1	33.3(±1.5)	0.6	0.4	23.4(±3)	1.5	30(±2)	6(±1.7)
800[e]	2,770	[1]	τ	0.1	0.4	9.2		0.3	68	1.2	17.3	3.3
		[1]	Laves	3	0.7	24.5	0.1	0.2	14.4	1.4	48	7.8
		[3]	χ	1.6(±0.01)	0.5	14.5(±0.7)	0.1	0.15	25.6(±0.4)	1.7	51(±0.4)	4.9(±0.1)
		[1]	σ[d]	1.2	0.2	9.6	0.1	0.1	31.4	1.6	49.7	6
900[e]	2,770	[2]	σ[d]	1.3		10.3	0.1	0.2	29.8	1.8	50.5(±0.3)	5.8

Table 9 (continued)

Aging Temperature (°C)	Aging Time (h)	Phases Analyzed (Number of Spectra)		Composition[a] (wt %) Si	P	Mo	Ti	V	Cr	Mn	Fe	Ni
						Matrix Analyses[f]						
As-fabricated		[2]	γ	1.4(±0.1)		3.7(±0.4)			18	2.5	61.1	13.2(±0.2)
600	10,000	[3]	γ	1.5(±0.4)		3.5(±0.5)			18.5(±0.4)	1.9(±0.1)	62(±1)	12.6(±0.4)
650	100	[2]	γ	1.6(±0.5)		3.4(±0.4)			18.9(±0.2)	1.4(±0.1)	62.2(±0.5)	12.6
650	10,000	[2]	γ	0.9(±0.1)		1.4(±0.1)			18.6(±0.1)	1.8(±0.4)	65(±1)	12.5(±0.5)
		[3]	Broad beam analyses	1.3(±0.1)		1.8(±0.2)			19.1(±0.2)	2(±0.1)	63.5(±0.2)	12.3(±0.4)

[a]Includes elements with atomic numbers (Z) equal to or greater than Al (Z = 13).

[b]Unless otherwise indicated, analyses are for intergranular particles on extraction replicas.

[c]Grain boundary phase, analyzed on replica.

[d]Grain boundary phase, analyzed in-foil.

[e]In-foil analyses for all phases present.

[f]Unless otherwise indicated, these were in-foil, spot mode measurements made in matrix regions that are precipitate-free or in-between particles.

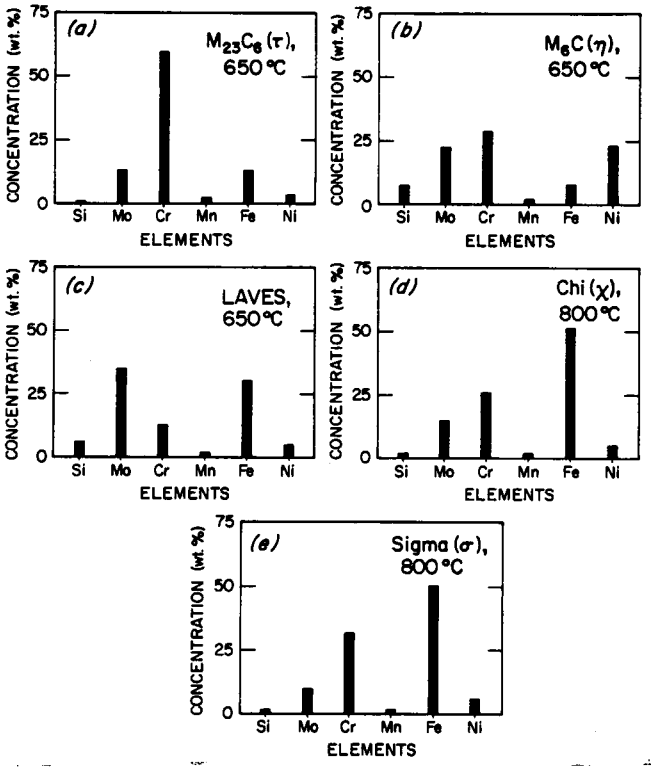

Fig. 37. Histograms of compositional distributions of metallic elements in the various phases found in thermally aged SA (DO-heat) 316: (a) $M_{23}C_6$ (τ), (b) M_6C (η), (c) Laves, (d) χ, and (e) σ, with aging temperatures indicated. These are averaged compositions of quantitative analysis of XEDS spectra obtained from many particles either on replicas (a–c) or in-foil (d,e). Data are also listed in Table 9.

correspondingly increased; the slight increase in nickel reflected the presence of η phase at 650 and 700°C. Large, blocky aluminum-rich particles (possibly Al_2O_3, but light elements like oxygen or carbon are not detectable here) were also detected at 800°C, as indicated in Fig. 31, p. 146).

The individual phase compositions showed little temperature sensitivity, except for Laves, and virtually no time dependence. There was no discernible compositional variation among the many morphological variants

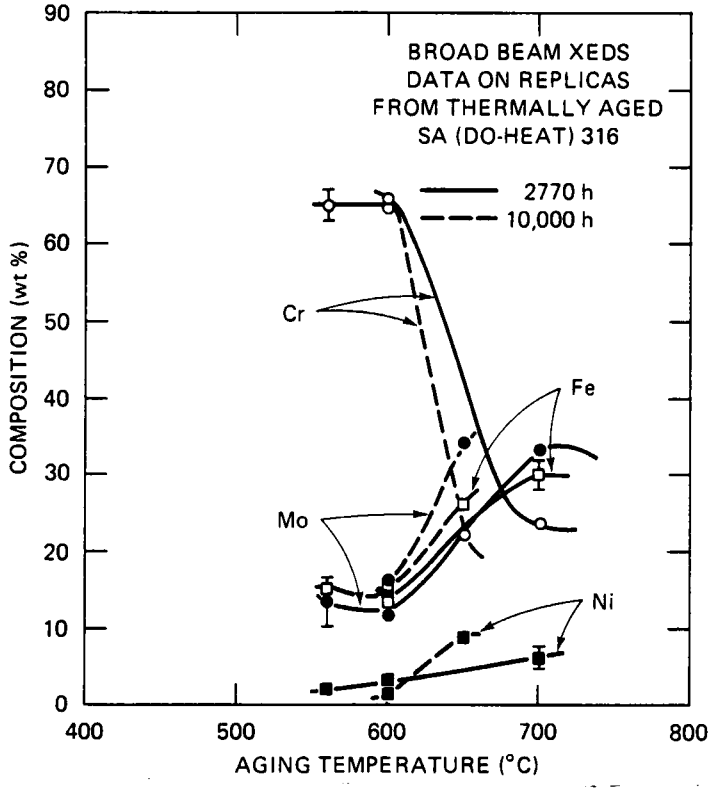

Fig. 38. Broad beam averaged compositions of the total precipitate for chromium, molybdenum, iron, and nickel plotted as functions of temperature for aging times of 2770 and 10,000 h. Samples at 560 and 600°C contained only $M_{23}C_6$ (τ) phase, so that averaged phase compositions were used. Analysis at 650 and 700°C included τ, M_6C (η), and Laves phases on extraction replicas. Data are also found in Table 9.

observed for τ and Laves phases (see Table 9). There were, however, detectable variations in composition between intra- and intergranular particles of τ phase, but only in silicon, molybdenum, and iron concentrations. Laves phase demonstrates less temperature sensitivity in this work at 650 to 700°C and slightly differing trends at 700 to 800°C than found by Williams[402] (silicon and molybdenum decrease and nickel slightly increases from 700 to 800°C in this work).

Austenite matrix composition (also given in Table 9) showed little effect of precipitation at 600°C, but decreased measurably in

silicon and particularly molybdenum at 650°C after 10,000 h, consistent with considerable Laves formation at the latter condition (see Fig. 32, p. 147).

Helium Preinjected and Thermally Aged SA 316

These data included much longer aging times at lower temperatures than previous work on helium preinjected and aged SA 316, and better resolution of the as-injected damage structure. Positive identification was made on much smaller defects at lower temperatures as interstitial Frank loops. Loop and bubble evolutions seemed sluggish compared to observations by Mazey and Francis,[42] but bubble microstructural data were very consistent. These data uniquely identify effects of helium on thermal precipitation ($M_{23}C_6$ destabilized, intermetallics formation enhanced).

Dislocation Evolution

The fine, dense, "black-dot" loop damage, produced via cold helium preinjection, coarsened during long-term aging at 400°C and above to produce larger Frank loops at 600°C; the loop structure was gone at 700°C (Table 10 and Fig. 39). Previous work[42-44] at shorter times observed little change below 600°C and then rapid loop disappearance at 600 to 750°C (cf Figs. 31, p. 146, and 39). Figure 40 shows that the coarsening at 400 to 600°C after 10,000 h was clearly resolvable, via TEM, from the as-injected condition. Plots of N_ℓ, d_ℓ, and Λ in Fig. 41 indicate that while loops grew, N_ℓ fell steeply from the as-injected state to significantly reduce Λ as the dislocation structure recovers.

Table 10. Dislocation and Cavity Microstructural Data for Helium Preinjected (110 at. ppm) and Thermally Aged SA 316

Temperature (°C)	Aging Time (h)	Dislocation Data: Loops[a] Network (m/m^3)	Loops[a] Diameter (nm)	Loops[a] Concentration (m^{-3})	Total Concentration (m/m^3)	Cavity Data: Diameter (nm)	Concentration (m^{-3})	Swelling (%)	Helium Fraction[b]
As-injected		None[c]	~2.2	~3.9×10^{23}	2.7×10^{15}		None[d]		
400	1,000	None	5.2	6.4×10^{21}	1.1×10^{14}		None		
400	10,000	None	5.3	8.6×10^{21}	1.4×10^{14}		None		
500	10,000	None	9.8	$8.2(\pm 4) \times 10^{21}$	2.5×10^{14}		None		
600	1,000	~10^{12}	46.2	6.5×10^{20}	9.4×10^{13}		None		
600	10,000	~10^{12}	28±2.5	3.4×10^{20}	3×10^{13}	2.73[e]	$7 \pm 1.5 \times 10^{21}$	0.008	0.44
700	10,000	1–1.4 × 10^{13}		None	1–1.4 × 10^{13}	5.5±0.6[e]	$3.3 \pm 1.3 \times 10^{20}$	0.004	0.12

[a]All are identified as Frank interstitial type.

[b]Fraction of helium calculated, assuming that all cavities are equilibrium helium bubbles, divided by the amount of helium preinjected.

[c]Network concentration is less than 10^{12} m/m^3.

[d]Bubbles less than 1.5–2.0 nm in diameter are virtually unresolvable.

[e]These appear to be bubbles.

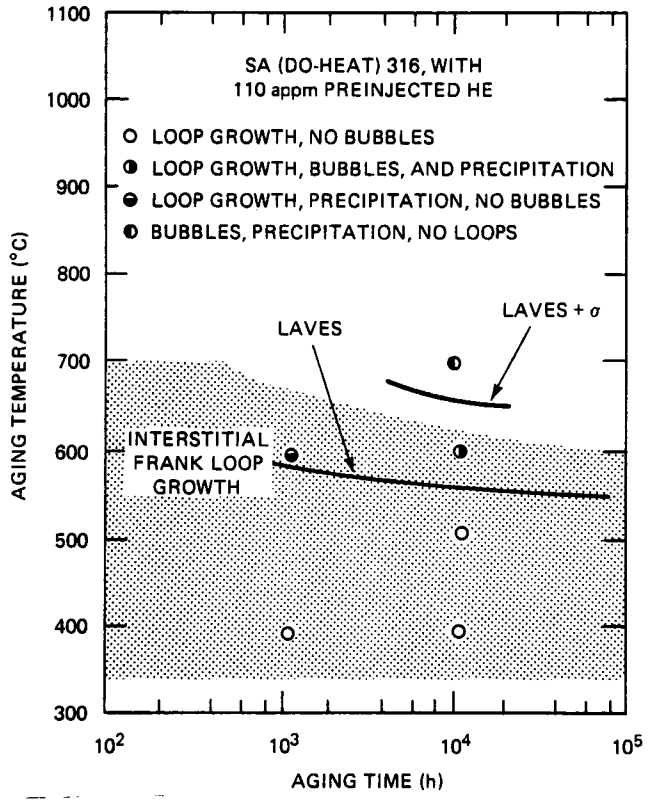

Fig. 39. Loop, bubble, and precipitate microstructural observations plotted as functions of aging temperature and time for SA (DO-heat) 316 cold preinjected with 110 at. ppm He. Quantitative loop and cavity microstructural data are found in Table 10. The effects of helium on the precipitation phenomena can be seen by comparing this figure with Fig. 31, p. 146.

However, during this recovery, the apparent interstitial content of the loop structure reached a minimum at 400°C and then, surprisingly, increased from 400 to 600°C [Fig. 41(c)].

The above observations have the greatest impact because loop nature was positively identified. Loops at 400 to 600°C were identified on the basis of contrast experiments (described on pp. 136—137 of Chap. III and summarized in Fig. 42) as Frank interstitial loops; the tiny loops in the as-injected material were very difficult to completely

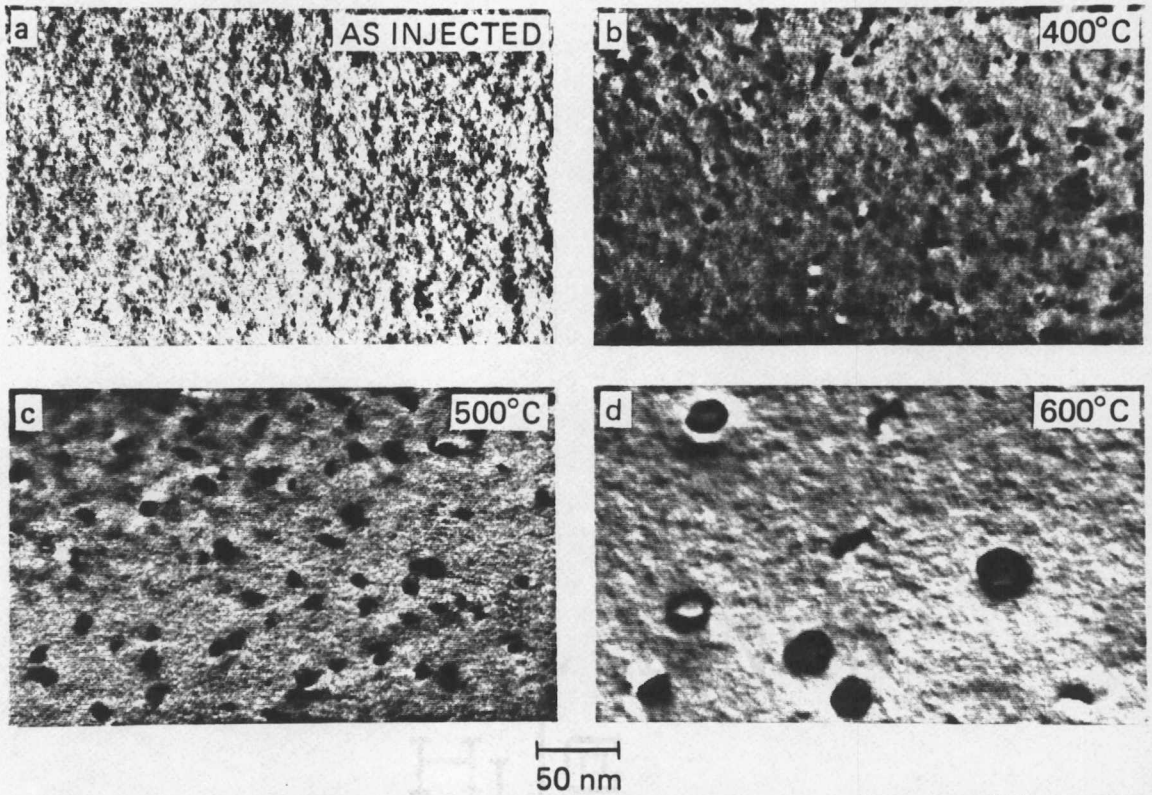

Fig. 40. Comparison of loop structures of helium preinjected (110 at. ppm) SA (DO-heat) 316. (a) As-injected, and then after aging for 10,000 h at (b) 400°C, (c) 500°C, and (d) 600°C. All pictures are taken with g_{200}, s = 0. Loops in (b)—(d) are positively identified as Frank interstitial loops; loops in (a) appear to be similar. Quantitative data are found in Table 10 and in Fig. 41.

identify, but image behavior similar to the larger loops suggests that these, too, were interstitial Frank loops. In all samples 2½ D imaging indicated that all loops had the same nature,[474] and were therefore not mixtures of vacancy and interstitial type loops. In samples aged at 500°C or below, black/white images did not rotate with $\bar{g}$ to demonstrate that the defects were loops[469,471] [as in Fig. 42(a) and (b)], and black/white images were parallel to g_{111} type vectors [Fig. 42(b)], consistent with Frank loops[471] ($\bar{b}$ = 1/3<111>). The fault planes were

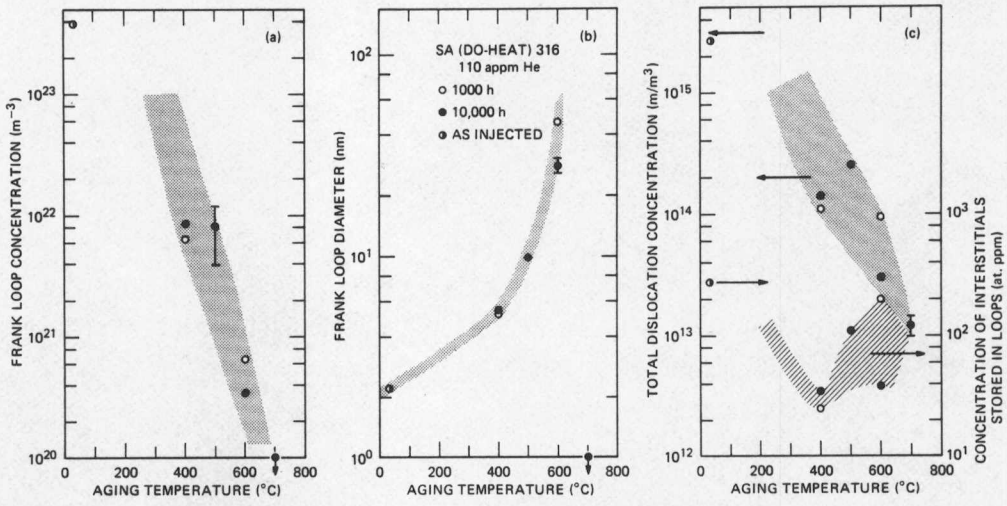

Fig. 41. (a) Frank loop concentration (N_ℓ), (b) Frank loop diameter (d_ℓ) and total dislocation concentration (Λ) plotted as functions of aging temperature after 1000 and 10,000 h for helium preinjected SA (DO-heat) 316 (110 at. ppm). No loops are observed at 700°C. Data are also listed in Table 10. Interstitial defect storage in the loop structure [also in (c)] was calculated using an atomic density on (111) planes of 1.54×10^{19} atoms/m^2 and an overall atom density of 8.338×10^{28} atoms/m^3.

actually visible in the WBDF images [fault streaks in diffraction pattern show that these were (111) planes] for the larger loops at 500 and 600°C [Fig. 42(c) and (f), respectively]. The sense of black/white contrast with $\bar{g}$ (either $\bar{g} \cdot \bar{\ell}$ = plus or minus), for known defect depth from the foil surface, indicated that small loops at 400 and 500°C were interstitial[104,471] [see Fig. 42(d) and (e)]. Inside/outside contrast behavior of larger Frank loops at 600°C also proved that they were interstitial[471] [see Fig. 42(g) and (h)]. Mazey and Francis[42] also identified Frank loops as interstitial in helium injected SA 316 aged for short times at 650°C.

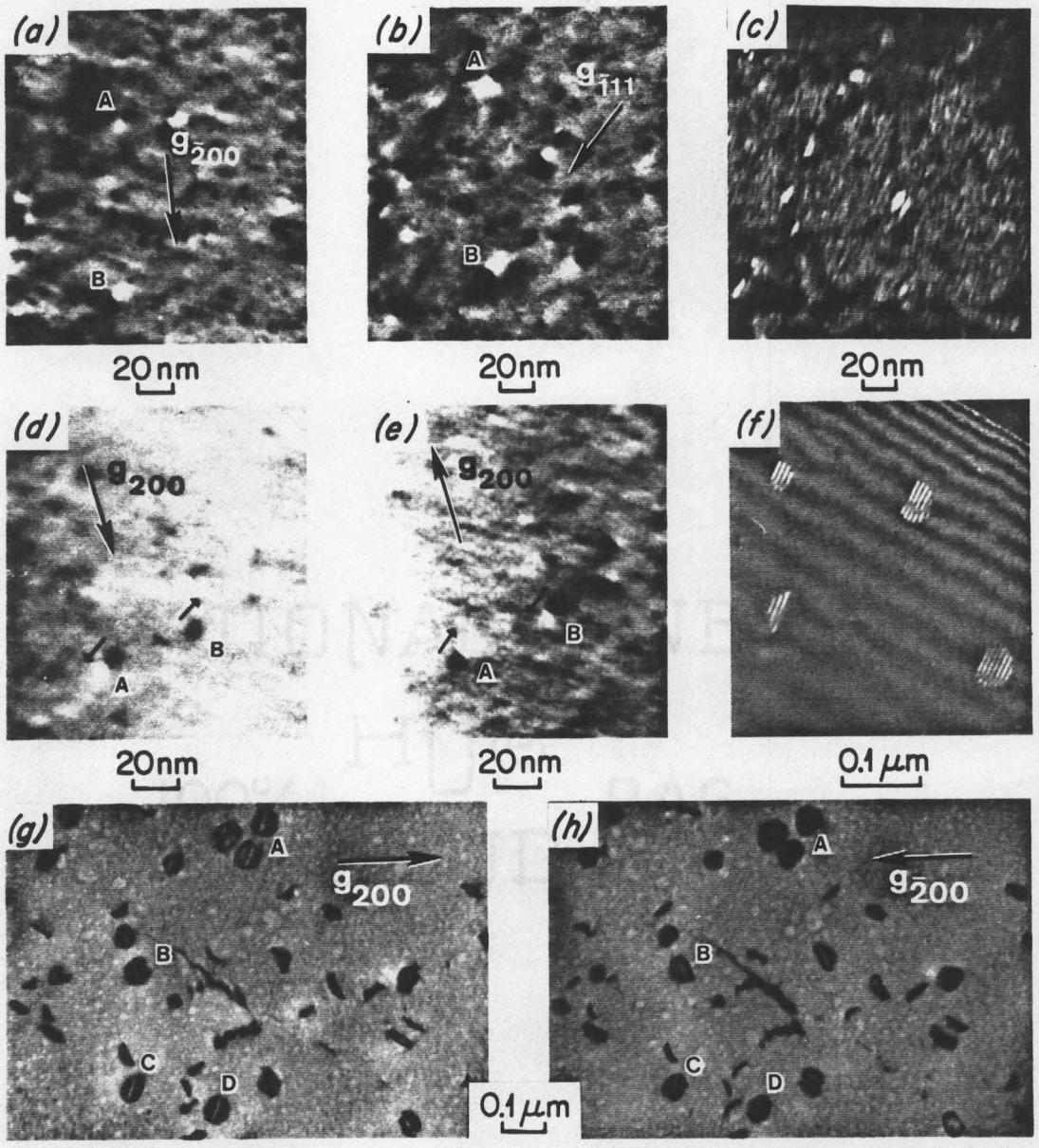

Fig. 42. Microscopy which identifies Frank interstitial loops found in helium preinjected SA (DO-heat) 316 aged at 400°C for 1000 h [(a), (b),(d), and (e)], at 500°C for 10,000 h (c), and at 600°C for 1000 h [(f),(g), and (h)]. The defects are loops because the images do not rotate with g in (a) and (b) [BF, s = 0, with $g_{\bar{1}11}$ and $g_{\bar{2}00}$ near $(0\bar{1}1)$ zone]. WBDF imaging shows faults on (111) planes in (c) and (f) (g_{200}, + $g/3_g$). $g \cdot \ell$ = + for A and = − for B (g_{200} and ℓ pointing from black to white) demonstrates that these are interstitial loops for (d) BF and (e) CDF, with A and B depths being 0.47 ε_g and 0.73 ε_g, respectively, from the top surface. Larger loops are interstitial as well because g_{200} is reversed in (g) and (h) [s = 0, BF near (011) zone]; loops A, C, and D are on $(\bar{1}11)$ planes so that $g \cdot b = -2/3$ for strong fault contrast when the image is inside the loop (see Chap. III, pp. 136, 137).

The concentrations of interstitials atoms stored in the loop structure were calculated using total concentration of loop area multiplied by the atomic density on (111) planes; 1.54×10^{19} atoms/m^2 (see Fig. 41). The interstitial loops increased their apparent interstitial content during growth, suggesting vacancy emission similar to the evaluation by Mazey and Francis. These data therefore suggest that somehow the matrix had less than its equilibrium vacancy concentration (probably due to helium clusters and/or bubbles absorbing vacancies[42]) as will be discussed later.

Cavity Evolution

Bubbles were observed only at 600 and 700°C after 10,000 h (Fig. 43), and were not found after 600°C and 1,000 h (see Table 10, p. 156). The fine, dense bubble microstructures found at 600°C coarsened at 700°C (size doubled and concentration was 50 times less, Table 10). The size distribution broadened with temperature, while the average size increase was small [Fig. 43(d)]. The size distribution and the bubble-encrusted dislocations (Fig. 44) suggest coalescence coarsening, probably aided by recovery motion of the network formed as loops grew and unfaulted.[42] Indeed, very few bubbles were located at loops at 600°C. The largest bubbles were found at the grain boundaries, particularly at σ phase particle interfaces (Fig. 44); by contrast, some of the smallest bubbles were found at intergranular Laves particle interfaces. Bubble formation observations and statistics were consistent with data by Mazey and Francis.[42]

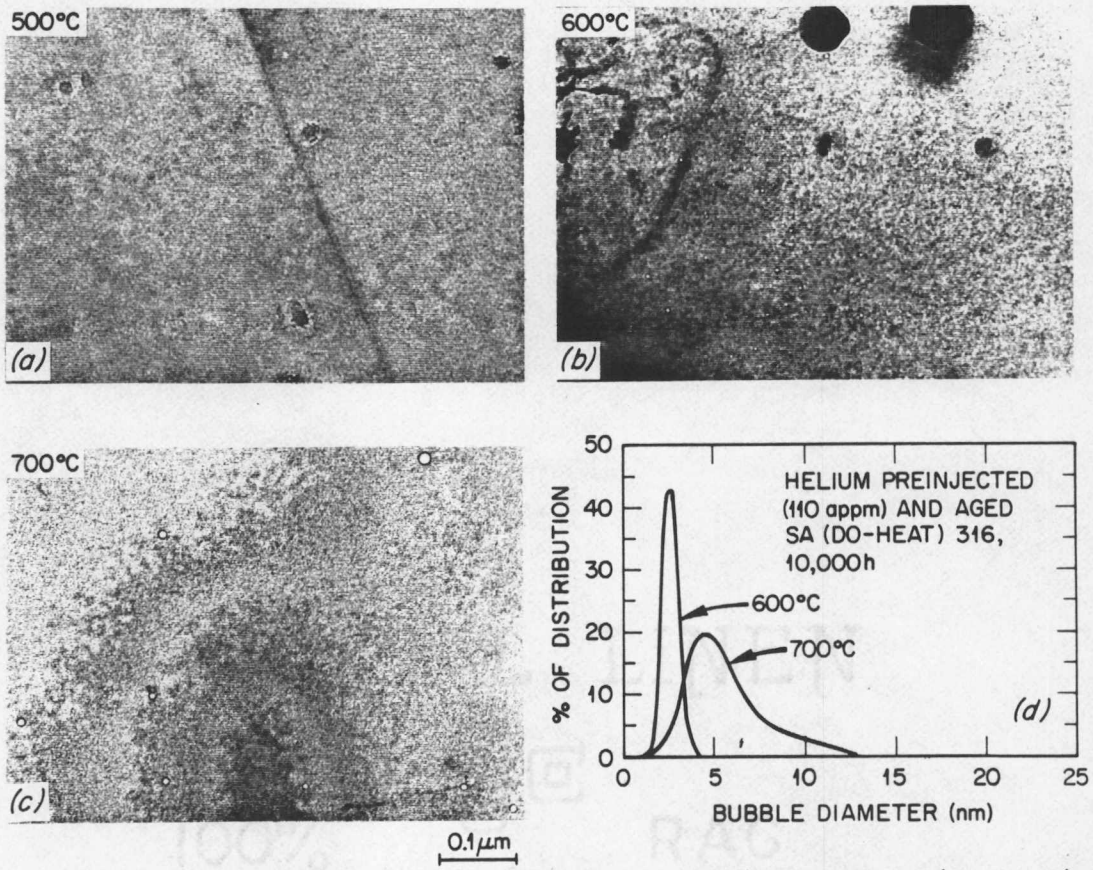

Fig. 43. Bubble evolution in helium preinjected SA (DO-heat) 316, aged for 10,000 h at (a) 500°C, (b) 600°C, and (c) 700°C. Bubbles were observed in (b) and (c), but not in (a). Bubble size distributions at 600 and 700°C are shown in (d). Quantitative data are found in Table 10.

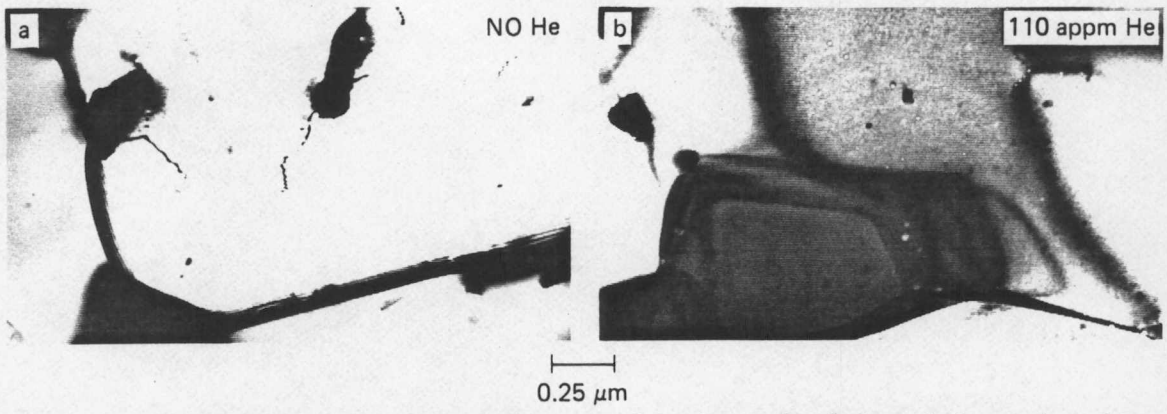

Fig. 44. A comparison of grain boundary in (a) uninjected and (b) helium preinjected SA (DO-heat) 316 aged for 10,000 h at 700°C to illustrate bubble formation at the boundaries and at the interfaces of σ phase particles in (b).

The helium inventory, assuming that the bubbles were in equilibrium, was calculated using Eq. (3), p. 37, Chap. II [manipulated to give the number of gas atoms (n)] and using the nonideal equation of state developed by Brearley and MacInnes[177] for densely packed helium gas [assuming a surface energy (γ) of 1.5 J/m^2]. The bubbles could not account for all the preinjected gas, containing 44% at 600°C and only 12% at 700°C. Escape of large amounts of helium after preinjection seems unlikely,[89,97] particularly since the ratio of retained interstitials to helium atoms suggest two to three vacancies per helium atom in the as-injected condition [Fig. 41(a)]. These data, therefore, imply either highly overpressured bubbles, or a significant amount of unresolved helium/vacancy clusters in the matrix.

Precipitation

Precipitation was observed in helium preinjected SA (DO-heat) 316 at 600 and 700°C, but not at 500°C (see Fig. 39, p. 157), consistent with the behavior of aged, uninjected material (Fig. 31, p. 146). However, $M_{23}C_6$ (τ) was conspicuously absent in the helium preinjected material at 600°C. Instead, Laves began to form at grain boundaries after 1000 h and continued to develop there and in the matrix after 10,000 h [see Fig. 45(a) and (b)]. Many other $M_{23}C_6$ particles were found at dislocations in addition to those encrusted about TiN inclusions; however, clusters of matrix Laves particles were found only around TiN inclusions in the preinjected material [Fig. 45(b)]. The missing $M_{23}C_6$ in the preinjected material was only a minor perturbation to the normal precipitation at 700°C which was

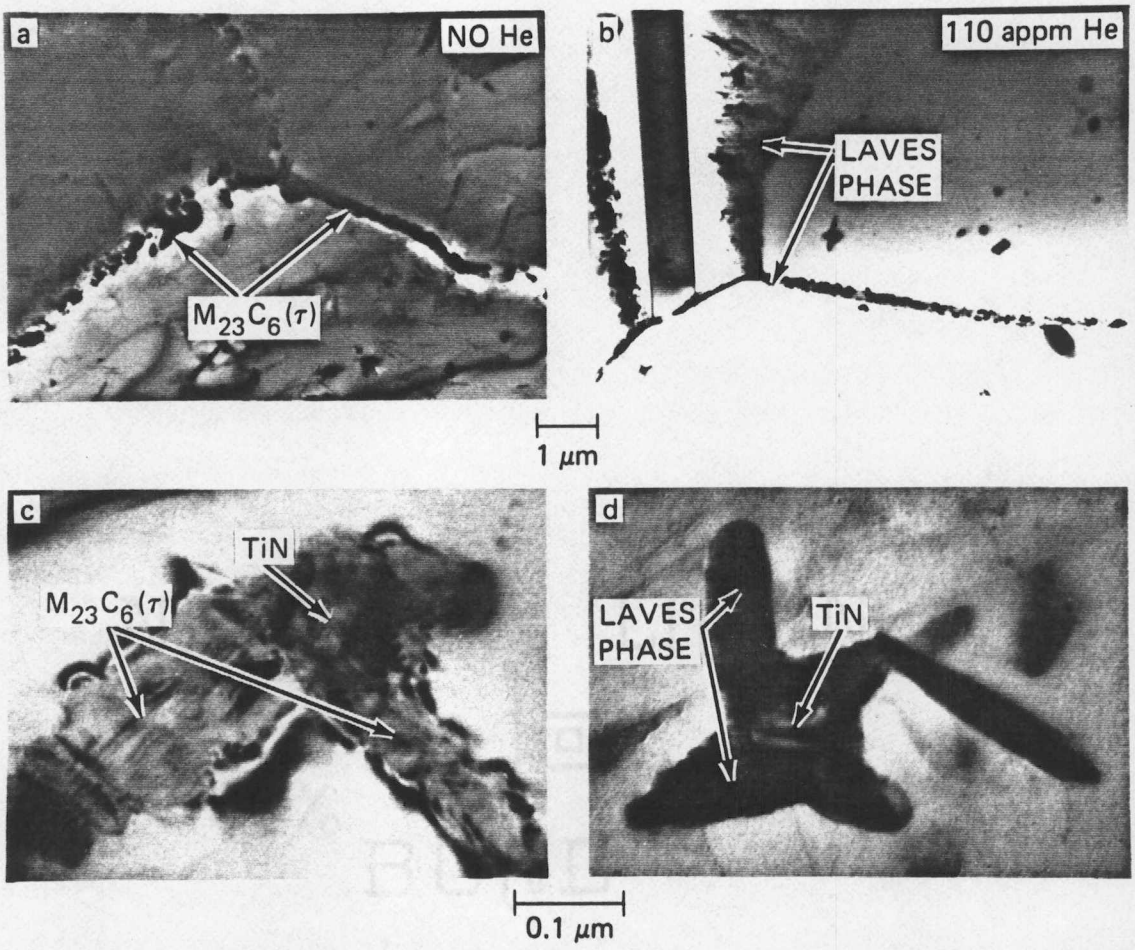

Fig. 45. A comparison of precipitation in SA (DO-heat) 316 aged for 10,000 h at 600°C without (a),(c) and with (b),(d) preinjected helium; (a) and (b) show grain boundaries and matrix at lower magnification and (c) and (d) show TiN inclusions in the matrix at higher magnification. The uninjected material contained solely $M_{23}C_6$ (τ) phase, whereas the helium preinjected material contained only Laves phase. The $M_{23}C_6$ was also found on matrix dislocations, whereas the Laves particles were found exclusively on TiN particles.

dominated by intermetallic formation [see Fig. 32, p. 147 and Fig. 44];

σ particles, however, seemed larger in the helium injected material.

Relative to previous work, these data are generally consistent; however, the DO-heat of SA 316 is more prone toward precipitate-associated void formation (particularly at lower fluences and temperatures) and less prone toward Frank loop formation than other heats of steel. Observations of fine bubbles below 600°C, G phase in SA 316, and γ' (Ni_3Si) at fluences below 30 to 40 dpa are new. This work uniquely identifies the acicular needles as two phosphide phases with high phosphorus enrichments. Quantitative microstructural data on voids are more detailed, and data on precipitation are new compared to previous work. Quantitative AEM matrix and precipitate phase compositional data are consistent with others, but fluence dependencies for several phases and the broad beam measurement are new.

Dislocation Evolution

Dislocation generation was ten or more times greater at 500 to 630°C during EBR-II irradiation than during thermal aging (Table 11 and Fig. 46). Dislocation concentrations were similar at both temperatures after 8.4 dpa (6–8 × 10^{13} m/m^3), but developed a strong temperature dependence after 31 to 36 dpa. While dislocation content nearly doubled with fluence at 500 to 525°C, it fell by ~66% at 625 to 630°C (Fig. 46). Many more and smaller Frank loops were found together with network at the lower temperature at 8.4 dpa, but loops were gone at both temperatures at higher fluence (Table 11). Other workers[38–40,113–116] find many more loops (10 to 100 times more) than found here in the SA

Table 11. Dislocation and Cavity Microstructural Data for SA 316 Irradiated in EBR-II

Irradiation Temperature (°C)	Displacement Damage Level (dpa)	Helium Content (at. ppm)	Dislocation Data				Cavity Data				
				Loops[a]							
			Network (m/m^3)	Diameter (nm)	Concentration (m^{-3})	Total Dislocation Concentration (m/m^3)	Type	Diameter (nm)	Concentration (m^{-3})	Helium Fraction[b]	Swelling (%)
500	8.4	5	$7.4(\pm2) \times 10^{13}$	50[c] 134[c]	5.6×10^{18} 7.6×10^{18}	7.8×10^{13}	Ppt voids	5.3(±8)	$5.4\pm1.6 \times 10^{18}$	1(8.9)[d]	0.05±0.03
500	8.4	5+110 PI[e]		18	1.1×10^{21}	6.4×10^{13}	Bubbles	2.1	2.1×10^{22}	0.7	0.01
							Bubbles	1.8	3.4×10^{21}	0.43	
							Matrix voids	23	2.5×10^{19}	0.1(2.9)[d]	0.27±0.1
525	31	19	1.9×10^{14}			1.9×10^{14}	Ppt voids	56	1.8×10^{19}	0.47(13.8)[d]	
625	8.4	5	$5.1\pm0.6 \times 10^{13}$	10–250	$<5 \times 10^{17}$	$\sim5.7 \times 10^{13}$	Bubbles	3	8.6×10^{19}	0.04	
							Ppt voids	57.6	6.7×10^{18}	0.96(56.5)[d]	0.16
625	8.4	5+110 PI	$3.4\pm0.8 \times 10^{13}$			3.4×10^{13}	Bubbles	2.8	9.5×10^{21}	0.64	0.01
							Bubbles	4.8	1.2×10^{20}	0.16	
630	36	22	2×10^{13}			2×10^{13}	Matrix voids	65	2.8×10^{18}	0.07(1.5)[d]	1.5±0.3
							Ppt voids	166	4.5×10^{18}	0.77(16.4)[d]	

[a]Identified as Frank interstitial loops, unless otherwise indicated.

[b]Fraction of total helium present that would be contained in these cavities if they were equilibrium bubbles. When voids and bubbles are present, helium is first partitioned to the bubbles and divided among the void components in proportion to their relative volume fraction. Numbers less than one indicate excess helium elsewhere in the system.

[c]Bimodal Frank loop distribution.

[d]Excess void volume compared to an equilibrium bubble with the same amount of helium partitioned to it.

[e]PI — Preinjected Helium.

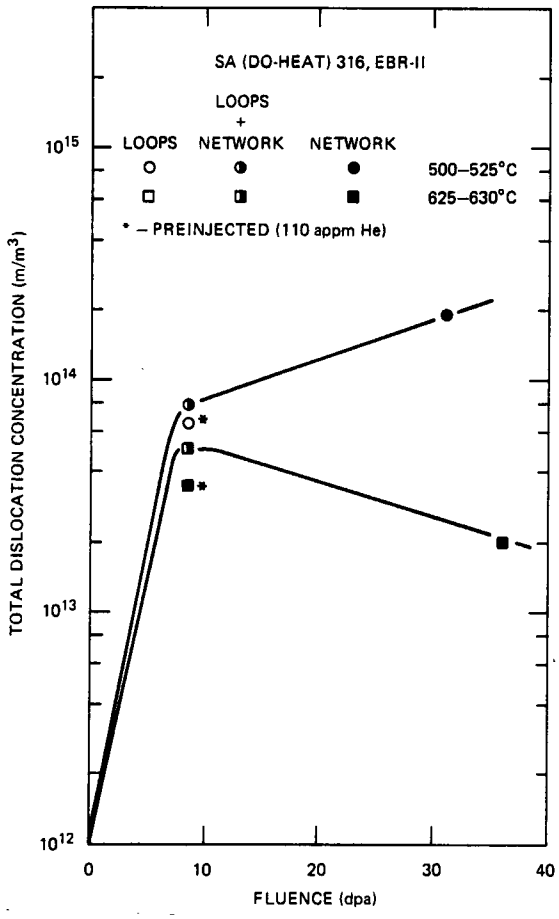

Fig. 46. Dislocation evolution as functions of fluence in SA (DO-heat) 316 irradiated in EBR-II at 500 to 525°C and 625 to 630°C. Results for cold helium preinjected samples are also included. Data are also found in Table 11.

(DO-heat) 316, particularly at higher fluences at 500 to 525°C. Total dislocation concentrations in SA (DO-heat) 316 are similar or slightly lower compared to most previous data (cf. Figs. 6, p. 30, and Fig. 46), but are much lower and more temperature dependent than indicated by Garner and Wolfer.[127]

Cavity Evolution

Voids associated with precipitate particles dominated at both temperatures and fluences, but matrix voids were found only at higher fluences (Table 11 and Fig. 47). Together, Figs. 47 and 48 show that swelling increased with fluence due to continued void nucleation at 500 to 525°C with little additional growth, whereas by contrast continued void growth caused swelling to increase with fluence at 625 to 630°C. Figure 47 also shows that precipitation at both temperatures paralleled the void development trends; the growth of precipitate particles and their associated voids seem correlated.

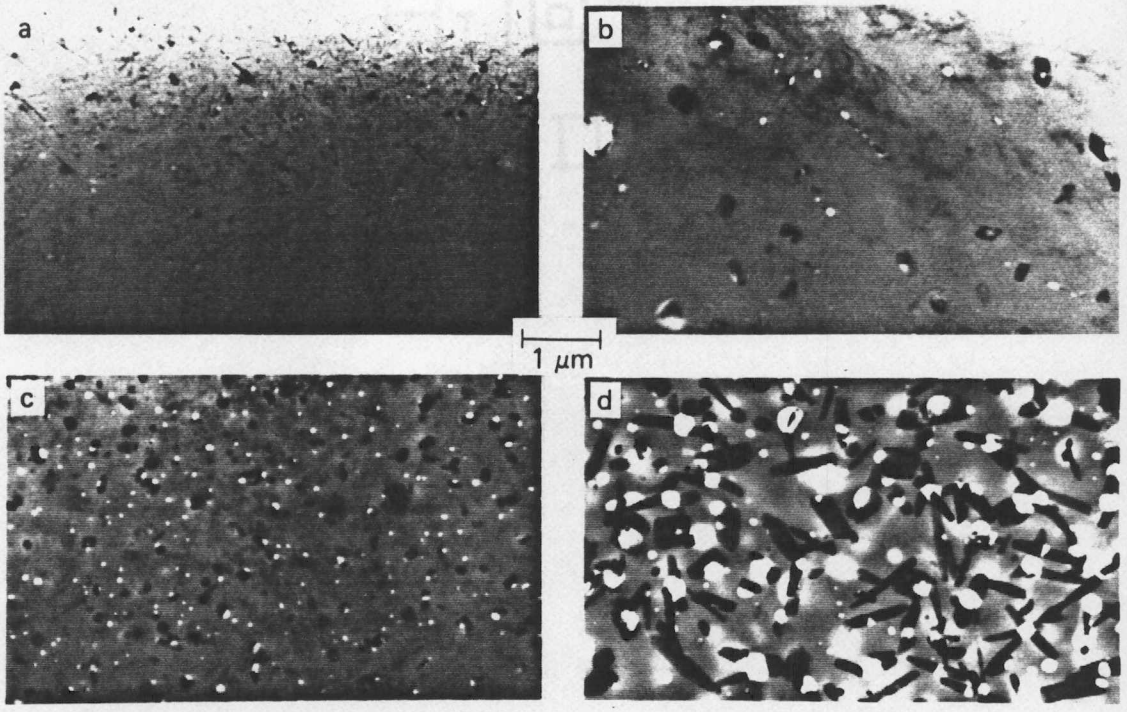

Fig. 47. Void evolution in SA (DO-heat) 316, irradiated in EBR-II at (a) 500°C, (b) 625°C to 8.4 dpa, (c) 525°C to 31 dpa, and (d) 630°C to 36 dpa. Void swellings are (a) 0.05%, (b) 0.16%, (c) 0.27%, and (d) 1.5%.

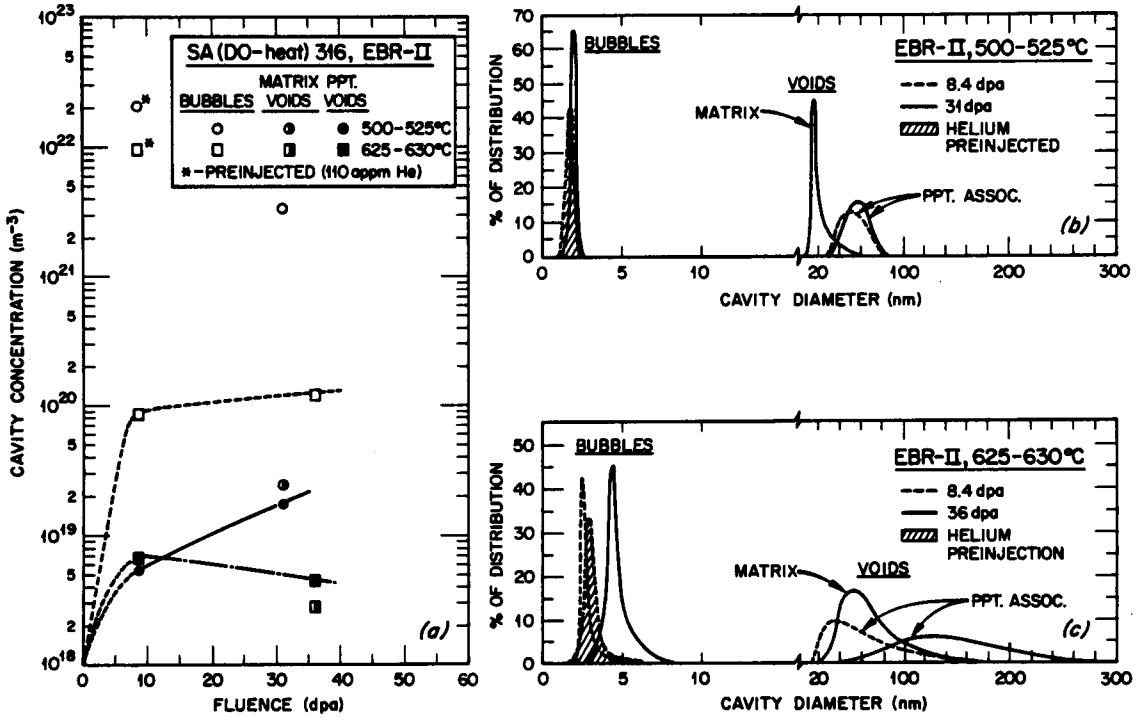

Fig. 48. Cavity microstructural evolution in EBR-II-irradiated SA (DO-heat) 316 at 500 to 630°C, showing (a) bubbles, matrix voids, and precipitate-associated void concentrations as functions of fluence, and (b,c) size distributions of bubbles and voids at 500 to 525°C and 625 to 630°C, respectively. Data for helium preinjected samples are also included. Data can be found in Table 11.

Bubble development was observed among voids under all conditions, except at 500°C and 8.4 dpa (Fig. 48), and these bubbles most likely serve as void nuclei. A fine, dense, and uniform dispersion of bubbles appeared after 31 dpa at 525°C [Figs. 48(a,b) and 49]; others observe bubbles only above 600°C.[38-40] Bubbles at 625 to 630°C were distributed only along some dislocation lines after 8.4 dpa [Fig. 50(a)], but then many more were found in the matrix as well as at dislocations at higher fluence. The broadened bubble size distribution that accompanied bubble growth with fluence in Fig. 48(c) suggests additional nucleation as well,

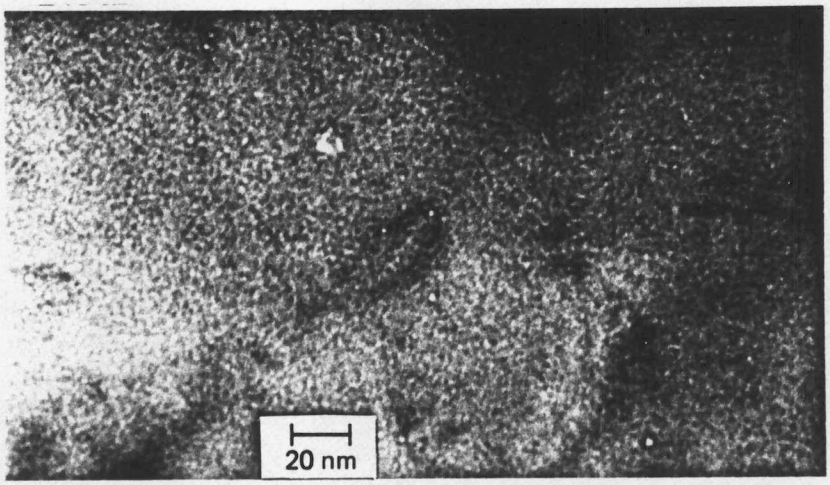

Fig. 49. Fine matrix bubbles observed in SA (DO-heat) 316 irradiated in EBR-II at 525°C to 31 dpa.

consistent with Fig. 48(a). Indeed, the configuration of bubbles in trails near dislocations, with a size gradient such that the smallest ones are nearest the dislocations [Fig. 50(b)], suggests that the bubbles were formed and then released by migrating dislocations.

Precipitation

A. Microstructural Data

Small amounts (PVF) of precipitation occurred at 500 to 630°C after 8.4 dpa, and the amounts progressively increased with fluence, with a larger increase at the higher temperatures (Table 12 and Figs. 47 and 51). The relative amounts of Laves and M_6C (η) were nearly equal at 630°C and 36 dpa, but η dominated at all other conditions (better seen in Table 12 than in Fig. 51); $M_{23}C_6$ was conspicuously absent compared to aged material (cf. Fig. 32, p. 147, and Fig. 51). Minor amounts of

Table 12. Precipitate Microstructural Data for SA 316 Irradiated in EBR-II

Irradiation Temperature (°C)	Displacement Damage Level (dpa)	Helium Content (at. ppm)	Phases	Size[a] (nm)	Concentration (m^{-3})	Relative Phase Fraction (%)	Total Volume Fraction (%)
500	8.4	5	γ' (Ni_3Si)	20–40[b]	$0.6–1.8 \times 10^{19}$	4.5	0.4
			A+B Phosphides	120–1000[c]	$10^{20}–10^{21}$	20	
			η (M_6C)	70–110[b]	$0.4–1.1 \times 10^{19}$	62	
			G			12.5	
500	8.4	5+110 PI[d]	None				
525	31	19	A+B Phosphides	54[c]	5.5×10^{19}	7	1.4
			η	100–130[b]	2.4×10^{19}	93	
625	8.4	5	B Phosphide	160–1000[c]	1.2×10^{19}	17	0.4
			Laves			17	
			η	243[b]	3.8×10^{18}	66	
625	8.4	5+110 PI	η	284[b]	3×10^{19}	30	2.5
			Laves [+τ ($M_{23}C_6$) + σ][f]	660[e]		70	
630	36	22	η	300[b]	1.1×10^{19}	60	2.6±1.3
			Laves	700[g] 500–600[e]		40	

[a]Maximum linear dimension (typical shapes for other dimensions can be seen in Appendix A).

[b]Blocky or platelike morphology.

[c]Thin rod or lath morphology.

[d]PI — Preinjected helium.

[e]Thicker, wider lath morphology for Laves (see Appendix A).

[f]These phases are found at grain boundaries.

[g]Thick rod morphology for both phases.

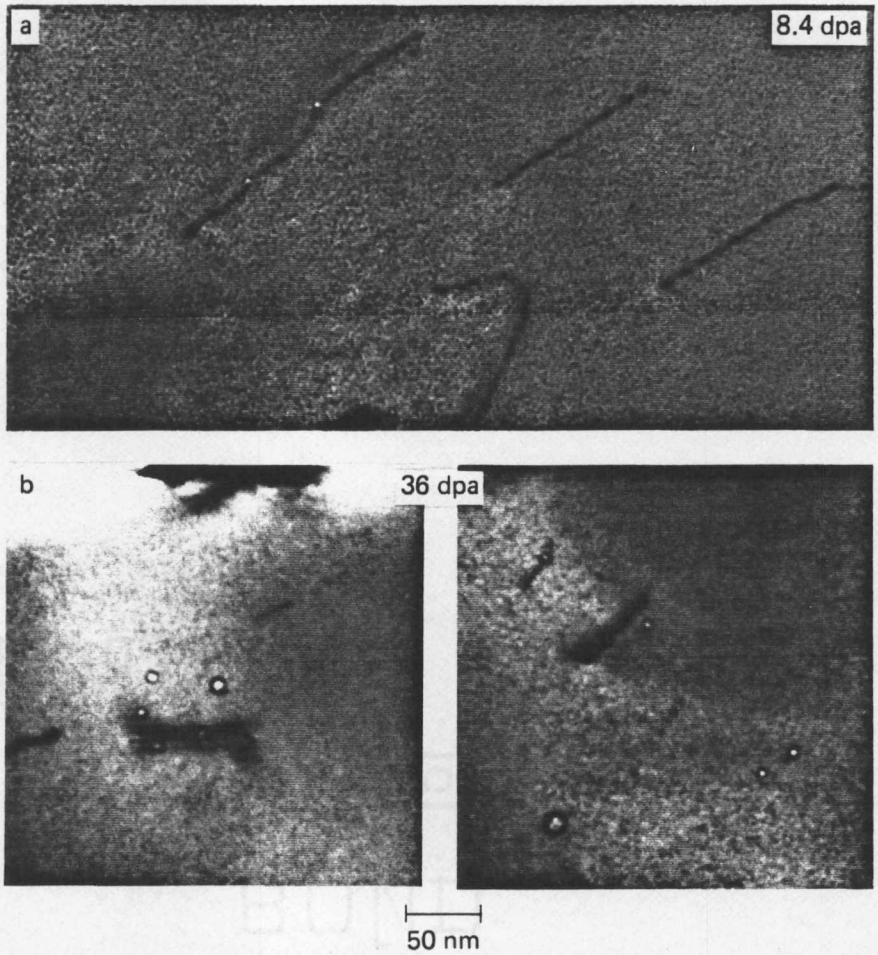

Fig. 50. Bubble development in SA (DO-heat) 316 irradiated at 625 to 630°C in EBR-II to (a) 8.4 dpa and (b) 36 dpa. Several small bubbles were found at some of the dislocations in (a), but in (b) many more bubbles are found at and near dislocations. Size gradients were seen in (b), with the smallest bubbles at the dislocations, which suggests that bubbles form at dislocations and are then released as the dislocations migrate.

irradiation-induced phases (G and γ' and/or phosphides A + B) were found in all samples, except the one at 630°C and 36 dpa. Others investigating SA 316 find no G phase and find no γ' at fluences less than 30 to 40 dpa.[223,297,402,417]

Enhanced formation of η phase at the expense of τ is in disagreement with other work that indicates τ as the major

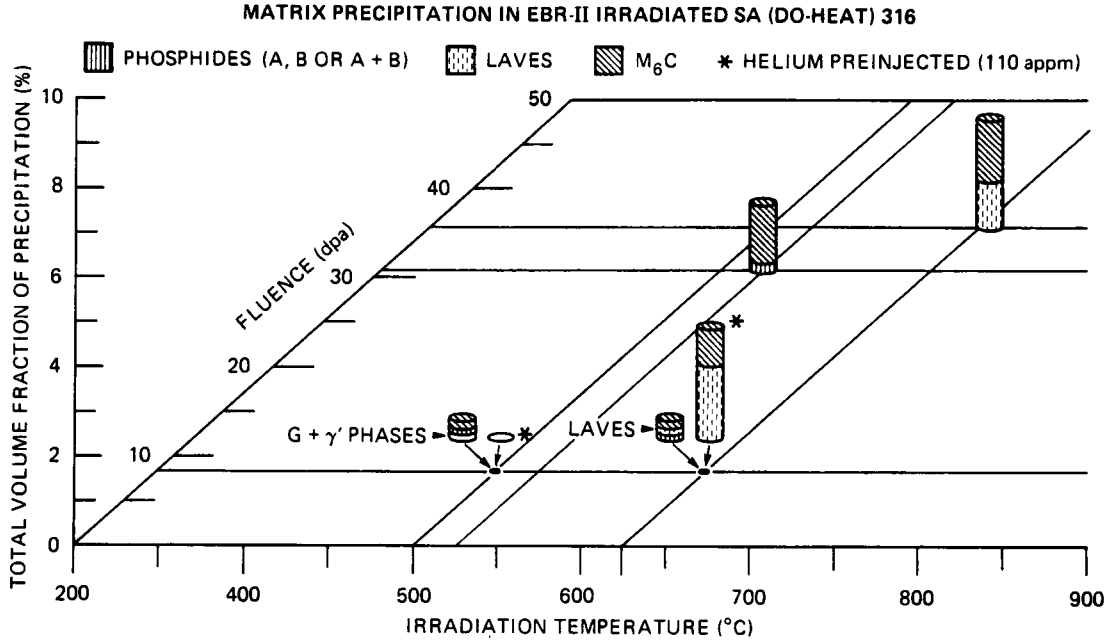

Fig. 51. A plot of relative and total phase volume fraction for matrix precipitation as functions of temperature and fluence for EBR-II-irradiated SA (DO-heat) 316. Samples preinjected with helium are also included. Data can also be found in Table 12.

phase,[38-40,116,222,223,297] or that suggest that τ transforms to η,[116,297-300,426] but does agree with Brun et al.[306] and Williams.[402] These two phases were clearly distinguishable by their crystal structures and habits (see Appendix B). The η (001) ZAP revealed the missing (200) reflections that verify the diamond cubic structure (see Appendix B); somehow, however, diffraction was nonideal because these reflections were not extinct on other ZAPs. Further, the matrix η particles always had an irregular crystal habit, in contrast to the regular epitaxial relationship found for τ (occasional particles found only at grain boundaries), even under irradiation (see Appendix B).

Evidence for two phosphide phases came mainly from compositional information because electron diffraction on particles of this phase was

quite difficult. Electron diffraction did, however, indicate that neither phase was Laves, and supported the possibilities of Fe_2P and/or Fe_3P phases. Both phosphides had needle morphologies, with needle axes parallel to orthogonal <001> or <011> austenitic crystal directions (see Appendix A), but the needles were A phosphides at lower temperatures and B phosphides at higher temperatures. Many investigators have observed, but have not identified, acicular needles in irradiated SA 316;[38-40,116,414] others have identified <001> acicular needles as Fe_2P (ref. 364) and Cr_3P (ref. 365) in unirradiated steels.

Microstructurally, precipitate particles were larger and more abundant in EBR-II irradiated compared to aged material, but more so at lower than at higher temperatures (cf. Fig. 34, p. 149, and Fig. 52); the phosphide needles contribute most to the difference. Phosphide needle growth was fairly insensitive to temperature at 8.4 dpa, but these needles shrank at 500 to 525°C and apparently dissolved at 625 to 630°C as fluence increased [Table 12 and Fig. 52(b)]. The high concentration of needles at 8.4 dpa decreased markedly with fluence, to suggest that the phosphides were also becoming unstable at 500 to 525°C. By contrast, η phase was stable and particle evolution paralleled void development. Eta particles grew larger at higher temperatures, particularly at higher fluence [Fig. 52(a)]. At 500 to 525°C, blocky η nucleation continued with fluence, whereas at 625 to 630°C, the concentration of blocky η particles remained fairly constant; thick rod-like particles of η and Laves replaced previous phosphide needles as fluence increased at 625 to 630°C [Fig. 47, p. 168, and Fig. 52(b)].

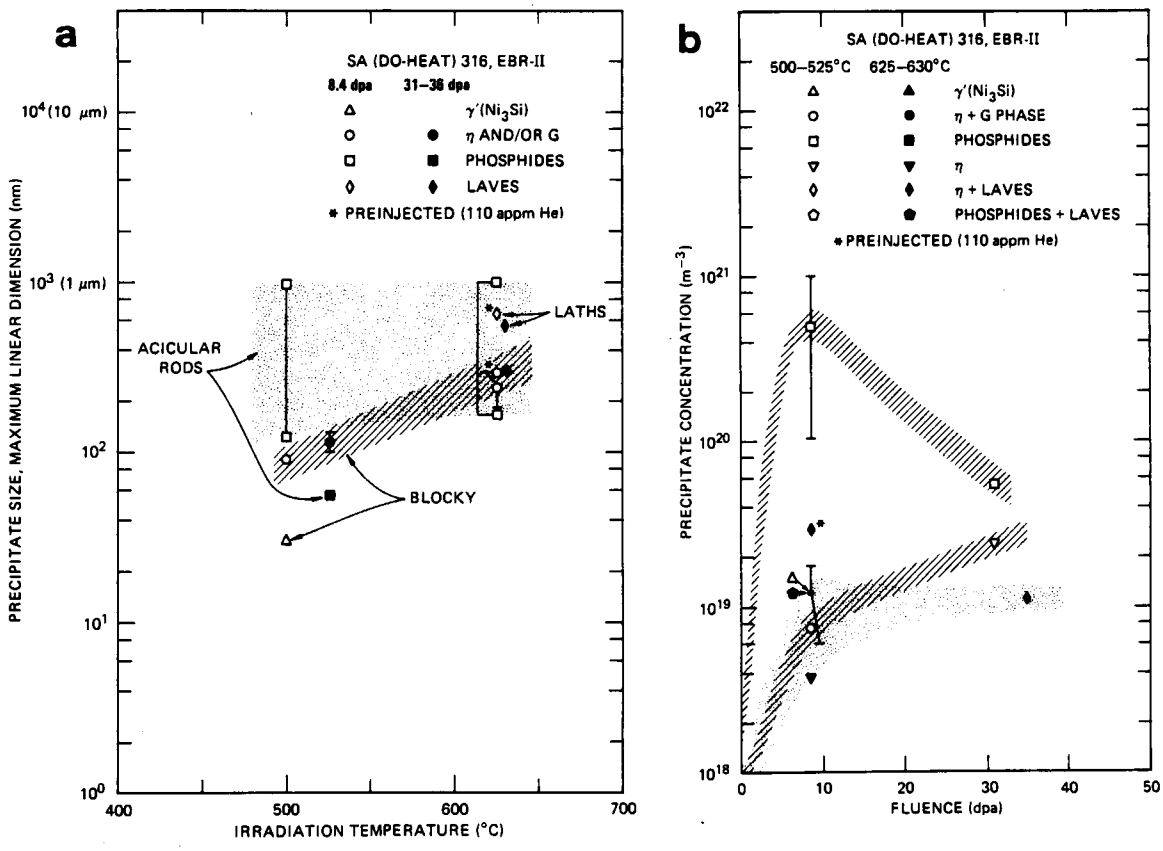

Fig. 52. (a) Particle size (d_p) (maximum linear dimension) for various morphological variants and (b) particle concentrations plotted as functions of temperature and fluence, respectively, for various phases formed in EBR-II irradiated SA (DO-heat) 316. Data for samples preinjected with helium are included. Data can also be found in Table 12.

Precipitation was much coarser in this work than reported by Brager and Straalsund,[38] but similar to data by Bloom and Stiegler.[40]

Compared to the clustered nucleation of precipitate particles that suggested site deficiency under aging, particle formation seemed quite easy under irradiation, particularly at sinks expected to experience RIS, like voids and inclusions. Figure 53 shows η phase growing around the large voids at 625°C and 8.4 dpa and radiation-induced

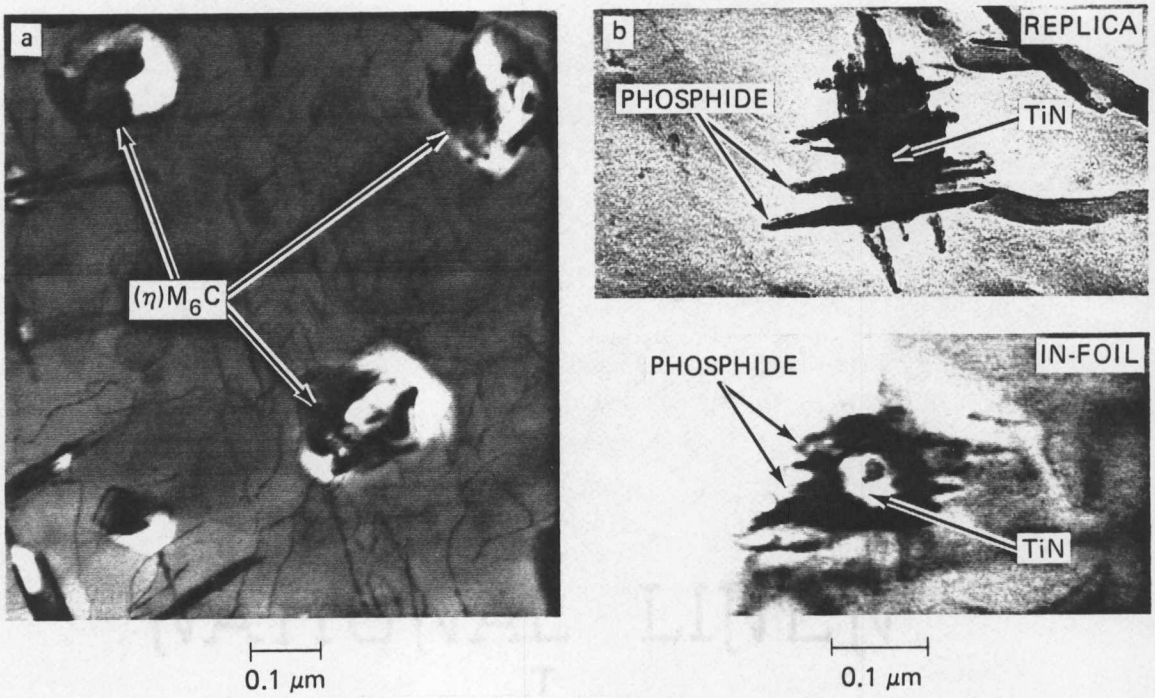

Fig. 53. Sympathetic nucleation and/or coupled growth of (a) M_6C (η) phase particles around voids, and (b) phosphide B needles clustered about TiN particles in SA 316 irradiated in EBR-II at 625°C to 8.4 dpa.

B phosphide encrusted around TiN particles. In the same sample, the largest phosphide or Laves laths were associated with larger voids [Fig. 47(d), p. 168], and at lower temperature, G phase particles seem to be found only in conjunction with voids (see Appendix A). Finally, at 630°C and 36 dpa clusters of several Laves rods formed around common voids. Together these data suggest an important role of sinks (i.e., voids) in precipitate formation and stability, probably as sites to sustain RIS.

B. Microcompositional Data

Under EBR-II irradiation, most phases were highly enriched in nickel and silicon and lower in molybdenum and chromium (Table 13 and Fig. 54) compared to thermal phases (Table 9, p. 151 and Fig. 37, p. 153); RIS therefore appeared to be the most dominant influence on precipitate phase formation and/or compositional alteration. Radiation-induced G and γ' (Ni_3Si) phases were most enriched in nickel and silicon, and G was uniquely rich in manganese. The radiation-modified η and Laves phases had higher nickel, much higher silicon and had lower molybdenum concentrations than did their thermal counterparts; however, chromium content was little affected in Laves and actually increased slightly in η. Compositions of γ', G, η, and Laves phases were consistent with or similar to data reported by others.[41,223,306,402,426] The phosphides, however, were peculiar for this work compared to others.

Both the A and B phosphides were incredibly rich in phosphorus ($\sim 10^3$ times more than the matrix level); they were primarily distinguishable on the basis of compositional differences. They were compositionally quite flexible, suggesting wide solubility limits, similar to Laves phase. Compositional differences were subtle at 500°C and 8.4 dpa, but the B phosphide always had less silicon and nickel and more iron than A (see Table 13); at 31 dpa and 525°C, greater compositional contrast developed, with the B phase having significantly more P, Mo, Cr, and Fe, but much less Ni and Si than A. There were clear morphological differences as well at 500 to 525°C, with the A phosphides being the familiar acicular needles while the B phosphides were small blocky

Table 13. XEDS Compositional Information for Matrix and Precipitate Phases in SA 316 Irradiated in EBR-II

Irradiation Temperature (°C)	Displacement Damage Level (dpa)	Helium Content (at. ppm)	Phases Analyzed [Number of Spectra]	Composition[a] (wt %) Si	P	Mo	Ti	V	Cr	Mn	Fe	Ni
			Precipitate Phase Analyses[b]									
500	8.4	5	[5] M_6C (η)	8.8(±0.5)	1	6.7(±1.5)		0.3	40(±1)	1.8	5.4(±1)	36(±2)
			[8] A Phosphide	8(±1)	13(±1)	9.6(±2.5)		0.3	25(±2.8)	3.6	15.7(±2.5)	25(±2.4)
			[3] B Phosphide	3.7(±0.7)	16(±1.4)	11.5(±3)		0.3	25.5(±1.6)	1.8	24(±2)	17.5(±1.3)
			[6] G	12.4(±1)	1	4.3(±2)			9.2(±0.6)	8.3(±1)	4.1(±0.2)	61(±2.6)
			[4] Broad beam analyses	7.3(±0.8)	2.3(±0.5)	8.3(±0.7)	3.7	0.6	32.8(±1.3)	7.6(±2)	14.7[c] (±1)	23[c] (±1.2)
525	31	19	[10] η	9(±1)	1	10(±5)	0.5	0.5	33.6(±4)	1.2	13.6(±3)	30.5(±3)
			[4] A Phosphide	15(±4)	17(±2)	9.7(±5)		0.3	9(±6)	1.2	8(±6.7)	40(±13.6)
			[2] B Phosphide	2(±0.2)	28(±0.5)	15(±3)		0.6	16(±1.3)	2	18(±0.4)	20(±2.5)
			[4][d] η	8(±0.6)	1	10(±4.6)		0.4	37.4(±4)	1	12.5(±3)	29.7(±2)
			[1][d] $M_{23}C_6$ (τ)	2.4	0.3	7.8		0.2	60.4	1.8	16.8	10.4
			[2] Broad beam analyses	8.1(±0.3)	0.8	9(±0.1)	0.8	0.2	35.2(±0.4)	1.4	13(±0.1)	31.7(±0.5)
625	8.4	5	[4] η	8.2(±0.7)	1.4	11.7(±1)		0.4	36(±0.8)	1.7	6.6(±0.8)	33.4(±1.2)
			[10] B Phosphide	5(±2.5)	16.3(±2.3)	20(±5)		0.3	20.4(±4)	2.6	20.5(±3)	15(±3)
			[9] Laves	8(±1.2)	1.4	26.5(±3.4)	0.6	0.3	19(±2.5)	3	24.5(±3)	17(±5.5)
			[3] Broad beam analyses	7.1(±0.7)	4.6(±2.6)	16.4(±1.5)	2.4	0.2	29.3(±2)	1.4	11.6(±2.7)	27(±3.6)
625	8.4	5+110 PI[e]	[5] η	8.3(±0.8)	0.2	17.7(±1.2)	0.4	1.2	32.8(±1.2)	1	8.7(±3)	29.4(±1.3)
			[2][d] η	7.8(±0.8)	0.3	19(±0.6)		0.8	31	1.1	10.8	29.4(±1.3)
			[2][d] τ	3.5(±1)	0.2	16(±0.6)	1	0.6	48(±0.8)	1.8	17.5(±3.7)	11.4(±4)
			[5] Laves	6(±0.6)	0.3	29(±1.4)		0.4	22(±2.1)	1.5	33(±1.6)	7.3(±0.8)
			[4] Broad beam analyses	5.8(±0.4)	0.7	24.8(±2)	0.5	0.5	26(±1.4)	1.8	27(±2)	12.5(±2)
630	36	22	[4] η	7.4(±0.3)	0.5	16.8(±1.7)	0.5	1	32(±0.3)	2	10(±1)	30(±1)
			[5] Laves	6.5(±0.5)	0.5	26(±0.7)	0.6	0.6	18(±0.6)	2.5	30(±1)	15.6(±1.3)
			[4] Broad beam analyses	4.7(±1.4)	0.5	17(±3.4)	0.3	0.5	26.8(±1.3)	2.1	21.8(±1)	26.5(±2.4)

Table 13 (continued)

Irradiation Temperature (°C)	Displacement Damage Level (dpa)	Helium Content (at. ppm)	Phases Analyzed [Number of Spectra]	Composition[a] (wt %) Si	P	Mo	Ti	V	Cr	Mn	Fe	Ni
				Matrix Analyses[f]								
525	31	19	[2] Near voids[g]	2.0		2			18.3	2.2	60.4	15
			[1] Near ppt-associated voids	1.8		3.5			21	2.2	60	11.5
			[3] In-between voids and ppts	2.2(±0.3)		3(±0.1)			20.7(±0.7)	2.2	59.4(±0.4)	12.4(±0.8)
625	8.4	5	[4] In-between voids	0.8(±0.5)		1.6(±0.3)			19.5(±1.4)	1.9	63.6(±1.4)	13.4(±1.5)
			[1] Near void[h]	1.2		1.9			20.5		65	11.9
625	8.4	5+110	[5] In-between ppts	0.8(±0.2)		1.6(±0.4)			19.3(±0.4)	2.7	62.4(±1)	13.1(±0.5)
630	36	22	[4] Near voids[g]	0.5(±0.3)		1.5(±0.3)			18.8(±0.5)	1.5	64.5(±1.5)	13.4(±2)
			[2] Near ppts	0.6(±0.1)		1.8			20.1(±0.5)	1.2	66(±1)	10.3(±1.5)
			[3] In-between ppts and voids	0.5(±0.2)		2.1(±0.4)			19.1(±0.7)	1.4	65.3(±0.2)	11.5(±1)
			[3] Broad beam analyses	0.8(±0.1)		2.3(±0.3)			18.3(±0.2)	1.5	64.7(±0.5)	12.3(±0.1)

[a]Includes elements with atomic numbers (Z) equal to or greater than Al (Z = 13).

[b]Unless otherwise indicated, analyses are for intergranular particles on extraction replicas.

[c]These are inconsistent with phase fractions determined using the other elemental values. These could be higher and lower, respectively, if there were matrix background on the replica.

[d]Grain boundary phase particles.

[e]PI = Preinjected helium.

[f]Unless otherwise indicated, these analyses were made in matrix, described below, and in spot mode.

[g]Small voids encompassed or nearly enclosed in the foil.

[h]Large voids that have been etched near foil edge.

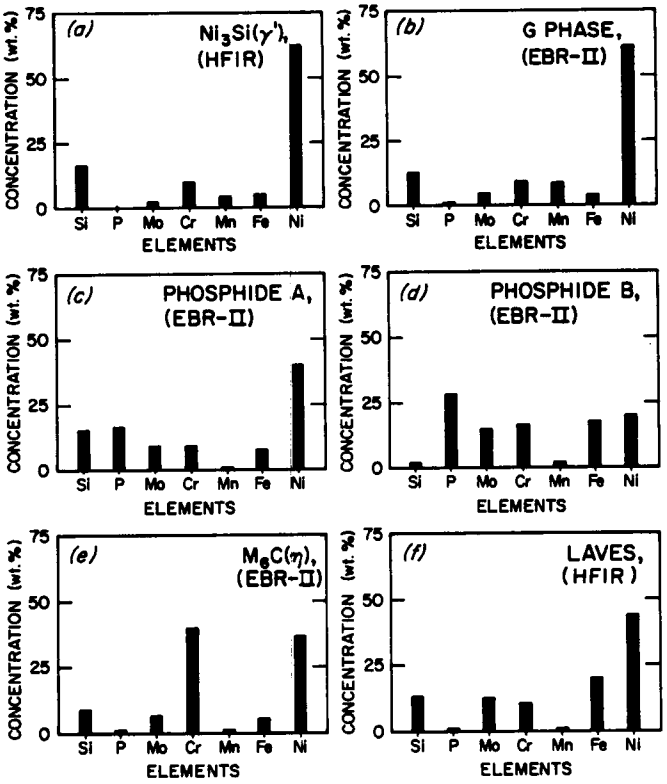

Fig. 54. Histograms of metallic element composition for the various radiation-induced or -modified phases formed in neutron-irradiated SA (DO-heat) 316. (a) γ' in HFIR at 425 to 450°C, 9.2 dpa, (b) G phase in EBR-II at 500°C, 8.4 dpa, (c),(d), and (e) phosphides and η in EBR-II at 525°C, 31 dpa, and (f) Laves in HFIR at 530 to 555°C, 47 dpa. All were analyzed on extraction replicas.

particles (Fig. 55). However, the acicular needles were now B instead of A phosphides at 625°C and 8.4 dpa (see Appendix A). These phases contain far more phosphorus than reported by either Lee et al.[41] or Bentley and Leitnaker[364] for the Fe_2P type phase. Both phases seemed to be radiation induced, but compositional coupling to RIS was less obvious for B.

The η and τ phases remained compositionally distinct under irradiation and quite similar to their thermal compositions (Table 13), a

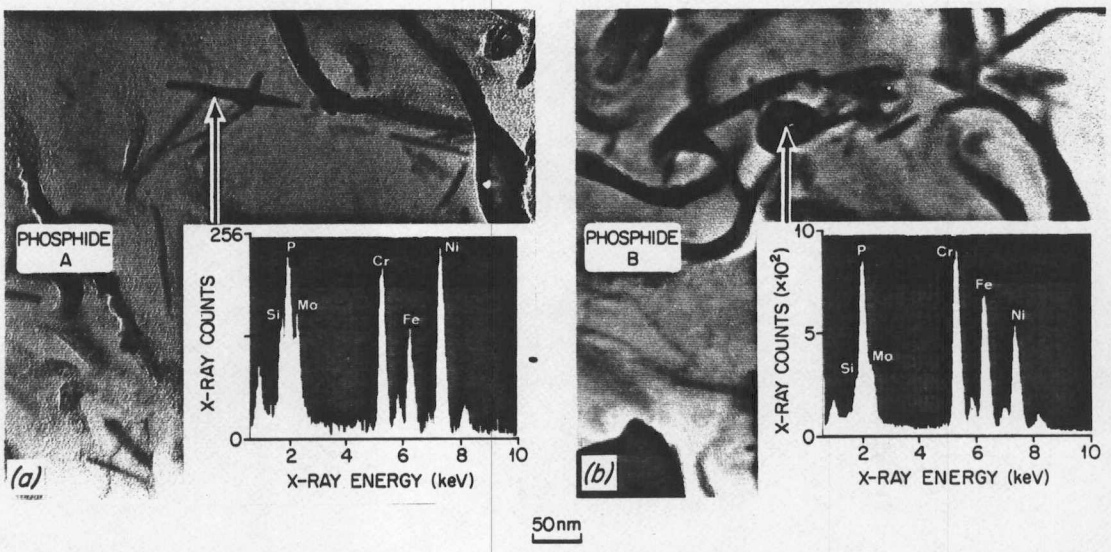

Fig. 55. Correlation between morphology and characteristic XEDS spectra which helped distinguish between phosphides A and B in SA (DO-heat) 316 irradiated in EBR-II at 500°C to 8.4 dpa. Similar correlations are found at higher fluence. Data are found in Table 13.

very important point for the claim that η was enhanced by irradiation at the expense of τ, compared to aged material. Particles of η were always found to be nickel- and silicon-rich, whereas τ particles, found only at 525°C sparsely at grain boundaries, were always depleted of these elements, even at 31 dpa (see Fig. 56). This strongly suggests that η was enhanced and τ retarded on the basis of their compositional compatibility couplings to RIS (positive and negative, respectively). These results agree with data by Brun et al.[306] and Williams,[402] but contradict observations by others that τ becomes nickel and silicon rich.[116,297-300,426]

The phases showed little compositional dependence on irradiation conditions, except for temperature sensitivity of molybdenum contents for the η and B phosphide phases and fluence sensitivity for the A phosphide

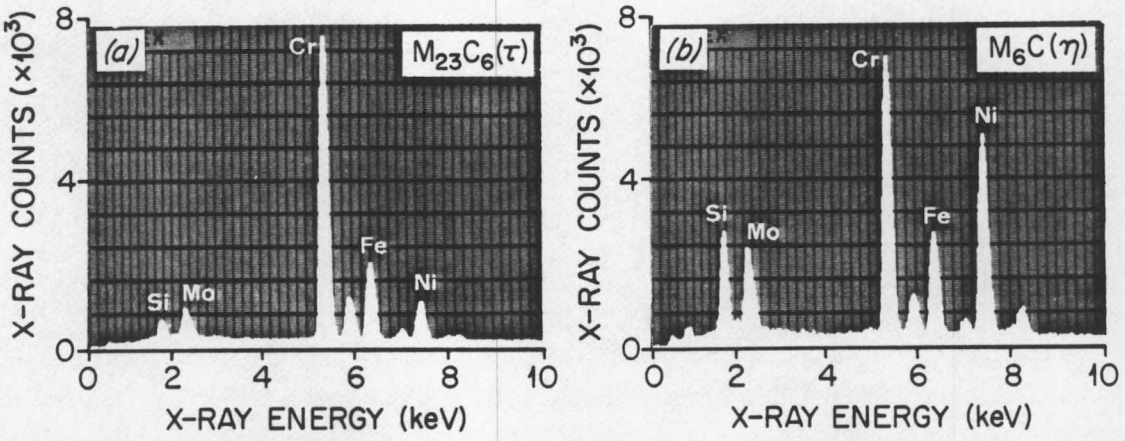

Fig. 56. Characteristic XEDS spectra of (a) $M_{23}C_6$ (τ) and (b) M_6C (η) particles found at grain boundaries on a replica produced from SA (DO-heat) 316 irradiated in EBR-II to 31 dpa at 525°C. Particles of η are always very nickel- and silicon-rich relative to τ.

phase (Table 13). The broad-beam overall precipitate composition similarly showed minor sensitivities, except for molybdenum (temperature dependence) and manganese and phosphorus (temperature and fluence dependencies) contents; the broad-beam compositions more reflected changing relative portions of phases than individual phase compositions (Table 13 and Fig. 57). The A phosphide became significantly richer in nickel and silicon but poorer in chromium and iron as fluence increased (Table 13). The molybdenum and nickel levels were altered by RIS in η produced under irradiation compared to thermal aging, but only the molybdenum level showed significant temperature sensitivity, increasing with irradiation temperature [Fig. 57(a)]. Behavior of the B phosphide for nickel and molybdenum was parallel to η.

Broad-beam compositions were generally similar to the η phase composition, reflecting its dominance, except at 630°C and 36 dpa where Laves precipitation caused the nickel to drop slightly with temperature

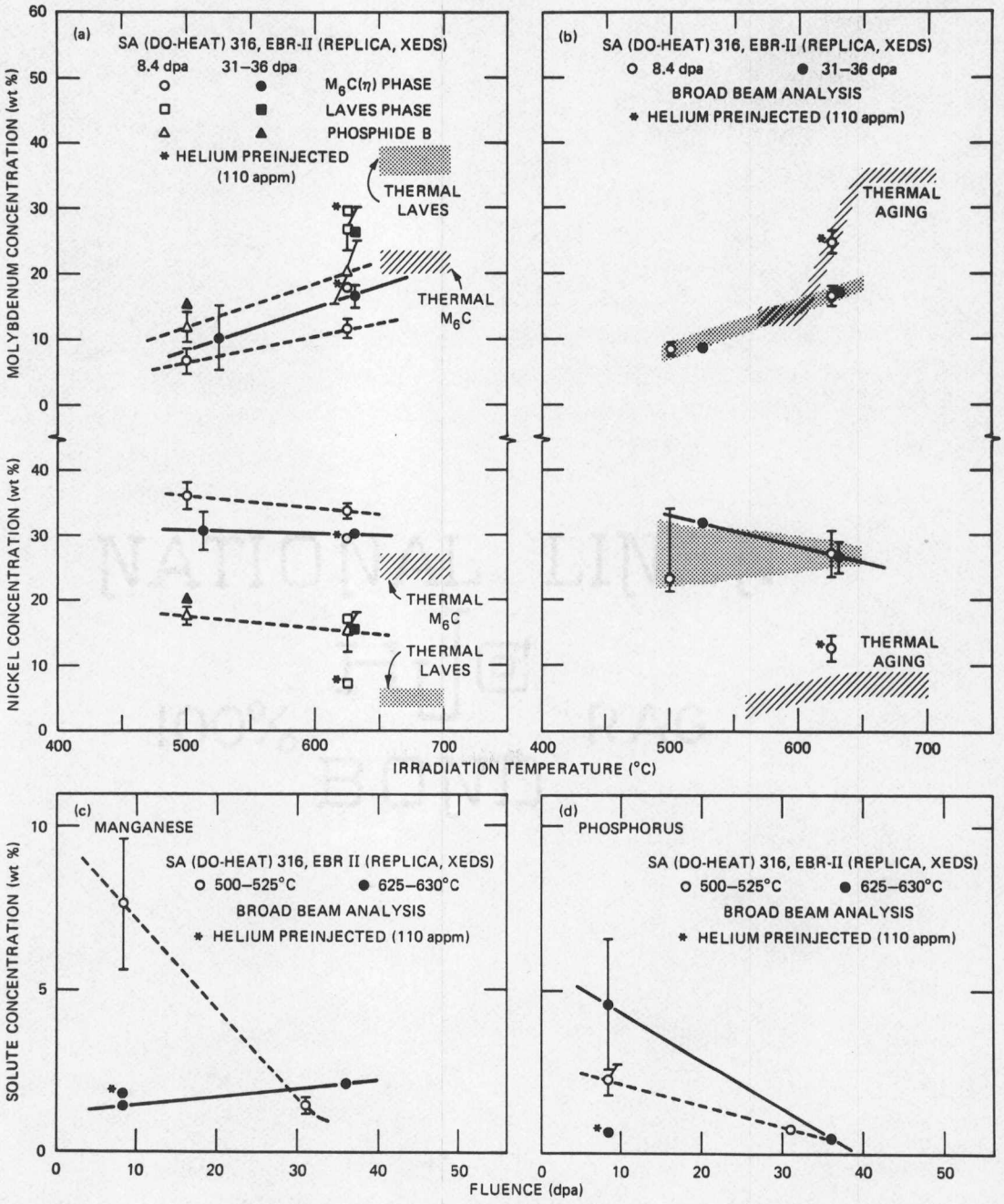

Fig. 57. Individual phase (a) and broad-beam whole precipitate (b–d) compositional analyses from XEDS performed on extraction replicas for molybdenum and nickel contents as functions of temperature (a,b) and manganese (c) and phosphorus (d) contents as functions of fluence. These results are for SA (DO-heat) 316 irradiated in EBR-II; compositional data can be found in Table 13, p. 178. Thermal aging trend bands are included from Table 9, p. 151, and Fig. 38, p. 154. Data on helium preinjected material are also included.

at 31 to 36 dpa [Fig. 57(b)]; however, nickel was always much higher than in thermal precipitation. Despite phase differences, molybdenum content was similar for irradiated and thermally aged broad-beam analyses at lower temperature, but was then depressed at higher irradiation temperatures as RIS reduced the molybdenum in both η and Laves phases. Manganese and phosphorus levels in the broad beams were initially high due to formation of the G and phosphide phases [Fig. 57(c),(d)], but then decreased with both temperature and fluence as these phases became unstable (remember that by contrast, phosphorus content of B phosphide increased with fluence). Phosphorus and manganese enrichments suggest these elements may be involved in RIS; Brimhall et al.[329] also have observed phosphorus segregation under irradiation. Correlation of these transient phases and elemental enrichments correlates with the disappearance of Frank loops from the dislocation structure, suggesting that loop formation and sustained, intense RIS may be coupled.

Finally, matrix XEDS analyses revealed local RIS effects near sinks under all conditions observed; however, the matrix in-between sinks was only perturbed at 630°C and 36 dpa where void formation and precipitation were maximum (Table 13, p. 178). Regions containing voids (which did not intersect the surface) were nickel-rich and molybdenum-poor relative to matrix in-between sinks. Regions near precipitate particles were always nickel-poor, but molybdenum contents varied with temperature; molybdenum was higher at 525°C than at 625 to 630°C. The matrix in-between sinks became lower in nickel (11.5 wt %) relative to unirradiated material (see Table 9, p. 151) only at 630°C after 36 dpa.

These data support the concepts of "microalloy" formation around sinks due to RIS and agree with LeNaour et al.[116] and Brun et al.[306] who also find nickel enrichment at voids; these data are also consistent with their suggestion that matrix nickel depletion either accompanies or follows void formation rather than preceding it.

Helium Preinjected and EBR-II-Irradiated SA 316

In general, data on preinjected SA 316 are new. Void formation was suppressed and loop evolution altered, consistent with the observations by Harkness et al.[46] (SA 304 with ~100 at. ppm He). Data revealing effects of preinjected helium on precipitation are new. Helium preinjection suppressed RIS, but apparently allowed thermal processes to be enhanced.

Dislocation Evolution

Helium preinjection eliminated network and caused a more refined loop structure to develop at 500°C relative to uninjected material; by contrast, loop formation was eliminated from the network in preinjected material at 625°C (Table 11, p. 166, Fig. 46, p. 167, and Fig. 58). Helium preinjection, however, only slightly reduced the total dislocation concentrations. The dislocation network was spatially nonuniform in preinjected material at 625°C; dislocations were heavily tangled around precipitate clusters with few found in-between.

Dislocation loops in helium preinjected material were larger and less concentrated under irradiation at 500°C than found under aging (cf. Table 10, p. 156, with Table 11, p. 166). Frank loops under irradiation

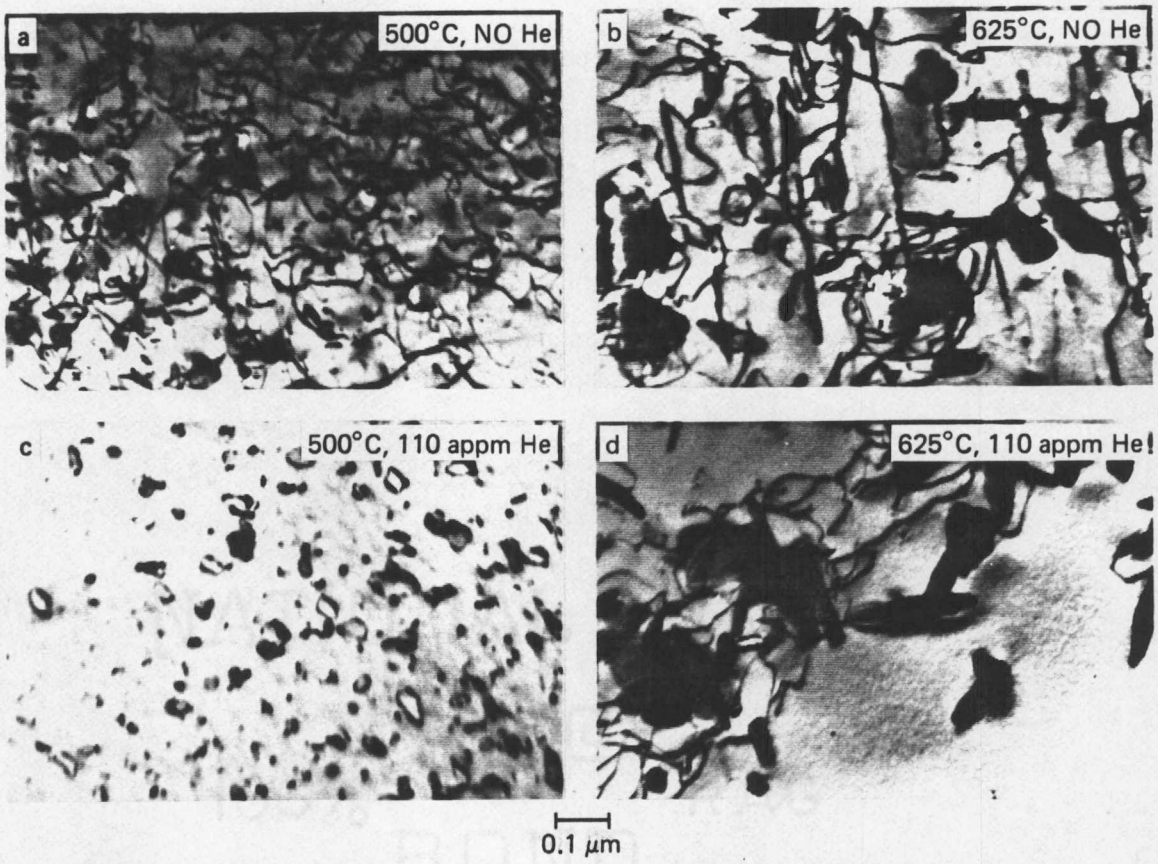

Fig. 58. The effects of 110 at. ppm preinjected helium on dislocation evolution in SA (DO-heat) 316 irradiated side by side in EBR-II to 8.4 dpa at 500°C (a,c) and at 625°C (b,d). Data can be found in Table 11, p. 166. Network and Frank loops were found in (a) and (b), whereas only Frank loops were found in (c). No loops were found in (d).

were also positively identified as interstitial type. Previous identification as prismatic loops by Maziasz[165] was incorrect. The total dislocation content was less (a factor of 4) and the interstitial content retained in loops was much less (a factor of 200) for irradiated compared to aged material. These results suggest that loop development in preinjected material was enhanced by irradiation at 500°C.

Cavity Evolution

Helium preinjection greatly enhanced bubble formation, but completely suppressed void formation, compared to uninjected material irradiated at 500 to 625°C (Table 11, p. 166; Fig. 48, p. 169, and Fig. 59). Bubble size under irradiation was little affected by the helium preinjection [Fig. 48(b), p. 170 and Fig. 60]. Bubbles appeared much earlier under irradiation at 500°C, due to preinjection, and were somewhat more concentrated than the bubbles that eventually did appear in uninjected material at higher fluence (Fig. 48, p. 169). At 625°C, however, helium preinjection greatly increased bubble nucleation (by ~10^2). Bubble nucleation in the preinjected and irradiated SA 316 was fairly temperature insensitive.

Bubble sizes and concentrations in the helium preinjected SA 316 were similar under irradiation at 625°C to material aged for 10,000 h at

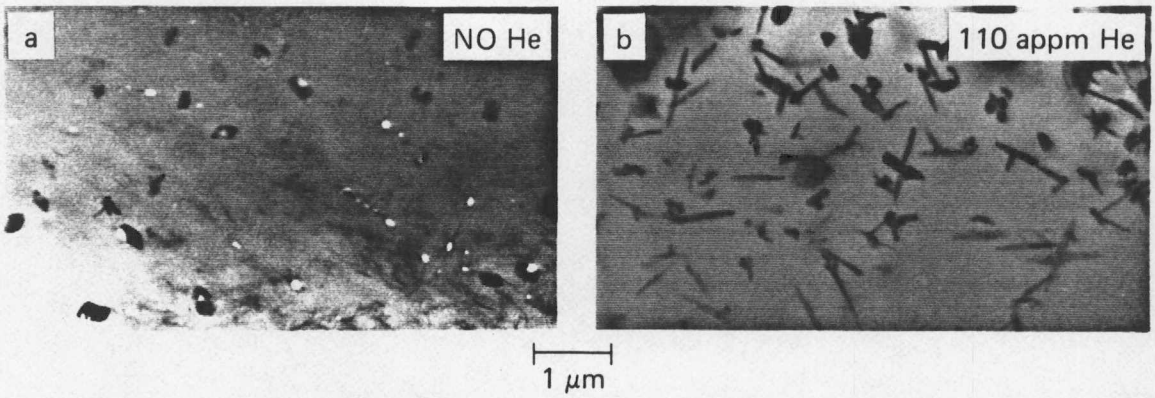

Fig. 59. The effect of preinjected helium on void formation and precipitation in SA (DO-heat) 316 irradiated side by side in EBR-II at 625°C to 8.4 dpa. Voids and irradiation induced precipitate phases were absent in (b). Precipitate microstructural data are found in Table 12, p. 171, and compositional data in Table 13, p. 178.

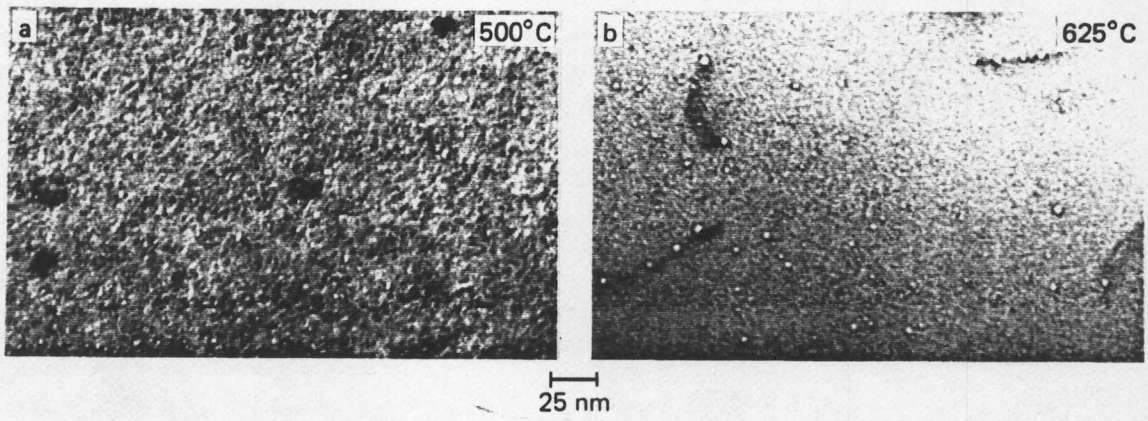

Fig. 60. The effect of irradiation temperature on bubble formation in helium preinjected SA (DO-heat) 316, irradiated in EBR-II to 8.4 dpa at (a) 500°C and (b) 625°C. Bubbles were slightly coarser at the higher temperature. Data can be found in Table 11, p. 166.

600°C (cf. Table 10, p. 156 with Table 11, p. 166). However, bubble formation was clearly enhanced by irradiation in the injected SA 316 at 500°C relative to aging. The bubbles contained more (but still not all) of the preinjected helium under irradiation than they did during aging (Table 11, p. 166).

Precipitation

A. Microstructural Data

Helium preinjection eliminated precipitation at 500°C, but enhanced it at 625°C, compared to uninjected material irradiated to 8.4 dpa (~3300 h) (see Table 12, p. 171, and Figs. 51, p. 173, and Fig. 59). At both temperatures, irradiation-induced phases did not form in the preinjected material; at 625°C, however, η formation was enhanced, and Laves formation greatly enhanced as a result of the helium preinjection

(Fig. 51, p. 173). At 625°C in preinjected SA 316, the relative proportions of η and Laves under irradiation were now similar to thermal precipitation found in uninjected material aged at 650°C; however $M_{23}C_6$ (τ) was still absent under irradiation in the matrix (but was found sparingly at grain boundaries together with σ) (see Table 12, p. 171, and cf. Figs. 51, p. 173 and 59).

Precipitate particles were much coarser, but only slightly more abundant in the preinjected material irradiated at 625°C; coarse Laves rods and laths replaced the fine phosphides found in uninjected material (Table 12, p. 171, and Figs. 52, p. 175, and 59). The precipitation in the preinjected material, however, did parallel phase evolution found at higher fluence in uninjected material irradiated at 630°C, or in uninjected material aged at 650°C (cf. Table 8, p. 144, with Table 12, p. 171, and Fig. 34, p. 149, with Fig. 52, p. 175). Two points are worth noting: (1) many precipitate particles again nucleated in clusters under irradiation in the preinjected material, just as they did in thermally aged material (cf. Fig. 36, p. 150, and Fig. 59); by contrast precipitate particles were discrete in the uninjected irradiated material. Again it seemed as though helium preinjection was somehow favoring thermal over irradiation-induced phenomena. (2) Although preinjection made precipitates coarser, precipitate-assisted void formation did not occur; this would suggest that crucial factors other than simply precipitate size influence operation of this important void formation mechanism.

B. Microcompositional Data

Compositionally, helium preinjection appeared to eliminate the effects of RIS on precipitation at 625°C, consistent with the disappearance of the irradiation-induced phases microstructurally at both temperatures. These effects were more subtle for the individual compositions of the η and Laves phases, but were more obvious in the broad beam compositions (Table 13, p. 178, and Fig. 57, p. 183). Contrary to the normal effects of RIS, helium preinjection resulted in slightly higher molybdenum (more so for η) and lower nickel (more so for Laves) concentrations in these phases, bringing them closer to their thermal compositions [Fig. 57(a), p. 183]. Again, broad-beam measurements revealed considerable molybdenum increase and nickel decrease in the precipitate due to the preinjection, causing a closer approach to thermally aged precipitation under irradiation than observed for uninjected material [Fig. 57(b)]. Consistently, phosphorus segregation was also removed because no phosphide phases were found [Fig. 57(d)]. These results together suggest suppressed RIS and enhanced thermal precipitate behavior. These data also support the suggestion that phosphorus was somehow involved with intense RIS in the uninjected material.

HFIR Irradiated SA 316

Cavity data on high fluence specimens are consistent with, but more detailed than previous work.[49,165,389,401] Lower fluence and temperature microstructural/compositional data are new, as are precipitate

microstructural data at higher fluence. Cavity and precipitate compositional data at 530 to 555°C and 47 dpa agree with data by Brager and Garner[227] on a duplicate specimen. Void and RIS/precipitate behavior in HFIR fell in-between the behavior extremes defined by EBR-II irradiation with and without preinjected helium due to intermediate levels of early bubble nucleation. Several other key results were observations of extremely nickel-rich Laves phase at 530 to 555°C and 47 dpa, coupled void and γ' (Ni_3Si) formation at 425 to 450°C, and void formation at 600 to 640°C with little effect of RIS on the precipitation. These results suggest that RIS and void formation are separable phenomena which are more tightly coupled at lower than at higher temperatures in HFIR.

Dislocation Evolution

Dislocation development in HFIR was generally similar to the trends observed in other reactors. Dislocation loops were found without network at 55 to 350°C. The structure progressed with increased temperature to loops plus network at 425 to 450°C, and then to solely network at ~500°C and above (Figs. 61 and 62; Table 14) for fluences less than 20 dpa. A mixture of "black-dot" and larger Frank loops was found at 55°C and 7.8 dpa (Fig. 63). Contrast behavior and 2½ D imaging suggested that the defects were all loops of similar, but yet unknown, nature. Others[111] observe "black-dot" loop damage below 300°C, but not the larger Frank loops.

"Black-dot" loop damage was no longer observed at 325 to 350°C, but Frank loop size (d_ℓ) was constant as both Frank loop (N_ℓ) and total

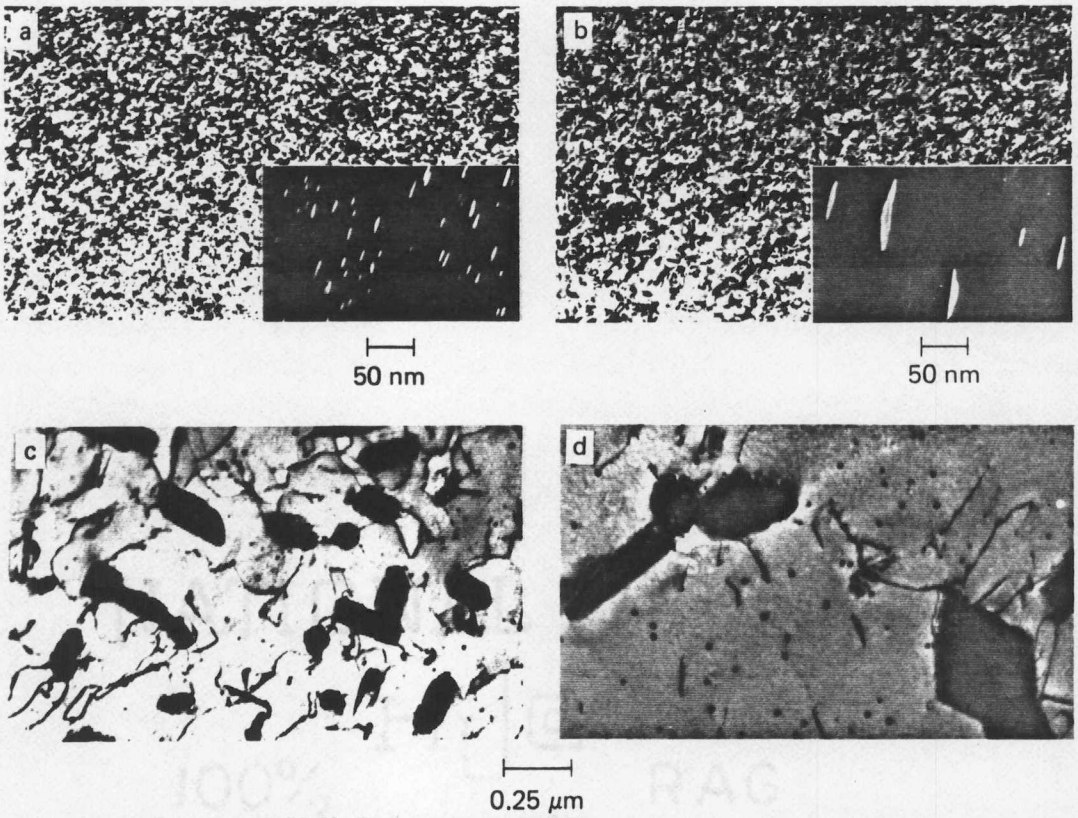

Fig. 61. Dislocation development with increased temperature for SA (DO-heat) 316 irradiated in HFIR to 5.3 to 12 dpa at (a) 325 to 350°C, (b) 425 to 450°C, (c) 515 to 540°C, and (d) 615 to 640°C. All large micrographs are at the same low magnification. (a) and (b) include higher magnification dark-field inlays of the Frank loops imaged with (111) stacking fault satellite streaks near g_{200}.

dislocation (Λ) concentrations increased somewhat from 55 to 350°C [Fig. 62(a–c)]. At 425 to 450°C, d_ℓ and N_ℓ decreased dramatically as network appeared, before loops were completely removed from the structure at higher temperature [Figs. 61(a,b) and 62(a–c)]. Network concentrations steeply declined from 350 to 640°C and above [Fig. 61(b–d) and Fig. 62(c)]; at the highest temperatures, where fluence dependencies were weak, dislocation densities in HFIR were similar to well-annealed

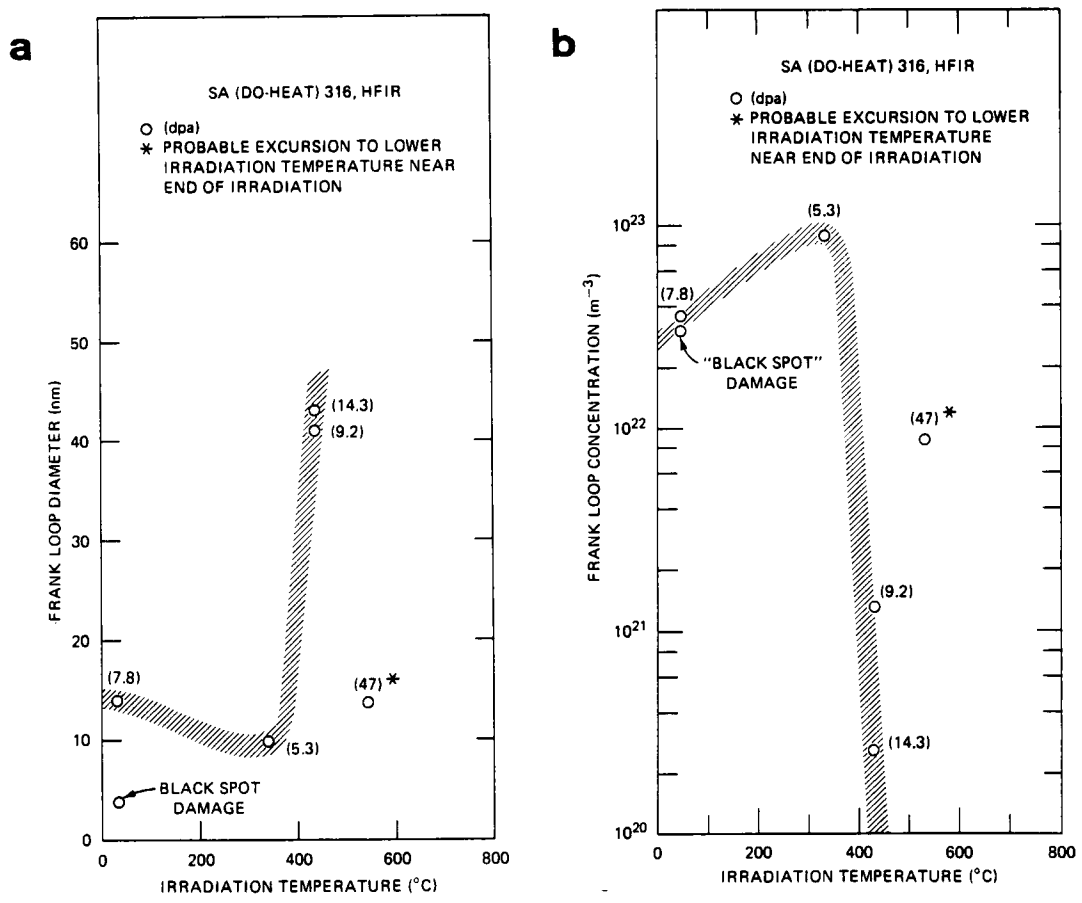

Fig. 62. Dislocation evolution in SA (DO-heat) 316 irradiated in HFIR with (a) loop diameter (d_ℓ), (b) loop concentration (N_ℓ), (c) total dislocation concentration (Λ) plotted as functions of temperature, and (d) Λ plotted as a function of fluence. Data can also be found in Table 14.

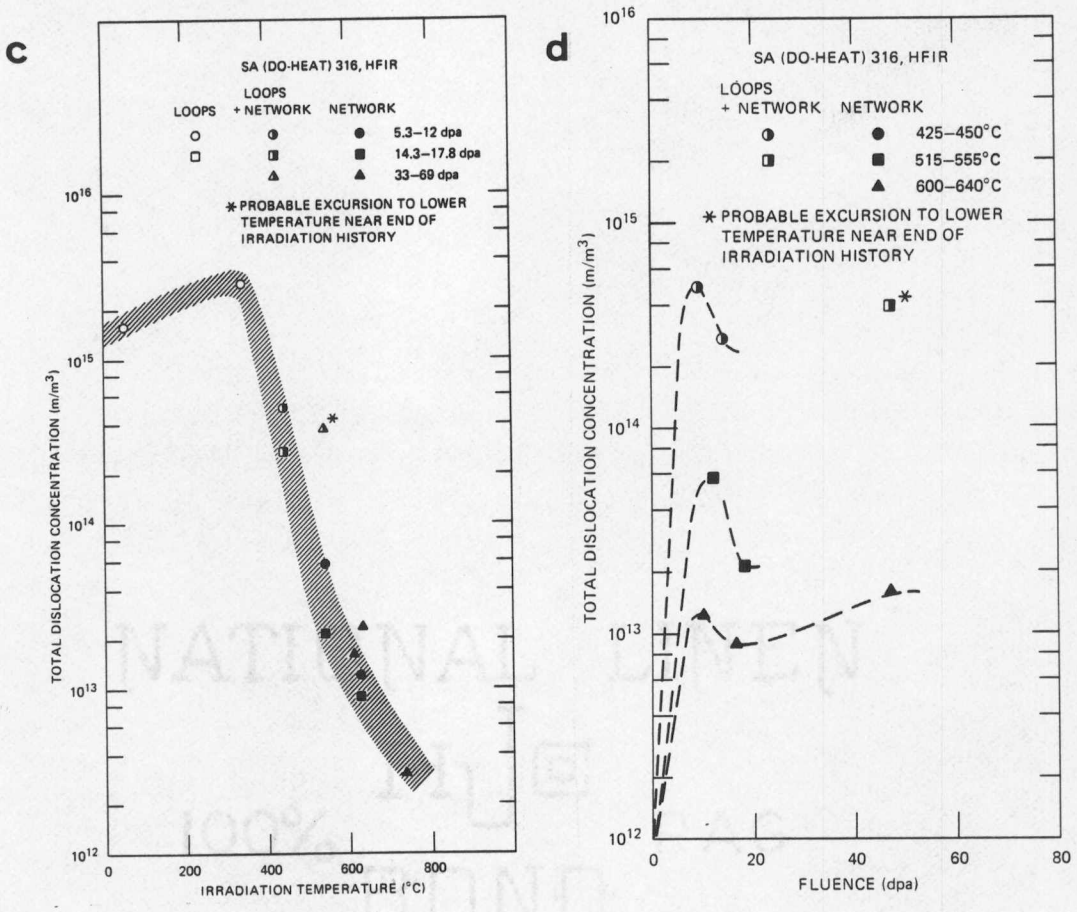

Fig. 62 (Continued)

material after ~69 dpa at 730 to 755°C. For loops, temperature sensitivities of d_ℓ and N_ℓ were much greater than those found in EBR-II[38-40] [cf. Figs. 6(a,b), p. 30, with Fig. 62(a,b)]; Λ's in HFIR were lower than found by others in EBR-II at 500 to 555°C [but similar to SA (DO-heat) 316 in EBR-II] and at 615 to 640°C [cf., Fig. 6(e), p. 31, Fig. 46, p. 167, and Fig. 62(c)]. HFIR dislocation data did, however, resemble long-term thermal aging data above 550°C [cf., Fig. 29, p. 143 and Fig. 62(c)].

Table 14. Dislocation and Cavity Microstructural Data for SA 316 Irradiated in HFIR

Irradiation Temperature (°C)	Displacement Damage (dpa)	Helium Content (at. ppm)	Dislocation Data				Cavity Data					
				Loops[a]								
			Network (m/m^3)	Diameter (nm)	Concentration (m^{-3})	Total Dislocation Concentration (m/m^3)	Type	Diameter (nm)	Concentration (m^{-3})	Helium Fraction[b]	Total Cavity Swelling (%)	Swelling[c] (%)
55	7.8	270		3.7[d] 14	3×10^{22} 3×10^{22}	1.6×10^{15}	None					
325–350	5.3	180		10	9.1×10^{22}	2.9×10^{15}	None					0.19
425–450	9.2	380	$2.4 \pm 0.1 \times 10^{14}$	41	1.3×10^{21}	4.9×10^{14}	Bubbles Voids	2.3 13.5	1.4×10^{22} 1.1×10^{21}	0.17 0.83(1.4)[e]	0.18±0.04	0.55
425–450	14.3	780	$2.4 \pm 0.3 \times 10^{14}$	43	2.5×10^{20}	2.7×10^{14}	Bubbles Matrix voids Ppt voids	1.6 21 34.5	1.1×10^{22} 4.3×10^{20} 1.4×10^{20}	0.03 0.48(1.3) 0.49(1.3)	0.65±0.3	1.2
515–540	12	600	$5.6 \pm 1 \times 10^{13}$			5.6×10^{13}	Bimodal	5.6 12.7	$5.1 \pm 1.4 \times 10^{21}$ 2.4×10^{20}	0.38 0.13	0.09±0.01	0.08
525–550	17.8	1020	$2.1 \pm 0.3 \times 10^{13}$			2.1×10^{13}	Bimodal	10.5 17.4	1.5×10^{21} 3.6×10^{20}	0.3 0.23	0.2±0.06	0.26
530–555	47	3000	[f]	13.7[g]	8.8×10^{21}	3.8×10^{14}	Bubbles[g] Matrix voids Ppt voids	2.2 35 76	2.7×10^{23} 1×10^{21} 3×10^{20}	0.36 0.237(4.3) 0.399(4.3)	9.7	
615–640	10	440	$1.2 \pm 0.1 \times 10^{13}$			1.2×10^{13}	Bubbles	18.7	1.8×10^{20}	0.3	0.07	0.12
615–640	16.6	880	$9 \pm 6 \times 10^{12}$			9×10^{12}	Bubbles	18.9	3.2×10^{20}	0.27	0.13	0.38
600–625	47	3000	$1.6 \pm 0.8 \times 10^{13}$			1.6×10^{13}	Matrix voids Ppt voids	50 335	4.5×10^{20} 1.2×10^{18}	0.88 0.12(1.8)	9.3±1.5	

Table 14 (continued)

Irradiation Temperature (°C)	Displacement Damage (dpa)	Helium Content (at. ppm)	Dislocation Data				Cavity Data					
				Loops[a]								
			Network (m/m^3)	Diameter (nm)	Concentration (m^{-3})	Total Dislocation Concentration (m/m^3)	Type	Diameter (nm)	Concentration (m^{-3})	Helium Fraction[b]	Total Cavity Swelling (%)	Swelling[c] (%)
580–605	64	4000					Matrix voids Ppt voids	60 300	1.7×10^{20} 4.2×10^{17}		4–5	
625–650	33.5	2000	2.4×10^{13}			2.4×10^{13}	Bubbles	60	1.6×10^{20}	0.74	$1.8 \pm 1.7(0.1)^h$	
730–755	53	3300					Bubbles	38.5	4.8×10^{20}	0.48	$1.8 \pm 1.8(0.1)$	
730–755	68.5	4140	3×10^{12}			3×10^{12}	Bubbles	110	4.6×10^{19}	0.32	$7.3 \pm 3.0(3.0)$	

[a]Identified as Frank interstitial loops, unless otherwise indicated.

[b]Fraction of the total helium contained in these cavities if they were equilibrium bubbles. Among both bubbles and voids, helium is first partitioned to the bubbles and then divided among the various void components, in proportion to their relative volume fractions. Numbers less than one indicate excess helium elsewhere in the system.

[c]Immersion density determinations made by M. L. Grossbeck, ORNL.

[d]"Black spot" damage, tentatively identified as loops, but nature unknown.

[e]Excess void volume compared to an equilibrium bubble with the same amount of partitioned helium.

[f]Network was difficult to image, but seemed quite low compared to loop component.

[g]Anomalous appearance of loops and fine bubbles at this temperature and fluence are at least in part due to excursion to lower temperatures and irradiation creep late in the irradiation history due to excessive swelling that caused the specimen to bend.

[h]Portion of the total percentage swelling that was due to large grain boundary cavities.

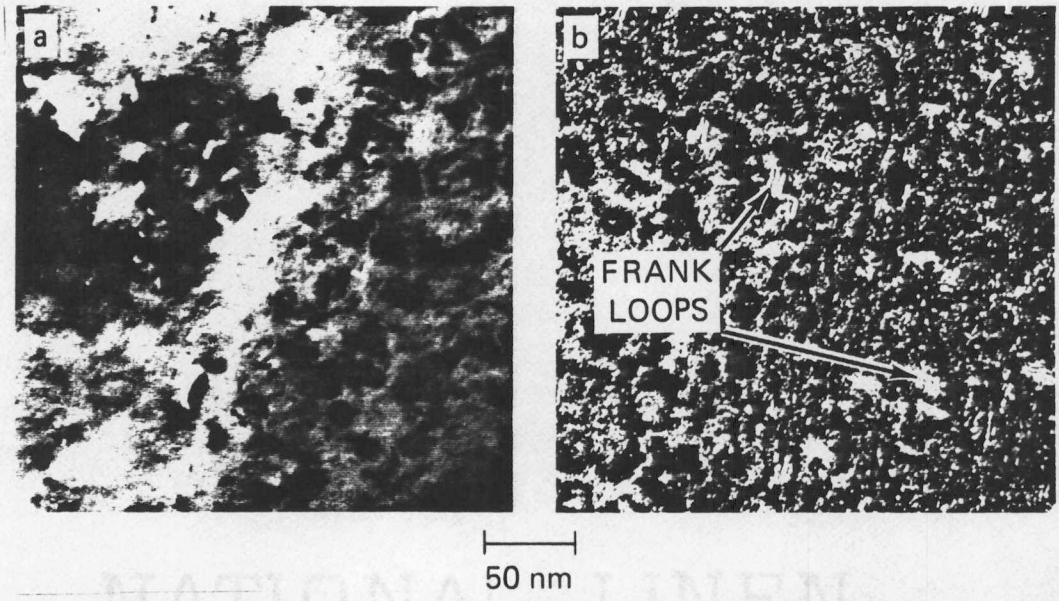

Fig. 63. Mixed Frank interstitial and "black-dot" loop damage in SA (DO-heat) 316 irradiated at 55°C to 7.8 dpa in HFIR. These are (a) bright-field, g_{200}, S = 0, and (b) weak beam dark field, g_{200} $+g/3_g$ micrographs of the same area.

Dislocation concentrations increased and peaked with fluence (<20 dpa) at levels that declined with temperature, but only tended toward saturation at 615 to 640°C and 47 dpa (at Λ = 1 to 2 × 10^{13} m/m^3) [Fig. 62(d)]. At 425 to 450°C, d_ℓ remained constant while loop N_ℓ decreased with fluence. Again, Λ behavior in HFIR was similar, but values were slightly lower than found by others in EBR-II[38,39,116] [cf. Fig. 6(f), p. 30, and Fig. 62(d)]; for SA (DO-heat) 316, values were initially lower in HFIR but then became similar to EBR-II with increased fluence [cf., Fig. 46, p. 167, and Fig. 62(d)]. The dislocation behavior in HFIR at 530 to 555°C and 47 dpa was, however, anomalous.

As indicated in Table 7, p. 131, only the specimen at 530 to 555°C and 47 dpa was bent, apparently due to excessive void swelling and sticking subassembly parts that did not accommodate the expansion. Many fine Frank loops plus network were found and Λ was very high; the loops were the key clue, since none occurred at lower fluence [Fig. 61(c) and 62(a-c)]. The loops suggest that the irradiation temperature was 100 to 150°C lower. Bending, to short-circuit the insulating gas gap that maintains the elevated temperature, should only have occurred after sufficient void swelling to generate the necessary stresses and, hence, near the end of the irradiation history. As will be seen later, behavior of the void and precipitate microstructural components suggests that most of the irradiation history was normal (Yang and Garner indicate the microstructural components can respond differently to temperature transients[57]).

In summary, the HFIR data compared to EBR-II data suggest increased helium generation has only the minor effect on dislocation evolution of loop eliminating loops at 500 to 650°C.

Cavity Evolution

Cavities formed at 425 to 450°C and above, but voids were only found at 425 to 450°C for fluences less than 20 dpa (Table 14 and Figs. 64 and 65). Bubbles were observed over the entire range of conditions except at 580 to 640°C and 47 to 64 dpa, where all cavities seemed to be voids. Low fluence swelling therefore peaked at 425 to 450°C, as matrix and precipitate-associated voids grew and coarsened amid a constant background of many fine bubbles present at ~9 to 14 dpa

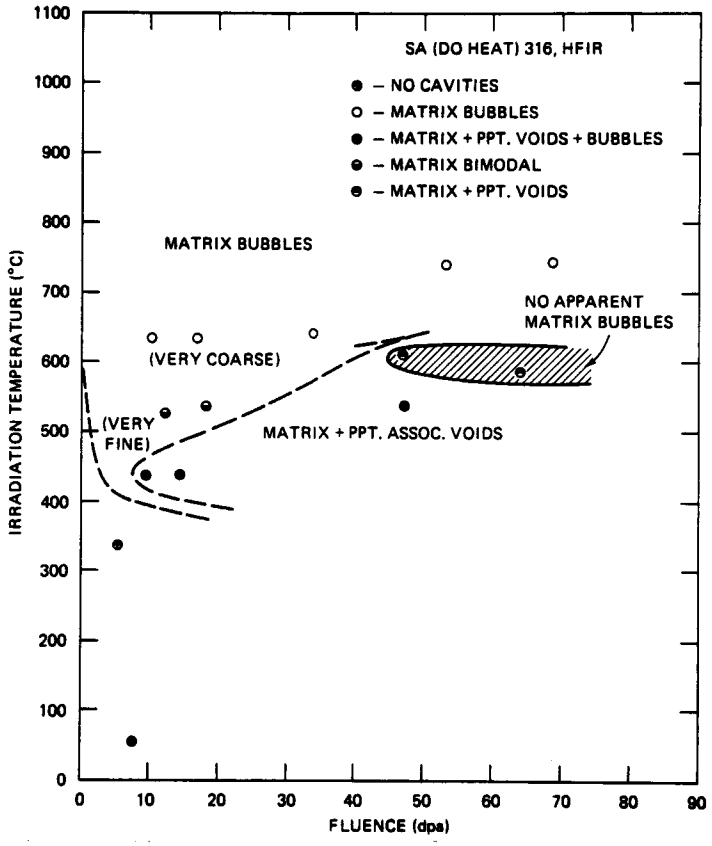

Fig. 64. Cavity character plotted as functions of temperature and fluence for HFIR irradiated SA (DO-heat) 316. Regions indicate combinations of fine and coarse bubble formation and matrix and precipitate-associated void formation. Data are also found in Table 14.

[Figs. 65(a), 66 and 67]. Void formation was delayed at 515 to 640°C, while bubbles formed and evolved in the interim (Figs. 64, 65, 67 and 68); as before, these cavities seemed to be bubbles because there is more helium than they can accommodate [by contrast, voids provide more than enough cavity volume (see Table 14)]. At 515 to 550°C, bimodal bubble distributions developed, grew, and coarsened with fluence, while at 600 to 640°C bubbles continued to nucleate into a single sized population, with little growth from 10 to 18 dpa [see Figs. 65(b,c), 67, and

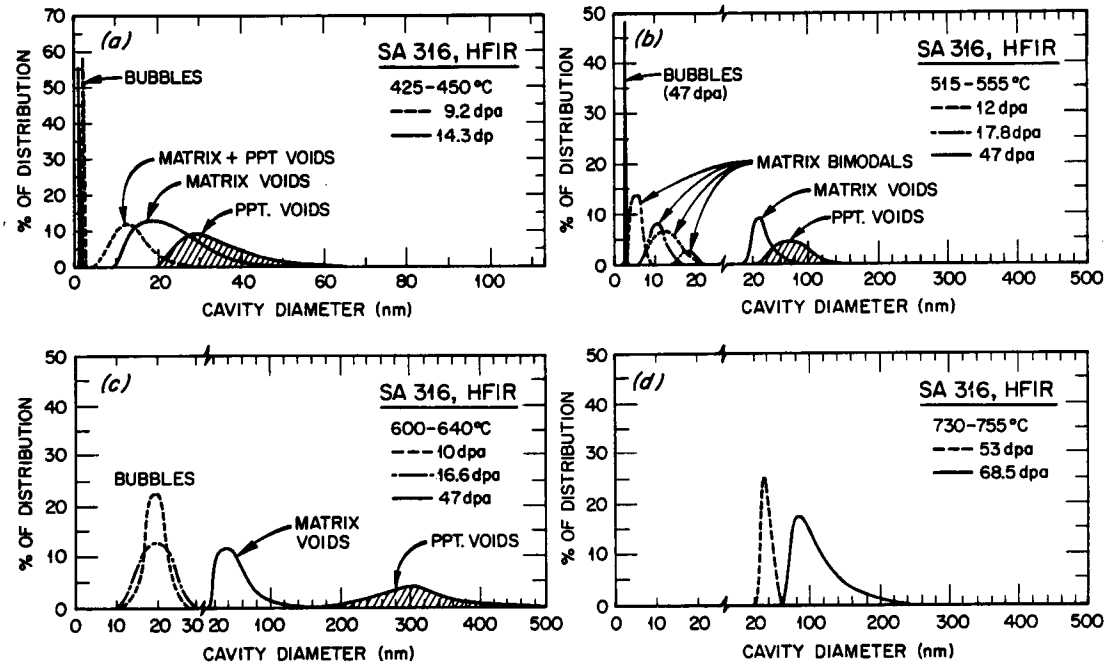

Fig. 65. Evolution of cavity sizes (d_b and d_v) and distributions with fluence increased for SA (DO-heat) 316 irradiated in HFIR at (a) 425 to 450°C, (b) 515 to 555°C, (c) 600 to 640°C, and (d) 730 to 755°C. Bubbles and matrix and precipitate-associated voids are distinguished. Precipitate-associated void formation ceased above ~650°C, and bimodal matrix cavity distributions were only observed at 515 to 555°C. Data can also be found in Table 14, p. 195.

and 68]. Bubble configurations at 515 to 550°C suggested that the bimodal was due to coalescence coarsening aided by migrating dislocations [Fig. 68(a)]. Despite the delay at 515 to 640°C, the bubbles eventually converted into abundant matrix and precipitate-associated voids after 47 dpa at 515 to 640°C. The voids had a normal coarsening relationship with temperature (Figs. 65 and 68). Finally, precipitate-assisted void swelling ceased above ~650°C, but was replaced by formation of large grain boundary and matrix cavities that behaved more like bubbles than voids [Figs. 64, 65(c,d), 67, 69, and 70]. High fluence swelling

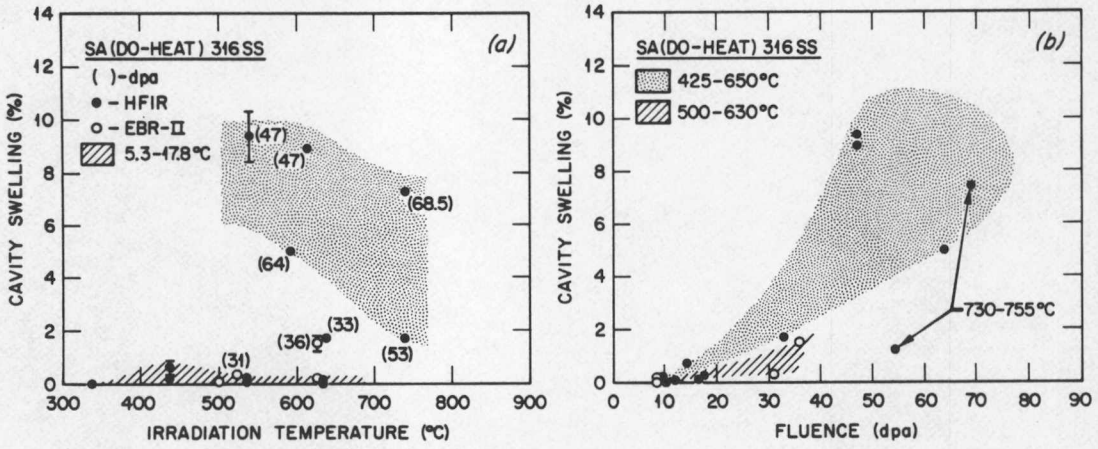

Fig. 66. Swelling plotted as functions of (a) temperature and (b) fluence for SA (DO-heat) 316 irradiated in HFIR. EBR-II data are also included for comparison. Swelling increases with fluence and appears maximum at 500 to 650°C. Swelling appears enhanced in HFIR compared to EBR-II at 500 to 650°C. Data are found in Tables 11 (p. 166) and 14.

therefore peaked at 500 to 650°C and developed rapidly due to voids, but continued more sluggishly at higher temperatures due to coarse bubble formation (Table 14 and Fig. 66).

Increased helium generation enhanced early bubble nucleation (by factors of from 2–5 to 10^2) in HFIR compared to EBR-II for SA (DO-heat) 316 irradiated at 500 to 630°C, but nowhere near the enhancement caused by helium preinjection in EBR-II [cf. Figs. 48(a), p. 169, and 67]. Early bubble nucleation, however, apparently caused a sufficiently cavity sink dominated system, so that early void formation in HFIR was suppressed relative to EBR-II (cf. Figs. 47, p. 168, and 68). Particularly important was the elimination of precipitate-assisted void formation, despite the many coarse precipitate particles present in HFIR, similar to the result obtained for helium preinjected material in EBR-II

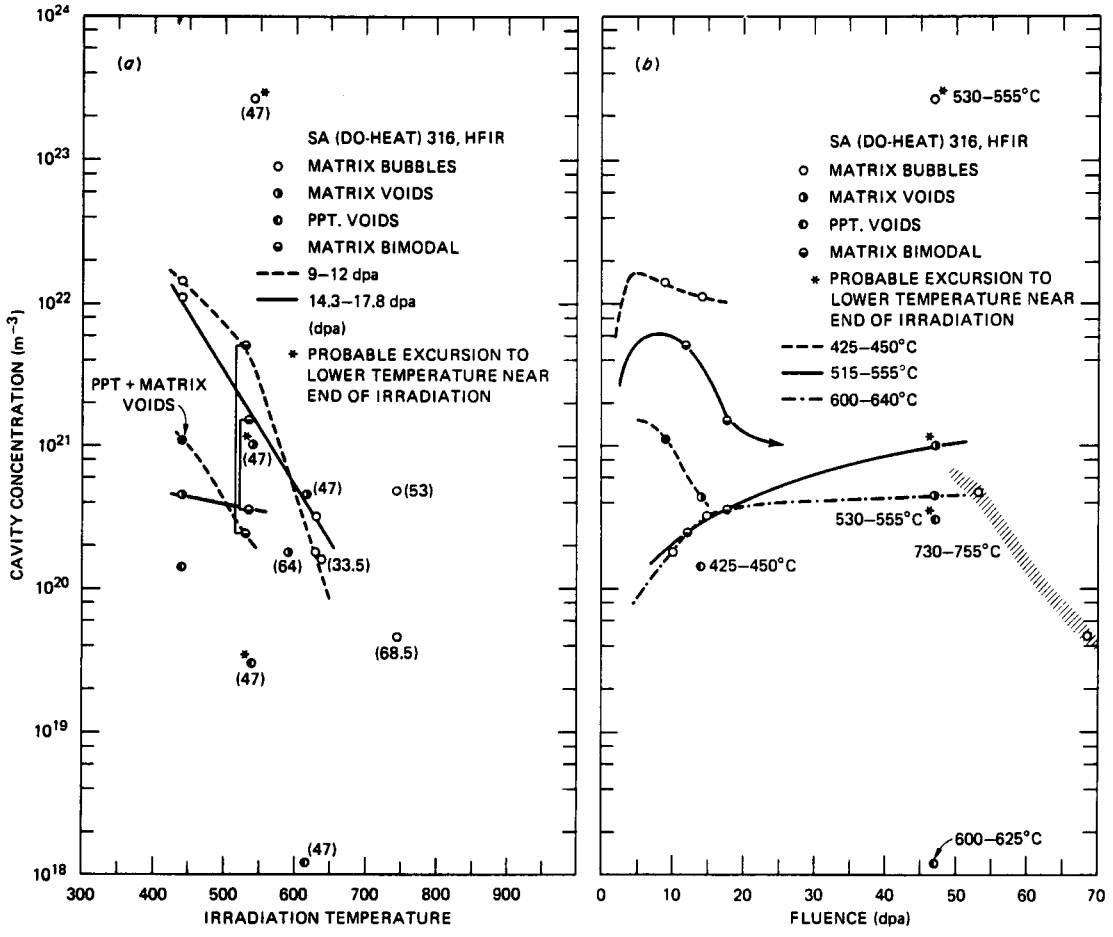

Fig. 67. Plots of concentrations of the various cavity components found in HFIR irradiated SA (DO-heat) 316 as functions of (a) irradiation temperature and (b) fluence. An abnormal irradiation history may be partially, but not completely, responsible for the anomalously high bubble concentration at 530 to 555°C and 47 dpa. Data are also found in Table 14, p. 195.

at 625°C. When helium bubbles became unstable and converted to voids in HFIR, matrix voids were more abundant and precipitate voids larger than found in EBR-II; swelling was thus enhanced in HFIR (Fig. 66). By contrast, voids strongly increased in size and decreased in concentration with increased temperatures[222] [see Fig. 10(a,c), p. 51]. Secondly, as in all previous cases with bubbles, the high temperature cavities again

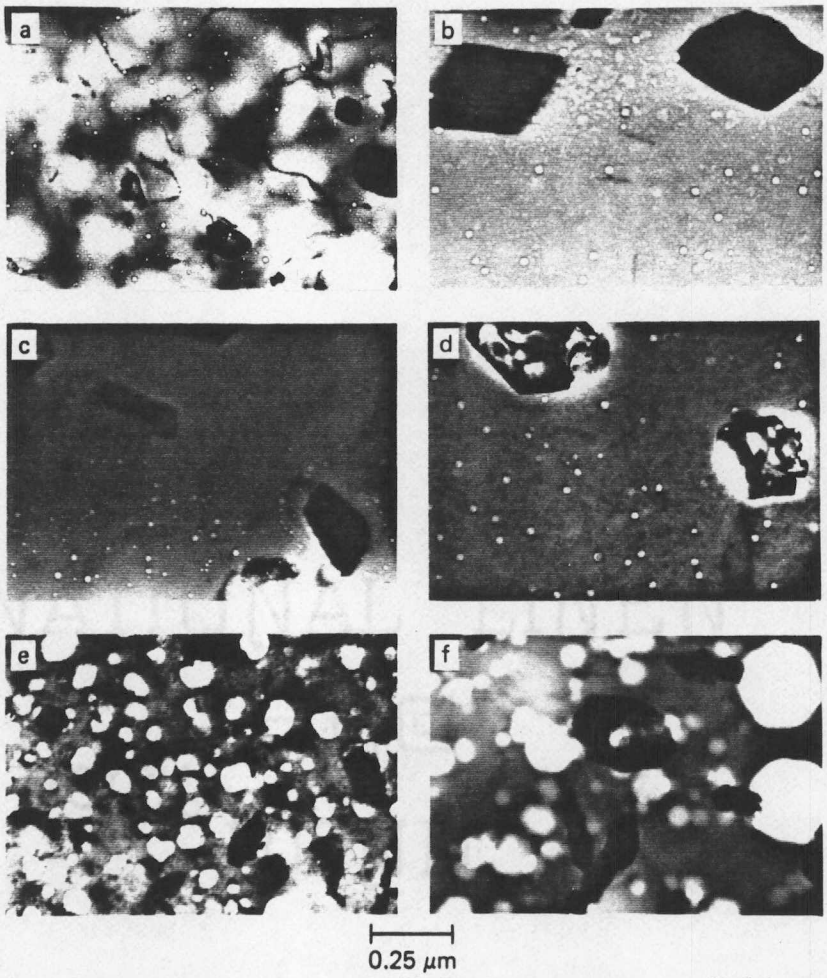

Fig. 68. Cavity evolution in SA (DO-heat) 316 irradiated in HFIR at 515 to 555°C (a,c,e) and 600 to 640°C (b,d,f) as functions of fluence; (a) 12 dpa, (b) 10 dpa, (c) 17.8 dpa, (d) 16.6 dpa, and (e),(f) 47 dpa. Voids were found only at the highest fluence. Data are found in Table 14.

cannot account for all the generated helium (Table 14, p. 195). Thirdly, matrix cavities at the higher temperatures were clearly smaller than corresponding grain boundary cavities; this is the usual relationship for bubbles, but is contrary to the relationship found for voids in either EBR-II or HFIR. Figure 70 indicates that increased helium generation tremendously increased the sizes and concentrations of grain

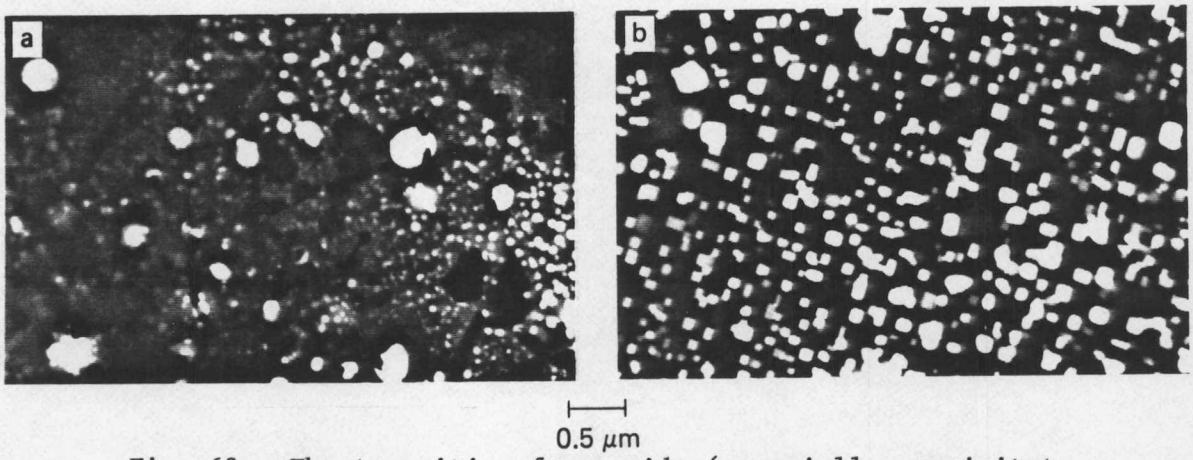

Fig. 69. The transition from voids (especially precipitate-associated voids) to coarse, high-temperature bubbles for SA (DO-heat) 316 irradiated in HFIR at (a) 580 to 605°C and (b) 730 to 755°C to 64 to 68.5 dpa and 4000 to 4140 at. ppm He.

boundary bubbles (comparing EBR-II and HFIR irradiated material at 600 to 630°C); increased temperature in HFIR further coarsened the grain boundary cavity structures. Finally, the matrix cavities at 730 to 755°C coarsened, apparently via coalescence as bubbles do rather than growing as voids [Figs. 65(d) and 67(b)]. Many of the cubic shaped cavities in Fig. 69 appeared to have coalesced along their orthogonal axes to form peculiar rectangular shapes, whereas at all other conditions in HFIR, cavities were equiaxed.

Lastly, we note the appearance of many fine bubbles among voids 530 to 555°C and 47 dpa in HFIR [mentioned earlier, see Figs. 65(b) 67, and 71]. Similar bubbles were found by Brager and Garner[227] in a duplicate of this same specimen. It is, however, unique to this work that these fine bubbles were not observed among the coarser bubbles which developed at low fluences. Unlike the loops found at 47 dpa,

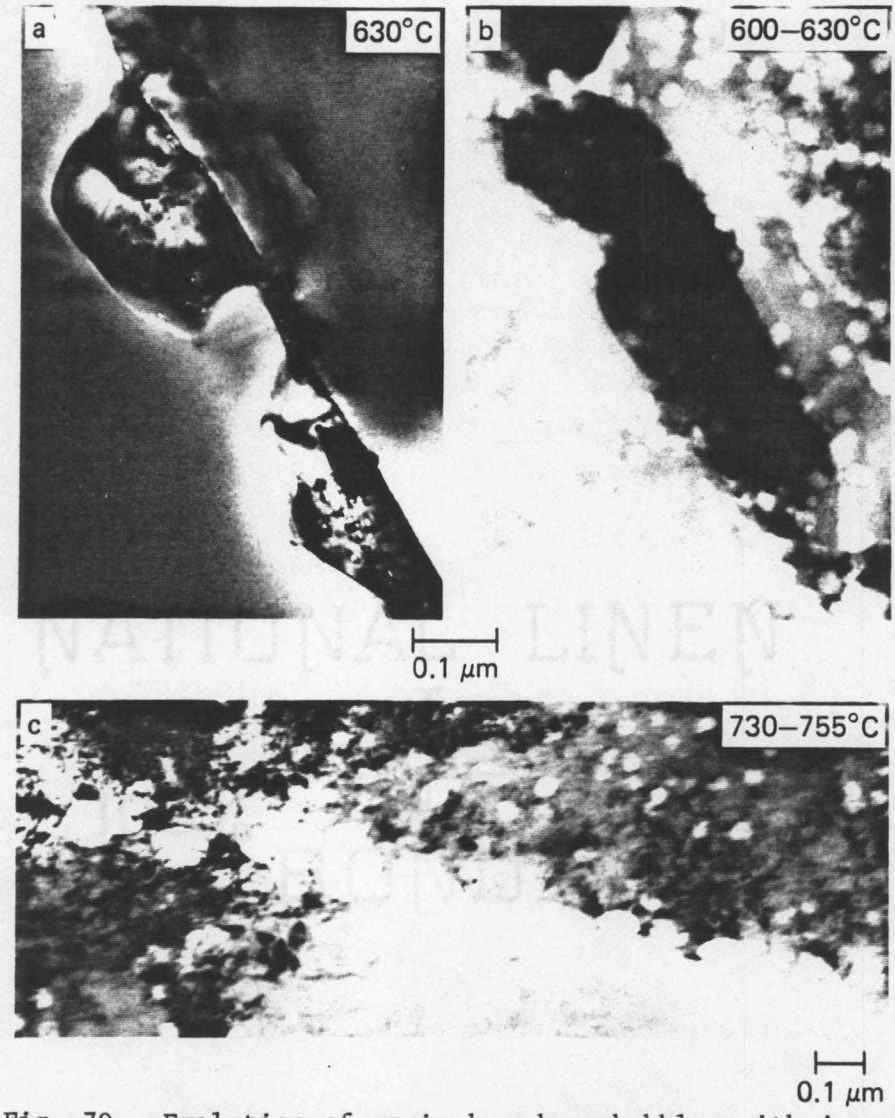

Fig. 70. Evolution of grain boundary bubbles with increased helium generation at 600 to 630°C, comparing SA 316 irradiated in (a) EBR-II to 36 dpa and 22 at. ppm He and (b) HFIR to 47 dpa and 3000 at. ppm He, and with increased temperature for the high helium generation in HFIR, comparing (b) with (c) HFIR irradiated at 730 to 755°C to 53 dpa and 3300 at. ppm He. Data are also shown in in Table 14, p. 195.

the bubbles cannot be dismissed as anomalous because similar fine bubbles appear at higher fluence among voids in EBR-II at 525°C. However, the lower temperature and the stress history present perturbations

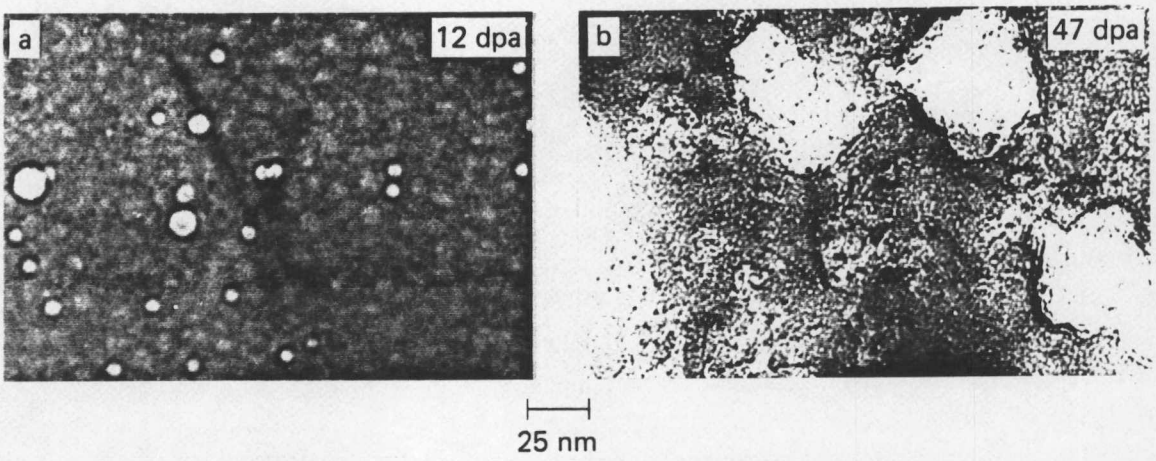

Fig. 71. Strange appearance of many fine bubbles among voids; these were not visible among coarser bubbles at lower fluence, comparing SA (DO-heat) 316 irradiated in HFIR at 515 to 555°C to (a) 12 dpa and (b) 47 dpa. The high fluence specimen bent, due to void swelling, and probably experienced stress and lower temperatures late in its irradiation history. However, similar bubbles were also found among voids in EBR-II at 525°C to 31 dpa (see Fig. 49, p. 170).

which likewise cannot be discounted, both would favor more and finer bubbles. Fine bubble formation during or after void nucleation is intriguing, but clearly does not have the same strong effect found for fine bubble formation which precedes void nucleation.

In summary, the HFIR data reveal delayed and then enhanced void swelling at 500 to 650°C relative to EBR-II data. Helium alters void swelling behavior through increased bubble nucleation which then affects the balance between dislocation and cavity sink strengths in the system. Helium extends cavity swelling to higher temperatures beyond the normal void cutoff because very coarse matrix and grain boundary bubbles develop.

Precipitation

A. Microstructural Data

Precipitation occurred only at 425 to 450°C and above, for fluences greater than 5 to 10 dpa (Fig. 72, Table 15). The amounts (PVFs) of precipitate were small at 425 to 450°C, but generally increased with temperature; fluence dependencies of PVF, however, varied with temperature

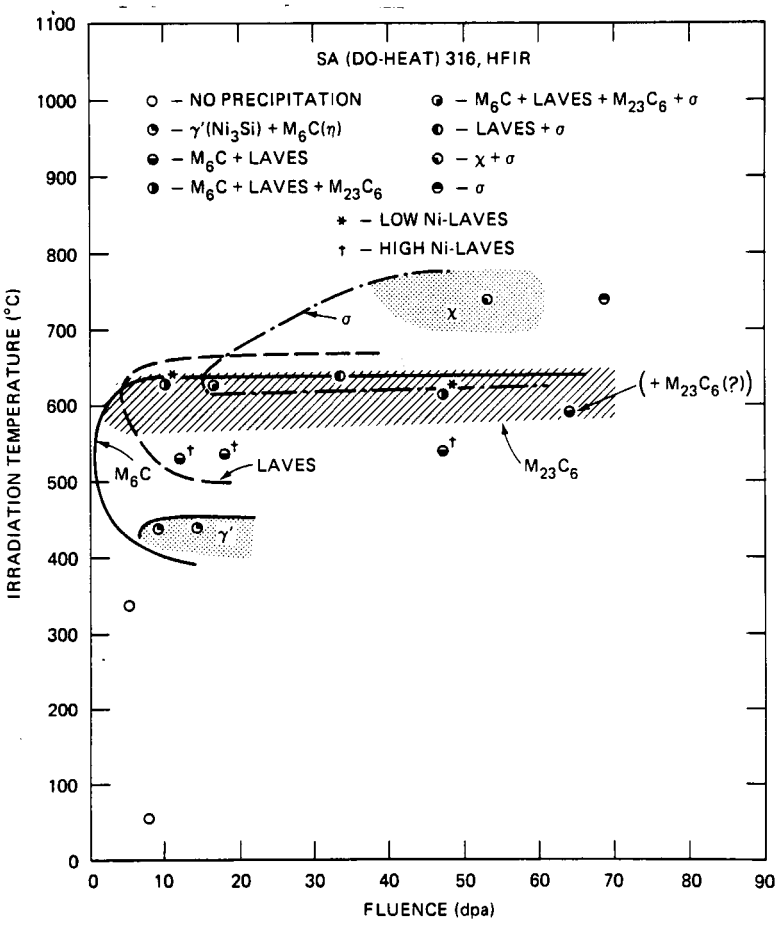

Fig. 72. A plot of precipitate phase formation (grain boundary phases included) as functions of temperature and fluence for SA (DO-heat) 316 irradiated in HFIR. Phase identification data can be found in Table 15. Also indicated are RIS effects (high RIS-high nickel, low RIS-low nickel) for Laves phase.

Table 15. Precipitate Microstructural Data on SA 316 Irradiated in HFIR

Irradiation Temperature (°C)	Displacement Damage (dpa)	Helium Content (at. ppm)	Matrix Precipitate Data				
			Phases Present	Size[a] (nm)	Concentration (m^{-3})	Fraction, % Relative Phase	Fraction, % Total Volume
55	7.8	270	None				
325–350	5.3	180	None				
425–450	9.2	380	γ′ (Ni_3Si) η(M_6C)	11.3[b] 22.5[b]	4×10^{21} 4.3×10^{20}	72 28	0.56
425–450	14.3	740	γ′ η(and/or G)	19[b] 50[b]	3.6×10^{20} 1.7×10^{19}	55 45	0.28
515–540	12	600	η Laves	120[b] 220[c]	2.6×10^{19}	90 10	1.8
525–550	17.8	1020	η Laves	190[b] 263–1120[d](99)[e]	9.6×10^{18}		1.14
530–555	47	3000	η Laves	110[b] 140[c]	1.5×10^{20}	75 25	4.3
615–640	10	440	η Laves τ($M_{23}C_6$)	280[b] 720[f] 1600[d] (160)[e]	1.7×10^{19}	18 64 18	3±1
615–640	16.6	880	η(and/or τ) Laves (+ some σ)[g]	40–326[b] 960–1360[b]	1.8×10^{19}		2.5
600–625	47	3000	η Laves τ	107[b] 444[d](79)[e]	1.3×10^{19}		1–1.5
625–650	33.5	2000	Laves σ[h]	283[d] (262 by 44)[i]	1.4×10^{18}	Mainly Laves	1 or more
730–755	53	3300	χ (σ)[h]	820[d] (345 by 76)[i]	7.3×10^{17}	Mainly χ	1.7 or more
730–755	68.5	4140	σ[h]	12–23 μm by 5–8 μm	$<5 \times 10^{17}$	100	3–5

[a]Maximum linear dimension (typical shapes and other dimensions can be found in Appendix A).

[b]Blocky or platelike morphology.

[c]Thicker, rodlike morphology.

[d]Wide, thin lath morphology.

[e]Number in parentheses indicates typical lath width.

[f]Larger, rectangular plates of normally blocky phase.

[g]Small amounts of sigma phase forming in conjunction with other intragranular phases.

[h]Massive grain boundary particles.

[i]Numbers in parentheses indicate width and thickness, respectively.

(Fig. 73). Gamma prime (Ni_3Si) dominated the precipitation at 425 to 450°C, but then the major phase progressed from M_6C (η) at 515 to 555°C to Laves at 600 to 640°C for lower fluences; σ phase dominated at the highest temperature and fluence (Fig. 73). The precipitate character therefore evolved from radiation induced at 425 to 450°C to radiation modified at 515 to 555°C and finally to enhanced thermal phase formation at 600°C and above (cf. Figs. 32, p. 147, and 73, and see p. 103, Chap. II). Maximum PVFs were found at the highest fluence at 530 to 555°C and at 730 to 755°C. More γ′ and Laves phases formed at lower temperatures in HFIR than in EBR-II (cf. Fig. 51, p. 173, and Fig. 73), but the G and phosphide phases were eliminated in HFIR. $M_{23}C_6$ and

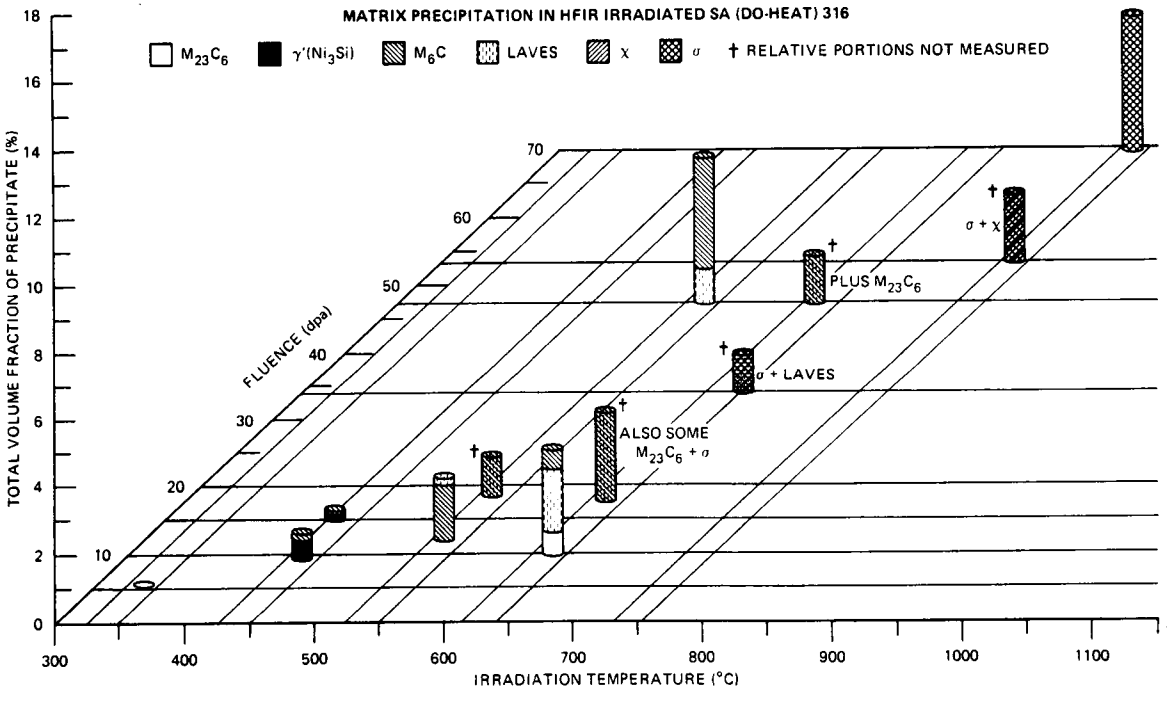

Fig. 73. A plot of relative and total phase volume fractions for matrix precipitation as functions of temperature and fluence for HFIR irradiated SA (DO-heat) 316. Data are also found in Table 15.

σ phases were found in HFIR but not in EBR-II at 600 to 640°C. Compared to aged (DO-heat) 316, Laves, σ, and η phase formations were shifted to lower temperatures in HFIR (~50 to 75°C lower) and the amount of η was greatly increased, as it replaced $M_{23}C_6$ (τ) at the lower temperatures (cf. Fig. 32, p. 147, and Fig. 73).

Particle growth of the various phases generally increased with temperature; particle sizes of some phases, however, peaked and then decreased with fluence (Fig. 74). Particle nucleation (N_p) at lower

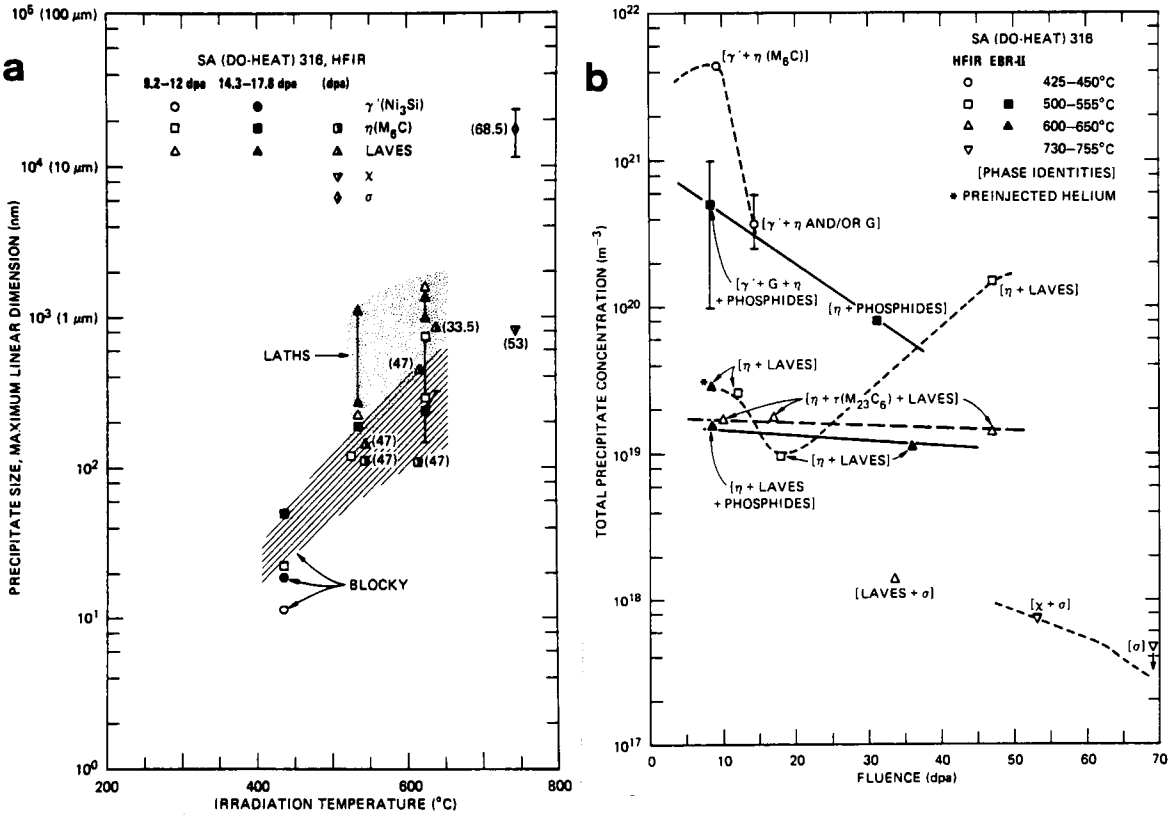

Fig. 74. Phase particle sizes (d_p), represented by the maximum linear dimension, for various morphological variants as functions of temperature and (b) total precipitate concentrations (N_p) as functions of fluence for SA (DO-heat) 316 irradiated in HFIR at various conditions. Data are found in Table 15 and various morphologies are schematically illustrated in Appendix A.

fluence was greatest at 425 to 450°C, but then dropped steeply until leveling out with temperature from 500 to 640°C, before finally declining steeply again above 650°C; N_p, however, varied differently with fluence, depending upon the temperature (Fig. 74). At 425 to 450°C, the decrease in N_p with fluence reflected dissolution of small, intermediate sized γ' particles even though η particles grew and coarsened; although η increased, the loss of γ' reduced the PVF with fluence (Figs. 74, 75;

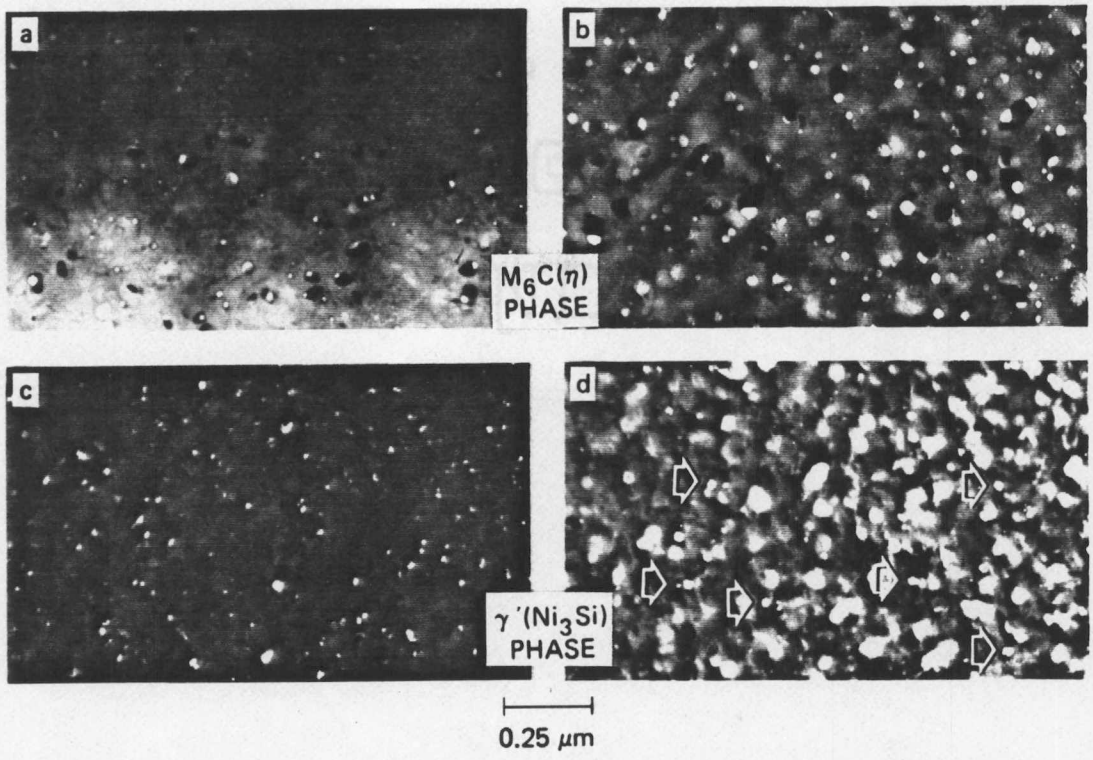

Fig. 75. Microstructural evolution of (a) and (b) M_6C phase, using bright-field imaging, and (c) and (d) γ' (Ni_3Si) phase, using dark-field imaging, for SA (DO-heat) 316 irradiated in HFIR at 425 to 450°C to 9.2 dpa (a),(c) and 14.3 dpa (b),(d). Arrows in (d) point out the largest γ' particles; larger bright images correspond to surface pits (possibly due to poor aperture placement). Data are also found in Table 15.

Table 15). Instead of coarsening at 515 to 555°C, η particles became smaller and more abundant with fluence above 18 dpa; the Laves phase evolved into coarse laths at 12 to 18 dpa before apparent dissolution/reprecipitation led to many smaller blocky and rodlike particles at higher fluence [Figs. 74 and 76(a),(c),(e)]. Despite

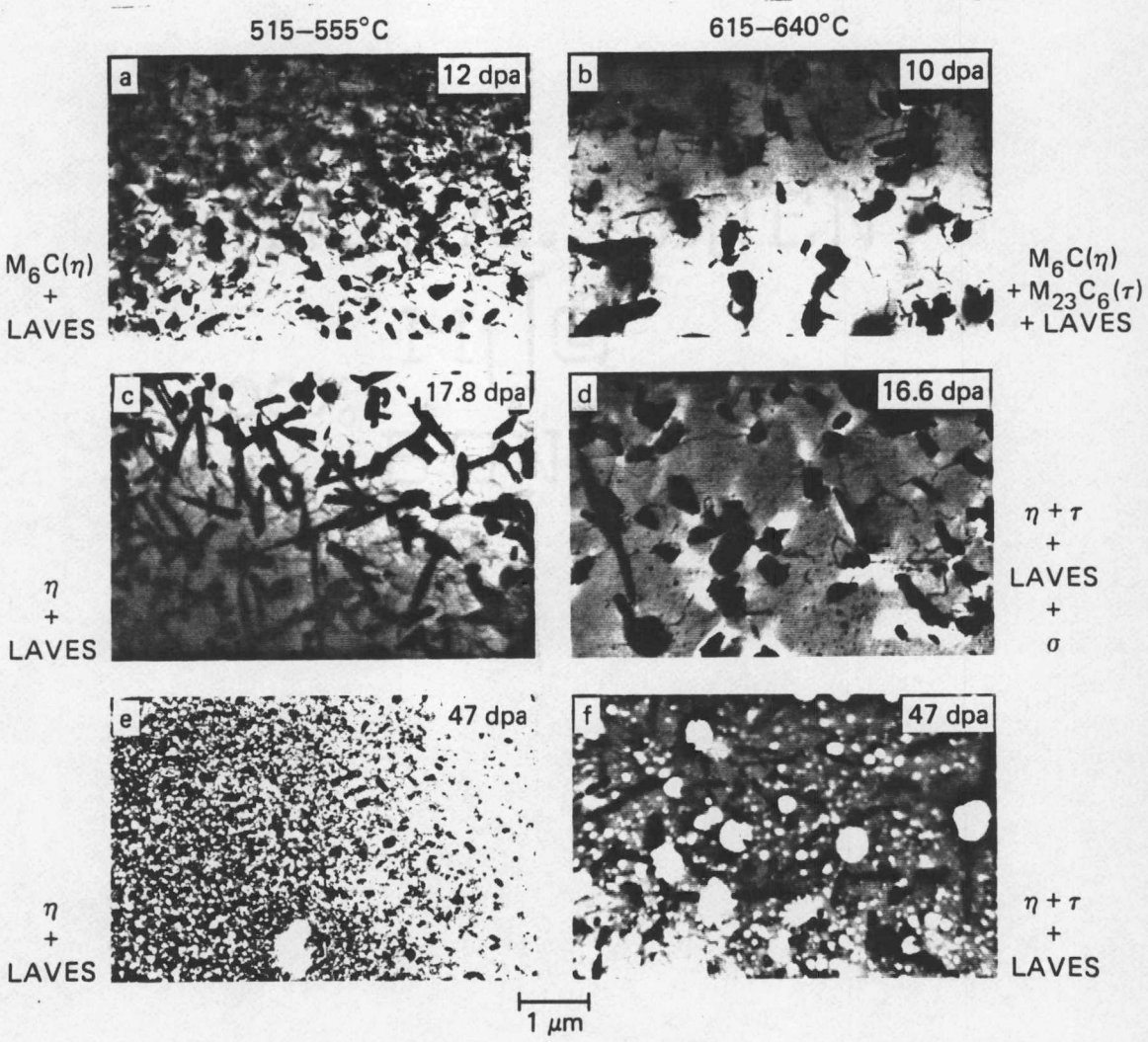

Fig. 76. Precipitate development in SA (DO-heat) 316 irradiated at 515 to 555°C (a),(c),(e) and 615 to 640°C (b),(d),(f) for fluences ranging from 10 to 47 dpa. Irradiation conditions and phases present are indicated. Data are also found in Table 15.

Fig. 76(c) suggesting maximum precipitation at ~18 dpa, the Laves thin laths present contribute little to the PVF; the blocky particles, although finer, contribute substantially to the PVF, thus causing maximum precipitation at 47 dpa [Figs. 73 and 76(a),(c),(e)]. At 600 to 640°C, the early precipitate microstructure remained quite stable with fluence, but did show hints of particle shrinkage (particularly Laves laths) as voids developed at 47 dpa [Figs. 74 and 76(b),(d),(f)]. Coarse Laves, χ, and massive σ particles form at still higher temperatures (Fig. 74). Intragranular σ phase particles at 615 to 640°C could be seen engulfing clusters of Laves and other phases at lower fluences; intergranular σ phase particles at 730 to 755°C were enormous (Fig. 77).

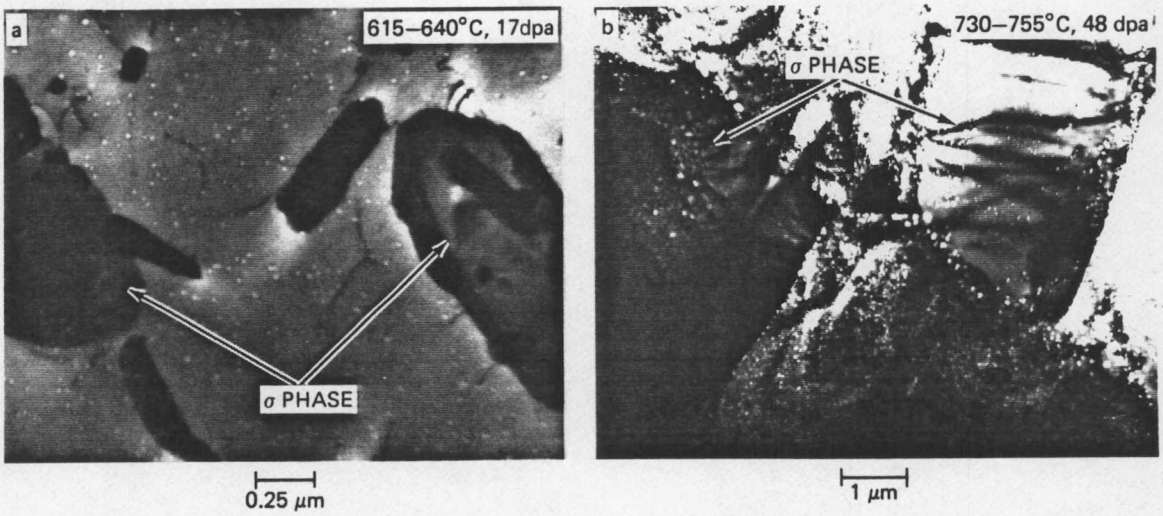

Fig. 77. Sigma phase formation in SA (DO-heat) 316 irradiated in HFIR to (a) 17 dpa at 615 to 640°C and (b) 48 dpa at 730 to 755°C. Sigma particles are engulfing regions containing smaller M_6C (η), $M_{23}C_6$ (τ), and Laves particles in (a) and are forming as enormous intergranular particles in (b).

In general precipitation in HFIR experiments reflected strong effects of RIS at 555°C and below, but the intensity of RIS appeared to be intermediate to that found comparing both uninjected and helium preinjected SA (DO-heat) 316 irradiated in EBR-II at 500°C (cf. Fig. 51, p. 173, and Fig. 73). At 600°C and above, thermal precipitation was even more enhanced in HFIR than found for the helium preinjected material irradiated in EBR-II at 625°C (judged from τ and σ formation). At lower temperatures, η and Laves phases were enhanced in HFIR relative to aging, but τ was retarded (cf., Fig. 31, p. 146 and Fig. 73). Precipitate particles in HFIR were coarser than found in EBR-II, but were similar and more abundant than found under aging (cf. Fig. 34, p. 149, Fig. 52, p. 175, and Fig. 74). Formation of γ' was accelerated in HFIR at 425 to 450°C compared to EBR-II data of others,[223,297,402,417] and formations of σ and χ phases were definitely enhanced (cf., Fig. 18, p. 108, and Fig. 72).

To summarize, HFIR data on SA 316 suggest that increased helium generation enhances radiation induced precipitation at the lowest temperatures, but favors modified or enhanced thermal precipitation as RIS is reduced or eliminated at higher temperatures. These changes parallel the effects of helium on void/bubble behavior. Void formation seemed most tightly coupled to precipitate development at lower irradiation temperatures.

B. Microcompositional Data

At 425 to 450°C, RIS was evident in HFIR produced precipitates at low fluence, as both η and especially γ' were highly enriched in nickel

and silicon and very low in molybdenum [particularly η (Table 16)]. However, with increased temperature, RIS effects developed more slowly at 515 to 555°C with fluence (evident in Laves phase composition); the initial lower intensity in HFIR was judged by the lack of radiation induced phases relative to EBR-II irradiation at 500 to 525°C. At 600 to 640°C virtually no evidence of RIS was found over the fluence range of 10 to 47 dpa. The Laves phase composition in HFIR exhibited the strongest sensitivity to temperature and fluence (cf. Fig. 57, p. 183, and Fig. 78) found for that phase in this or other work on SA 316.[402] These compositional results show more directly the temperature dependent behavior inferred from the precipitate microstructural data. The compositions of η and Laves found after 47 dpa at 530 to 555°C agreed very well with similar data from a duplicate specimen examined by Brager and Garner,[227] as did our respective broad-beam-averaged compositional measurements. (They, however, found G phase and this work did not.)

Similar to EBR-II irradiations, the η phase composition changed only slightly with temperatures and fluence, with molybdenum concentrations showing the most sensitivity to temperature. The Laves compositions, on the other hand, ranged widely with temperature and fluence, with molybdenum and nickel concentrations showing the greatest sensitivities [Fig. 78(a)]. Molybdenum contents in η were depressed further from thermal levels as temperature decreased at lower fluences; similarly, nickel contents were enhanced and increased slightly with decreasing temperature. Both elements in η showed little change with fluence at 515 to 555°C, and they returned to their thermal concentrations as

Table 16. XEDS Compositional Data for Precipitate Phases in SA 316 Irradiated in HFIR

Irradiation Temperature (°C)	Displacement Damage (dpa)	Helium Content (at. ppm)	Phases Analyzed [Number of Spectra]	Composition,[a] (wt %) Si	P	Mo	Ti	V	Cr	Mn	Fe	Ni
				Precipitate Extraction Replicas[b]								
425–450	9.2	380	[1] M_6C (η)	4.4	6.2	5		0.5	29		10.5	44.5
			[4] η	7(±1)	0.6	3.6(±1.2)		0.3	39(±1.3)	1.4	15(±3.3)	34.3(±1.4)
			[3] η[c]	4.3(±1.2)		4.8(±0.4)		0.1	37(±2)	1.7	14.8(±0.4)	38(±1.5)
			[2] Ni_3Si (γ')	16.3(±1)		2.8			9.7(±0.3)	4.3	5(±0.6)	62(±1.3)
			[3] Broad beam analysis	5.3(±0.4)		2.9(±0.4)		0.3	37.2(±1.2)	1.5	16.7(±1.4)	36(±1.4)
515–540	12	600	[6] η	6.4(±1)		15.7(±0.8)		1.1	32.4(±1)	1.2	10.4(±0.5)	32.7(±1.4)
			[11] Laves	7(±3)		25(±4)		0.4	15.7(±6.5)	1	24.6(±3)	25(±4)
			[1] P-rich Laves	5.8	12	35.4		1.1	5.1	0.3	18.5	22.7
			[1] Fe-Cr phase			4.5		0.7	39	0.8	48	7
			[2] Broad beam analysis	9.4(±1.8)		15.5(±0.1)		1.1	31.8(±1)	1.5	10.1(±0.5)	30.6(±0.4)
530–555	47	3000	[7] η	8.7(±1.7)	0–1	15(±1.4)		1.2	32.5(±2.4)	0.7	11.3(±0.6)	30.5(±1)
			[10] Laves	13(±1.6)	0–1.4	12(±2)			10(±2.3)	0.6	20(±3.7)	44(±5.3)
			[1] η[c]	6	1.2	10	0.3	1.8	35	0.6	12.1	33
			[4] Broad beam analysis	13(±1.2)	1	11.5(±0.3)	0.4	1.6	26.4(±1.7)	1	12.7(±1.7)	32.8(±1)
615–640	10	440	[5] η	8.6 (±1)	0.5	17.4(±0.8)	0.3	3	32(±2)	1.0	7.1(±0.2)	30.4(±1.7)
			[6] $M_{23}C_6$ (τ)	3(±2)	0.4	13(±1)	0.2	1.5	62(±5)	1.3	11.5(±2)	7(±4)
			[8] Laves	7.5(±2)	1	29.4(±1.4)	0.2	0.7	17.5(±0.7)	1.5	35(±2.6)	7.4(±0.8)
			[3] Broad beam analysis	6(±0.5)	0.7	23.4(±1)	0.5	1.4	28.4(±2.6)	1.3	27(±1.3)	11.2(±0.7)
600–625	47	3000	[1] η	6.5		24		1.5	28	1	13	26
			[2] Laves	5		44(±2)		0.7	12(±2.5)	0.5	30.8(±0.4)	7.3(±0.3)

[a]Includes elements with atomic numbers (Z) equal to or greater than Al (Z = 13).

[b]Unless otherwise indicated, analyses are for individual, intragranular particles.

[c]Grain boundary phase particles.

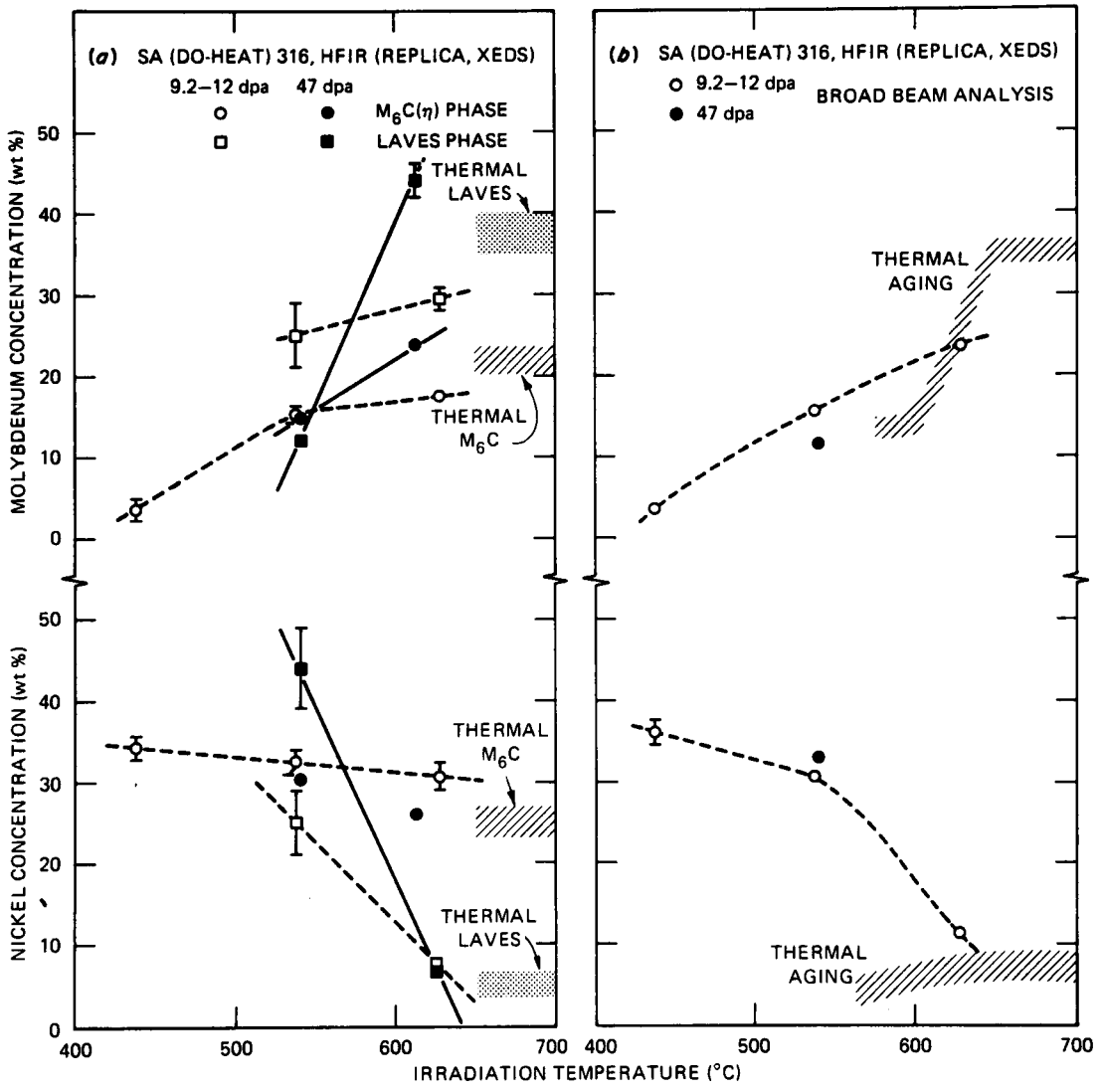

Fig. 78. (a) Individual phase and (b) broad beam whole precipitate compositional analyses from XEDS performed on extraction replicas for molybdenum and nickel concentrations as functions of temperature at several fluences for SA (DO-heat) 316 irradiated in HFIR. Compositional data can be found in Table 16. Thermal aging trend bands are included from Table 9, p. 151, and Fig. 38, p. 154.

as fluence increased at 600 to 640°C [Fig. 78(a)]. The molybdenum content of Laves phase was also depressed below thermal levels at low fluences in HFIR, but then increased slightly at higher temperature.

Nickel, however, for Laves was tremendously increased above thermal levels at 515 to 540°C, but then restored at higher temperatures. With increased fluence to 47 dpa, molybdenum content of Laves phase was further depressed at 530 to 555°C, whereas it actually increased above the thermal concentration at 600 to 625°C. The nickel concentration continued to increase with fluence for Laves phase at 530 to 555°C, but showed little change at 600 to 625°C [Fig. 78(a)]. Overall, these data illustrate that RIS effects became progressively stronger at 515 to 555°C, while RIS was suppressed at 615 to 640°C. Clearly, temperature and fluence dependencies of the various phases were stronger in HFIR than in EBR-II [cf., Fig. 57(a), p. 183, and Fig. 78].

The broad beam measurements further confirmed these trends. Molybdenum contents were low at 425 to 450°C and increased with temperature to reach normal thermal levels at 615 to 640°C [Fig. 78(b)]. The slight decline of molybdenum with fluence at 515 to 555°C reflected the strong molybdenum behavior of Laves, but tempered by the fact that Laves was only a small fraction of the η dominated precipitate (Fig. 73, p. 209). Overall, broad beam compositions reflected the dominance of η phase, except at the highest temperature, where Laves dominated. The η phase was not really the dominant phase at 425 to 450°C (Figs. 73 and 75), but γ′ did not extract proportionately with η phase so that γ′ was lacking on the replica. Normal extraction solutions dissolve γ′ and special solutions are required to obtain this phase alone.[300] The broad beam measurements showed tremendous nickel enrichment at 425 to 555°C (even higher with γ′) but a steep decline to thermal levels at 615 to

640°C, reflecting a major presence of nickel-poor Laves and τ phases. Broad beam measurements were not made at 600 to 625°C and 47 dpa because, unfortunately, the replica was very poor, allowing only a few individual particle analyses; the sample was destroyed in the initial attempt, so that another replica could not be made. Broad beam measurements at 515 to 555°C showed silicon concentrations that were much higher and more fluence dependent in HFIR than found for any of the other samples in this work. Silicon increased with fluence, consistent with increased RIS (Fig. 79). No evidence was found in the HFIR specimens of the strong phosphorus and manganese segregations observed in EBR-II.

Finally, trace vanadium contents were detected in all phases and in broad beam measurements that were higher in HFIR irradiations relative

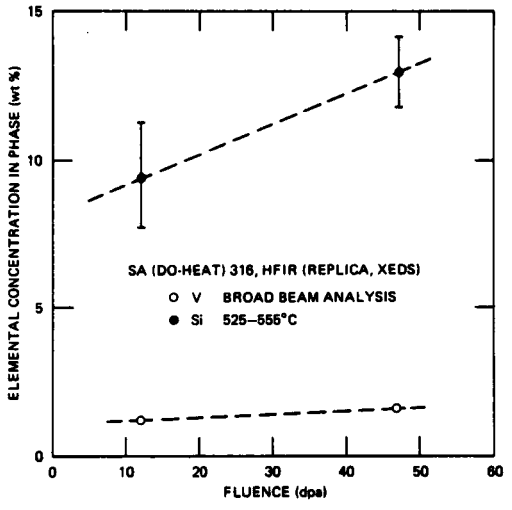

Fig. 79. Silicon and vanadium concentrations as functions of fluence for whole precipitate broad beam XEDS analyses performed on extraction replicas obtained from SA (DO-heat) 316 irradiated in HFIR at 515 to 555°C at 12 and 47 dpa. Data can also be found in Table 16.

to either EBR-II irradiation or thermal aging (Table 16 and Fig. 79). This reflects vanadium production via transmutation reactions unique to HFIR, mentioned earlier (pp. 20–23, Chap. II). However, the lack of temperature and fluence sensitivity suggests simply innocuous absorption into the precipitate phases, with no apparent involvement in RIS.

In summary, these compositional results together with microstructural data revealed maximum RIS at 425 to 450°C, moderate RIS at 515 to 555°C whose effects increase with fluence (but at a lower intensity relative to EBR-II), and virtually no RIS at 600°C and above.

CHAPTER V

DISCUSSION

This discussion consolidates the many experimental details presented into several simpler mechanisms which either explain data trends or the coupled co-development of several microstructural components. The emphasis is primarily on the phenomena of void formation and precipitation, and on how helium affects these. The discussion is divided into three major sections. The first section presents the mechanisms and coupled behaviors from data in this work. The second section compares findings and ideas with similar or conflicting ideas, assumptions, or results for theory/modeling work by others. Finally, the last section deals with suggestions for future work and with the impact which these results or their implications have on fusion applications of SA 316. The first two sections are each further subdivided into separate discussions of dislocation, cavity, and precipitation developments.

Microstructural Couplings and Mechanisms Suggested from the Data

The effect of helium to either increase or induce bubble nucleation is the consistent thread that strings together the various microstructural changes when helium generation or content is increased in different exposure environments. This is an expected consequence of the strong interaction between helium and vacancies. To the degree that bubbles nucleate as the dominant sinks in the system, void formation is

suppressed; when bubbles later coarsen, this effect is diminished, and then considerable void swelling ensues. Similarly, as bubble nucleation increases, RIS becomes more dilute to progressively reveal thermal phase behavior under neutron irradiation, often hidden beneath the veneer of normal radiation-induced processes.

Dislocation Evolution

New insights into dislocation development under neutron irradiation from this work are: (a) that RIS may be involved with loop development and (b) that loop development is hindered when bubbles are the dominant sinks. Loop growth via vacancy emission in helium-preinjected and aged material is not new (suggested by Mazey and Francis[42] in 1975) or directly relevant to dislocation evolution under irradiation; however, a new facet is the suggestion that the matrix is below its equilibrium vacancy content (this agrument is very important for consistently rationalizing bubble and precipitate behavior in these same samples later in the discussion). Dislocation data trends, couplings to the behavior of other microstructural components, and mechanisms which these suggest, are summarized in Table 17.

Vacancy emission seems the most plausible explanation for interstitial loop growth and coarsening to allow both dislocation recovery and increased apparent interstitial contents during aging at 400 to 600°C. Other possible explanations are that interstitials remain (either supersaturated or trapped) from the α-particle injection or that interstitials are produced during aging. The latter is unlikely — interstitials are

Table 17. A Summary Correlation of Data Trends and Couplings, Suggested Mechanisms, and Their Comparison with Theory/Modeling Work for Dislocation Evolution in SA 316

Data on Dislocation Evolution		Mechanisms Suggested from Data
Behavior Trends	Microstructural Couplings	
• Frank interstitial loops, induced by preinjection, grow and increase their stored interstitial content during aging at 400 to 600°C	• Frank loop development precedes visible bubble formation in helium injected and aged material	• Frank interstitial loops can grow by vacancy emission when helium/vacancy clusters coalesce to create an undersaturated system
• Frank loop structure is fairly temperature insensitive in HFIR at 55 to 350°C	• Frank loops are found in the network only when voids and irradiation induced phases are present in EBR-II and HFIR	• Cavity-dominated sink structures reduce the net biased flow of interstitials to the dislocation structures to interfere with loop development
• Frank loops do not saturate, but are removed as network develops with fluence (EBR-II and HFIR, 400 to 650°C)	• Frank loop development is either retarded (EBR-II plus preinjected helium, 500°C) or eliminated in bubble dominated sink systems	• Misfitting (and generally incoherent) particles can generate dislocations during growth
• Preinjected helium retards loop evolution at 500°C, and accelerates or eliminates it at 625°C (EBR-II)	• Dislocations are tangled around coarse precipitate particles during aging and higher temperature irradiation. Λ peaks with maximum precipitate nucleation during aging	• Intense RIS is somehow needed to sustain loop formation in the network
• Increased helium generation eliminates loops in HFIR at 500 to 640°C		
• Λ nearly saturates with fluence in EBR-II and and HFIR, but decreases strongly with temperature at 500 to 650°C (2×10^{14} to 2×10^{13} m/m^3)		

Comparison of Data Couplings and Mechanisms with Theory/Modeling Work of Others

Agreement	Difference/Disagreement
• Consistent with general trends for loop nucleation and growth (Hayns, 1975; Ghoniem and coworkers, 1979, 1980) at 400 to 650°C; steeply decreasing N_ℓ at 400°C and above is more consistent with Ghoniem and coworkers.	• The interdependence of loop generation and RIS (and possibly precipitation) and the unfaulting of loops and their interaction with the network may contribute to the lack of saturation in the loop structure that most predict
• Consistent with dynamic picture of dislocation structures as loops unfault to generate network which recovers by annihilation (Garner and Wolfer, 1982).	• Saturation Λ values can be more temperature sensitive than anticipated and much lower than 6×10^{14} m/m^3 (Garner and Wolfer, 1982).

much more difficult to form than vacancies (higher formation energy) without irradiation. Several observations seem to contradict the remaining interstitial argument: (a) There were already many more interstitials than helium atoms contained in the as-injected dislocation structure (about three interstitials to each helium atom), (b) free interstitials should be able to migrate to sinks or recombine with vacancies at room temperature in steels, and (c) aging at 400°C eliminates rather than adds interstitials as the as-injected loop structure recovers. If vacancy emission were occurring from the loops, then it seems logical that the matrix was below its equilibrium vacancy content, with normal vacancy sources (grain boundaries and dislocation lines) somehow shut off. Vacancy undersaturation could result if helium/vacancy clusters and developing bubbles are strong vacancy sinks. By contrast, vacancy emission from the loops into an equilibrium matrix without such sinks would cause a local supersaturation to develop to drive the vacancies to diffuse back into the loops.

Two consistent, yet mutually exclusive, mechanisms are identified which affect loop development under irradiation. When loops are the recipients of net interstitial fluxes, RIS should also be intense. When bubbles are the dominant sinks, however, they rob the dislocation structure, including loops, of its normally biased interstitial flux. This is analogous to the agruments usually made for reduced loop nucleation in the network-dominated dislocation structures of heavily cold-worked materials.[123,124] Best supporting data for the bubble domination effect comes from HFIR samples irradiated above 450°C, and the preinjected

sample irradiated in EBR-II at 625°C (see Table 11, p. 166; Table 14, p. 195). More loop nucleation would normally be expected in these lower concentrations of network, rather than less;[123,124] early bubbles may help themselves become the dominant sinks by interferring with loop nucleation. Loop development in the helium preinjected material irradiated in EBR-II is more complicated because loops exist prior to irradiation. The as-injected loop structure could have disappeared at 625°C by either growing or shrinking; loop development only seems sluggish at 500°C because loops plus network are found in the uninjected control specimen (see Table 11, p. 166). Conversely, when bubbles are not the dominant sinks, both RIS and loop development increase, suggesting the two are related.

A connection between loop development and RIS in EBR-II and HFIR is suspected because loops are only found in the network when radiation-induced phases also form. The HFIR data at 425 to 450°C, however, suggest more than a mere coincident relationship (see Tables 14, p. 195, and 15, p. 208, and Fig. 75, p. 211). In this case, N_ℓ decreased with fluence while both Λ and d_ℓ remained constant; at the same time the smallest γ' particles were dissolving, suggesting phase instability and decreased RIS intensity. Despite these changes, voids attached to η phase particles both continue to coarsen. Possibly RIS plays a more important role in sustaining loop nucleation when the network develops than in nucleating the initial loop structure.

Cavity Evolution

Before discussing mechanisms, several important couplings of void formation to the development of other microstructural components should be noted. Firstly, without exception, early (<20 dpa) void formation coincides with the presence of both loops (in the network) and radiation-induced phases in EBR-II and HFIR. Irradiation-induced phases usually indicate very intense RIS. Secondly, at all fluences, voids were associated only with phases which couple positively (i.e., which are compositionally compatible) with RIS. Only one exception was found — at 600 to 640°C and 47 dpa in HFIR. In this case, voids developed on nickel-poor Laves phase particles. However, since these Laves particles also appeared to be slowly dissolving, the observation still supports the idea that stable co-development of both voids and their associated precipitate particles requires that the phase be compatible with RIS. Cavity data trends and other couplings of cavity to precipitate or dislocations development are summarized in Table 18, together with suggested mechanisms.

Several mechanisms which contribute fairly new insight into void formation are: (a) the role of negative misfitting phases as interstitially biased sinks, and (b) bubbles evolving into void nuclei by growth or coalescence, particularly at migrating dislocations. Other mechanisms which extend or reinforce previous ideas are: (a) coalescence and subsequent overpressurization of helium/vacancy clusters or bubbles to cause vacancy absorption as they re-equilibrate, and (b) suppressed void formation when bubbles become the dominant sinks to

Table 18. A Summary Correlation of Data Trends and Couplings, Suggested Mechanisms, and Their Comparison with Theory/Modeling Work for Cavity Evolution

Data on Cavity Evolution		Mechanisms Suggested from Data
Behavior Trends	Microstructural Couplings	
• Very temperature sensitive bubble microstructures form in preinjected SA 316 aged 10,000 h at 600 to 700°C • Early voids form at precipitate particles in EBR-II. With increased fluence, $\bar{d}_v$ remains constant as voids continue to nucleate at 500 to 525°C, but at 625 to 630°C N_v is nearly constant as voids continue to grow • Bubbles form and coarsen at migrating dislocations at 625 to 630°C in EBR-II. Bubbles appear to coalesce at migrating dislocations at 515 to 555°C in HFIR • Preinjected helium causes tremendous nucleation of fine bubbles to suppress void formation in EBR-II at 500 to 625°C • Voids form at 425 to 450°C and <20 dpa in HFIR, but bubbles predominate at higher temperatures • Voids are larger and more abundant at higher fluences in HFIR at 500 to 640°C than in EBR-II • Many fine bubbles form among voids in EBR-II and HFIR at higher fluences at 500 to 555°C • Coarse bubbles form instead of voids at 650°C and above in HFIR	• Voids only form at low fluences when loops are present in the network (EBR-II and HFIR) • Voids only form at low fluence when radiation induced phases are present (EBR-II and HFIR) • Voids are only associated with precipitate particles of phases that couple positively to RIS [EBR-II and HFIR (except 600 to 625°C, 47 dpa)] • Voids do not form, even at precipitates, when high concentrations of bubbles are present early at 500 to 650°C (EBR-II and HFIR)	• Helium/vacancy clusters coalesce to overpressurize as they form bubbles, thus depleting the matrix of vacancies • Bubbles become larger than their critical size by growth or coalescence, either in the matrix (lower temperature) or at migrating dislocations (higher temperatures or bubble densities) • Early bubble sink dominated systems eliminate the net bias to stop void formation, even at coarse precipitate particles • Negative misfitting, (and often irradiation-induced phases) can act as additional biased sinks to aid void formation

Comparison of Data Couplings and Mechanisms with Theory/Modeling Work of Others

Agreement	Disagreement
• Confirms that if helium causes sufficient bubble nucleation to dominate the total sink strength, voids do not form (Odette and Frei, 1974; Odette and Langley, 1976; Stoller and Odette, 1982). • Confirms that if bubbles become unstable, more helium increases void nucleation (Stoller and Odette, 1982; early nucleation work by Katz, Wiedersich, and Russell). • Confirms precipitate-assisted void growth (Mansur, 1981). • Consistent with helium/vacancy clusters and/or bubbles migrating and coalescing during void nucleation (Singh and Foreman, 1975, 1981). • Confirms the critical radius work of many for conversion of bubbles to voids. • Confirms the coincidence relationship suggested between voids and irradiation-induced phases (Brager and Garner, 1978). • Consistent with the importance of impurity segregation for void nucleation (Wolfer and Mansur, 1980) • Consistent with the actual void nucleation and growth calculations made for SA 316 in HFIR (Ghoniem and Takata, 1982).	• It may not be valid to assume that increased helium generation does not change N_v (Yoo and Mansur, 1979; Glasgow et al., 1981). • It may not be valid to assume that void nucleation terminates at low fluence followed only by void growth • Voids do not form in nickel-poor regions, but are nickel-rich and may themselves be the major cause of nickel depletion in the matrix (Brager and Garner, 1979–83).

eliminate the net system bias. Several of these mechanisms are straightforward while others require some logical arguments to establish.

One straightforward mechanism is that negative misfit phases should attract interstitial defects due to the opposite sense of their strain fields; such phases should at least be biased toward interstitials as the particles grow. The possibility of such an effect has been mentioned by Mansur et al.,[265] but this work specifically identifies the negative misfitting phases as Fe_2P, γ', and Laves (which also are usually radiation-induced or -modified). An analogous interstitial bias has also been suggested for η phase,[390] on the basis of its strong chemical affinity for silicon and nickel atoms, which should be diffusing interstitially in order to strongly segregate under irradiation [see the diffusion gradients pictured in Fig. 17(b), p. 101]. Another obvious mechanism is the bubble sink effect on void formation. If bubbles are the dominant sinks in the system, the net biased flow of interstitials to dislocations (which permits the vacancy supersaturation) will be eliminated, because Frenkel pairs are mutually annihilating at these neutral sinks. Furthermore, the observation that voids fail to form at coarse precipitate particles reinforces this assessment because the collector effect should operate if a vacancy supersaturation were available. By contrast, when many fine bubbles develop after voids form at 500 to 555°C in both reactors, they have no apparent effect on the voids; this emphasizes that bubbles must dominate early to interfere with void formation.

In the helium-preinjected material, the driving force behind bubble evolution is not directly obvious from these experiments, but can be reasonably inferred on the basis of both the interstitial loop growth data and previous theoretical work. Helium/vacancy clusters and bubbles (if overpressured) are the most likely sinks for vacancies to undersaturate the matrix and vacancies and allow growing interstitial loops to act as vacancy sources. From the work on bubble theory prior to 1970, coalescence (via various migration modes) was the most likely avenue for bubble growth without displacive irradiation (see Chap. II, pp. 37–46). Clusters and bubbles absorb vacancies when overpressured. Further, when equilibrium bubbles coalesce or impinge upon helium/vacancy clusters, they also overpressurize and must be relieved by vacancy absorption {remember, larger bubbles require more vacancies per helium atom [Eq. (4), p. 43]}. Reduced system pressure and surface energy may help drive the system toward coalescence coarsening, but bubbles behaving as vacancy sinks is really the only logical explanation for a vacancy deficiency in the lattice.

Finally, the mechanism of dislocation aided bubble growth and/or coalescence seems to be an important source of void nuclei at higher temperatures or in dense, bubble-dominated microstructures. Because critical sizes in FBR irradiated steels rapidly become large above 550°C,[185] formation and growth of subcritical bubbles appear to occur while dislocations migrate in EBR-II at 625 to 630°C. Dislocations are envisioned to be sinks for helium atoms; furthermore, climbing dislocations should also collect matrix helium trapped in vacancies. Fluxes

of vacancies and the insolubility of the helium should allow the helium to agglomerate into bubbles along the dislocations. Bubbles which then are large and too slow to continue migrating with the dislocation would be released; upon release, these bubbles further expand in the vacancy supersaturation[185] away from the dislocation sink. The observations in Fig. 50 (p. 172) are consistent with this scenario. At higher bubble concentrations (injected material in EBR-II at 625°C and material in HFIR at 515 to 555°C), coarsening of bubble-dominated microstructures also appears aided by coalescence along climbing dislocations. However, consistent with a lack of vacancy supersaturation in these cases, many of the largest bubbles are found at the dislocations instead of in the matrix. Coalescence coarsening would also continually diminish the role of bubbles as dominant sinks, to eventually allow void formation at higher fluences (as observed in the HFIR case at 500–650°C).

Precipitate Evolution

This work suggests several important and relatively new insights into precipitation under neutron irradiation: (a) irradiation-induced processes (particularly RIS) mask or oppose thermal processes, to produce the unnatural precipitation usually found under neutron irradiation, (b) enhanced thermal processes are revealed when bubble sinks sufficiently dilute RIS, and (c) interstitial fluxes can help stabilize negative misfitting phases (which, in turn, are usually radiation-induced or -modified). These data support and extend insight into several previously introduced mechanisms: (a) RIS produces "microalloy" regions around sinks to influence phase formation and/or stability at

these sites, (b) RIS stabilizes phases which couple positively with these microalloys and retards those that couple negatively, on the basis of intrinsic phase solute enrichment/depletion characteristics, and (c) helium induces bubble-dominated sink structures that dilute or eliminate RIS. Interestingly, only Laves and the phosphide phases show significant compositional fluence dependence; coincident microstructural instability further suggests dissolution and reprecipitation for the phases as the influence of RIS increases. Finally, these data indicate possible involvements of phosphorus and manganese with intense RIS. As before, precipitation data trends and couplings to the development of other microstructural components are summarized in Table 19, together with suggested mechanisms.

Generally, precipitate nucleation in this work varies directly with the concentrations of dislocations and voids, consistent with incoherent/misfitting phases requiring heterogeneous nucleation sites. Clustered particle nucleation occurs during aging at 650 and 700°C (see Fig. 36, p. 150, and data by Stoter[363]) most probably because $M_{23}C_6$ (τ) particles reject silicon and/or nickel interfacially, to then stimulate formation of the silicon and/or nickel-rich Laves and M_6C (η) phase particles. This behavior parallels the action of RIS, because it forces silicon and nickel enrichments to occur at nucleation sites and precipitate interfaces as RIS would when they are sinks for point defects under irradiation.

These data indicate, as many others also find, that RIS separates the original, uniform alloy into a composite of microscopic regions of

Table 19. A Summary Correlation of Data Trends and Couplings, Suggested Mechanisms, and Their Comparison with Theory/Modeling Work for Precipitate Evolution in SA 316

Data on Precipitate Evolution		Mechanisms Suggested from Data
Behavior Trends	Microstructural Couplings	
• Incoherent phase particles nucleate heterogeneously in most cases (aging, EBR-II, HFIR)	• Precipitate nucleation varied directly with dislocation density comparing EBR-II, HFIR, and thermal aging	• Heterogeneous nucleation site availability influences particle distributions and possibly phase selection and stability
• With helium preinjection, Laves (negative misfit) replaces τ (positive misfit) under aging	• Peaks in precipitate nucleation and in dislocation density with temperature coincide during aging	• Many irradiation-induced or -modified phases are negative misfitting, and may be stabilized by interstitial fluxes
• In EBR-II, helium preinjection eliminates radiation-induced phases; no precipitation occurs at 500°C but thermal precipitation is enhanced at 625°C	• Irradiation-induced phase formation always coincided with early void formation and the formation of Frank loops in the dislocation network	• Potential precipitate phases are enhanced or retarded, depending on the positive or negative compatibility of their intrinsic elemental solubilities with RIS
• Thermal phases are Mo and Cr rich, most are Si rich (except τ) but Ni poor (except η)	• When helium bubbles dominate the total sink strength, radiation-induced phases are eliminated and RIS is reduced or suppressed at 500 to 550°C; at 600°C or above, RIS is eliminated and thermal precipitation is enhanced (HFIR and EBR-II with helium preinjection)	• Precipitation under irradiation is the result of a dynamic competition between opposing enhanced thermal and radiation-induced processes
• Phases are generally very Ni and Si rich and Mo poor in EBR-II at 500 to 620°C and in HFIR at 500 to 555°C relative to thermal precipitation		• RIS causes new microalloy regions to form around sinks such as voids, inclusions, or growing precipitate particles to influence phase development or stability
• RIS effects on precipitation are negligible in HFIR at 600 to 640°C and in EBR-II with preinjection at 625°C	• G, phosphide, η, and Laves particles often develop at or with voids and at inclusions in EBR-II at 500 to 630°C or at voids in HFIR at 425 to 555°C	• Bubble-dominated sink structures dilute RIS and can allow enhanced thermal precipitation to develop under neutron irradiation
• η dominates the precipitation at 500 to 550°C in EBR-II and HFIR	• Composition evolution of Laves and phosphides with fluence in EBR-II or HFIR is accompanied by microstructural changes, including dissolution or reprecipitation	• Phosphorus and possibly manganese can be involved in intense RIS
• Laves forms with η or dominates at 600 to 640°C in EBR-II and HFIR		
• τ is retarded in EBR-II and HFIR (except at 600 to 640°C in HFIR)		
• Irradiation-induced phases form in EBR-II at 500 to 625°C, but are present only at 425 to 450°C in HFIR (low fluence)		
• P and/or Mn segregate strongly at low fluences in EBR-II, particularly at 500°C		

Table 19 (continued)

Comparison of Data Couplings and Mechanisms with Theory/Modeling Work of Others

Agreement

- Incoherent phase nucleation would depend on and vary with availability of appropriate sites (general).
- Confirms the importance of vacancies to stabilize oversized misfitting phases (Silcock and Tunstall, 1964; Beckitt and Clark, 1967; and Russell, 1969).
- Supports the idea that RIS induces precipitation when local solute contents near sinks exceed solubility limits (Lam et al., 1978; Barbu and Martin, 1977).
- Supports the suggestion that local regions near sinks actually become like new microscopic alloys which then form normal thermal phases appropriate for the new alloy (Lee et al., 1981; Williams and Titchmarsh, 1981; Maziasz, 1982).
- Supports the suggestion that phases and local "microalloys" are distinct thermodynamic entities and that solute enrichment/depletion characteristics for both must couple positively for phase formation and stability (Maziasz, 1979; 1982).
- Consistent with interstitial fluxes causing the most intense RIS (i.e., Si and Ni in type 316) (Johnson and Lam, 1976; Lam et al., 1978).
- Consistent with suggestions that interstitial fluxes (and intense RIS) should stabilize negative misfitting, irradiation-induced phases (Lee et al., 1981; Maziasz et al., 1981).
- Confirms that high sink concentrations can dilute RIS to suppress radiation-induced precipitation (Kenik, 1979; Odette, 1979; Maziasz, 1982).
- Consistent with the view that many competing factors affect phase stability under irradiation (Russell, 1977).

Difference/Disagreement

- Many negative misfit phases are stabilized while the positive misfit $M_{23}C_6$ phase is destabilized under irradiation (Maydet and Russell, 1977; Russell 1979).
- Inconsistent with "infiltration-exchange" mechanisms for compositional changes of $M_{23}C_6$ and Laves phases and transformation of $M_{23}C_6$ into M_6C (Brager and Garner, 1981).
- Inconsistent with the view that large amounts of helium will not change phase evolution very much (Brager and Garner, 1982).

new alloys ("microalloys"), with the alloys at and in-between sinks changing to complement each other as the original solute must be conserved. Although irradiation introduces different phases and proportions than found when aging the original bulk steel, phase formation more closely corresponds to the normal aging behavior of the new "microalloy" regions. This concept has been advanced by several,[41,165,402] and is strongly supported by aging studies of steels modified to model

the effects of RIS at sinks,[366,370] as mentioned earlier (Chap. II, pp. 105–107, 118–119, and Fig. 19, p. 115). The effects of helium in this work further demonstrate that if the effects of RIS are eliminated in situ under irradiation, then "microalloys" do not form and the precipitation returns to the thermal behavior of the original alloy. Particles of G, Laves, and η (RIS modified at lower temperature phases) and the largest phosphide particles are associated exclusively with voids; this suggests that these phases depend upon other sinks to initiate, supersaturate, and sustain their RIS-produced "microalloys", as pictured in Fig. 19(b), p. 115. Several additional factors however, appear to influence the formation and stability of other phases which do not show such strong sink association.

One obvious stabilizing factor for negative misfitting phases would be biased interstitial fluxes (see Table 19). This is simply the corollary to their behavior as interstitially biased sinks for void swelling (Table 18, p. 227). Most irradiation-induced γ' and phosphide rods do not form in conjunction with other sinks in this work, and they are the most negative misfitting phases (particularly Fe_2P; see Table 4, p. 81). Dislocations could aid their nucleation, but when dislocations continue to climb and migrate they cannot develop "microalloy" regions the way that stationary sinks can. There are, however, two avenues by which the interstitial fluxes can stabilize the negative misfitting phases. Besides the obvious benefit of the defect-strain interaction, biased interstitial fluxes would allow the maximum buildups of the solutes which they drag to these sinks (Si and Ni in this case), because

the interstitial-drag mechanisms allow the most intense RIS.[352,353] Conversely, when bubbles are the dominant sinks and they eliminate the net biased flow of interstitials to other sinks, these phases should consistently cease to form. Further evidence of the importance of point defect/phase misfit interactions comes from the effect that helium preinjection has on precipitation in aged SA 316 (Table 19); the negative misfitting Laves phase completely replaces the normal and positive misfitting τ phase, consistent with the vacancy deficiencies implied earlier.

Possibly the overriding factors affecting phase formation and stability under irradiation are the compositional natures of the potential phases themselves. Actually, two closely related and reinforcing mechanisms stem from data that support this idea (see Table 19). Firstly, phases are enhanced or stabilized by RIS when their intrinsic solute enrichment/depletion characteristics couple positively with their surrounding "microalloy" compositional environments. Conversely, when phases couple negatively, RIS retards or destabilizes them. Secondly, RIS actively opposes thermal processes that also occur under irradiation; Precipitation therefore reflects the net effect of this dynamic competition, particularly at higher irradiation temperatures.

Figure 80 shows that the major influence of irradiation or phase formation in stainless steels is RIS; as RIS intensity increases, the positive compositional coupling must also increase for the phase formation to be stabilized by RIS. The irradiation-induced G and γ' phases have silicon and nickel as their major constituents, and they couple

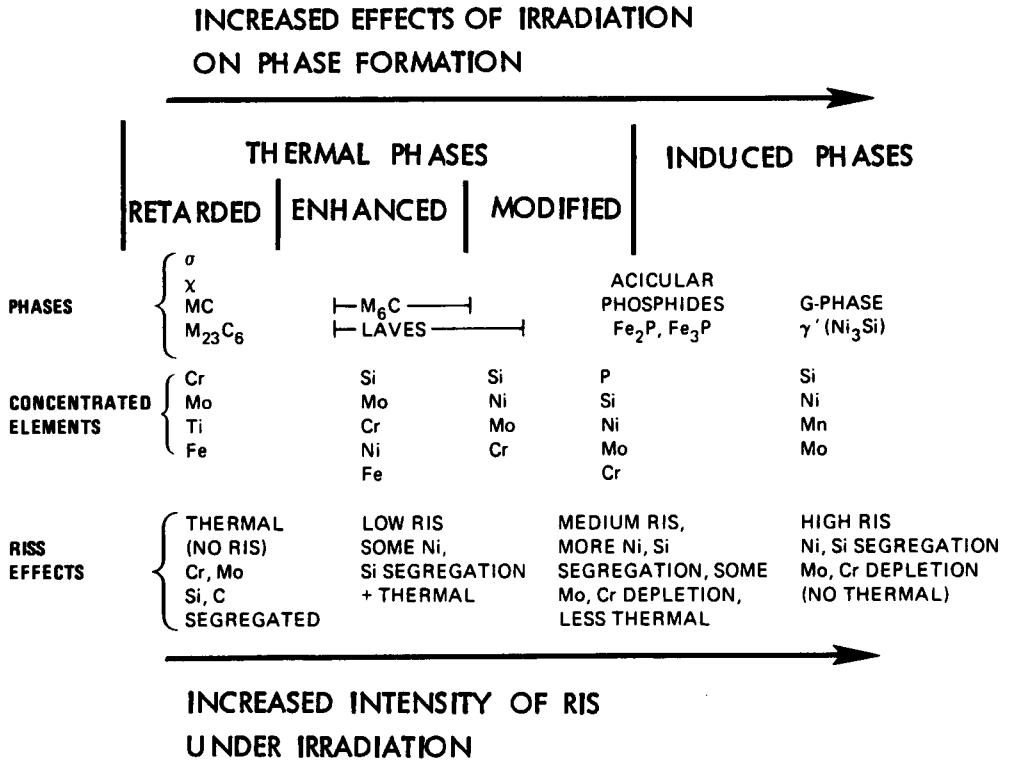

Fig. 80. A spectrum of correlated phase formation, compositional enrichments, and RIS effects for neutron irradiated type 316 stainless steel. This illustrates the natural progression from irradiation-retarded to irradiation-induced phases with increased RIS, which reflects the degree of compositional coupling between the phases and RIS. In the columns of elements, order reflects both perceived importance of the elements to that phase group and generally decreasing concentration, from top to bottom. Individual phase enrichment/depletion characteristics can be found in Table 4, p. 81.

almost perfectly with the effects of RIS. Conversely, the phases that reject nickel and silicon and enrich in chromium and molybdenum are retarded because they couple negatively with RIS. The intermediate phases trade off to varying degrees the positive RIS stabilization due to their silicon and/or nickel enrichments against the negative aspects of chromium

and molybdenum enrichments. However, as the thermal phases maintain their compositional characters, to match or oppose RIS, they also demonstrate that they are distinct thermodynamic entities themselves, whose natures cannot be totally violated just because they are forming under irradiation.

The mechanism of RIS itself is a dynamic opposition between point defect induced solute buildups and depletions under irradiation, and the thermal normal back-diffusion that works to eliminate them. In like manner, several facets of phase development reflect active opposition by RIS to suppress normal thermal effects while it induces other new ones. RIS actively appears to hold back τ phase formation, even if it nucleates, by building up interfacial nickel and silicon which the phase cannot accommodate [see Fig. 19(b2), p. 115]; without such direct hindrance, it seems that vacancy supersaturation (due to positive misfit of τ) and chromium/molybdenum enrichments away from sinks would actually benefit τ formation under irradiation. A more balanced opposition can be seen when the natural molybdenum and/or chromium enrichments of Laves and η occur, despite the effects of RIS. Activity gradients still cause these elements to enrich in the phase even though opposing RIS fluxes do lower the enrichments relative to thermal levels. While this competition may seem an obscure point during normal irradiation, it becomes a major factor in explaining the changes in precipitation that occur when helium dilutes or suppresses RIS under irradiation.

The most obvious effect of increased helium is that it eliminates the formation of irradiation-induced phases in both HFIR and EBR-II,

except at 425 to 450°C in HFIR (Table 19). When bubbles dominate the microstructures (void suppression), RIS is also diluted or suppressed. Judging from Fig. 80, thermal precipitation behavior is nearly restored by helium preinjected and EBR-II irradiated material at 500 to 625°C. Thermal precipitation, including the normally retarded τ and σ phases, is found in HFIR at 600 to 640°C, while radiation-modified precipitation at 500 to 555°C, and radiation-induced precipitation at 425 to 450°C are found. Together, these data indicate a progressive decrease in RIS intensity as bubble concentrations increase; however, higher concentrations of early bubbles are required to completely suppress RIS than are required to suppress void formation. The obvious mechanism is sink dilution of RIS, induced by the bubbles, as several have proposed.[135,165,251] However, a new insight suggested by this work is that thermal precipitation becomes enhanced as RIS is suppressed. This was the reason for belaboring the obscure evidence for underlying thermal effects during normal, high-RIS irradiation.

Finally, the EBR-II data also suggest that somehow phosphorus and manganese are involved with intense RIS (Table 19). The best evidence is their enrichments to irradiation-induced phases (phosphorus in the A and B phosphides and manganese in the G phase). Phosphorus segregation has been observed at ion-irradiated surfaces,[329] but manganese segregation is not generally observed. The enrichment of phosphorus compared to the matrix is tremendous ($\sim 10^3$ times greater), whereas manganese is enriched only several times relative to the matrix. Helium preinjection

eliminates both effects when RIS is diluted. Manganese may be segregating strictly due to its normal activity in the G phase; the manganese content is lower than calculated for the ideal $Mn_6Ni_{16}Si_7$ compound (~9 as compared to ~23 wt %). However, two problems arise: (a) If manganese does not segregate via RIS, where did the original manganese enrichment come from to initiate G phase formation? (b) If manganese does segregate via RIS, why does it not segregate to all sinks? Phosphorus appears more likely to be undergoing nonequilibrium segregation, but via which mechanism of RIS — interstitial drag, vacancy drag, or Inverse Kirkendall? Speculation is useless beyond this and more experiments are needed.

Comparison of Microstructural Couplings and Mechanisms with Theory/Modeling Work of Others

Dislocation Evolution

Generally, previous theoretical work on dislocation evolution under irradiation has not considered the effects of either bubble-dominated sink structures or RIS on loop development.[123-127] Some points of agreement or difference/disagreement with previous theory or modeling work are also listed in Table 17 (p. 223).

Hayns[123] and Ghoniem and coworkers[124-126] have done rate theory work on loop nucleation and growth in the 400 to 650°C range, and for very short irradiation (~10^{-2} dpa) times. Their general trends of decreasing loop concentration and increasing size with temperature are consistent with this work. The loop concentrations in this work (500°C)

are low compared to those calculated by Hayns[123] and Ghoniem and Sharafat,[125] but somewhat similar to those calculated by Ghoniem and Chow.[124] However, remember that SA (DO-heat) 316 is a low loop forming heat of steel. The temperature dependence of loop formation in this work is steeper than Hayns or Ghoniem and Sharafat find, but does fall within the range shown by Ghoniem and Chow for variable di-interstitial binding energies. Loop nucleation does not saturate, but ceases, due to loop unfaulting and interaction with network, and possibly due to decreased RIS, as suggested earlier.

Garner and Wolfer[127] also present a model for dislocation network density evolution. These data confirm the importance of the dynamic picture that they present, for loops growing and then unfaulting to form network, which in turn eventually recovers by mutual dislocation annihilation. However, these data clearly differ from their predicted temperature-independent saturation Λ of $\sim 6 \times 10^{14}$ m/m^3 (reached after ~30 dpa). Data in this work show lower Λ's with much more temperature dependence in EBR-II at 500 to 625°C, and even lower Λ's in HFIR. The difference may stem from the fact that loop nucleation in this work stops at higher fluence, whereas they assume it continues.

Cavity Evolution

This work is generally consistent with rate theory treatments of void swelling. However, because the amount of theoretical work is so large, this section focuses only on a portion of the work related to the main theme of helium effects and/or void swelling under neutron

irradiation. Some points of agreement or differences/disagreement with previous theory or modeling efforts are also listed in Table 18 (p. 227). In general, few consider a role for negative misfitting phases acting as interstitially biased sinks or the possibility of a role of dislocations in bubble growth or coalescence to promote them above their critical size. These data suggest bubble overpressurization in many cases, but this is not a measurement and could reflect the assumptions by which the calculations are made; however, it does seem most likely for preinjected and aged specimens. Finally, this work introduces several additional avenues for RIS to affect void formation by stabilizing loops and irradiation-induced phases.

First, consider the effects of increased helium generation or content on void formation. These data overwhelmingly confirm the early work of Odette and co-workers[31,180] and, more recently, Stoller and Odette[25,181] which indicated that increased early bubble nucleation, sufficient to make them the dominant sinks in the system, would suppress void formation. These data also confirm the same work by Stoller and Odette that explored the other possibility of enhanced void swelling, when bubble nucleation is enhanced but these do not become dominant sinks. This result also was often implied for increased helium in early void nucleation work by Wiedersich and Katz[281] and by Russell.[280] The HFIR void data at higher fluences are also consistent with actual void nucleation and growth calculations made by Ghoniem and Takata[98] for SA 316 irradiated in HFIR, despite some differences in early microstructural evolution. The match between predictions and the data for actual

matrix void sizes would be improved by: (a) the irradiation temperature revisions made in this work, (b) separating these cavity data into matrix and precipitate void components, and (c) removing the grain boundary contribution to the total swelling. These data differ significantly with the assumptions made by Yoo and Mansur[273] and by Glasgow et al.[182] when they treat the effect of increased helium on void growth. They assume the same void concentrations found without helium, whereas these data show large increases in void concentration, due to helium, when voids are able to form. Increased swelling in HFIR compared to EBR-II does resemble the predictions at high temperatures made by Yoo and Mansur, but not due to enhanced void formation, as they suggest.

Next, consider several other general aspects of void formation. These data conflict with the common perception that void nucleation terminates at low fluences, followed only by void growth (Table 18, p. 227). Indeed, these EBR-II data show that nucleation continues at 500 to 625°C to 36 dpa, particularly at the lower temperatures. Most of the detailed data in this work are consistent with and emphasize the importance of the theory/modeling work done on the critical radius concept for conversion of bubbles to voids. Bubble sizes in EBR-II at 625 to 630°C, with and without preinjected helium, are consistently smaller than the critical radii calculated by Mansur and Coghlan;[185] however, at lower temperatures in EBR-II and at most temperatures in HFIR the bubble sizes are often much larger than the critical sizes calculated, particularly at the highest HFIR temperatures. This difference probably reflects the assumptions, however, that dislocations are the dominant sinks and that

normal FBR vacancy supersaturations are present (the high cavity concentrations in HFIR appear to eliminate both effects). Consistently, however, most theories imply that critical radii become infinite or ill-defined if the vacancy supersaturation or net bias is eliminated. Furthermore, the increased bubble nucleation, which accompanies increased helium, tends to dilute the helium accumulated per bubble as well as increase the critical radii, as discussed by Stoller and Odette.[35]

These data confirm that precipitate association assists void growth, as Mansur[266] indicates, and show this to be a major or the dominant mode of void swelling in most cases. Additional insights, however, suggested from these data are: (a) the bubble-dominated sink structures, induced by increased helium, also control the bubble size for void conversion at precipitates, and (b) the assisting particle must be a RIS-compatible phase (positive coupling) in order to survive or stably grow with the growing void.

This work suggests that subcritical bubbles grow and coalesce under irradiation, much as they do under aging, particularly in cavity sink-dominated systems. As mentioned earlier, dislocations can aid growth and coalescence of bubbles that migrate with them. Most, however, do not assume that bubbles or clusters migrate. Only Singh and Foreman[283,284] allow their helium/vacancy clusters to migrate and coalesce prior to void nucleation, to conceptually support the suggested growth mechanism involving bubble migration.

Finally, we consider RIS effects on void formation. The coupling of RIS to void development is consistent with work by Wolfer and

Mansur[288] suggesting impurity segregation to aid void nucleation. Coupled void and irradiation-induced phase development in these data also confirm the original suggestion of such a coupling by Brager and Garner,[297] but not via the avenue of matrix compositional evolution, as they often imply.[37,298-300] From data like those summarized in Fig. 13 (p. 74), they imply that silicon, nickel, and carbon depletions from the matrix by the precipitation triggers either the void formation or growth found in the "steady-state" swelling regime;[227] they suggest the critical nickel level for this effect is ~9%. Several key questions, though, are:

1. How much nickel and silicon (and carbon?) does the precipitation really deplete from the matrix?

2. Do the voids really form when either the local or surrounding matrix is nickel poor?

For the DO-19 sample (HFIR, 535 to 555°C, 47 dpa), which both Brager and Garner and this author have measured,[227] the 4.3 vol % of precipitate is found enriched to 33 to 35 wt % of nickel; this precipitate can only reduce the remaining matrix to 12 wt % Ni from its original 13 wt %. However, the matrix in-between voids could easily be reduced to ~8 to 9 wt % (they find ~8%) by RIS shells around the voids, if these shells are enriched to ~20 wt % (they find 21% in another sample and LeNaour et al.[116] find about 20%) and are 20- to 40-nm thick (shell size increases with void size[353]). Void formation or growth would not follow, but in fact must precede the severe matrix nickel depletion, if void growth itself must cause that depletion. LeNaour et al.[116] also suggest that

nickel enrichment at voids causes matrix nickel depletion. The precipitation could accommodate half the original silicon. However, matrix carbon could be totally depleted, if the η phase is stoichiometric M_6C, or carbon remains in solution, if the η phase is M_5Si (ref. 372), and the Laves contains no carbon. Regarding the second question, small voids seem always to be nickel rich, and voids remain nickel rich even when attached to nickel-rich precipitates.[306] Any void should act as a sink for RIS. Again, a drastic nickel reduction in the surrounding matrix would not precede the formation of voids if they are required to drive that segregation. Possibly Brager and Garner[227,300] have found voids in nickel-poor foil regions because those voids were too large and those regions of the foil experienced disproportionate nickel loss from inside the voids during polishing, as found by Maziasz.[308]

Precipitate Evolution

As mentioned in Chap. II, very little theory/modeling work on phase stability under irradiation applies directly to type 316 stainless steel. Moreover, work considering neutron irradiation is sparse. But it does, however, seem somewhat unexpected from more recent work that:
(a) negative misfitting phases should form under irradiation, and
(b) thermal precipitation should be enhanced when the effects of RIS are suppressed. Some points of agreement or points of difference/disagreement with previous theory on modeling work are also listed in Table 19 (p. 232).

Although it is generally regarded that incoherent and misfitting phases nucleate incoherently, few include the benefits or hinderances of these sites (either their concentrations or their natures) in assessments of phase stability under irradiation. The simple idea that RIS causes precipitation by exceeding solubility limits at sinks was suggested by Barbau and Martin[442] and by Lam et al.[444] for binary alloys; the concept does extend to complex steels, but composition deviations are far more complex. However, formal RIS theory up to this point has not considered sinks other than the several test voids examined by Johnson and Lam,[353] and the free surfaces included in general. The normal loss terms for defect flows to sinks in the rate theory-point defect conservation equations [see Eqs. (6) and (7), pp. 59, 60], which give the effects of microstructure, have also not been included.

Regarding the phases themselves, the perception that irradiation-induced phases are new or strange has been tempered by the suggestions that RIS produces "microalloys," which are really just different alloy compositions found within the much wider multicomponent phase field that normally includes the original alloy;[41,165,363,402,425] these microalloys then behave as though they are being aged at the irradiated temperature. These same authors further suggest that the phases themselves maintain their thermal enrichment/depletion characteristics under irradiation. These data, however, add insight into the degree to which the thermal phase compositions are flexible under the influence of RIS in type 316 stainless steel and add evidence for the retardation of $M_{23}C_6$ (τ). These concepts directly oppose the "infiltration-exchange"

the thermal phase compositions are flexible under the influence of RIS in type 316 stainless steel and add evidence for the retardation of $M_{23}C_6$ (τ). These concepts directly oppose the "infiltration-exchange" of $M_{23}C_6$ to make it silicon- and nickel-rich under irradiation, as suggested by Brager and Garner[298-300] and others.[116] These data do not support the transformation of $M_{23}C_6$ into M_6C either. Although Laves phase in this work evolves compositionally with fluence, as Brager and Garner find, the microstructural changes suggest that the compositional adjustments do not favor Laves stability. However, these differences are more subtle and could reflect sensitivity to flux or small temperature variations for Laves. Laves dissolution and reprecipitation also seem evident, though, during its compositional evolution in EBR-II irradiated 20%-cold-worked type 316 stainless steel.[165]

The irradiation-induced phases do generally appear to be unstable with increasing fluence in EBR-II and HFIR, particularly for the tiny γ' and phosphide particles: this could, however, reflect cascade dissolution effects. The instabilities may also result from a slight decrease in RIS intensity (see Fig. 80, p. 236), as microstructure evolves.

Suppression of radiation-induced phase and diluted RIS, when helium causes increased sink concentrations, supports earlier suggestions of such effects by Kenik[135] and Odette,[251] and later by Maziasz.[165] However, this work adds several new insights regarding RIS dilution effects: (a) thermal phase formation is enhanced under irradiation above about 550°C, (b) RIS dilution varies in proportion to the early

Garner[36,37,227] suggest that helium does not affect RIS or precipitation, from comparison of EBR-II and HFIR data on 20%-cold-worked (CW) (DO-heat) 316 stainless steel and from comparison of one CW sample (600 to 625°C, 47 dpa) with one SA sample (535 to 555°C, 47 dpa) in HFIR. Maziasz,[165] from the same comparison of CW (DO-heat) 316 in EBR-II and HFIR (but also including thermal aging data) claims significant effects of helium, consistent with this thesis work; Farrell et al.[131] recently concur. Several discrepancies in phase identification have been pointed out,[165] which may contribute to the differences in conclusions. This thesis data definitely contributes additional evidence for the effects of helium on precipitation and RIS, although it is still not clear how long the effects will endure.

Finally, these data disagree with the results of Russell and coworkers[435-437,443] that positive misfit phases should be stabilized and negative misfit phases destabilized by vacancy supersaturation under neutron irradiation. To the contrary, the positive misfitting $M_{23}C_6$ is retarded and the negative misfitting γ', Fe_2P phosphide, and Laves phases are normally stabilized in this work. The problem may be in their assumption that the interstitial supersaturation is zero. Furthermore, this work definitely shows that RIS is the dominant factor in phase formation and stability in SA 316 under neutron irradiation. Strictly on the basis of misfits, however, it may be that the accumulation of defects to sinks as well as their supersaturations in the matrix should be considered. For helium injected and aged materials, this work supports the importance of vacancies to the formation of $M_{23}C_6$ (refs. 341, 359), as

this normally dominant phase fails to form in the vacancy undersaturation suggested by the data at 600°C. Conversely, Laves phase, which is undersize, does form, suggesting that it is stabilized by the vacancy deficiency.

To summarize, these data agree with the concept that many competing factors affect phase stability under irradiation,[435,437,439,440] in the absence of helium. Few anticipate the dominant role that RIS is found to play in the austenitic stainless steels. There is the general perception (possibly derived from higher damage rate experiments) that systems are highly driven to manifest very unnatural behavior under irradiation. This work, however, suggests that thermal processes still play a significant role, and are even effective in opposing some of the irradiation-induced effects, particularly under neutron irradiation. The peculiar effects of helium bring the situation of precipitation under irradiation back full circle to that perceived by Brinkman and Wiedersich[413] in 1964; apart from RIS, thermal precipitation should be enhanced under irradiation.

Suggested Future Experimental Work and Implications for Fusion Application

Several areas of new work arise from opened questions raised and by the need to better understand mechanisms suggested from these data. RIS dilution and bubble sink domination clearly can be transient effects whose duration depends on the degree of bubble nucleation achieved for a given amount of helium. Experiments at higher neutron fluence are

needed to assess the durations of RIS and void suppressions; these should also include more variations of early bubble nucleation to ascertain dependencies of these effects on the bubble concentration. Bubble nucleation can be manipulated by varying helium injection amounts and modes (hot versus cold) or by preirradiations in HFIR or ORR followed by long-term irradiation in FFTF, to test microstructural stability. Low and intermediate fluence data are important to track the microstructural evolution and to better determine how loop evolution, void formation, and phase stability are related.

For fusion, these data definitely indicate the danger of helium-enhanced void formation for SA 316, even at low fluences, above ~350°C. However, below ~350°C, the use of SA 316 appears safe and may actually be advantageous when considering welding. At higher temperatures, the SA 316 behavior reveals mechanisms which support efforts to gain the insight that undergirds the development of advanced irradiation-resistant alloys for fusion. The mechanism of bubble coarsening that precedes void formation in SA 316 helps to explain the benefits of tiny MC carbides to swelling resistance, as these trap fine bubbles at their interfaces. The effect of bubble dilution on RIS, as well as the couplings among RIS, phase stability and void formation, helps suggest that MC stability (negative RIS coupling), and hence swelling resistance, may be better for fusion than that found during FBR irradiation. Stress and flux effects have not been combined with the effects of helium for fusion; these may be more easily studied in SA 316 for application to alloy development as well.

CHAPTER VI

CONCLUSIONS

Conclusions and Summary of Results

Thermally Aged SA 316

1. Dislocation concentrations were low ($<3 \times 10^{13}$ m/m^3) and were generated during precipitate development; maximum network content at 550 to 700°C occurred coincident with peak precipitate nucleation.

2. Precipitation occurred at ~550 to 900°C, with maximum particle nucleation at ~600 to 700°C and maximum volume fraction at 800°C. The dominant phases progressed with temperature from $M_{23}C_6$ (τ) (560 to 600°C) to Laves (650 to 700°C) to χ (800°C) and finally to σ (900°C). A minor amount of M_6C (η) formed at 650 to 700°C. The phases were generally enriched in molybdenum and/or chromium. Laves and η were both enriched in silicon, but only η was enriched in nickel.

Helium Preinjected and Aged SA 316

3. Injection caused fine, concentrated "black-spot" loop damage which visibly coarsened upon aging at 400°C and above for times longer than 10,000 h. Frank interstitial loops grew, apparently by vacancy emission, while the total dislocation density was reduced, and yet the apparent stored interstitial content of the loops increased.

4. Fine bubbles formed after 10,000 h at 600 and 700°C, but not after 1000 h at 600°C; they coarsened considerably with temperature. The bubbles may not contain all the injected helium.

5. Helium preinjection caused Laves to replace $M_{23}C_6$ (τ) at 600°C, and eliminated τ from its normal mixture with Laves and σ phases at 700°C, thus altering thermal precipitation behavior.

EBR-II Irradiated SA 316

6. EBR-II irradiation at 500 to 630°C considerably increased dislocation generation compared to thermal aging (tenfold or more). Strong temperature dependence developed at higher fluences, with a low concentration at higher temperature (2×10^{13} m/m^3 at 630°C after 36 dpa).

7. Nearly all early voids were associated with precipitates at 500 to 630°C, but void swelling developed via continued void nucleation at 500 to 525°C, and via continued void growth at 625 to 630°C, as fluence increased. Swelling increased with fluence and/or temperature (but was only 1.5% at 630°C and 36 dpa). Bubbles appeared to be the major void nuclei. Many fine bubbles appeared in the matrix after 31 dpa at 500 to 525°C, but at higher temperatures bubbles formed, coalesced, and were then released by migrating dislocations.

8. Matrix precipitation was enhanced at 500 to 525°C but developed sluggishly at 625 to 630°C compared to aged SA 316. In contrast to thermal aging, M_6C (η) was the dominant phase under most conditions and completely replaced $M_{23}C_6$. At 630°C and 36 dpa, however, M_6C (η) and Laves phase were found in similar portions. Many small particles of irradiation-induced phases (G, γ', and A+B phosphides) formed at higher fluences, but these were minor contributors to the total precipitate volume. Strong phosphorus (500–625°C) and manganese (500°C) segregations

occurred at 8.4 dpa. The net effect of RIS caused the phases to be highly enriched in nickel and silicon and depleted in molybdenum and chromium compared to thermal precipitation. The irradiation-induced phases became unstable at higher fluences and apparently dissolved.

Helium-Preinjected and EBR-II Irradiated SA 316

9. Helium preinjection most strongly affected Frank loops in the dislocation structure; the loop structure was refined at 500°C, but eliminated at 625°C.

10. Preinjected helium greatly enhanced early bubble nucleation but totally suppressed void formation at 500 to 625°C after 8.4 dpa.

11. Helium preinjection virtually eliminated RIS at 500 to 625°C. No precipitation occurred at 500°C, whereas thermal precipitation was considerably enhanced at 625°C.

HFIR Irradiated SA 316

12. The dislocation structure progressed from "black-dot" plus Frank loops (55 to ~300°C) to Frank loops plus network (425 to 450°C) to loose network (500 to 640°C) with increased temperature at lower fluences. Dislocation concentrations peaked with fluence at 10 to 20 dpa but decreased with increased temperature; saturation was evident only at 615 to 640°C. At 500 to 640°C, dislocation concentrations are slightly lower and loops are absent relative to EBR-II irradiated specimens.

13. Frank loops and possibly the high concentrations of fine bubbles observed at 530 to 555°C after 47 dpa were considered anomalous,

because high void swelling appeared to force the specimen to bend, thus lowering temperatures late in the irradiation history.

14. Below 20 dpa, voids formed only at 425 to 450°C, coincident with copious $\gamma'(Ni_3Si)$ formation. Many bubbles formed at higher temperatures, but not below 350 to 400°C. Considerable void formation eventually occurred at 515 to 640°C, however, and swelling was then enhanced compared to EBR-II irradiation. Precipitate-associated void formation ceased above 650°C, as coarse matrix and huge grain boundary high-temperature bubbles predominated.

15. Precipitation occurred at 425 to 450°C and above, with $\gamma'(Ni_3Si)$ dominating at 425 to 450°C, $M_6C(\eta)$ at 515 to 555°C, Laves at 615 to 640°C and, finally, χ and σ dominating at 650°C and above. The amount of precipitate increased with temperature, but varied with increased fluence. At lower temperatures, RIS was strong (nickel and silicon enrichment, molybdenum depletion), but RIS diminished rapidly above 550°C; the result was nearly thermal precipitation at the higher temperatures.

Comparison with Previous Data

16. Data were generally in agreement with others, but with minor discrepancies. Thermally, the DO heat of SA 316 was prone toward formation of intermetallic compounds and fewer carbides than other heats of steel. Preinjected and aged material seemed more sluggish for bubble and loop evolutions than found by others. Under EBR-II irradiation, the SA (DO-heat) 316 was more prone to have precipitate-associated voids than matrix voids and contained fewer loops than other heats of steel.

Conclusions and Summary of Discussion

Suggested Couplings and Mechanisms from Results

17. Dislocation evolution and precipitate evolution appeared coupled during both aging and neutron irradiation. These data further suggested that Frank loop formation and RIS were somehow connected. Consistently, loop nucleation was minimal in bubble dominated sink structures. The role of migrating dislocation lines to drag, coalesce, and then distribute bubbles in the matrix appeared to be the major source of void nuclei at 625°C in EBR-II, and at 500 to 565°C in HFIR.

18. Void formation and irradiation-induced precipitation appeared mutually coupled through their dependence upon RIS (except at 600 to 640°C in HFIR). Increased helium content uncoupled the two phenomena, particularly when bubbles became the dominant sinks to shut off void formation and/or to dilute RIS. When bubbles were dominant sinks in either EBR-II or HFIR, they shut off precipitate-associated void growth as well. Increased helium either stimulated or prevented void formation, depending upon the contribution of bubbles to the total sink strength and their coarsening behavior. In helium preinjected and aged material, helium clusters and/or bubbles migrate and coalesce to cause a vacancy deficient matrix which then allows interstitial Frank loops to grow.

19. Precipitate nucleation in SA 316 was sensitive to the availability of heterogeneous nucleation sites, especially under aging. RIS caused the formation of radiation-induced or -modified phases to become

dependent upon the development of "microalloy" regions around sinks, particularly during EBR-II irradiation. However, phase formation then proceeds according to normal thermodynamics in the "microalloy" regions as if they were being aged. These data suggest that negative misfit phases were stabilized, either by vacancy deficiencies or interstitial fluxes. The phases (except Laves) exhibit limited compositional flexibility under irradiation; they either coupled positively (to form) or negatively (not to form) with the solute fluxes of RIS. Helium effects suggested a dynamic opposition between thermal processes and RIS that allowed thermal precipitation to be enhanced when RIS was suppressed. Finally, phosphorus and manganese were somehow involved when RIS was most intense.

Comparison of Results with Theory and Modeling Efforts

20. Dislocation data were generally consistent with loop trends predicted by previous loop nucleation and growth theory, the data were consistent with the stronger temperature dependencies indicated by Ghoniem and coworkers.[124-126] These data also confirmed the work of Garner and Wolfer[127] which indicated the importance of unfaulting and recovery processes in dislocation evolution under irradiation; however, these same data show far more temperature dependence for saturation dislocation densities than Garner and Wolfer anticipated. Loop nucleation sensitivities to RIS, helium content, and heat-to-heat variations in composition are not usually considered by theory.

21. Helium/bubble effects data overwhelmingly supported the work of Odette and coworkers,[25,31,180,181] which indicated that increased bubble nucleation either stimulated or suppressed void formation, to the extent that these bubbles dominated the total sink strength. The HFIR data also were reasonably consistent with nucleation and growth work of Ghoniem and Takata.[98] These data support the critical radius growth theories, but many experimentally determined critical radii appear larger than anticipated. These data confirmed the precipitate-assisted growth theory of Mansur,[266] but introduced the concepts that a bubble-dominated matrix can shut this mechanism off and that the phase particles must be RIS compatible. These data suggest that negative misfitting phases may act as interstitial sinks to aid void development. Further, this work indicates that dislocation dragging and coalescence of bubbles may be a major mechanism in enlarging bubbles beyond their critical size for conversion to voids. Finally, these data supported the coupling between void formation and RIS effects first proposed by Brager and Garner,[297] but not the crucial role of matrix nickel content which they imply.

22. Phase stability theories have failed to foresee the dominant role played by RIS in phase formation, stability, and compositional modification in neutron irradiated type 316 stainless steels. This work disagrees with the view advanced by Brager and Garner that $M_{23}C_6$ can become enriched in nickel and silicon or transform to M_6C. These data also indicate that some negative misfitting phases are stabiliized by neutron irradiation, contrary to the predictions of Russell and coworkers.

This work does confirm the idea that high concentrations of sinks (like bubbles) dilute RIS. However, this work further reveals that thermal processes are also enhanced under irradiation and that these oppose the radiation-induced processes influencing precipitation. Therefore, when RIS is suppressed by increased helium bubble nucleation, thermal precipitation is enhanced.

Suggested Future Experimental Work and Implications for Fusion Application

23. New work should include high fluence exposure and more variable starting microstructures (helium levels and distributions) to better understand the helium perturbation of normal behavior of SA 316 under EBR-II irradiation. New HFIR or ORR data should investigate earlier stages of microstructural development and the effects of flux and stress. Shorter time agings of helium-preinjected material at higher temperatures would reveal more details about loop growth and unfaulting and their relationship to bubble and phase evolutions.

24. These data suggest useful fusion application of SA 316 at temperatures of ~350°C or below, but dangerous helium-enhanced void swelling, even at low fluence, for higher irradiation temperatures. However, results on bubble suppression of void formation and dilution of RIS support the arguments that undergird the development of advanced alloys for fusion application.

REFERENCES

REFERENCES

1. R. E. Gold et al., Nucl. Technol./Fusion 1 (1981) 169–237.

2. P. J. Maziasz and T. K. Roche, J. Nucl. Mater. 103&104 (1982) 797–802.

3. J. O. Stiegler and E. E. Bloom, J. Nucl. Mater. 41 (1971) 341–344.

4. J. L. Straalsund, H. R. Brager, and J. J. Holmes, "Effects of Cold Work on Void Formation in Austenitic Stainless Steels," pp. 142–155 in Radiation-Induced Voids in Metals, eds. J. W. Corbett and L. C. Ianniello, USAEC CONF-710601 (1972).

5. E. E. Bloom and J. O. Stiegler, J. Nucl. Mater. 35 (1970) 244–246.

6. R. M. Brick, R. B. Gordon, and A. Phillips, Structure and Properties of Alloys, McGraw-Hill, New York, 1965, pp. 217–358.

7. F. B. Pickering, "Introduction: The Metallurgical Evaluation of Stainless Steel," pp. 1–42 in The Metallurgical Evaluation of Stainless Steel, ed., F. B. Pickering, American Society for Metals, Metals Park, OH, and The Metals Society, London, England, 1979.

8. The Making, Shaping and Treating of Steel, ed., H. E. McGannon, U.S. Steel, 9th ed., 1971.

9. B. Weiss and R. Stickler, Met. Trans. 3 (1972) 851–866.

10. J. E. Spruiell, J. A. Scott, C. S. Ary, and R. L. Hardin, Met. Trans. 4 (1973) 1533–1544.

11. D. V. Edmunds and R.W.K. Honeycombe, "Precipitation in Iron-Base Alloys," pp. 121–160 in Conf. Proc. Precipitation Processes in Solids, eds., K. C. Russell and H. I. Aaronson, The Metallurgical Society of AIME, Warrendale, PA (1978).

12. J. R. Keller, "The Selection of Cladding and Structural Materials," pp. 477–481 in Reactor Handbook, Vol. I Materials, ed., C. R. Tipton, 2nd ed., USAEC, Interscience Publ., Inc., New York, 1960.

13. S. H. Bush, "Materials for Nuclear Reactors," pp. 381–398 in The Science of Materials Used in Advanced Technology, eds., E. R. Parker and U. Colombo, John Wiley & Sons, New York, 1973.

14. J. E. Irvin and A. L. Bement, "Nature of Radiation Damage to Engineering Properties of Various Stainless Steels," pp. 278–327 in Effects of Radiation on Structural Materials, ASTM-STP 426, American Society for Testing and Materials, 1967.

15. A. F. Rowcliffe, G.J.C. Carpenter, H. F. Merrick, and R. B. Nicholson, "An Electron Microscope Investigation of High Temperature Embrittlement of Irradiated Stainless Steels," pp. 161–199 in Effects of Radiation on Structural Materials, ASTM-STP 426, American Society for Testing and Materials, 1967.

16. D. R. Olander, Fundamental Aspects of Nuclear Reactor Fuel Elements, Technical Information Center (TIC), USERDA, TID-26711-P2 (1976).

17. R. P. Smith and D. W. Cissel, "Past and Present Role of Fast Breeder Reactors in the United States of America," pp. 29–56 in Proc. Inter. Symp. Design, Construction and Operation Experience of Demonstration Liquid Metal Fast Breeder Reactors, IAEA, Vienna, STI/PUB/490 (1978).

18. J. Moore, "Past and Present Role of Fast Breeder Reactors in The United Kingdom," pp. 89–103 in Proc. Inter. Symp. Design, Construction and Operation Experience of Demonstration Liquid Metal Fast Breeder Reactors, IAEA, Vienna, STI/PUB/490 (1978).

19. B. A. Chin, R. J. Neuhold, and J. L. Straalsund, Nucl. Technol. 57 (1982) 426–435.

20. C. Cawthorne and E. J. Fulton, "The Influence of Irradiation Temperature on the Defect Structures in Stainless Steel," pp. 446–460 in Symp. The Nature of Small Defect Clusters, Vol. 2, ed., M. J. Makin, AERE Harwell, AERE-R-5269 (1966).

21. C. Cawthorne and E. J. Fulton, Nature **216** (1967) 575–576.

22. P. R. Heubotter and T. R. Bump, "Implications of Metal Swelling in Fast Reactor Design," pp. 84–124 in Radiation-Induced Voids in Metals, eds., J. W. Corbett and L. C. Ianniello, USAEC CONF-710601 (1972).

23. D. I. Norris, Radn. Effects **14** (1972) 1–37 and **15** (1972) 1–22.

24. Radiation Effects in Breeder Reactor Structural Materials, eds., M. L. Bleiberg and J. W. Bennett, TMS-AIME, New York (1977).

25. F. L. Ribe, Nucl. Technol. **34** (1977) 179–208.

26. C. C. Baker and M. A. Abdou, STARFIRE — A Commercial Tokamak Fusion Power Plant Study, Argonne National Laboratory, Argonne, IL, ANL/FFP-80-2 (September 1980).

27. R. W. Conn, J. Nucl. Mater. 85&86 (1979) 9—16.

28. E. E. Bloom, F. W. Wiffen, P. J. Maziasz, and J. O. Stiegler, Nucl. Technol. 31 (1976) 115—122.

29. G. L. Kulcinski, D. G. Doran, and M. A. Abdou, "Comparison of Displacement and Gas Production Rates in Current Fission and Future Fusion Reactors," pp. 329—351 in Properties of Reactor Structural Alloys after Neutron or Particle Irradiation, ASTM-STP-570, American Society for Testing and Materials, 1975.

30. T. A. Gabriel, B. L. Bishop, and F. W. Wiffen, Nucl. Technol. 38 (1978) 427—433.

31. G. R. Odette and M. W. Frei, "Potential Effects of Interactions Between Transmutants and Displaced Atoms in Controlled Thermonuclear Reactor First Walls," pp. 485—499 in Proc. of First Topical Meeting on the Technology of Controlled Nuclear Fusion, USAEC, Technical Information Center, CONF-740402-P2 (1974).

32. K. Farrell, Radn. Effects 53 (1980) 175—194.

33. G. R. Odette, P. J. Maziasz, and J. A. Spitznagel, J. Nucl. Mater. 103&104 (1981) 1289—1304.

34. N. H. Packan and K. Farrell, J. Nucl. Mater. 85&86 (1979) 677—681.

35. R. E. Stoller and G. R. Odette, "The Effect of Helium on Swelling in Stainless Steel: Influence of Cavity Density and Morphology," pp. 275—294 in Effects of Radiation on Materials: Eleventh Conference, eds., H. R. Brager and J. S. Perrin, American Society for Testing and Materials, ASTM-STP-782 (1982).

36. H. R. Brager and F. A. Garner, J. Nucl. Mater. 103&104 (1981) 993—998.

37. H. R. Brager and F. A. Garner, J. Nucl. Mater. 108&109 (1982) 347—358.

38. H. R. Brager and J. L. Straalsund, J. Nucl. Mater. 46 (1973) 134—158.

39. P. J. Barton, B. L. Eyre, and D. A. Stow, J. Nucl. Mater. 67 (1977) 181—199.

40. E. E. Bloom and J. O. Stiegler, "Effect of Irradiation on the Microstructure and Creep-Rupture Properties of Type 316 Stainless Steel," pp. 360–382 in Effects of Radiation on Substructure and Mechanical Properties of Metals and Alloys, ASTM-STP-529, American Society for Testing and Materials (1973).

41. E. H. Lee, P. J. Maziasz, and A. F. Rowcliffe, "The Structure and Composition of Phases Occurring in Austenitic Stainless Steels in Thermal and Irradiation Environments," pp. 191–218 in Conf. Proc. Phase Stability During Irradiation, eds., J. R. Holland, L. K. Mansur, and D. I. Potter, The Metallurgical Society of AIME, Warrendale, PA (1981).

42. D. J. Mazey and S. Francis, "Observations of Dislocation Structure and Cavities Formed by Annealing in Type 316 Steel after Ion Irradiation at Ambient Temperature," pp. 257–262 in Consultant Symp. The Physics of Irradiation Produced Voids, ed., R. S. Nelson AERE Harwell Report, AERE-R-7934 (January 1975).

43. D. J. Mazey and R. S. Nelson, "The Influence of Pre-Injected Helium on Void Swelling in Ion Irradiated Stainless Steel," pp. I-240–I-258 in Conf. Proc. Radiation Effects and Tritium Technology for Fusion Reactors, eds., J. S. Watson and F. W. Wiffen, USERDA, CONF-750989, Vol. 1 (1976).

44. F. A. Smidt and A. G. Pieper, "Helium Mobility and Bubble Formation in Type 316 Stainless Steel, Aluminum, and Vanadium," pp. 352–368 in Properties of Reactor Structural Alloys after Neutron or Particle Irradiation, ASTM-STP-570, American Society for Testing and Materials (1975).

45. E. E. Bloom and J. O. Stiegler, J. Nucl. Mater. **36** (1970) 331–334.

46. S. D. Harkness, B. K. Kessel, and S. G. McDonald, J. Nucl. Mater. **46** (1973) 159–168.

47. R. D. Cheverton and T. M. Sims, HFIR Core Nuclear Design, Oak Ridge National Laboratory Report, ORNL-4621 (July 1971).

48. J. A. Spitznagel, F. W. Wiffen, and F. V. Nolfi, J. Nucl. Mater. **85&86** (1979) 629–646.

49. P. J. Maziasz, F. W. Wiffen, and E. E. Bloom, "Swelling and Microstructural Changes in Type 316 Stainless Steel Irradiated under Simulated CTR Conditions," pp. I-259–I-288 in Conf. Proc. Radiation Effects and Tritium Technology for Fusion Reactors, eds., J. S. Watson and F. W. Wiffen, USERDA, CONF-750989, Vol. 1 (1976).

50. M. T. Robinson, "The Dependence of Radiation Effects on the Primary Recoil Energy," pp. 397–429 in Radiation-Induced Voids in Metals, eds., J. W. Corbett and L. C. Ianniello, USAEC CONF-710601 (1972).

51. M. T. Robinson, "The Theory of Radiation-Induced Defect Production," pp. 1–20 in Proc. Inter. Conf. Fundamental Aspects of Radiation Damage in Metals, eds., M. T. Robinson and F. W. Young, Jr., USERDA CONF-751006-P1 (1975).

52. M. T. Robinson, "The Theory of Radiation-Induced Defect Production," pp. 1–27 in Radiation Damage in Metals, eds., N. L. Peterson and S. D. Harkness, American Society for Metals, Metals Park, OH (1976).

53. D. N. Seidman, "Field Ion Microscopy Studies of the Defect Structure of the Primary State of Damage of Irradiated Metals," pp. 28–57 in Radiation Damage in Metals, eds., N. L. Peterson and S. D. Harkness, American Society for Metals, Metals Park, OH (1976).

54. K. L. Merkle, "Defect Production by Energetic Particle pp. 58–94 in Radiation Damage in Metals, eds., N. L. Peterson and S. D. Harkness, American Society for Metals, Metals Park, OH (1976).

55. F. W. Young, "Defect Annealing Processes in Metals," pp. 95–124 in Radiation Damage in Metals, eds., N. L. Peterson and S. D. Harkness, American Society for Metals, Metals Park, OH, (1976).

56. M. W. Thompson, Defects and Radiation Damage in Metals, Cambridge University Press, Great Britain (1969).

57. F. Seitz, Disc. Faraday Soc. **5** (1949) 271.

58. G. H. Kinchin and R. S. Pease, Rep. Prog. Phys. **18** (1955) 1.

59. M. T. Robinson, Phil. Mag. **12** (1965) 741–765.

60. J. Lindhard, V. Nielson, and M. Scharff, Kg. Danske Videnskab. Selskab, Mat. Fys. Medd. **33** (1963) 14.

61. J. Lindhard, V. Nielson, M. Scharff, and P. V. Thomsen, Kg. Danske Videnskab. Selskab, Mat. Fys. Medd. **33** (1963) 10.

62. "Recommendations for Displacement Calculations for Reactor/Accelerator Studies in Austenitic Steels," Nucl. Eng. Des. **33** (1975) 91.

63. O. S. Oen and M. T. Robinson, Appl. Phys. Lett. **2** (1963) 83.

64. J. A. Brinkman, J. Appl. Phys. **25** (1954) 961.

65. A. K. Seeger, "On the Theory of Radiation Damage and Radiation Hardening," pp. 250–273 in Proc. 2nd UN Inter. Conf. Peaceful Uses of At. Energy, Geneva, Vol. 6, United Nations, New York (1958).

66. J. B. Gibson, A. N. Goland, M. Nilgram, and G. H. Vineyard, Phys. Rev. **120** (1960) 1229–1253.

67. J. R. Beeler, Jr., "Computer Simulation of Radiation-Induced Void Nucleation and Growth," pp. 684–738 in Radiation-Induced Voids in Metals, eds., J. W. Corbett and L. C. Ianniello, USAEC CONF-710601 (1972).

68. I. M. Torrens and M. T. Robinson, "Computer Simulation of Atomic Displacement Cascades in Metals," pp. 739–756 in Radiation-Induced Voids in Metals, eds., J. W. Corbett and L. C. Ianniello, USAEC CONF-710601 (1972).

69. J. R. Beeler, Jr., Phys. Rev. **150** (1966) 470–487.

70. M. T. Robinson and I. M. Torrens, Phys. Rev. B **9** (1974) 5008.

71. H. L. Heinisch, J. Nucl. Mater. **103&104** (1981) 1325–1330.

72. H. L. Heinisch, J. Nucl. Mater. **108&109** (1982) 62–66.

73. D. G. Doran, Rad. Effects **2** (1970) 249.

74. H. L. Heinisch, D. G. Doran, and D. M. Schwartz, "Simulation of Short-Term Annealing of Displacement Cascades in Face Centered Cubic Metals," pp. 191–200 in Effects of Radiation on Materials: Tenth Conference, ASTM-STP-725, American Society for Testing and Materials (1981).

75. M. L. Jenkins and C. A. English, J. Nucl. Mater. **108&109** (1982) 46–61.

76. C. A. English, J. Nucl. Mater. **108&109** (1982) 104–123.

77. F. W. Wiffen and J. O. Stiegler, "Recent Progress in CTR Bulk Radiation Effects Studies," pp. 135–147 in Proc. Second Topical Meeting on the Technology of Controlled Nuclear Fusion, USERDA CONF-760935 (1976).

78. G. R. Odette and D. G. Doran, "Radiation Damage Analysis as Applied to Fusion Reactor First Walls," pp. 1485–1500 in Proc. Second Topical Meeting on the Technology of Controlled Nuclear Fusion, USERDA CONF-760935 (1976).

79. A. N. Goland, J. Nucl. Mater. 85&86 (1971) 453–461.

80. J. Weitman, N. Daverhög, and S. Farvolden, Trans. Am. Nucl. Soc. 13 (1970) 557.

81. I. R. Birss, J. Nucl. Mater. 34 (1970) 241–259.

82. W. N. McElroy and H. Farrar IV, "Helium Production in Stainless Steel and Its Constituents as Related to LMFBR Development Programs," pp. 187–229 in Radiation Induced Voids in Metals, eds., J. W. Corbett and L. C. Ianniello, USAEC CONF-710601 (1972).

83. T. A. Gabriel, J. D. Amburgey, and N. M. Greene, Nucl. Sci. Engr. 61 (1976) 21–32.

84. I. R. Birss, J. Nucl. Mater. 34 (1970) 241–259.

85. F. W. Wiffen et al., "The Production Rate of Helium During Irradiation of Nickel in Thermal Spectrum Fission Reactors," to be published in Journal of Nuclear Materials.

86. R. Blackburn, Met. Rev. 11 (1966) 159–176.

87. D. J. Reed, Rad. Effects 31 (1977) 129–147.

88. D. E. Rimmer and A. H. Cottrell, Phil. Mag. 2 (1957) 1345–1353.

89. W. Bauer and W. D. Wilson, "Helium Migration in Metals," pp. 230–247 in Radiation Induced Voids in Metals, eds., J. W. Corbett and L. C. Ianniello, USAEC CONF-710601 (1972).

90. W. D. Wilson and C. L. Bisson, Rad. Effects 19 (1973) 53–58.

91. D. Kaletta, Rad. Effects 47 (1980) 237–252.

92. W. Schilling, "Diffusion of Helium in Metals," pp. 303–308 in Proc. of Yamada Conf. V, Point Defects and Defect Interactions in Metals, eds. J. Takamura, W. Doyama, and M. Kiritani, University of Tokyo Press, Japan (1982).

93. N. M. Ghoniem, S. Sharafat, and L. K. Mansur, "The Kinetics of the Interaction Between Helium and Displacement Damage in Irradiated Materials," pp. 865–868 in Proc. of Yamada Conf. V, Point Defects and Defect Interactions in Metals, eds., J. Takamura, W. Doyama, and M. Kiritani, University of Tokyo Press, Japan (1982).

94. B. Russell and I. J. Hastings, J. Nucl. Mater. 17 (1965) 30–36.

95. J. R. Cost and D. L. Johnson, J. Nucl. Mater. 36 (1970) 230–233.

96. W. D. Wilson, "Theory of Diffusion and Trapping of Hydrogen and Helium in Metals, a Review," pp. 1025–1044 in Fundamental Aspects of Radiation Damage in Metals, eds., M. T. Robinson and F. W. Young, Jr., USERDA CONF-751006-P2 (1975).

97. N. M. Ghoniem, S. Sharafat, J. Williams, and L. K. Mansur, "A Theory of Helium Transport and Clustering in Materials Under Irradiation," J. Nucl. Mater. 117 (1983) 98.

98. N. M. Ghoniem and M. L. Takata, J. Nucl. Mater. 105 (1982) 276–292.

99. G. L. Kulcinski, "Radiation Damage: The Second Most Serious Obstacle to Commercialization of Fusion Power," PP. I-17–I-72 in Conf. Proc. Radiation Effects and Tritium Technology for Fusion Reactors, eds., J. S. Watson and F. W. Wiffen, USERDA CONF-750989, Vol. 1 (1976).

100. K. Farrell and R. T. King, Met. Trans. 4 (1973) 1223.

101. J. F. Bates, F. A. Garner, and F. M. Mann, J. Nucl. Mater. 103&104 (1981) 999–1004.

102. F. M. Mann, "Transmutation of Alloys in MFE Facilities as Calculated for REAC (A computer code system for activation and transmutation)," Hanford Engineering Laboratory Report, HEDL-TME81-37 (August 1982).

103. F. A. Garner, F. M. Mann, and H. R. Brager, "Measurement and Calculation of Solid Transmutants Formed in AISI 316," pp. 198–209 in DAFS Quart. Progr. Rept. Sept. 30, 1981, DOE/ER-0046/7.

104. M. R. Rühle, "Transmission Electron Microscopy of Irradiation-Induced Defects," pp. 255–291 in Radiation Induced Voids in Metals, eds., J. W. Corbett and L. C. Ianniello, USAEC CONF-710601 (1972).

105. R. E. Smallman and K. H. Westmacott, J. Appl. Phys. 30 (1959) 603.

106. M. J. Makin, A. D. Whapham, and F. J. Minter, Phil. Mag. 6 (1961) and 7 (1965) 285.

107. H.G.F. Wilsdorf and D. Kuhlmann-Wilsdorf, J. Nucl. Mater. 5 (1962) 178.

108. J. S. Aranigo, J. R. Low, Jr., and U. E. Wolff, Radiation Effects on the Mechanical Properties and Microstructure of Type 304 Stainless Steel, USAEC Report ADED-4552, General Electric Company, Vallecitos Atomic Laboratory, April 13, 1964.

109. E. E. Bloom, W. R. Martin, J. O. Stiegler, and J. R. Weir, J. Nucl. Mater. 22 (1967) 68.

110. P. J. Maziasz, Trans. Am. Nucl. Soc. 39 (1981) 433.

111. E. E. Bloom, J. O. Stiegler, and C. J. McHargue, Rad. Effects 14 (1972) 231.

112. L. E. Thomas and J. M. Beeston, J. Nucl. Mater. 107 (1982) 159.

113. J. I. Bramman et al., "Void Swelling and Microstructural Changes in Fuel Pin Cladding and Unstressed Specimens Irradiated in DFR," pp. 479–507 in Radiation Effects in Breeder Reactor Structural Materials, eds., M. L. Bleiberg and J. W. Bennett, TMS-AIME, New York (1977).

114. H. R. Brager, J. L. Straalsund, J. J. Holmes, and J. F. Bates, Met. Trans. 2 (1971) 1893.

115. H. R. Brager and J. L. Straalsund, J. Nucl. Mater. 47 (1973) 105.

116. L. LeNaour, M. Vouillon, and V. Levy, "Influence of Dose and Dose Rate on the Microstructure of Solution-Annealed 316 Irradiated Around 600°C," pp. 310–324 in Effects of Irradiation on Materials: Eleventh Conf., ASTM-STP-782, American Society for Testing and Materials, 1982.

117. D. J. Mazey, J. Nucl. Mater. 35 (1970) 60–66.

118. L. K. Mansur, Nucl. Technol. 40 (1978) 5.

119. A. D. Brailsford and R. Bullough, J. Nucl. Mater. 44 (1972) 121–135.

120. For a list of theoretical work, see references in R. M. Mayer and L. M. Brown, J. Nucl. Mater. 95 (1980) 46.

121. L. M. Brown, A. Kelly, and R. M. Mayer, Phil. Mag. **19** (1969) 721.

122. M. Kiritani, J. Phys. Soc. Japan **35** (1973) 95.

123. M. R. Hayns, J. Nucl. Mater. **56** (1975) 267.

124. N. M. Ghoniem and D. D. Cho, Phys. Stat. Sol. a **54** (1979) 171.

125. N. M. Ghoniem and S. Sharafat, J. Nucl. Mater. **92** (1980) 121.

126. N. M. Ghoniem, J. Nucl. Mater. **89** (1980) 359.

127. F. A. Garner and W. G. Wolfer, "A Model for the Evolution of Network Dislocation Density in Irradiated Metals, pp. 1073–1087 in Effects of Irradiation on Materials: Eleventh Conf. ASTM-STP-782, American Society for Testing and Materials, 1982.

128. H. R. Brager et al., "Stress-Affected Microstructural Development and the Creep-Swelling Interrelationships," pp. 727–756 in Radiation Effects in Breeder Reactor Structural Materials, eds., M. L. Bleiberg and J. W. Bennett, TMS-AIME, New York (1977).

129. T. M. Williams, J. Nucl. Mater. **79** (1979) 28.

130. N. H. Packan and K. Farrell, "Radiation-Induced Swelling in an Austenitic Alloy: Observations and Interpretation of the Effects of Helium," to be published in Nuclear Technology.

131. K. Farrell, P. J. Maziasz, E. H. Lee, and L. K. Mansur, Radn. Effects **78** (1983) 277–295.

132. S. C. Agarwal et al., J. Nucl. Mater. **85&86** (1979) 653.

133. W. J. Choyke et al., J. Nucl. Mater. **85&86** (1979) 647.

134. S. Wood et al., "Microstructural Development in Dual-Ion Bombarded 316 Stainless Steel," pp. 455–469 in Effects of Radiation on Materials: Tenth Conference, ASTM-STP-725, American Society for Testing and Materials, 1981.

135. E. A. Kenik, J. Nucl. Mater. **85&86** (1979) 659.

136. E. A. Kenik and E. H. Lee, "Influence of Injected Helium on the Phase Instability of Ion-Irradiated Stainless Steel, pp. 493–503 in Conf. Proc. Phase Stability under Irradiation, eds., J. R. Holland, L. K. Mansur, and D. I. Potter, The Metallurgical Society of AIME, Warrendale, PA (1981).

137. R. S. Barnes and D. J. Mazey, Proc. Roy Soc. London **A275** (1963) 47.

138. J. O. Stiegler and E. E. Bloom, J. Nucl. Mater. 33 (1969) 173–185.

139. J. J. Holmes, R. E. Robbins, J. L. Brimhall, and B. Mastel, Acta Met. 16 (1968) 955.

140. R. S. Barnes and D. J. Mazey, Phil. Mag. 5 (1960) 1247.

141. P. Vela and R. Russell, J. Nucl. Mater. 19 (1966) 321–326.

142. P. Vela and B. Russell, J. Nucl. Mater. 19 (1966) 327–340.

143. A. F. Rowcliffe, J. Nucl. Mater. 18 (1966) 60–65.

144. R. Nagasaki et al., "Behavior of Helium Gas Bubbles in Neutron-Irradiated Beryllium and Beryllium Alloys," pp. 331–347 in Radiation Damage in Reactor Materials, IAEA-SM-120, Vol. 2, International Atomic Energy Agency, Vienna, 1969.

145. P. Lindhagen, "Observations on Helium Bubbles in an Irradiated 18 Cr-27 Ni Austenitic Stainless Steel," pp. 401–408 in Radiation Damage in Reactor Materials, IAEA-SM-120, Vol. 2, International Atomic Energy Agency, Vienna, 1969.

146. D. N. Braski, H. Schroeder, and H. Ullmaier, J. Nucl. Mater. 83 (1979) 265–277.

147. P. J. Goodhew and S. K. Tyler, Proc. Roy Soc. London A377 (1981) 151–184.

148. E. Ruedl, O. Gautsch, and E. Storoste, Rad. Effects 15 (1972) 275–276.

149. K. Shiraishi and T. Murata, J. Nucl. Sci. Technol. 3 (1966) 466–472.

150. I. O. Smith and B. Russell, J. Nucl. Mater. 35 (1970) 137–157.

151. G. K. Walker, J. Nucl. Mater. 37 (1970) 171–176.

152. J. Rothaut and H. Schroeder, J. Nucl. Mater. 103&104 (1981) 1023–1034.

153. K. Y. Chen and J. R. Cost, J. Nucl. Mater. 52 (1974) 59–74.

154. D. A. Woodford, J. P. Smith, and J. Moteff, J. Nucl. Mater. 29 (1969) 103–110.

155. H. Shinno et al., J. Nucl. Mater. 97 (1981) 291–299.

156. R. S. Nelson, J. Nucl. Mater. 31 (1969) 153.

157. J. A. Turnbull and R. M. Cornell, J. Nucl. Mater. 36 (1970) 161–168.

158. J. A. Turnbull and R. M. Cornell, J. Nucl. Mater. 41 (1971) 156–160.

159. O. Gautsch, J. Nucl. Mater. 35 (1970) 109–114.

160. W. R. Martin and J. Weir, "Solutions to the Problems of High Temperature Irradiation Embrittlement," pp. 440–457 in Effects of Radiation on Structural Materials, ASTM-STP 426, American Society for Testing and Materials, 1967.

161. H. R. Brager and R. E. Robbins, Trans. Met. Soc. AIME 242 (1968) 2010–2011.

162. A. J. Manley and D. Rhodes, "Helium Generation and Distribution in Thermal Reactor Irradiated 20% Cr, 25% Ni, Nb Stabilized Stainless Steel," pp. 103–107 in Proc. Inter. Conf. Irradiation Embrittlement and Creep in Fuel Cladding and Core Components, British Nuclear Energy Society, London, 1973.

163. R. E. Robbins, J. Nucl. Mater. 33 (1969) 101–102.

164. F. W. Wiffen and E. E. Bloom, Nucl. Technol. 25 (1975) 113–123.

165. P. J. Maziasz, J. Nucl. Mater. 108&109 (1982) 359–384.

166. G. W. Greenwood, A.J.E. Foreman, and D. E. Rimmer, J. Nucl. Mater. 4 (1959) 305–324.

167. G. W. Greenwood and M. V. Speight, J. Nucl. Mater. 10 (1963) 140–144.

168. P. G. Shewmon, Trans. Met. Soc. AIME 230 (1964) 1134–1137.

169. E. E. Gruber, J. Appl. Phys. 38 (1967) 243–250.

170. F. A. Nichols, J. Nucl. Mater. 30 (1969) 143–165.

171. L. E. Willertz and P. J. Shewmon, Met. Trans. 1 (1970) 2217–2223.

172. M. V. Speight, J. Nucl. Mater. 12 (1964) 216–220.

173. R. S. Barnes, J. Nucl. Mater. 11 (1964) 135–148.

174. J. R. Willis and R. Bullough, J. Nucl. Mater. 32 (1969) 76–87.

175. J. R. Cost and K. Y. Chen, J. Nucl. Mater. 67 (1977) 265–272.

176. W. G. Wolfer, "High-Density Equation of State for Helium and Its Applications to Bubbles in Solids," pp. 201–212 in Effects of Radiation on Materials: Tenth Conf., eds. H. R. Brager and J. S. Perrin, American Society for Testing and Materials, ASTM-STP-725, 1981.

177. D. R. Bearley and D. A. MacInnes, J. Nucl. Mater. 95 (1980) 239–252.

178. R. Bullough and R. C. Perrin, "Growth, Stability, and Interactions of Voids and Gas Bubbles in Solids," pp. 233–251 in Radiation Damage in Reactor Materials, IAEA-SM-120, Vol. 2, International Atomic Energy Agency, Vienna, 1969.

179. F. V. Nolfi, Jr., and H. Wiedersich, Acta Met. 22 (1974) 1087–1097.

180. G. R. Odette and S. C. Langley, "Modeling of Synergistic Effects of Displaced Atom and Transmutant Damage in Fission and Fusion Environments," pp. I-395–I-416 in Conf. Proc. Radiation Effects and Tritium Technology for Fusion Reactors, eds., J. S. Watson and F. W. Wiffen, USERDA, CONF-750989, Vol. I, 1976.

181. R. E. Stoller and G. R. Odette, J. Nucl. Mater. 103&104 (1981) 1361–1365.

182. B. B. Glasgow, A. Si-Ahmed, W. G. Wolfer, and F. A. Garner, J. Nucl. Mater. 103&104 (1981) 981–986.

183. M. R. Hayns, "The Transition from Gas Bubble to Void Growth," AERE Harwell Report AERE-R-8806 (May 1979).

184. J. R. Townsend, J. Nucl. Mater. 108&109 (1982) 544–549.

185. L. K. Mansur and W. A. Coghlan, "Mechanisms of Helium Interaction with Radiation Effects in Metals and Alloys," to be published in Journal of Nuclear Materials.

186. S. D. Harkness and Che-Yu Li, "A Model for Void Formation in Metals Irradiated in a Fast-Neutron Environment," pp. 189–214 in Radiation Damage in Reactor Materials, IAEA-SM-120, Vol. 2, International Atomic Energy Agency, Vienna, 1969.

187. B. Mastel and J. L. Brimhall, J. Nucl. Mater. 28 (1968) 115–117.

188. J. E. Cunningham, "Severe Radiation Damage to Aluminum Alloys," Oak Ridge National Laboratory Report, ORNL-TM-2138 (1968).

189. J. L. Brimhall and B. Mastel, J. Nucl. Mater. 29 (1969) 123.

190. J. O. Stiegler, K. Farrell, C.K.H. DuBose, and R. T. King, "High-Fluence Neutron Irradiation Damage in Aluminum," pp. 215–232 in Radiation Damage in Reactor Materials, IAEA-SM-120, Vol. 2, International Atomic Energy Agency, Vienna, 1969.

191. J. L. Brimhall and B. Mastel, Rad. Effects 3 (1970) 203.

192. R. C. Rau, R. L. Ladd, and J. Moteff, J. Nucl. Mater. 33 (1969) 324.

193. F. W. Wiffen and J. O. Stiegler, J. Metals 117 (1968) A.

194. Y. Adda, "Report on the CEA Program of Investigations of Radiation-Induced Cavities in Metals: Presentation of Some Results," pp. 31–83 in Radiation-Induced Voids in Metals, eds., J. W. Corbett and L. C. Ianniello, USAEC CONF-710601, 1972.

195. J. O. Stiegler, "Void Formation in Neutron-Irradiated Metals," pp. 292–337 in Radiation-Induced Voids in Metals, eds., J. W. Corbett and L. C. Ianniello, USAEC CONF-710601, 1972.

196. D. O. Northwood, "Irradiation Damage in Zirconium and Its Alloys," At. Energy Rev. 15-4 (1977) 547–609.

197. M. Kiritani and S. Yoshida, J. Phys. Soc. Japan 18 (1963) 215.

198. J. N. Greenwood, D. R. Miller, and J. W. Suiter, Acta Met. 2 (1954) 250.

199. R. S. Barnes, Proc. Phys. Soc. 65 (1952) 512.

200. R. S. Nelson and D. J. Mazey, "Void Formation in Stainless Steel During Charged-Particle Irradiation at Elevated Temperatures," pp. 157–163 in Radiation Damage in Reactor Materials, IAEA-SM-120, Vol. 2, International Atomic Energy Agency, Vienna, 1969.

201. G. L. Kulcinski, J. L. Brimhall, and H. E. Kissinger, "Production of Voids in Pure Metals by High-Energy Heavy-Ion Bombardment," pp. 449–478 in Radiation-Induced Voids in Metals, eds., J. W. Corbett and L. C. Ianniello, USAEC CONF-710601, 1972.

202. R. S. Nelson et al., "Void Formation in Metals During Ion Bombardment," pp. 430–448 in Radiation-Induced Voids in Metals, eds., J. W. Corbett and L. C. Ianniello, USAEC CONF-710601, 1972.

203. K. Urban, Phys. Stat. Solidi 3 (1970) K167–K168.

204. K. Urban, Phys. Stat. Solidi 4 (1971) 761–772.

205. D.I.R. Norris, Nature 227 (1980) 830.

206. M. Ohring, Mater. Sci. Eng. 7 (1971) 158–167.

207. F. A. Schmidt, Jr., and S. A. Metz, "Production of Vacancy Condensates by Laser Bombardments," pp. 613–629 in Radiation-Induced Voids in Metals, eds., J. W. Corbett and L. C. Ianniello, USAEC CONF-710601, 1972.

208. "How Do We Solve the Void Problem?" Agenda Discussion Section, pp. 400–408 in Irradiation Effects on Structural Alloys for Nuclear Reactor Applications, ASTM-STP-484, American Society for Testing and Materials, 1970.

209. J. J. Holmes and J. L. Straalsund, Trans. Am. Nucl. Soc. 13 (1970) 559.

210. T. Lauritzen, A. Withrop, and U. Wolff, Nucl. Eng. Design 9 (1969) 265.

211. J. M. Leitnaker, E. E. Bloom, and J. O. Stiegler, J. Nucl. Mater. 49 (1973/74) 57.

212. E. E. Bloom, J. O. Stiegler, A. F. Rowcliffe, and J. M. Leitnaker, Scripta Met. 10 (1976) 303–308.

213. J. F. Bates, "Irradiation-Induced Swelling Variations Resulting from Compositional Modifications of Type 316 Stainless Steels," pp. 369–387 in Properties of Reactor Structural Alloys After Neutron or Particle Irradiation, ASTM-STP-570, American Society for Testing and Materials, 1975.

214. F. A. Garner et al., "Summary Report on the Alloy Development Intercorrelation Program Experiment," pp. 147–175 in Correlation of Neutron and Charged Particle Damage, ed., J. O. Stiegler, USERDA CONF-760673 (1976).

215. F. A. Garner and J. J. Laidler, "Review of Charged Particle Intercorrelation Programs," pp. 177–240 in Correlation of Neutron and Charged Particle Damage, ERDA CONF-760673 (1976).

216. W. G. Johnston, N. H. Packan, and F. A. Smidt, "Summary of Workshop Discussion," pp. 313–347 in Correlation of Neutron and Charged Particle Damage, ERDA CONF-760673 (1976).

217. N. H. Packan, K. Farrell, and J. O. Stiegler, J. Nucl. Mater. 78 (1978) 143–155.

218. L. K. Mansur, J. Nucl. Mater. 78 (1978) 156–160.

219. A. D. Brailsford and L. K. Mansur, J. Nucl. Mater. 71 (1979) 110–116.

220. J. O. Stiegler and L. K. Mansur, Ann. Rev. Mater. Sci. 9 (1979) 405–454.

221. S. D. Harkness and Che-Yu Li, Met. Trans. 2 (1971) 1457–1470.

222. T. A. Kenfield, W. K. Appleby, H. J. Busboom, and W. L. Bell, J. Nucl. Mater. 75 (1978) 85–97.

223. E. H. Lee, A. F. Rowcliffe, and E. A. Kenik, J. Nucl. Mater. 83 (1979) 79–89.

224. F. A. Garner, "The Influence of Reactor Spectra and Irradiation Temperature on the Swelling of AISI 316 Stainless Steel," to be published in DAFS Quarterly Progress Report, DOE/ET-0065.

225. F. A. Garner, J. J. Laidler, and G. L. Guthrie, "Development and Evaluation of a Stress-Free Swelling Correlation for 20 Percent Cold-Worked Type 316 Stainless Steel,"pp. 208–226 in Irradiation Effects on the Microstructure and Properties of Metals, ASTM-STP-611, American Society for Testing and Materials, 1976.

226. W. K. Appleby, E. E. Bloom, J. E. Flinn, and F. A. Garner, "Swelling in Neutron-Irradiated 300-Series Stainless Steels," pp. 509–541 in Radiation Effects in Breeder Reactor Structural Materials, eds., M. L. Bleiberg and J. W. Bennett, TMS-AIME, New York (1977).

227. H. R. Brager and F. A. Garner, J. Nucl. Mater. 117 (1983) 159–176.

228. P. J. Maziasz and M. L. Grossbeck, "Swelling and Microstructure of HFIR-Irradiated 20%-Cold-Worked Types 316 and 316 + 0.23 wt % Ti," pp. 43–69 in ADIP Quart. Progr. Rept. Dec. 31, 1980, DOE/ER/0045/5.

229. P. J. Maziasz and M. L. Grossbeck, "Microstructural Development in 20%-Cold-Worked Type 316 Stainless Steel and Titanium-Modified Type 316 Stainless Steel Irradiated in the HFIR: Fluence Dependence of the Cavity Component," pp. 28–56 in ADIP Quart. Progr. Rept. Mar. 31, 1981, DOE/ER/0045/6.

230. D. W. Keefer and A. G. Pard, J. Nucl. Mater. 45 (1972/73) 55–59.

231. J. S. Armijo and T. Lauritzen, "Deuteron-Generated Void Formation in Austenitic Stainless Steels," pp. 479–498 in Radiation-Induced Voids in Metals, eds., J. W. Corbett and L. C. Ianniello, USAEC CONF-710601 (1972).

232. S. G. McDonald and A. Taylor, "Void Swelling Behavior of Types 304 and 316 Stainless Steel Irradiated with 4-MeV Ni^+ Ions," pp. 228–243 in Effects of Radiation on Substructure and Mechanical Properties of Metals and Alloys, ASTM-STP-529, American Society for Testing and Materials (1973).

233. F. A. Garner et al., "Simulation of High Fluence Swelling Behavior in Technological Materials," pp. 543–569 in Radiation Effects in Breeder Reactor Structural Materials, eds., M. L. Bleiberg and J. W. Bennett, TMS-AIME, New York (1977).

234. M. J. Makin et al., "UKAEA Void Simulation in Fast Reactor Structural Materials," pp. 645–665 in Radiation Effects in Breeder Reactor Structural Materials, eds., M. L. Bleiberg and J. W. Bennett, TMS-AIME, New York (1977).

235. M. Terasawa et al., "The Influence of Metallurgical Variables on Void Swelling in Type 316 Steel," pp. 687–707 in Radiation Effects in Breeder Reactor Structural Materials, eds., M. L. Bleiberg and J. W. Bennett, TMS-AIME, New York (1977).

236. J. N. McGruer et al., J. Nucl. Mater. **74** (1978) 174–177.

237. F. V. Nolfi, Jr., and G. Ayrault, "Microstructural Evolution During Dual-Ion Irradiation of Candidate Fusion Reactor Materials," p. B.2 in Inter. Conf. Irradiation Behavior of Metallic Materials for Fast Reactor Core Components, eds., J. Poirier and J. M. Dupouy, Ajaccio, France (1979).

238. G. Ayrault, H. A. Hoff, F. V. Nolfi, Jr., and A.P.L. Turner, J. Nucl. Mater. **103&104** (1981) 1035–1040.

239. J. A. Spitznagel et al., J. Nucl. Mater. **103&104** (1981) 1463–1468.

240. M. Shimada and H. Kamei, J. Nucl. Mater. **103&104** (1981) 1481–1486.

241. A. Kolayama, G. Ayrault, and B. A. Loomis, "Influence of Helium Injected Schedule and Prior Thermomechanical Treatment on the Microstructure of Ion-Irradiated Type 316 Stainless Steel," pp. 151–166 in DAFS Quart. Progr. Rept. November 1982, DOE/ER/0046/1.

242. J. A. Hudson, J. Nucl. Mater. **60** (1976) 89–106.

243. T. M. Williams, D. R. Arkell, and B. L. Eyre, J. Nucl. Mater. **68** (1977) 69–81.

244. T. M. Williams, D. R. Arkell, and B. L. Eyre, J. Nucl. Mater. **88** (1980) 111–120.

245. J. M. Makin, J. Nucl. Mater. **107** (1982) 133–147.

246. F. A. Garner, "The Microchemical Evolution of Irradiated Stainless Steels," pp. 165–190 in Conf. Proc. Phase Stability under Irradiation, eds., J. R. Holland, L. K. Mansur, and D. I. Potter, The Metallurgical Society of AIME, Warrendale, PA (1981).

247. T. T. Claudson, J. J. Holmes, J. L. Straalsund, and H. R. Brager, pp. 165–187 in Radiation Damage in Reactor Materials, IAEA-SM-120, Vol. 2, International Atomic Energy Agency, Vienna, 1969.

248. P. T. Heald and M. V. Speight, Acta Met. **23** (1975) 1389–1399.

249. W. G. Wolfer, L. K. Mansur, and J. A. Sprague, "Theory of Swelling and Irradiation Creep," pp. 841–864 in Radiation Effects in Breeder Reactor Structural Materials, eds., M. L. Bleiberg and J. W. Bennett, TMS-AIME, New York (1977).

250. K. C. Russell, Acta Met. **26** (1978) 1615–1630.

251. G. R. Odette, J. Nucl. Mater. **85&86** (1979) 533–545.

252. H. Wiedersich, Radn. Effects **12** (1972) 111–125.

253. S. B. Fisher and K. R. Williams, Radn. Effects **14** (1972) 165–170.

254. F. S. Ham, J. Appl. Phys. **30** (1959) 915.

255. W. G. Wolfer and M. Ashkin, J. Appl. Phys. **47** (1976) 791–800.

256. M. R. Hayns, J. Nucl. Mater. **79** (1979) 323–337.

257. V. F. Sears, J. Nucl. Mater. **39** (1971) 18–26.

258. L. K. Mansur, P. R. Okamoto, A. Taylor, and Che-Yu Li, "Surface Reaction Limited Void Growth," pp. 272–289 in Properties of Reactor Structural Alloys after Neutron Irradiation, ASTM-STP-570, American Society for Testing and Materials (1975).

259. P. J. Maziasz and M. L. Grossbeck, J. Nucl. Mater. **103&104** (1981) 987–992.

260. B. Loomis, G. Ayrault, S. Gerber, and Z. Wang, "Cavity Formation and Solute Segregation in Dual-Ion Irradiated Fe-20 Ni-15 Cr Alloy," pp. 145–156 in DAFS Quart. Progr. Rept. August 1982, DOE/ER/0046/10.

261. N. H. Packan and K. Farrell, "Ion Damage in 316 Stainless Steel Over a Broad Dose Range," pp. 885–894 in Effects of Radiation on Materials: Eleventh Conference, eds., H. R. Brager and J. S. Perrin, American Society for Testing and Materials, ASTM-STP-782 (1982).

262. A. D. Brailsford, R. Bullough, and M. R. Hayns, J. Nucl. Mater. 60 (1976) 246.

263. A. D. Brailsford and R. Bullough, J. Nucl. Mater. 69&70 (1978) 434–450.

264. L. K. Mansur and M. H. Yoo, J. Nucl. Mater. 74 (1978) 228.

265. L. K. Mansur, M. R. Hayns, and E. H. Lee, "Mechanisms Affecting Swelling in Alloys with Precipitates," pp. 359–382 in Conf. Proc. Phase Stability under Irradiation, eds., J. R. Holland, L. K. Mansur, and D. I. Potter, The Metallurgical Society of AIME, Warrendale, PA (1981).

266. L. K. Mansur, Phil. Mag. A 44 (1981) 867–877.

267. A. D. Brailsford and L. K. Mansur, J. Nucl. Mater. 103&104 (1981) 1403–1408.

268. L. K. Mansur, W. A. Coghlan, and A. D. Brailsford, J. Nucl. Mater. 85&86 (1979) 591–595.

269. M. Yoo, J. Nucl. Mater. 68 (1977) 193–204.

270. N. M. Ghoniem and G. L. Kulcinski, J. Nucl. Mater. 69&70 (1978) 816.

271. N. M. Ghoniem and G. L. Kulcinski, Radn. Effects 41 (1979) 81–89.

272. N. M. Ghoniem and H. Gurol, Radn. Effects 55 (1981) 209–222.

273. M. H. Yoo and L. K. Mansur, J. Nucl. Mater. 85&86 (1979) 571–575.

274. K. C. Russell, Acta Met. 19 (1971) 753–758.

275. J. L. Katz and H. Wiedersich, J. Chem. Phys. 55 (1971) 1414.

276. K. C. Russell, Acta Met. 20 (1972) 899–907.

277. B.T.M. Loh, Acta Met. 20 (1972) 1305–1311.

278. J. L. Katz and H. Wiedersich, J. Nucl. Mater. 46 (1973) 41–45.

279. H. Wiedersich, J. J. Burton, and J. L. Katz, J. Nucl. Mater. 51 (1974) 287.

280. K. Russell, J. Nucl. Mater. 61 (1976) 330–333.

281. H. Wiedersich and J. L. Katz, "The Nucleation of Voids and Other Irradiation-Produced Defect Aggregates," pp. 21–59 in Correlation of Neutron and Charged Particle Damage, ed., J. O. Stiegler, USERDA CONF-760673 (1976).

282. H. Wiedersich and B. O. Hall, J. Nucl. Mater. 66 (1977) 187.

283. B. N. Singh and A.J.E. Foreman, "The Influence of Vacancy Flux Supersaturation and Gas Concentration on Void Nucleation," pp. 205–211 in Consult. Symp. the Physics of Irradiation Produced Voids, ed., R. S. Nelson, AERE Harwell Report AERE-R-7934 (1975).

284. K. C. Russell, Acta Met. 26 (1978) 1615–1630.

285. J. R. Beeler, Jr., and M. F. Beeler, "Attrition and Stabilization of Void Nuclei: Critical Nucleus Size," pp. 289–302 in Effects of Radiation on Substructure and Mechanical Properties of Metals and Alloys, ASTM-STP-529, American Society for Testing and Materials (1973).

286. W. G. Wolfer and M. H. Yoo, "The Effect of Stress-Induced Diffusion on Void Nucleation," pp. II-458–II-474 in Conf. Proc. Radiation Effects and Tritium Technology for Fusion Reactors, eds., J. S. Watson and F. W. Wiffen, USERDA CONF-750989, Vol. II (1976).

287. L. K. Mansur and W. G. Wolfer, J. Nucl. Mater. 69&70 (1978) 825–829.

288. W. G. Wolfer and L. K. Mansur, J. Nucl. Mater. 91 (1980) 265–276.

289. B. N. Singh and A.J.E. Foreman, J. Nucl. Mater. 103&104 (1981) 1469–1474.

290. B. O. Hall, J. Nucl. Mater. 103&104 (1981) 1391–1396.

291. N. M. Ghoniem, J. Nucl. Mater. 89 (1980) 359–371.

292. L. K. Mansur, J. Nucl. Mater. 83 (1979) 109–127.

293. H. Venker and K. Ehrlich, J. Nucl. Mater. 60 (1976) 347–349.

294. A. D. Marwick, J. Phys. F 8 (1978) 1849–1861.

295. S. J. Rothman, L. J. Nowicki, and G. E. Murch, J. Phys. F. 10 (1980) 383–398.

296. F. A. Garner and W. G. Wolfer, J. Nucl. Mater. 102 (1981) 143–150.

297. H. R. Brager and F. A. Garner, J. Nucl. Mater. 73 (1978) 9–19.

298. H. R. Brager and F. A. Garner, "Dependence of Void Formation on Phase Stability in Neutron-Irradiated Type 316 Stainless Steel," pp. 207–232 in Effects of Radiation on Structural Materials, ASTM-STP-683, American Society for Testing and Materials, 1979.

299. H. R. Brager and F. A. Garner, "Microchemical Evolution of Neutron-Irradiated Stainless Steel," pp. 470–483 in Effects of Radiation on Materials: Tenth Conf., ASTM-STP-725, American Society for Testing and Materials, 1981.

300. H. R. Brager and F. A. Garner, "Analysis of Radiation-Induced Microchemical Evolution in 300 Series Stainless Steels," pp. 97–114 in Advanced Techniques for Characterizing Microstructures, eds., F. W. Wiffen and J. A. Spitznagel, TMS-AIME, Warrendale, PA, 1982.

301. F. A. Garner, "Acceleration of Irradiation Creep with Fluence: Absence of a Definitive Microstructural Record," pp. 101–112 in DAFS Quart. Progr. Rept. Sept. 30, 1982, DOE/ER-0046/11.

302. W. G. Wolfer, F. A. Garner, and L. E. Thomas," On Radiation-Induced Segregation and the Compositional Dependence of Swelling in Fe-Ni-Cr Alloys," pp. 1023–1041 in Effects of Radiation on Materials: Eleventh Conf., ASTM-STP-782, American Society for Testing and Materials, 1982.

303. D. L. Porter, J. Nucl. Mater. 92 (1980) 155–159.

304. D. L. Porter, J. Nucl. Mater. 79 (1979) 406–411.

305. L. E. Thomas, "Analytical Electron Microscopy of Neutron-Irradiated Reactor Alloys," pp. 594–597 in Proc. Fortieth Annual EMSA Meeting, ed., G. W. Bailey, Claitors Publ. Div., Baton Rouge, LA, 1982.

306. G. Brun, J. LeNaour, and M. Vouillen, J. Nucl. Mater. 101 (1981) 109–123.

307. A. D. Marwick, W.A.D. Kennedy, D. J. Mazey, and J. A. Hudson, Scripta Met. 12 (1978) 1015–1020.

308. P. J. Maziasz, "Identification of Preferential Polishing Effects Using Broad Probe AEM," pp. 196–197 in Proc. Forty-First Annual EMSA Meeting, ed., G. W. Bailey, San Francisco Press, Inc., 1983.

309. A. C. Damask and G. J. Dienes, Acta Met. 12 (1964) 797.

310. J. R. Manning, "Basic Mechanisms of Atomic Redistribution in Alloys Undergoing Irradiation," pp. 3–22 in Conf. Proc. Phase Stability During Irradiation, eds., J. R. Holland, L. K. Mansur, and D. I. Potter, The Metallurgical Society of AIME, Warrendale, PA, 1981.

311. F. Seitz, Physics Today, (June 1952) 6–9.

312. T. H. Blewitt and R. R. Coltman, Phys. Rev. 85 (1952) 384.

313. Y. Adda, M. Beyeler, and G. Brebec, Thin Solid Films 25 (1975) 107–156.

314. R. Sizmann, J. Nucl. Mater. 69&70 (1968) 386–412.

315. S. J. Rothman, "Effects of Irradiation on Diffusion in Metals and Alloys," pp. 189–211 in Phase Transformations During Irradiation, ed., F. V. Nolfi, Jr., Applied Science Publishers, New York, 1983.

316. L. S. Darken and R. W. Gurry, Physical Chemistry of Metals, McGraw Hill Publ. Co., New York, NY, 1953.

317. P. G. Shewmon, Diffusion in Solids, McGraw Hill Publ. Co., New York, NY, 1963.

318. J. R. Manning, Diffusion Kinetics for Atoms in Crystals, D. Van Norstrand Co., Princeton, NJ, 1968.

319. L. Darken, Trans. AIME 174 (1948) 184.

320. J. W. Christian, The Theory of Transformations in Metals and Alloys, Part I, 2nd ed., Pergamon Press, Oxford, England, 1975.

321. T. R. Anthony, "Solute Segregation and Stresses Generated Around Growing Voids in Metals," pp. 630–646 in Radiation-Induced Voids in Metals, eds., J. W. Corbett and L. C. Ianniello, USAEC CONF-710601, 1972.

322. G. S. Hartley, Trans. Faraday Soc. 42 (1946) 6.

323. A. D. Smigelskas and E. O. Kirdendall, Trans. AIME 171 (1947) 130.

324. P. R. Okamoto and H. Wiedersich, J. Nucl. Mater. 53 (1974) 336–345.

325. P. R. Okamoto, S. D. Harkness, and J. J. Laidler, Trans. Am. Nucl. Soc. 16 (1973) 70.

326. E. A. Kenik, Scripta Met. 10 (1976) 733–738.

327. P. R. Okamoto and L. E. Rehn, J. Nucl. Mater. 83 (1979) 2–23.

328. V. K. Sethi and P. R. Okamoto, "Irradiation-Induced Segregation in Complex Alloys," pp. 109–121 in Conf. Proc. Phase Stability During Irradiation, eds., J. R. Holland, L. K. Mansur, and D. I. Potter, The Metallurgical Society of AIME, Warrendale, PA, 1981.

329. J. L. Brimhall, D. R. Baer, and R. H. Jones, J. Nucl. Mater. 103&104 (1981) 1379–1384.

330. M. P. Seah and E. D. Hondros, Proc. Roy. Soc. London A 335 (1973) 191–212.

331. E. D. Hondros, "Energetics of Solid-Solid Interfaces," pp. 77–100 in Interfaces Conf., Melbourne 1969, ed. R. C. Gifkins, The Australian Institute of Metals, Buttersworth, London, 1969.

332. E. D. Hondros, "Interfacial Energies and Composition in Solids," pp. 1–30 in Conf. Proc. Precipitation Processes in Solids, eds., K. C. Russell and H. I. Aaronson, The Metallurgical Society of AIME, Warrendale, PA, 1978.

333. T. Ogura, C. J. McMahon, Jr., H. C. Feng, and V. Vitek, Acta Met. 26 (1978) 1317–1330.

334. R. E. Howard and A. B. Lidiard, Phil. Mag. 11 (1965) 1179–1187.

335. R. E. Hanneman and T. R. Anthony, Acta Met. 17 (1969) 1133–1140.

336. P. V. Ramasubramanian and D. F. Stein, Met. Trans. 4 (1973) 1735–1742.

337. C. L. Briant and R. A. Mulford, Met. Trans. 13A (1982) 745–752.

338. M. L. Wayinan and J. T. Gray, Acta. Met. 22 (1974) 349–355.

339. J.S.T. van Aswegen and R.W.K. Honeycombe, Acta Met. 10 (1962) 262–264.

340. J. M. Silcock and W. J. Tunstall, Phil. Mag. 10 (1964) 361–389.

341. F. R. Beckitt and B. R. Clark, Acta Met. 15 (1967) 113–129.

342. M. Yoshida, Scripta Met. 16 (1978) 787–790.

343. H. Wiedersich and N. Q. Lam, "Theory of Radiation-Induced Segregation," pp. 1–46 in Phase Transformations During Irradiation, ed., F. V. Nolfi, Jr., Applied Science Publishers, New York, 1983.

344. L. E. Rehn and P. R. Okamoto, "Non-Equilibrium Segregation in Irradiated Alloys," pp. 247–290 in Phase Transformations During Irradiation, ed., F. V. Nolfi, Jr., Applied Science Publishers, New York, 1983.

345. P. R. Okamoto, L. E. Rehn, and R. S. Averback, J. Nucl. Mater. 108&109 (1982) 319–330.

346. H. Wiedersich and P. R. Okamoto, "Efects of Radiation-Induced Segregation on Phase Stability," pp. 23–41 in Conf. Proc. Phase Stability During Irradiation, eds., J. R. Holland, L. K. Mansur, and D. I. Potter, The Metallurgical Society of AIME, Warrendale, PA, 1981.

347. P. H. Dederichs et al., J. Nucl. Mater. 69&70 (1978) 176–199.

348. D. I. Potter, L. E. Rehn, P. R. Okamoto, and H. Wiedersich, "Void Swelling and Segregation in Dilute Nickel Alloys," pp. 377–385 in Radiation Effects in Breeder Reactor Structural Materials, eds., M. L. Bleiberg and J. W. Bennett, TMS-AIME, New York, NY, 1977.

349. L. E. Rehn, P. R. Okamoto, D. I. Potter, and H. Wiedersich, J. Nucl. Mater. 74 (1978) 242–251.

350. H. Takahaski, S. Ohnuki, and T. Takeyama, J. Nucl. Mater. 103& 104 (1981) 1415–1420.

351. H. Wiedersich, P. R. Okamoto, and N. Q. Lam, "Solute Segregation During Irradiation," pp. 801–819 in Radiation Effects in Breeder Reactor Structural Materials, eds., M. L. Bleiberg and J. W. Bennett, TMS-AIME, New York, NY, 1977.

352. R. A. Johnson and N. Q. Lam, Phys. Rev. B 13 (1976) 4364–4375.

353. R. A. Johnson and N. Q. Lam, J. Nucl. Mater. 69&70 (1978) 424–433.

354. H. Wiedersich, P. R. Okamoto, and N. Q. Lam, J. Nucl. Mater. 83 (1979) 98–108.

355. N. Q. Lam, A. Kumar, and H. Wiedersich, "Kinetics of Radiation-Induced Segregation in Ternary Alloys," pp. 985–1007 in Effects of Radiation on Materials: Eleventh Conf., ASTM-STP-782, American Society for Testing and Materials, 1982.

356. J. Shao and E. S. Machlin, Met. Trans. **10A** (1979) 585–590.

357. Selected Values of the Thermodynamic Properties of Binary Alloys, eds., R. Hultgren et al., American Society for Metals, Metals Park, Ohio, 1973.

358. R. H. Doremus and E. F. Koch, Trans. Met. Soc. AIME **218** (1960) 591.

359. W. C. Leslie, Acta Met. **9** (1961) 1004–1022.

360. K. F. Hale and D. McLean, J. Iron Steel Inst. (April 1963) 337–352.

361. M. H. Lewis and B. Hattersley, Acta Met. **13** (1965) 1159–1168.

362. Introduction to Analytical Electron Microscopy, eds., J. J. Hren, J. I. Goldstein, and D. C. Joy, Plenum Press, New York, 1979.

363. L. P. Stoter, J. Mat. Sci. **16** (1981) 1039–1051.

364. J. Bentley and J. M. Leitnaker, "Stable Phases in Aged Type 321 Stainless Steel," pp. 70–91 in Conf. Proc. The Metal Physics of Stainless Steels, eds., E. W. Collings and H. W. King, The Metallurgical Society of AIME, New York, 1979.

365. A. F. Rowcliffe and R. B. Nicholson, Acta Met. **20** (1972) 143–155.

366. T. M. Williams and J. M. Titchmarsh, J. Nucl. Mater. **98** (1981) 223–226.

367. R. F. Campbell, S. H. Reynolds, L. W. Ballard, and K. G. Carroll, Trans. Met. Soc. AIME **218** (1960) 723–732.

368. R. Benz, J. F. Elliott, and J. Chipman, Met. Trans. **5** (1974) 2235–2240.

369. M. Waldenström, Met. Trans. **8A** (1977) 1963–1977.

370. T. M. Williams and P. W. Lake, "Some Characteristics of a Diamond Cubic Phase Commonly Observed in Irradiated Austenitic Steels," to be published in Conf. Proc. Dimensional Stability and Mechanical Behavior of Irradiated Metals and Alloys, **2**, BNES, held April 11–13, 1983, London, England.

371. R. F. Decker and S. Floreen, "Precipitation from Substitutional Iron-Base Austenitic and Martentitic Solid Solutions," pp. 69–129 in Symp. Proc. Precipitation from Iron-Base Alloys, eds., G. R. Speich and J. B. Clark, Met. Soc. Conf. **28**, Gordon and Breach Science Publishers, New York, 1965.

372. H. H. Stadelmaier, "Metal-Rich Metal-Metalloid Phases," pp. 141–180 in Developments in the Structural Chemistry of Alloy Phases, Plenum Press, New York, 1969.

373. T. M. Williams, J. M. Titchmarsh, and P. R. Arkell, J. Nucl. Mater. **107** (1982) 222–244.

374. A. Westgren, Jernkant. Ann. **117** (1933) 501–512.

375. J. E. Bridge, Jr., G. N. Maniar and T. V. Philip, Met. Trans. **2** (1971) 2209–2214.

376. A. Inoue and T. Masumoto, Met. Trans. **11A** (1980) 739–747.

377. S. Hamar-Thibault, M. Durand-Chaire, and B. Andries, Met. Trans. **13A** (1982) 545–550.

378. A. Westgren, Jerkant. Ann. **117** (1933) 1–14.

379. J. M. Leitnaker, R. L. Klueh, and W. R. Laing, Met. Trans. **6A** (1975) 1949.

380. P. J. Maziasz, Scripta Met. **13** (1979) 621–626.

381. C. G. Bolten et al., "Properties and Microstructures of 316 Stainless Steel," p. 183 in Mechanical Behavior of Materials, Pergamon Press, London, 1979.

382. F. Laves, Zeitschn. Krist. **73** (1930) 203.

383. D. I. Bardos, K. P. Gupta, and P. A. Beck, Trans. Met. Soc. AIME, **221** (1961) 1087–1088.

384. E. G. Bain and W. E. Griffiths, Trans. Met. Soc. AIME **75** (1927) 166.

385. K. W. Andrews, Nature **164** (1949) 1015.

386. J. A. Spitznagel and R. Stickler, Met. Trans. **5** (1974) 1363–1371.

387. I.C.I. Okafer and O. N. Carlson, Met. Trans. **9A** (1978) 1651–1657.

388. A. S. Grot and J. E. Spruiell, Met. Trans. **6A** (1975) 2023–2030.

389. P. J. Maziasz, "Helium Trapping at Ti-Rich MC Particles in Ti-Modified Austenitic Stainless Steel," pp. 477–492 in Conf. Proc. Phase Stability During Irradiation, eds., J. R. Holland, L. K. Mansur, and D. I. Potter, The Metallurgical Society of AIME, Warrendale, PA, 1981.

390. P. J. Maziasz, J. A. Horak, and B. L. Cox, "The Influence of Both Helium and Neutron Irradiation on Precipitation in 20%-Cold-Worked Austenitic Stainless Steel," pp. 271–292 in Conf. Proc. Phase Stability During Irradiation, eds., J. R. Holland, L. K. Mansur, and D. I. Potter, The Metallurgical Society of AIME, Warrendale, PA, 1981.

391. P. J. Maziasz and N. J. Zaluzec, "Application of Quantitative EELS to Analysis of the Titanium Carbide Phase in Austenitic Stainless Steels," pp. 498–499 in Proc. Fortieth Annual EMSA Meeting, ed., G. W. Bailey, Claitor's Publ. Division, Baton Rouge, LA, 1982.

392. L. Hollan, Ann. Chim. **1** (1966) 437–448.

393. W. Jeitschko, Met. Trans. **1** (1970) 2963–2965.

394. A. Taylor and R. W. Floyd, J. Inst. Met. **81** (1952–53) 451.

395. P. K. Rastogi and A. J. Ardell, Acta Met. **19** (1971) 321–330.

396. J. K. Van Deen and F. Van der Woude, Acta. Met. **29** (1981) 1255–1262.

397. H. J. Beattie and F. L. Ver Snyder, Nature **178** (1956) 208.

398. F. X. Spiegel, D. Bardos, and P. A. Beck, Trans. Met. Soc. AIME 227 (1963) 575–579.

399. E. I. Gladyshevskii and L. K. Borusevich, transl. Russ. J. Inorganic Chem. **8** (1963) 997–1000.

400. J. M. Silcock, Met. Sci. (Dec. 1978) 561–570.

401. P. J. Maziasz, "Precipitation Response of Austenitic Stainless Steel to Simulated Fusion Irradiation," pp. 160–180 in Conf. Proc. Metal Physics of Stainless Steel, eds., E. W. Collings and H. W. King, The Metallurgical Society of AIME, New York, 1979.

402. T. M. Williams, "Precipitation in Irradiated and Unirradiated Stainless Steel," pp. 166–185 in Effects of Irradiation on Materials: Eleventh Conf., ASTM STP-782, American Society for Testing and Materials, 1982.

403. J. W. Christian, The Theory of Transformations in Metals and Alloys, Part I: Equilibrium and General Kinetic Theory, 2nd ed., Pergamon Press, New York, 1975.

404. R. B. Nicholson, "The Role of Interfaces in Precipitation Processes," pp. 139–158 in Inter. Conf. Interfaces, ed., R. C. Gifkins, The Australian Institute of Metals, Butterworths, Australia, 1969.

405. R. B. Nicholson, "Nucleation at Imperfections," pp. 269–312 in Phase Transformations, American Society for Metals, Metals Park, OH, 1970.

406. K. C. Russell, "Nucleation in Solids," pp. 219–268 in Phase Transformations, American Society for Metals, Metals Park, OH, 1970.

407. H. I. Aaronson, J. K. Lee, and K. C. Russell," Diffusional Nucleation and Growth," pp. 31–86 in Conf. Proc. Precipitation Processes in Solids," eds., K. C. Russell and H. I. Aaronson, The Metallurgical Society of AIME, Warrendale, PA, 1978.

408. H. I. Aaronson, C. Laird, and K. R. Kinsman, "Mechanisms of Diffusional Growth of Precipitate Crystals," pp. 313–396 in Phase Transformations, American Society for Metals, Metals Park, OH, 1970.

409. J. O. Nilsson and G. L. Dunlop, J. Microscopy **115** (1978) 235–242.

410. D. R. Gaskell, Introduction to Metallurgical Thermodynamics, McGraw Hill Book Company, New York, 1973.

411. Y. A. Chang and D. Naujock, Met. Trans. **3** (1972) 1693–1698.

412. D. R. Arkell and P.C.L. Pfeil, J. Nucl. Mater. **12** (1964) 145–152.

413. J. A. Brinkman and H. Wiedersich, "Mechanisms of Radiation Damage in Reactor Materials," pp. 3–39 in Symp. Flow and Fracture of Metals and Alloys in Nuclear Environments, ASTMSTP-380, American Society for Testing and Materials, 1965.

414. C. Brown, "Voids and Rod-Shaped Features in 316 Stainless Steel Irradiated to Low Doses in DFR," pp. 83–89 in Consultant Symp. The Physics of Irradiation Produced Voids, ed., R. S. Nelson, AERE Harwell Report, AERE-R-7934 (January 1975).

415. R. K. Williams, J. O. Stiegler, and F. W. Wiffen, "Irradiation Effects in Tungsten-Rhenium Alloys," Oak Ridge National Laboratory Report, ORNL-TM-4500 (1974), pp. 52–60.

416. V. K. Sikka and J. Moteff, Met. Trans. **5** (1974) 1514–1517.

417. C. Cawthorne and C. Brown, J. Nucl. Mater. **66** (1977) 201–202.

418. L. E. Thomas, Trans. Am. Nucl. Soc. **28** (1978) 151.

419. D. L. Porter and E. L. Wood, J. Nucl. Mater. **83** (1979) 90–97.

420. J. T. Stanley and K. R. Garr, Met. Trans. **6A** (1975) 531–535.

421. J. T. Stanley and L. E. Hendrickson, J. Nucl. Mater. **87** (1979) 69–78.

422. D. J. Mazey, D. R. Harries, and J. A. Hudson, J. Nucl. Mater. **89** (1980) 155–181.

423. R. M. Boothby and T. M. Williams, J. Nucl. Mater. **96** (1981) 64–70.

424. P. J. Maziasz, J. Nucl. Mater. **85&86** (1979) 713–717.

425. T. M. Williams and J. M. Titchmarsh, J. Nucl. Mater. 87 (1979) 398–400.

426. W.J.S. Yang, H. R. Brager, and F. A. Garner, "Radiation-Induced Phase Development in AISI 316," pp. 257–270 in Conf. Proc. Phase Stability During Irradiation, eds., J. R. Holland, L. K. Mansur, and D. I. Potter, The Metallurgical Society of AIME, Warrendale, PA, 1981.

427. W.J.S. Yang and F. A. Garner, "Relationship Between Phase Development and Swelling of AISI 316 During Temperature Changes," pp. 186–206 in Effects of Radiation on Materials, Eleventh Conf., ASTM-STP-782, eds., H. R. Brager and J. S. Perrin, American Society for Testing and Materials, 1982.

428. E. H. Lee, N. H. Packan, and L. K. Mansur, "Effects of Pulsed Dual-Ion Irradiation on Phase Transformations and Microstructure in Ti-Modified Austenitic Alloy," to be published in Journal of Nuclear Materials.

429. A. F. Rowcliffe and E. H. Lee, J. Nucl. Mater. **108&109** (1982) 306–318.

430. J. A. Hudson, J. Br. Nucl. Energy Soc. **14** (1975) 127–136.

431. J. A. Hudson, "Precipitation under Irradiation," pp. 284–313 in Conf. Proc. Precipitation Processes in Solids, eds., K. C. Russell and H. I. Aaronson, The Metallurgical Society of AIME, Warrendale, PA, 1978.

432. Workshop on Solute Segregation and Phase Stability During Irradiation, J. O. Stiegler, ed., J. Nucl. Mater. **83** (1979).

433. Conf. Proc. Phase Stability During Irradiation, eds., J. R. Holland, L. K. Mansur, and D. I. Potter, The Metallurgical Society of AIME, Warrendale, PA, 1982.

434. Phase Transformations During Irradiation, ed., F. V. Nolfi, Jr., Applied Science Publishers, New York, 1983.

435. K. C. Russell, "Effects of Irradiation on Stability of Alloy Phases," pp. 821–839 in Radiation Effects in Breeder Reactor Structural Materials, eds., M. L. Bleiberg and J. W. Bennett, The Metallurgical Society of AIME, New York, 1977.

436. K. C. Russell, J. Nucl. Mater. **83** (1979) 176–185.

437. H. J. Frost and K. C. Russell, "Precipitate Stability under Irradiation," pp. 75–113 in Phase Transformations During Irradiation, ed., F. V. Nolfi, Jr., Applied Science Publishers, New York, 1983.

438. G. Martin, J. L. Bocquet, A. Barbu, and Y. Adda, "Fundamental Aspects of the Evolution of, and Phase Changes in, Metals and Alloys Under Irradiation," pp. 899–915 in Radiation Effects in Breeder Reactor Structural Materials, eds., M. L. Bleiberg and J. W. Bennett, The Metallurgical Society of AIME, New York, 1977.

439. G. Martin, R. Cauvin, and A. Barbu, "Solid Solution Stability Under Irradiation," pp. 47–74 in Phase Transformations During Irradiation, ed., F. V. Nolfi, Jr., Applied Science Publishers, New York 1983.

440. P. Wilkes, J. Nucl. Mater. **83** (1979) 166–175.

441. R. S. Nelson, J. A. Hudson, and D. J. Mazey, J. Nucl. Mater. **44** (1972) 318–330.

442. A. Barbu and G. Martin, Scripta Met. **11** (1977) 771–775.

443. S. I. Maydet and K. C. Russell, J. Nucl. Mater. **64** (1977) 101–114.

444. N. Q. Lam, P. R. Okamoto, H. Wiedersich, and A. Taylor, Met. Trans. **9A** (1978) 1707–1714.

445. L. Kaufman, J. S. Watkins, J. H. Gittus, and A. P. Miodownik, "The Effects of Irradiation on Phase Stability," pp. 1065–1076 in Applications of Phase Diagrams in Metallurgy and Ceramics, Vol. 2, National Bureau of Standards, Spec. Publ. 496, 1977.

446. J. L. Bocquet and G. Martin, J. Nucl. Mater. **83** (1979) 186–199.

447. K. Urban and G. Martin, Acta Met. **30** (1982) 1209–1218.

448. J. P. Shepherd, Mat. Sci. J. **3** (1969) 229–234.

449. P. S. Sklad and T. E. Mitchell, Scripta Met. **8** (1974) 1113.

450. H. J. Frost and K. C. Russell, Acta Met. **30** (1982) 953–960.

451. L. M. Howe and M. H. Rainville, J. Nucl. Mater. **68** (1977) 215.

452. R. H. Jones, J. Nucl. Mater. **74** (1978) 163–166.

453. A. L. Chang and M. Baron, J. Nucl. Mater. **83** (1979) 214–222.

454. D. I. Potter, "Ion-Bombardment-Induced Instabilities in Ordered Precipitates," pp. 521–546 in Conf. Proc. Phase Stability During Irradiation, eds., J. R. Holland, L. K. Mansur, and D. I. Potter, The Metallurgical Society of AIME, Warrendale, PA, 1982.

455. P. Chou and N. M. Ghoniem, "Precipitate Dissolution by High Energy Cascade Dissolution," to be published in Journal of Nuclear Materials.

456. W. V. Vaidya, J. Nucl. Mater. **83** (1978) 223–230.

457. I.M.L. Lifshitz and V. V. Slyozov, J. Chem. Phys. **19** (1961) 35–50.

458. C. Wagner, Z. Elecktochemie **65** (1961) 581–591.

459. K. C. Russell, Scripta Met. **3** (1969) 313–316.

460. P. Wilkes, K. Y. Liow, and R. G. Lott, Rad. Effects **29** (1976) 249–251.

461. W. Kesternich and J. Rothaut, J. Nucl. Mater. **103&104** (1981) 845–852.

462. J. A. Horak, "Helium Implantation in Potential CTR Structural Materials," pp. 40–42 in Cont. Thermonucl. Matls. Technol. Progr. Annu. Prog. Rept., Oak Ridge National Laboratory Report, ORNL-5082, (October 1975).

463. E. E. Bloom, J. A. Woods, and A. F. Zulliger, "Description of EBR-II Subassembly X-100," Oak Ridge National Laboratory Report, ORNL-TM-3389 (June 1971).

464. F. W. Wiffen and P. J. Maziasz, J. Nucl. Mater. 103&104 (1981) 821–826.

465. P. J. Maziasz, "Microstructural Development of 20%-Cold-Worked Type 316 and 316 + Ti Stainless Steels Irradiated in HFIR: Temperature and Fluence Dependence of the Dislocation Component," pp. 54–97 in ADIP Semiann. Prog. Rept., Sept. 30, 1981, DOE/ER-0045/7.

466. M. L. Grossbeck and K. C. Liu, Nucl. Technol. 58 (1982) 538–547.

467. M. L. Grossbeck and P. J. Maziasz, "The Swelling of 20%-Cold-Worked Type 316 Stainless Steel Irradiated in HFIR to Helium Levels of 200–3700 at. ppm," pp. 82–85 in ADIP Quart. Prog. Rept. Mar. 31, 1978, DOE/ET-0058/1.

468. C.K.H. DuBose and J. O. Stiegler, "Semiautomatic Preparation of Specimens for Transmission Electron Microscopy," Oak Ridge National Laboratory Report, ORNL-4066 (February 1967).

469. P. Hirsch et al., Electron Microscopy of Thin Crystals, Robert E. Krieger Publ. Co., Huntington, NY, 1977.

470. L. E. Murr, Electron Optical Applications in Materials Science, McGraw-Hill, New York, 1970.

471. J. W. Edington, "Interpretations of Transmission Electron Micrographs," No. 3 of Monographs in Practical Electron Microscopy in Materials Science, Philips Technical Library, Netherlands, 1975.

472. J. E. Hilliard, "Measurement of Volume in Volume," pp. 44–76 and Ervin E. Underwood, "Surface Area and Length in Volume," pp. 77–127 in Quantitative Microscopy, eds., R. T. DeHoff and F. N. Rhines, McGraw-Hill Publ. Co., New York, 1968.

473. P. R. Okamoto and S. D. Harkness, J. Nucl. Mater. 48 (1973) 204–206.

474. J. B. Mitchell and W. L. Bell, Acta Met. 24 (1976) 147–152.

475. G. M. Michal and R. Sinclair, Phil. Mag. A 42 (1980) 691–704.

476. J. Bentley, "Advantages of a Field Emission Gun for a Combined Analytical and High Resolution Transmission Electron Microscope," pp. 72–73 in Proc. Thirty-Eighth Annual EMSA Meeting, ed., G. W. Bailey, Claitors Publ. Co., Baton Rouge, LA (1980).

477. J. Bentley, N. J. Zaluzec, E. A. Kenik, and R. W. Carpenter, "Optimization of an Analytical Electron Microscope for X-Ray Microanalysis: Instrumental Problems," pp. 581–594 in Scanning Electron Microscopy II, SEM, Inc., AMF, O'Hare, IL (1979).

478. P. J. Maziasz and G. R. Odette, "Wide Area Beam Averaged AEM of Precipitate Particles Extracted on Replicas from Type 316 Stainless Steel," pp. 198–199 in Proc. Forty-First Annual EMSA Meeting, ed., G. W. Bailey, San Francisco Press, Inc., San Francisco, CA (1983).

479. N. J. Zaluzec, "Quantitatiave X-Ray Microanalysis: Instrumental Considerations and Applications to Materials Science," pp. 121–167 (Chap. 4) in Introduction to Analytical Electron Microscopy, eds., J. J. Hren, J. I. Goldstein, and D. C. Joy, Plenum Press, New York, 1979.

480. N. J. Zaluzec, "On the Geometry of the Absorption Correction for Analytical Electron Microscopy," pp. 325–328 in Microbeam Analysis – 1981, ed., R. H. Geiss, San Francisco Press, Inc., San Francisco, CA (1981).

APPENDIXES

APPENDIX A

TABLE OF MORPHOLOGICAL VARIANTS AND APPROXIMATE SHAPE FACTORS FOR PHASES FOUND IN SA 316

PHASE	VARIANT	CRYSTAL HABIT	TEM EVIDENCE	ASSUMED SHAPE
	THERMAL AGING			
$M_{23}C_6(\tau)$	LATH-1 (560–800°C)[a]	CUBE ON CUBE	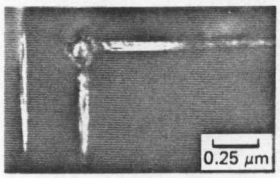	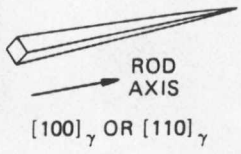 $[100]_\gamma$ OR $[110]_\gamma$
	LATH-2 (650–800°C)	CUBE ON CUBE		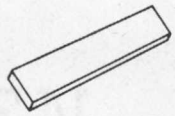
	CLUSTER-ROD (600–800°C)	CUBE ON CUBE	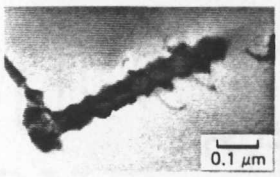	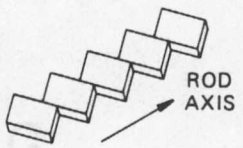 $[001]_\gamma$ OR $[011]_\gamma$
	BLOCKY (560–800°C)	CUBE ON CUBE	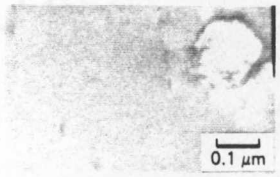	
	PLATE (560–800°C)	CUBE ON CUBE	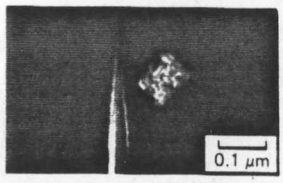	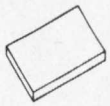

PHASE	VARIANT	CRYSTAL HABIT	TEM EVIDENCE	ASSUMED SHAPE
THERMAL AGING (CONT'D)				
LAVES	LATH (650–800°C)	LAVES[b] OR-I, II	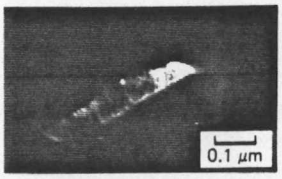	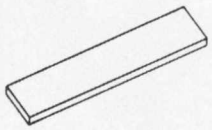
	BLOCKY (650–800°C)	LAVES OR-III	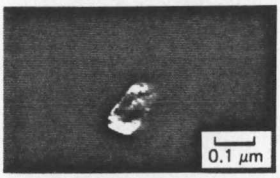	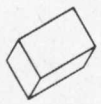
χ	ROD (800°C)	?		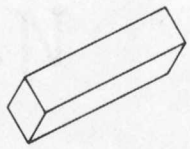
	BLOCKY (800°C)	CHI OR-II	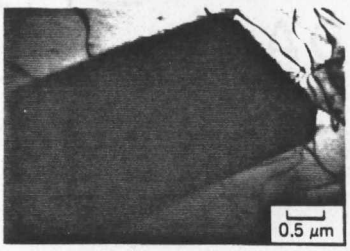	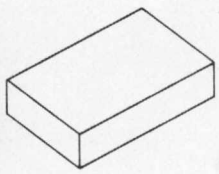
σ	GLOBULAR (650–900°C)	SIGMA OR-I OR II	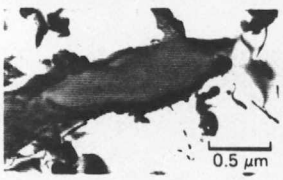	?

PHASE	VARIANT	CRYSTAL HABIT	TEM EVIDENCE	ASSUMED SHAPE
	EBR-II IRRADIATION			
γ'	EQUIAXED (500°C, 8.4 dpa)	CUBE ON CUBE	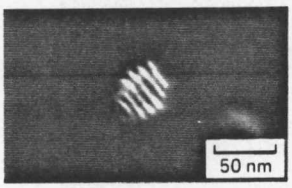	
PHOSPHIDE A	LATH OR ROD (500–525°C, 8.4–31 dpa)	?	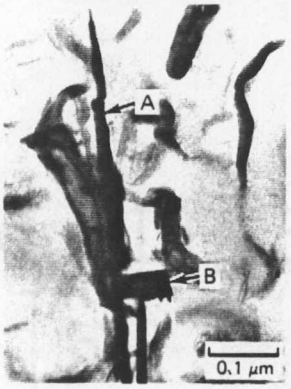	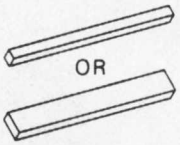
PHOSPHIDE B	BLOCKY (500–525°C, 8.4–31 dpa)	?		
PHOSPHIDE B	LATH OR ROD (625°C, 8.4 dpa)	?	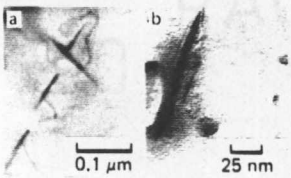	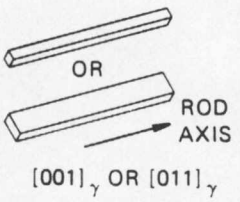
G PHASE	BLOCKY (500°C, 8.4 dpa)	?		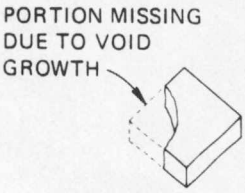

PHASE	VARIANT	CRYSTAL HABIT	TEM EVIDENCE	ASSUMED SHAPE
EBR-II IRRADIATION (CONT'D)				
$M_6C(\eta)$	BLOCKY	M_6C, OR-II	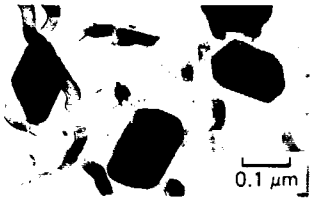	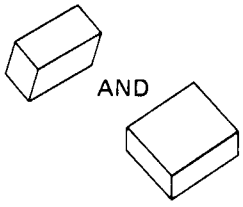
HFIR IRRADIATION				
LAVES	ROD	?	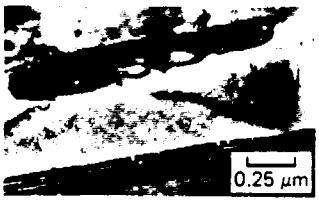	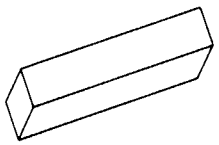
χ	PLATE	CHI, OR-I	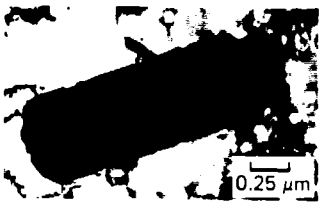	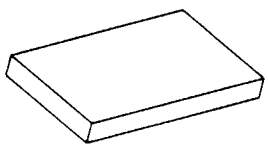

[a]( ) INDICATES THE TEMPERATURE RANGE OVER WHICH THIS PARTICULAR MORPHOLOGICAL VARIANT IS OBSERVED.

[b]THESE ORIENTATION RELATIONSHIPS (OR's) ARE DESCRIBED IN MORE DETAIL IN THE FOLLOWING APPENDIX.

[c]IN-FOIL TEM OF PHOSPHIDE B RODS.

[d]REPLICA TEM OF PHOSPHIDE B RODS.

[e]GENERAL PHENOMENON OF VOID GROWTH AT AN INTERPHASE BOUNDARY AND INTO BOTH PHASES. THIS OCCURS ON MANY OF THE RIS-COMPATIBLE PHASES THAT OCCUR UNDER IRRADIATION.

APPENDIX B

TABLE OF SOME CRYSTALLOGRAPHIC HABITS (OR ORIENTATION RELATIONS) FOR VARIOUS PHASES

PHASE	ORIENTATION RELATION (OR)	ELECTRON DIFFRACTION EVIDENCE	SUPERPOSITION ONTO $(001)_\gamma$ AUSTENITE STEREOGRAPHIC PROJECTION
$M_{23}C_6$ (τ) AND Ni_3Si (γ')	CUBE ON CUBE	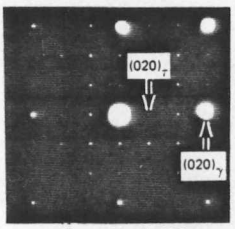 ZAP[a]: $(001)_\tau \parallel (001)_\gamma$	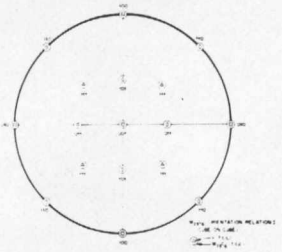
		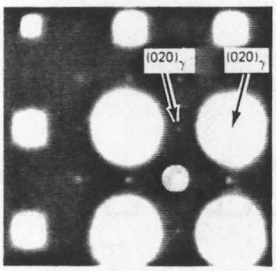 ZAP: $(001)_\gamma \parallel (001)_\gamma$	SIMILAR TO ABOVE
M_6C (η) AND POSSIBLY G-PHASE	OR-II (MANY VARIANTS)	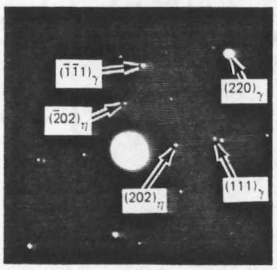 ZAP: $(010)_\eta$ NEARLY $\parallel (110)_\gamma$	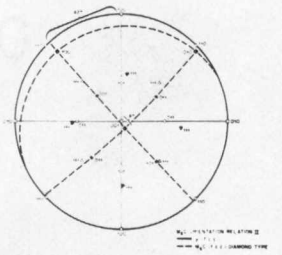
LAVES	OR-II	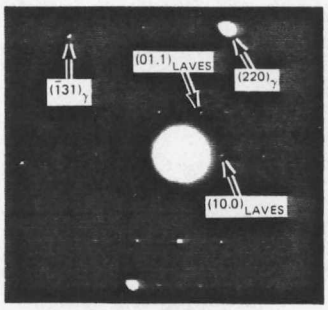 ZAP: $[12.\bar{2}]_{LAVES}$ NEAR $(1\bar{1}4)_\gamma$	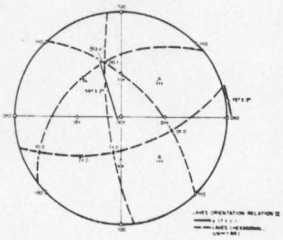

TABLE OF SOME CRYSTALLOGRAPHIC HABITS (OR ORIENTATION RELATIONS) FOR VARIOUS PHASES (CONT'D)

PHASE	ORIENTATION RELATION (OR)	ELECTRON DIFFRACTION EVIDENCE	SUPERPOSITION ONTO $(001)_\gamma$ AUSTENITE STEREOGRAPHIC PROJECTION
LAVES	OR-III	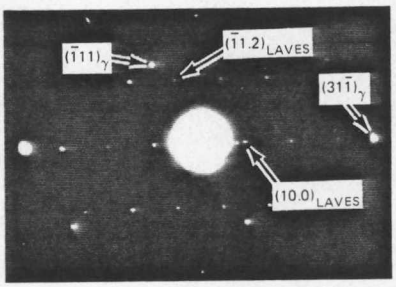 ZAP: $[1\bar{2}.1]_{LAVES}$ NEARLY $\parallel (1\bar{1}2)_\gamma$	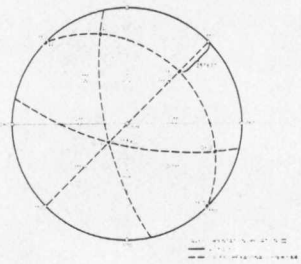
χ	OR-I	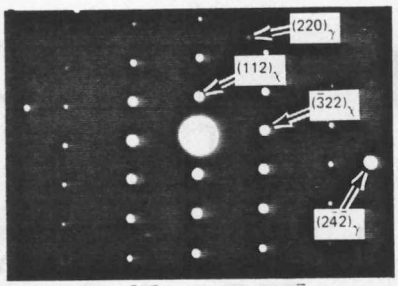 ZAP: $(\bar{6}8\bar{1})_\chi$ NEARLY $\parallel (1\bar{1}3)_\gamma$	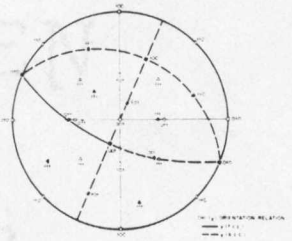
σ	OR-I	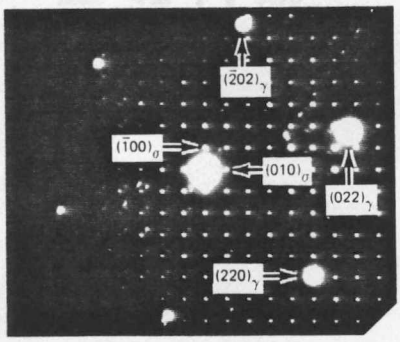 ZAP: $(001)_\sigma \parallel (1\bar{1}1)_\gamma$	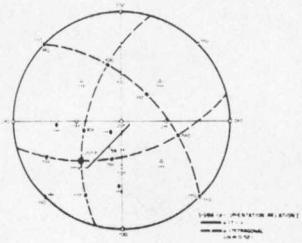

[a]ZAP – ZONE AXIS PATTERN

VITA

Philip James Maziasz was born in Dearborn, Michigan, on February 1, 1951. He attended Divine Child Catholic elementary and high schools in that city, and graduated from high school in June 1969. He graduated with highest honors and was elected to the National Honor Society. He entered the University of Michigan the following September, having been awarded Michigan Higher Education, Regents-Alumni and Evans scholarships. He graduated with a Bachelor of Science degree in Materials and Metallurgical Engineering in December 1973, with magna cum laude and Outstanding Achievement Award (undergraduate) honors. He also received the George H. Benzenberger Award and Dow Scholarship and was elected to Tau Beta Pi (president) and Alpha Sigma Mu honorary societies as an undergraduate.

Prior to graduation, he was married to Veronica Sadowski in May 1973 and then continued graduate studies at the University of Michigan after receiving a full traineeship from the Atomic Energy Commission. In June 1974 he attended the Summer Materials Science Institute at the Argonne National Laboratory to complete a master project on radiation damage to materials (radiation-induced solute segregation and the effect of titanium additions on void formation in austenitic stainless steel). He graduated with a Masters of Science degree in Nuclear Engineering (Nuclear Materials Option) in December 1974.

Prior to graduation he accepted employment at the Oak Ridge National Laboratory in the Radiation Effects and Microstructural Analysis Group of the Metals and Ceramics Division in October 1974.

He began as an associate metallurgical engineer on the Fusion Materials Program and then enrolled in the graduate school of the University of Tennessee in January 1975. He received a Doctor of Philosophy degree in Metallurgical Engineering in December 1984. He remains employed at the Oak Ridge National Laboratory as a research staff member. He is a member of the American Society for Metals and of the Electron Microscopy Society of America.

Mr. Maziasz has two sons, Andrew, born in September 1977, and Matthew, born in July 1984. Mr. Maziasz accepted Jesus Christ as Lord and Savior in 1973 and is a member of the Christian Business Men's Committee of U.S.A.